

Studies of Ginzburg-Landau theories for two-component chiral supercon- ductors

Fredrik Nicolai Krohg

Trondheim, June 25, 2021

Abstract

The symmetry of the superfluid A -phase of He³ has previously been suggested to describe the unconventional superconducting state of Sr₂RuO₄ which would make this material a chiral p -wave superconductor. In this thesis we discuss tools, results and techniques useful in the theoretical description of superconductors with this symmetry.

In Paper I we use field-integral techniques to investigate the effects of spin-orbit coupling on the coefficients of the phenomenological Ginzburg-Landau theory of chiral p -wave superconductors. We find that these coefficients have a non-linear anisotropic dependence on the spin-orbit coupling strength and direction in spin-space. This dependence necessitates two independent phenomenological parameters for the mixed gradient terms and the mixed component terms respectively, even in the weak-field limit when written using dimensionless variables.

In Paper II we use large-scale Monte-Carlo simulations to investigate the vortex-matter of a superconducting system that can be modelled by a Ginzburg-Landau theory with chiral p -wave symmetry such as the one investigated in Paper I, but now in the limit of vanishing spin-orbit coupling. We find that a square vortex lattice consisting of single-quanta vortices is stable at high temperatures close to $T_c(B)$. The single-quanta vortices merge into double-quantum vortices at lower temperature which together then stabilizes a triangular vortex lattice.

In Paper III we investigate a Z_2 Ising transition resulting from spontaneously broken time-reversal symmetry in the neutral sector of chiral p -wave symmetric superconductors subjected to zero external field.

We find that this transition is irrevocably tied to the superconducting transition for all realistic values of the phenomenological parameters in our model.

Preface

This thesis is submitted in partial satisfaction of the requirements of the degree Philosophiae Doctor (PhD) at the Norwegian University of Science and Technology, in Trondheim Norway.

The work that this thesis presents started in September 2015 and ended in early spring 2021 at the [Center for Quantum Spintronics \(QuSpin\)](#), NTNU. During this time, one year of accumulated time was dedicated to teaching duties at the Department of Physics, and half a year was devoted to completion of courses (30 ECTS) as pr. the requirements of the degree. The research was supervised by Prof. Asle Sudbø as main supervisor, and Prof. Jacob Linder as co-supervisor.

Computation-time was granted at the VILJE and FRAM supercomputers through the UNINETT σ igma2 e-infrastructure. The code was written in the [JULIA](#) programming language. The figures and plots were produced by the use of [JULIA](#) and [INKSCAPE](#). The thesis was written in [L^AT_EX](#) based on a [template](#) by [J. A. Ouassou](#) available under [CC BY 4.0 license](#), that was heavily modified.

Fredrik Nicolai Krohg
Oslo, June 2021

Acknowledgements

First I would like to thank my supervisor Prof. Asle Sudbø for his willingness to take on a PhD student that had little in regards to previous knowledge of condensed matter systems, for providing me with a steady stream of insights and ideas for interesting research topics and for his long patience with my own slow and sometimes meandering progress towards publishable results.

I would like to thank the rest of the people in our research group who I have come to know along the way; Troels Arnfred Bojesen who I met for the first time during my visit to the March Meeting in New Orleans in 2017, who shared my fascination for Japan and whom have been of invaluable assistance in understanding and troubleshooting the intricacies of Monte-Carlo algorithms and techniques. Stephan Rex, who apart from inspiring me to start running, helped me in times when I was stuck on mathematical technicalities and proved an excellent travelling companion. Peder Notto Galteland, who helped ease my introduction into the social circles of the theory-section as it stood back in 2015. Henning Goa Hugdal, whose gentle demeanor and generosity made him always approachable and provided a soothing presence in times of need. Even Thingstad, whose vast depth of knowledge in all things physics I both benefited from, and which inspired me greatly, who was an amazing partner in our task of inspiring the younger generation, and whose friendship I hold dearly. Håvard Homleid Haugen who has been an excellent collaborator with a keen eye for programming, and intuitive understanding, with whom I've had

numerous very stimulating discussions about physics and in general. Jonas Blomberg Ghini, whose outlook on life seems so much like my own and who I regret not getting to know sooner. And lastly, Eirik Erlandsen whose brilliant and vigorous gregariousness has been a source of tremendous amounts of laughter and joy.

In the department of physics at NTNU there are many others who deserve recognition and praise for their role in creating a friendly and interesting social environment. To mention everyone by name in such a long PhD as I have had would prove excessive and frankly a boring read. Therefore I will not attempt to make an exhaustive list but mention only a select few.

Of these, first I want to extend a thank you to all the post-docs and doctoral students who were already there in the “theory corridor” and in the (old) lunchroom when I started my PhD. You were all role models and people I respected greatly. People such as Sol, Alireza and Roberto. André, with whom I shared an interest in sci-fi. Eirik, whom I already knew from our masters program, Eirik Torbjørn Bakken who gave me a connection to the experimentalists at NTNU and Manu Linereas with whom I shared an office. During my stay at the March Meeting I travelled with Dag-Vidar who proved splendid and stimulating company. When I started my PhD it was my honor to start at the same time as the other doctoral students Sverre, Therese, Jabir, and Vetle. You have perhaps shaped my stay most of all and deserve special thanks for all our shared memories of running, climbing, conversations, painting and music. In this connection I also want to mention Marina, who we almost counted as a theorist for all her gifts of company during our lunch-breaks and outside of work.

The next generation of students included Martin and Øyvind. Two brilliant people: Martin with his many cat-stories and perceptive humor, and Øyvind with his thoughtfulness and warm smile. Also, I have to mention of-course Jeroen and his student Arnaud who I feel have been there almost from the beginning. Jeroen who contributed greatly to forming a sense of community among the doctoral students of what has become QuSpin, lifting the intelligence-level in all conversations he joined and making me aware of resources of learning I had previously missed. Arnaud, who I came to know better gradually as the years passed as having a great sense of humor and taste, and impor-

tantly: a willingness to join me for Beatz! Another co-conspirator in that endeavour has been Akash, a man I learned a great deal from not only about physics and its thinly veiled politics but also in areas of life, philosophy and sociology, one who has been integral in the culture of QuSpin and who it's been an absolute pleasure knowing.

I want to give a big thanks to Frode, my other office-mate and good friend whose many discussion on physical fitness have been inspiring and educational. I want to thank my good friends Matthias and Maximilian for many intelligent conversations over good food and drink, and foraging expeditions into the forests of Trondheim.

In the last generation of QuSpin students I would be remiss not to mention Atousa, Lina, Marion, Payel, Jonas and Longfei who have provided laughter, good company and engaging conversations, and whom I hope will have a nice and productive future in QuSpin in spite of the limitations that the pandemic enforces.

My fantastic family deserve recognition above everyone as the ones who have shown me unwavering support and love all through my life and this journey in spite of our long-standing geographical separation and my own need for seclusion when I immerse myself in my studies. To my mom and dad. To know that your door always is open should I fall, allows me the courage to continue walking. To my two brothers who endured the consequences of all my uncertainties, thank you for always letting our unity overshadow our differences. To my last sibling who in many ways reminds me much of myself, thank you for all your warm hugs and for showing me your strength. To my paternal grandfather and late grandmother who from an early age helped encourage my interest in science and maternal grandmother whose wisdom and love supersedes even Her long age.

A special thanks to David for providing much needed office-space and shelter during this time of corona. A huge thank you to my girlfriend, who perhaps more than anyone has had a front row seat in all the ups and downs in this long journey. I am so so grateful for all you have taught me, healed me and all the love you have given and continue to give.

Finally a big thank you to myself for staying the course and never yielding no matter how insurmountable the challenges have seemed.

List of papers

Paper I:

Fredrik Nicolai Krohg and Asle Sudbø

Derivation of Ginzburg-Landau free energy density containing mixed gradient terms of a $p + ip$ superconductor with spin-orbit coupling

Physical Review B **98**, 014510 (2018) [1]

Paper II:

Fredrik Nicolai Krohg, Håvard Homleid Haugen, Julien Garaud, Egor Babaev, and Asle Sudbø

Thermal fluctuations and vortex lattice structures in chiral p -wave superconductors: robustness of double-quanta vortices

Physical Review B **103**, 214517 (2021) [2]

Paper III:

Håvard Homleid Haugen, Egor Babaev, Fredrik Nicolai Krohg and Asle Sudbø

First order superconducting phase transition in chiral $p + ip$ system

arXiv:2106.01007 (2021) [3]

Contents

1	Introduction	1
1.1	A brief history of superconductivity	3
1.2	About this work	6
2	Statistical Mechanics	11
2.1	Canonical ensemble and the partition function	11
2.2	Calculating observables	13
2.3	Ginzburg-Landau model	14
3	Field Theory Methods	21
3.1	Quadratic Fermionic Field Integrals	22
3.2	Matsubara formalism	27
3.3	Hubbard-Stratonovich transformation	29
3.4	Field theory approximations	33
4	Group Theory	39
4.1	Irreducible representations	39
4.2	BCS Hilbert Space	40
4.3	Application of group elements	42
4.4	Single-particle Hamiltonian symmetries	48
4.5	Projection Operators	51
4.6	Symmetries of the Square Lattice	52
4.7	Square Lattice Harmonics	56
4.8	Decomposition of the Potential	60
5	Lattice Models	65
5.1	Discretizing derivatives	66
5.2	Including an external field	71
6	Monte-Carlo Techniques	77
6.1	Markov-Chain Monte-Carlo method	78
6.2	Metropolis-Hastings method	79
6.3	Thermalization procedures	82
6.4	Parallel tempering	86

6.5	Grid parallelization	88
6.6	Reweighting	90
7	Vortices in superconductors	97
7.1	Vorticity observables	98
7.2	Unconventional vortices	100
7.3	Ensembles of vortices	102
7.4	Observables of lattice symmetry	106
8	Outlook	113
	Bibliography	115

Introduction

Research into superconductors holds a vital key in the development of technologies that can reduce global emissions of greenhouse gasses and thus prevent large economic as well as human losses due to the effects of the climate crisis. In IPCC's special report, they state that in order to have no or limited overshoot in global temperature from the goal of 1.5 °C, the global net anthropogenic emissions of CO₂ need to decline by 45% compared to such emission levels in 2010, and this has to happen by 2030. The emission levels must then continue to decline, reaching net zero around 2050 [4]. In order for the member nations of the Paris Agreement to meet this goal, the NDC Synthesis report [5] highlights the need for further increase in the nations' contributions compared to those that are currently declared. Measures mentioned by member nations for mitigating the release of greenhouse gasses include renewable energy generation, electrification of the transport sector and more efficient electrical grids. Because of the non-traditional properties of superconductors, such materials could potentially be of great benefit in further strengthening such mitigation strategies.

In aircraft travel, designs for hybrid electric aircraft such as NASA's N3-X are underway. Analysis shows that fully utilizing high temperature superconductors in the propulsion system could provide as much as 3.5 times higher power-to-weight ratio than previous designs due to superconductors' high current-densities [6].

In Norway there has recently been a debate about the development of wind turbine parks close to population centers and in vulnerable natural habitats. Moving the wind power production from land to sea solves some of the debated issues but needs effective turbines. Including high temperature superconductors into the design of such off-shore wind-turbines is beneficial for much the same reasons as for aircraft design: the high power-density makes for a compact, lightweight and efficient construction [7, 8].

Other examples of future applications of superconductors include their use in more efficient power grids [9, 10], sustaining the high magnetic fields needed for nuclear fusion [11, 12] and for the operation of a particle collider more powerful than the LHC [13], faster, more efficient electronics for digital logic and memory devices and more robust quantum computers [14].

Superconductors also currently have numerous important applications. In the Chūō Shinkansen magnetic levitation line, which is currently under construction, the interaction between superconducting coils in the train and copper coils on both sides of the track provides levitation and guidance of the train at high speeds [15]. Superconductors are essential for generating the high strength magnetic fields needed in MRI imaging. They are also used in other medical settings such as measurements of the electrical currents in the heart (magnetocardiography), in measuring the concentration of iron stored in the liver (biomagnetic liver susceptometry) and cancer treatments through their role in particle accelerators [16].

All of this is the product of fundamental research into the electronic properties of metals and other materials that has shown that for some of them, at a critical temperature T_c , the electrical resistivity of the material suddenly vanishes and any external magnetic field is expelled. These are the two main properties that we associate with the phase of superconductivity. Zero resistivity means that electricity can travel through the material without losing any energy, in contrast to a normal conductor where energy is usually lost through heat. The expulsion of magnetic fields is called the Meissner effect and is in a sense the more fundamental of the two properties. On a microscopic level it is due to electrons forming paired states that share certain features in such a way that different pairs can behave as one. Because a macroscopic

number of states share these features, the quantum mechanical nature of such states which is usually only significant for tiny particles, becomes apparent through these non-classical macroscopically measurable effects.

1.1 A brief history of superconductivity

Superconductivity was first discovered in mercury at $T_c \approx -268.99^\circ\text{C}$ by Heike Kamerlingh Onnes in the Netherlands in 1911 [17]. The Meissner effect was then discovered in 1933 by W. Meissner and R. Ochsenfeld [18]. These discoveries happened without any previous theoretical prediction or explanation. Theoretical description was then gradually developed, first by a simple thermodynamic two-fluid model of electron densities by Garter and Casimir and then in 1935 by the phenomenological theory of the electromagnetic properties by H. and F. London [19]. WWII came and went and then a significant improvement on the London-model was published by V. L. Ginzburg and L. D. Landau in 1950 [20], which built on Landau's previous description [21] of a second order phase-transition by an order-parameter quantity. Based on this theory, Abrikosov introduced the concept of a type-II superconductor in 1952, which has negative surface energy and a mixed phase at non-zero magnetic field [22].

An attempt at a microscopic theory was given by Frölich in 1950 based on electron-phonon interaction [23]. Even though the perturbation theory he derived failed to predict important superconducting properties such as the Meissner effect, his Hamiltonian later became well known as a fruitful starting point for the application of field theoretic methods. In 1953 Pippard introduced a second length scale, the coherence length ξ , through a non-local modification of the London-model [24]. This length scale was a measure of the width of the interface between normal and superconducting regions. Although not a theory of superconductivity itself, Landau's Fermi-liquid theory which came in 1956 would prove crucial in the development of a microscopic theory and describes the electronic properties of many metals that at lower temperature become superconducting [25]. A complete microscopic theory of superconductivity was published by J. Bardeen, L. N. Cooper, and J. R. Schrieffer in 1957 [26, 27]. The BCS-theory was based on the idea that Fermi-liquid quasiparticles with opposite momentum

could form an attractive interaction through an intermediate interaction with a phonon. This would then lead to the formation of pairs that could form a condensate, and which implied an energy gap Δ between the energies of paired electrons and energies of normal quasiparticle states in the Fermi-sea. This year Abrikosov also published his prediction of the existence of a lattice of vortices in the mixed state of type-II superconductors [28].

A separate form of a microscopic theory appeared in 1958 by N. N. Bogoliubov in a series of papers [29–31]. This methodology of solving the Frölich Hamiltonian was presented in a book [32] by P. G. de Gennes and has since become known as the Bogoliubov-de Gennes or BdG equations.

The diagrammatic methods developed for high-energy physics was first applied by Gor'kov to the problem of superconductivity in 1958 when he calculated Green's functions based on the ideas of BCS-theory that reproduced its results [33]. He then in 1959 used these methods to prove that the Ginzburg-Landau theory follows from the BCS theory in the limit $T \rightarrow T_c$ [34]. The application of field theoretic methods was extensively developed by the work of Nambu, published in 1960, where he introduced the Nambu-spinor for calculating the Gor'kov Green's functions. A perturbation theory for these Green's functions were calculated by Éliashberg in the same year following a similar approach as Nambu, which later become known as the Éliashberg theory [35].

The understanding of the effects of impurities got an important contribution in 1959 by what is known as Anderson's theorem [36]. It says that any instability of the Fermi-surface that does not lift the Kramer degeneracy of time-reversed paired quasi-particles do not affect the mean-field transition temperature [37]. The idea of an energy gap in the excitation spectrum, which was integral to the BCS theory, was given strong experimental backing by the tunneling experiments of I. Giæver in 1960 [38]. Such experiments were given a theoretical understanding by B. D. Josephson in 1962, through what is now known as the Josephson effect [39].

From the framework of the Gor'kov Green's functions, a set of transport equations were derived for type-II superconductors in 1968 by

Eilenberger [40]. These equations were further simplified for the case of a dirty superconductor by Usadel in 1970 [41].

From the perspective of our work, the discovery of a new phase in He³ by Osheroff et al. in 1972 was of particular importance. Although a superfluid and not a superconducting phase, the *A*-phase of this system has an unconventional anisotropic pairing symmetry which was famously described by Leggett in his 1975 review article [42]. This is the same symmetry that we have considered in our work.

Superconductivity was found in the first heavy-fermion system CeCu₂Si₂ in 1979 by Steglich et al. [43]. The heavy-fermion superconductors are systems where the superconducting state consists of quasiparticles that are fermions with large effective masses and where the superconducting order is of an unconventional character. For a review see Ref. [44].

The first high- T_c superconductor was discovered in the form of La_{2-x}Ba_xCuO₄ by Bednorz and Müller in 1986 [45]. This was followed up one year later by the discovery of YBa₂Cu₃O_{7-x} by M. K. Wu et al. [46]. These discoveries ushered in an era of superconductivity research dominated by cuprates — ceramic compounds consisting of metal oxides between planes of CuO₂. These are truly unconventional superconductors in that their pairing symmetry is demonstrably non-isotropic. It was in 1987 proposed by V. J. Emery that antiferromagnetic spin-fluctuations could cause such an anisotropic pairing [47]. This theory of the cuprate superconductive mechanism was then extensively studied by P. Monthoux, D. Pines and D. J. Scalapino [48–50], among many others in the early 90s, however a consensus on its validity is yet to be reached due to its seeming inconsistency with normal state properties of the materials [51]. Through a group-theoretical approach, a vast array of unconventional symmetries and their Ginzburg-Landau theories and physical properties were enumerated by Sigrist and Ueda in 1991 [52]. By which of these symmetries the superconducting state of cuprates could be described was in the early 90s a topic of much discussion, however due in part to strong evidence from phase-sensitive SQUID measurements of YBCO by Wollmann et al. in 1993 [53], it was by 2000 firmly established as a $d_{x^2-y^2}$ symmetry [54].

In 1994, superconductivity was discovered in the perovskite structure of Sr₂RuO₄ by Y. Maeno et al. [55]. This proved that copper was

not a necessary ingredient for superconductivity in layered perovskite crystal structures and would be the starting point of a still-standing debate about its pairing symmetry which served as the immediate backdrop to our own research.

One of the phenomena that needs a theoretical explanation for a full understanding of superconductivity in the cuprate family of high- T_c superconductors is the pseudogap phase. Above the transition temperature, but below a characteristic temperature T^* there is a hitherto undiscovered phase in such compounds where the electronic density of states near the Fermi-surface continues to be suppressed by an energy gap Δ_{PG} . This phase was named the pseudogap phase by Ding et al. in 1996 [56], and its origin continues to be a hotly debated topic.

2008 marked the beginning of the “iron age” of superconductivity research by the discovery of the first iron-based superconductor $\text{La}[\text{O}_{1-x}\text{F}_x]\text{FeAs}$ by Y. Kamihara et al. [57]. The materials in this family of superconductors, called iron-pnictides, feature high T_c and several other exotic properties including nematic order [58]. For a review see Ref. [59].

Lastly one could argue that we now have entered a “hydrogen age”, as an increasing number of hydrogen-rich compounds are approaching room-temperature superconductivity when they are placed under insane pressures [60, 61]. It could also be argued that we are currently in a “topological age” as topological edge states in superconductors constitute a field under intense study [62] that potentially have far-reaching consequences through their immediate application to quantum computing. Others again, would surely argue that we are in a “graphene age” as novel forms of superconductivity have been observed in twisted layers of graphene [63]. Which age we are in, I suspect, depends on what field the researcher you are asking works on, and a clear answer will have to be postponed until seen through the coarse-grained eyes of history.

1.2 About this work

In the last section we saw how the research into the phenomena of superconductivity has blossomed into a myriad of different directions and sub-fields. Through all this research, an implicit motivation has been the search of one day finding a theory or a specific system of a

material that is superconducting at room temperature. This has become a goal, similar to how the alchemists searched for the philosopher's stone, that we still have not quite reached, but whose continued pursuit itself has borne numerous fruits.

As for this thesis, we have focused on a branch of unconventional superconductivity that pertains to the description of phases with $k_x \pm ik_y$ chiral p -wave pairing symmetry. The p in p -wave implies that the pairing states internal angular momentum has $l = 1$, i.e. it has a 1st order (linear) dependence on its internal angular momentum.¹ As we mentioned, this is the same kind of state that describes the real world system of the He³ superfluid A -phase. In that context it is often referred to as the ABM-state after Anderson Brinkman and Morel who first described this pairing state in the context of the BCS-theory [64] in 1961, and then demonstrated how this state was stable in the A -phase of He³ in 1973 [65]. It was for a long time thought that the unconventional superconducting phase of the perovskite compound Sr₂RuO₄ had such a pairing symmetry, with one of the chief reasons being that it clearly features spontaneously broken time-reversal symmetry. This formed in part the motivation for much of our work.

The determination of pairing symmetries is an important step in understanding what type of superconductivity is in a system because it leads to distinct experimental consequences. Roughly speaking one can think of the pairing symmetry as determining the \mathbf{k} dependence of the gap function

$$\Delta(\mathbf{k}) = \sum_m \eta_m b_m(\mathbf{k}), \quad (1.1)$$

where $b_m(\mathbf{k})$ are basis functions that depend on the point group symmetry of the system and \mathbf{k} determines a point on the Brillouin zone. Depending on these basis functions then, $\Delta(\mathbf{k})$ could have points or lines in the Brillouin zone where it vanishes, so-called point- or line-nodes. The existence of such nodes implies distinct signatures such as quadratic low temperature-dependence of the specific heat. Other examples of experimental signatures of unconventional symmetry include temperature-independent Knight-shift, magnetic field depen-

1. The letter-convention stands for “principal” and comes historically from the study of atomic emission spectra that result when electrons jump between different orbitals.

dent Kerr-angle rotation and unconventional symmetry of lattices of magnetic vortices. For an introduction to superconductors with unconventional pairing symmetries we highly recommend the lecture notes by Sigrist in Ref. [66] and [67].

Importantly, one may derive the form of the Ginzburg-Landau theory of the superconductor based solely on the pairing-symmetry as was done by Sigrist and Ueda for a large number of different symmetries in 1991 [52]. The Ginzburg-Landau theory is a phenomenological theory, meaning that it explains the effective phenomenon observable in superconductors without necessarily knowing all the microscopic details. As such, any correct microscopic theory should then reduce to the phenomenological Ginzburg-Landau theory in the limit of $T \rightarrow T_c$. As we mentioned, Gor'kov first did this for a conventional s -wave superconductor in 1959 through a Green's function approach [34]. One fruitful starting point for such a microscopic theory is the Hubbard-Hamiltonian

$$\hat{H} = \sum_{ijss'} H_{ij;ss'} \hat{c}_{is}^\dagger \hat{c}_{js'} + \mathcal{O}(\hat{c}^4), \quad (1.2)$$

which itself can be viewed as an effective theory of the underlying many-body quantum mechanics. In a Hubbard-theory, electrons can occupy sites in an atomic crystal lattice and hop from one site to another. Any long-range interaction such as the Coulomb interaction is then written in terms of how electrons at different sites interact through nearest neighbor terms, next-nearest neighbor terms, etc. In Chapter 3 we will describe some of the tools useful in deriving an effective Ginzburg-Landau theory from such a microscopic starting point. We then in Chapter 4 present the group-theory needed for deriving the requirements on such a microscopic theory, for this to result in a sought-after pairing-symmetry.

In the last chapter of Chapter 7, we present some tools useful when investigating magnetic vortices and vortex-lattices in chiral p -wave superconductors.

As was said by Leggett in his Nobel lecture, there are very few things that can be proved rigorously in condensed matter physics, by which he referred to analytic arguments [68]. To get around this difficulty, we have used Monte-Carlo techniques that relies on the power of computers to simulate physical consequences of a theoretical Ginzburg-

Landau model. Such techniques have a long history in our group of being successfully able to simulate superconductive systems. For a few examples, see [69–73]. Although similar techniques have been used for centuries, their modern form was first developed in the context of nuclear research in the Manhattan project. After the researchers had become familiar with the Monte Carlo casino in Monaco, they named it after the casino because of the technique’s reliance on random or pseudo-random numbers to calculate multidimensional integrals [74].

In our use of Monte-Carlo techniques, which we present in Chapter 6, they are used to calculate thermal averages of statistical-mechanical observables. The rough procedure is that first, the theory under investigation is discretized to a corresponding lattice model as described in Chapter 5, such that the probability of any configuration of fields on this numerical lattice can be computed. The theory then implies a probability distribution for how likely certain field-configurations are to materialize in a real system. Then, from a predetermined starting configuration, small changes are made incrementally to the numerical configuration in such a way as to yield numerous statistical samples of field configurations that follow the theoretical probability distribution after a sufficient number of incremental changes have been done. These samples of field configurations finally are used to calculate statistical averages, which corresponds to taking thermal averages in statistical mechanics of the observables we are interested in.

We begin this thesis in Chapter 2 with a brief review of some relevant aspects of statistical mechanics that should refresh what is meant by thermal averages of observables, how these are tied to probability distributions of system configurations, and a brief introduction to Landau and Ginzburg-Landau theory as it pertains to phase transitions.

CHAPTER 2

Statistical Mechanics

In statistical mechanics we attempt to describe an ensemble of particles that may be interacting to extract not precise information about what each and every particle is doing, but statistical information about what most of the particles are doing. One can imagine this process as zooming out from a detailed view of individual entities and viewing the resulting collection through squinted eyes. This amounts to treating the collection in a coarse-grained manner. Through such eyes, only the most significant behavior is perceptible such that it can be understood and described in a simplified way.

2.1 Canonical ensemble and the partition function

Most of the business of statistical mechanics is about calculating what is known as the partition- function. Once this function is known, all the heavy lifting is done since most important statistical quantities can be extracted from it following already established systematic steps. To calculate the partition function is theoretically very simple: we sum the quantity $e^{-\beta E_i}$ over all the possible states of the system. Every state is a particular configuration of things in the system, and since all things in the system have a certain energy, the energy of a system state is given by the sum of all these things' individual energy, plus any energy given by interactions between them. If we label each state of the system with the index i , then we can denote the energy of each

state E_i . The definition of the partition function Z in the canonical ensemble can then be written

$$Z = \sum_i e^{-\beta E_i}, \quad (2.1)$$

where $\beta = 1/(k_B T)$ and k_B is the Boltzmann constant,¹ given that the number of different possible states is countable.

As we can see, the essential ingredients needed to calculate the partition function is one: to be able to enumerate all possible states i of the system, and two: to be able to calculate their corresponding energies E_i . Since we have used the summation sign \sum_i in Eq. (2.1), we have assumed that there exists a countable number of different states. However, if there is one thing in the system that can change in a continuous fashion, which we would measure using the set of real numbers \mathbb{R} and some unit, then the number of states is infinite and uncountable. In this case we sum over the different numbers of states by simply integrating over the things that are continuous, and the unit of the partition function becomes the product of the units of the continuous variables (things) unless we normalize by some constant dimensionful quantity. In most cases, it is the position r and momentum p of particles in the system that are continuous, hence the definition of the partition function becomes²

$$Z \sim \sum_i \int d^3r \int d^3p e^{-\beta E_i(r,p)}. \quad (2.2)$$

The canonical partition function is directly related to the Helmholtz free energy F (often only referred to as the free energy) of the system through a simple exponential

$$Z = e^{-\beta F}. \quad (2.3)$$

Because of the exponentials inherent in the definition of Z , calculating realistic values often results in excessively high numbers. This is one

-
1. In SI units, the value of the Boltzmann constant is given by $k_B \approx 1.380\,649 \times 10^{-23} \text{ J K}^{-1}$
 2. The reason why there is a \sim sign in Eq. (2.2) is that technically there is a factor of Planck's constant h in the denominator for each $dr dp$ in the integral measure since this makes the partition function dimensionless and thus consistent with the definition in terms of countable number of states in Eq. (2.1).

of the reasons why it is more useful to work with F , rather than Z itself, since inverting Eq. (2.3) $F = -\ln(Z)/\beta$, reducing the value of Z through a logarithm.

2.2 Calculating observables

An observable in statistical mechanics is a quantity that we can both calculate from the statistical theory, and (at least in principle) go out and measure in the real world. In quantum mechanics, observables are restricted to operators that have real expectation-values, as opposed to the complex values the theory usually deals with. This is to enforce the connection between observables and measurements, which we intuitively understand to always be reducible to a series of real values, i.e. points on a line.

We are interested in statistical information on observables of systems consisting of several quantum mechanical particles. To get this information we need some kind of probability distribution of the different states of the system. We are imagining that we for each such state (indexed by j) can calculate a real number for the thing (observable) we are interested in measuring. Let's call this observable O . Then O is a statistical variable which takes a particular value o_j in the state j of the system. Since the state is quantum mechanical, it is usually denoted by a Dirac bracket $|j\rangle$. A real observable O corresponds to a Hermitian operator \hat{O} in quantum mechanics whose expectation value we can then write as $o_j = \langle j|\hat{O}|j\rangle$.

If we now let P_j be the probability distribution, i.e. the probability that the system exists in state j , then we know from probability theory that the expectation value of O is

$$\langle O \rangle = \sum_j o_j P_j. \quad (2.4)$$

The probability distribution P_j is in the canonical ensemble given by a Maxwell-distribution

$$P_j = e^{-\beta E_j} / Z, \quad (2.5)$$

normalized by the partition function Z . Inserting this we get

$$\langle O \rangle = \sum_j \frac{o_j e^{-\beta E_j}}{Z}. \quad (2.6)$$

The observable of specific heat at constant volume C_v is particularly important in the study of phase transitions since its thermal behavior can be used to classify these transitions into categories. The specific heat is the measure of how much energy must be transferred to the system for its temperature to change by an infinitesimal amount given constant volume of the system. Thus it is defined by the equation $C_v = (\frac{\partial E}{\partial T})_V$. In the canonical ensemble, this quantity is calculated by

$$C_v = k_B \beta^2 (\langle E^2 \rangle - \langle E \rangle^2) = -k_B \beta^2 \left(2 \frac{\partial F}{\partial \beta} + \beta \frac{\partial^2 F}{\partial \beta^2} \right). \quad (2.7)$$

From this form of the specific heat, we see that it can be interpreted as a measure of the variance or width of the distribution of energies, and also that it is related to the second derivative of the free energy. Any discontinuity in the second derivative of the free energy, thus implies a discontinuity in the specific heat.

2.3 Ginzburg-Landau model

The experimental discovery of superconductivity was a surprise to the scientists at the time. No theoretical model had so far predicted the properties that the experimentalists were measuring. The theoretical models in use at that time predicted a decrease in resistivity as the temperature was lowered, but its sudden disappearance was completely unprecedented and impossible to explain classically in a convincing manner. Therefore, superconductivity seemed to demand a radically different understanding of how electrons moved inside atomic structures.

2.3.1 Landau Model

Before such an understanding had been developed, Ginzburg and Landau took a shortcut and came up with a theory that could describe the phenomenon of superconductivity without knowing its microscopic origin. In other words, they treated superconductivity as a black box and instead of asking what was inside to give the box's output, they used the output to determine a small set of *material parameters* which could then be used to predict how the box would react to a large range of stimuli or conditions. Now, given a large enough number of parameters, you can usually construct a model to fit any set of experimental

observations that you like. The merit of this theory came from use of symmetry arguments to reduce this set into only a few parameters, which still allowed it to describe the observations, while also embedding the theory with great predictive power.

The Ginzburg-Landau (GL) theory of superconductivity is based on Landau's previous work on a theory of general second order phase-transitions.³ The approach is given by two ideas. The first is simply that the phase transition should be able to be characterized by the appearance of some kind of measurable order that can be described by a function Ψ which we call the *order parameter*. In the liquid-water to ice-transition, it is the position of the molecules that become ordered in a lattice.⁴ In the magnetization of a metal it is the individual spins that become ordered along a particular direction.

The second idea is that at the phase transition, it is the appearance of this order that should dominate the behaviour of the system, to the exclusion of all other effects. Thus, the system should be described in terms of the order-parameter, and since this is infinitesimally small close to the transition, the free energy can be expanded in a Maclaurin-series with respect to this parameter as

$$F = F_0 + c_1 \Psi + c_2 \Psi^2 + c_3 \Psi^3 + c_4 \Psi^4 + c_5 \Psi^5 + \dots \quad (2.8)$$

The real constants F_0 and c_i constitute the set of material parameters of the theory and this set can then be reduced by any symmetries that we suspect should be inherent in the underlying theory. For example, if Ψ should represent the order parameter of magnetization of a system of Ising-spins, which can point either up or down, then the free energy should be invariant to this global choice, i.e. we need to enforce that the free energy be invariant with respect to the transformation $\Psi \mapsto -\Psi$. Then all the constants c_i for odd i vanish.

In the case of superconductivity, the order parameter Ψ represents the probability amplitude of the collective state of the superfluid of

-
- 3. 2nd order phase-transitions are phase transitions of systems whose free energy has a discontinuous second order derivative at the transition point, but is continuous for lower orders. Since the specific heat is given by the second order derivative, then the specific heat is discontinuous in this case.
 - 4. The astute reader might have noticed that this example is a first order phase transition because of the existence of latent heat. Actually first order phase transitions can also be described by a modified Landau theory, however we will here focus on the second order kind.

Cooper-paired electrons such that $|\Psi|$ can be interpreted as the density of such electron pairs. Since Ψ is complex, it has to be combined with its complex conjugate Ψ^* in ways that yield real numbers to produce terms that are valid in the free energy, since F itself should be a real number. Furthermore, the phenomenon of superconductivity is produced as a result of the breaking of $U(1)$ symmetry, so F also needs to be $U(1)$ symmetric, i.e. it has to be invariant under the transformation $\Psi \mapsto e^{i\phi}\Psi$ for $\phi \in \mathbb{R}$. These restrictions result in the free energy

$$F = F_0 - a|\Psi|^2 + b|\Psi|^4, \quad (2.9)$$

when keeping the lowest order terms that produce a phase transition.

Thermodynamic equilibrium is reached at the minimum of free energy. This restricts $b \geq 0$ since negative b yields a free energy with no global minimum.⁵ The minimum is then found by the condition

$$\frac{\partial F}{\partial \Psi^*} = (-a + 2b|\Psi|^2)\Psi = 0, \quad (2.10)$$

which yields the possibilities $|\Psi| = 0$ or $|\Psi| = \sqrt{a/2b}$. The first case gives the energy $F = F_0$, while the second gives $F = F_0 - a^2/(4b)$. We see that the second case is energetically favorable, but only exists and is different from the first case when $a > 0$. Furthermore, the second case represents the ordered state, since in this case the order-parameter $|\Psi| \neq 0$, in the conventional Landau theory.⁶

It is the thermodynamic parameter of temperature that traditionally determines whether a system is in one phase or another. Looking at the free energy in Eq. (2.9), the order parameter Ψ is the dynamical variable of the theory while the explicit temperature dependence lies in the material parameters a and b . Denoting the critical temperature where the phase transition happens T_c , the dimensionless parameter $t = (T - T_c)/T_c$ is small close to the critical point which means that

-
- 5. If there is no such minimum, then we say that the theory is unbounded or divergent.
 - 6. Actually this only represents when Cooper-pairs are forming and the real onset of superconductivity is determined by the point in parameter-space where the gauge-mass becomes non-zero, which is closely related but not exactly the same as where the density of Cooper-pairs becomes non-zero. The real onset of superconductivity is thus more related to when the phase of the wave-function settles on a value.

it can be used to expand the temperature-dependence of the material parameters such that

$$\begin{aligned} a(T) &= a_0 + a_1 t + \dots \\ b(T) &= b_0 + b_1 t + \dots \end{aligned} \quad (2.11)$$

Now we argue for what terms to keep in these expansions. Since $a(T)$ should change sign at $t = 0$ based on the discussion of Eq. (2.10), then we only keep odd terms of a . Since we need $b(T) > 0$ for the theory to be thermodynamically stable it seems that b_0 is the important term that needs to be larger than any negative contributions from the other terms. Keeping only lowest order terms, then the expansions reduce to $a(T) = a_1(T - T_c)/T_c$ and $b(T) = b_0$. Since the ordered state is the solution of the theory when $a > 0$ and this ordered state exists at temperatures $T < T_c$ then $a_1 < 0$ and the final temperature dependence of a becomes $a(T) = -|a_1|(T - T_c)/T_c$. From this temperature dependence, it is straightforward to derive critical exponents, the specific heat, etc. See Ref. [75].

2.3.2 Gradient Terms

The simple Landau theory described above is a type of mean field theory in that there is no spatial dependence in the order parameter Ψ , and thus it gives a simplified picture that can only be valid far away from any defects or boundaries. This simple approach can be extended to include spatial variation by allowing terms with gradients of the order parameter in the free energy through a gradient expansion of f in

$$F = \int d^3r f(\Psi, \nabla\Psi, \nabla^2\Psi, \nabla^3\Psi, \dots). \quad (2.12)$$

Keeping only the lowest order in this expansion that is invariant under $U(1)$ symmetry, we get the term $|\nabla\Psi|^2$ added to the free energy F in Eq. (2.9).

Perhaps the single most important phenomenon of superconductivity from a theoretical standpoint is the fact that it expels magnetic fields, hence it is clear that any theory that attempts to explain superconductivity needs to have some way for the superconducting order to interact with magnetic fields. The standard way to achieve this is through the recipe of *minimal coupling*, where the vector potential A

times a constant is subtracted from any momentum in the previously neutral theory. Specifically, $\mathbf{p} \mapsto \mathbf{p} - q/c\mathbf{A}$, where q is the charge of the particle and c is the speed of light. Using this trick, then the free energy density becomes

$$f = f_0 - a|\Psi|^2 + b|\Psi|^4 + K|(\nabla + ig\mathbf{A})\Psi|^2, \quad (2.13)$$

by letting $g = q/\hbar c$, which is the form of the free energy in the Ginzburg-Landau theory of conventional s -wave superconductivity. The form of the gradient that results from minimal coupling is called the covariant derivative and is defined as

$$D_\mu = \partial_\mu + igA_\mu. \quad (2.14)$$

For unconventional symmetries, the form of the gradient terms can vary substantially from that in Eq. (2.13). Even if the transition can be described by a single component, i.e. a single function Ψ , then an unconventional symmetry could still lead to anisotropies in the gradient terms such that K in Eq. (2.13) becomes directionally dependent. An example is single-component pairing in a tetragonal crystal. The symmetry group of tetragonal crystals is denoted D_{4h} in the Schönflies notation and consists of four-fold rotations in, and mirror symmetry about, the xy -plane. The rotational symmetry makes the gradient isotropic in the plane, but because of the lack of symmetry in the z -direction, the gradient terms in general must take the form

$$K_1 \sum_{\mu=x,y} |(\partial_\mu + igA_\mu)\Psi)|^2 + K_2 |\partial_z + igA_z)\Psi|^2. \quad (2.15)$$

Even more complex gradient terms are possible when the order-parameter consists of multiple components, i.e. there are degenerate states that all give significant contributions to the physics at the phase-transition. A particular case of this is when the pairing state is an irreducible representation of the crystal symmetry-group that is multi-dimensional.⁷ In this case, instead of a single complex function Ψ describing the order, we need several complex functions η_i .

A chiral p -wave superconductor has a pairing state that belongs to such a two-dimensional irreducible representation. It comes from the

7. For a more detailed explanation of irreducible representations and group theory, see Chapter 4.

Γ_5 irreducible representation of the tetragonal symmetry group D_{4h} . This representation consists of two components η_x and η_y that combine to form the general gradient terms

$$\begin{aligned} & K_1[|D_x\eta_x|^2 + |D_y\eta_y|^2] + K_2[|D_x\eta_y|^2 + |D_y\eta_x|^2] \\ & + K_3[(D_x\eta_x)^*(D_y\eta_y) + \text{c.c.}] + K_4[(D_x\eta_y)^*D_y\eta_x + \text{c.c.}] \quad (2.16) \\ & + K_5[|D_z\eta_x|^2 + |D_z\eta_y|^2]. \end{aligned}$$

This is the general expression of the gradient terms in the model we have investigated in our work and can be found in Ref. [52].

CHAPTER **3**

Field Theory Methods

In this chapter we will give a short introduction to the use of Grassmann variables and complex numbers in the calculation of the field-integrals in the partition function. We will also describe how these variables can be used to transform the expression for the action through the Hubbard-Stratonovich (HS) transformation.

A field theoretic expression for the quantum mechanical partition function \mathcal{Z} is obtained by using a coherent state basis. A coherent state is the eigen-state of an annihilation operator; thus, it produces an eigenvalue when operated on by the annihilation operator. Letting \hat{H} be the quantum mechanical Hamiltonian of the system for which we are interested in calculating the partition function, μ be the chemical potential and \hat{N} be the number operator, then the partition function is defined as

$$\mathcal{Z} = \text{Tr}(e^{-\beta(\hat{H}-\mu\hat{N})}). \quad (3.1)$$

Inserting a basis of coherent states $\{|\xi\rangle\}$ when calculating the trace, we obtain a functional integral over the coherent state eigenvalues ξ_α and ξ_α^* by substituting these variables for c_α and c_α^\dagger respectively in the \hat{H} - and \hat{N} -operators. Here α symbolizes the set of quantum-numbers needed to specify a state. The functional integral then takes the form

$$\mathcal{Z} = \int \mathcal{D}[\xi^* \xi] e^{-\int_0^\beta d\tau \sum_\alpha [\xi_\alpha^*(\partial_\tau - \mu)\xi_\alpha + H(\xi_\alpha, \xi_\alpha^*)]}. \quad (3.2)$$

The integration variable τ is the imaginary time and a τ -dependence is implicit in the notation such that $\xi_\alpha = \xi_\alpha(\tau)$. This path-integral notation is a shorthand for a more involved expression where the imaginary time-dependence of τ is split into a collection of time-indexed coherent state eigenfunctions $\xi_{\alpha,\tau}$, and the integration measure is a product over these indices and the quantum-state indices α . For further detail we refer to Ref. [76] which we will follow for a large part of this chapter.

3.1 Quadratic Fermionic Field Integrals

Because of the anti-commuting property of the fermion annihilation operators, any coherent state has to have eigenvalues that anti-commute as well. This leads to Grassmann numbers being the central variables used in constructing the partition function when it is written in the convenient basis of coherent states.

3.1.1 Grassmann algebras

A Grassmann algebra is constructed on a set of generators $\{\xi_\alpha\}$ such that a specific product of the generators $\xi_{\alpha_1} \xi_{\alpha_2} \cdots \xi_{\alpha_n}$ together with a complex coefficient ϕ constitute a number in the algebra and the generators anti-commute such that $\xi_\alpha \xi_\beta = -\xi_\beta \xi_\alpha$. On such an algebra, differentiation can be defined such that

$$\frac{d}{d\xi_{\alpha_m}} \phi \xi_{\alpha_1} \cdots \xi_{\alpha_n} = (-1)^{m-1} \phi \xi_{\alpha_1} \cdots \xi_{\alpha_{m-1}} \xi_{\alpha_{m+1}} \cdots \xi_{\alpha_n}, \quad (3.3)$$

provided that the generator ξ_{α_m} is in the number, and 0 otherwise. The factors of (-1) comes from anti-commuting the generator ξ_{α_m} such that it is next to the differentiation operator. In Grassmann algebra, integration can (perhaps a little non-intuitively) be defined such that it acts in the same way as differentiation, i.e. generators have to be anti-commuted until they are next to the symbolic infinitesimal differential $d\xi_\alpha$, and then use

$$\int d\xi \xi = 1, \quad (3.4)$$

while

$$\int d\xi 1 = 0. \quad (3.5)$$

If the integral consists of several differentials of generators, then these differentials also have to be anti-commuted such that $d\xi_1 d\xi_2 = -d\xi_2 d\xi_1$. On an algebra consisting of $2n$ generators we define conjugation as a map from the first half of the generators $\{\xi_{\alpha_i}\}_{i=1}^n$ to the other half $\{\xi_{\alpha_i}^*\}_{i=1}^n$ and in such a way that when applied to a particular number

$$(\phi \xi_\alpha \xi_\beta)^* = \phi^* \xi_\beta^* \xi_\alpha^*, \quad (3.6)$$

for $\phi \in \mathbb{C}$.

3.1.2 Nambu Spinor

In the Nambu notation, we group spin-dependent Grassmann numbers ξ_\uparrow and ξ_\downarrow^* , which correspond to the annihilation- and creation-operators \hat{c}_\uparrow^\dagger and \hat{c}_\downarrow , in a vector called a Nambu spinor

$$\boldsymbol{\xi} = \begin{pmatrix} \xi_\uparrow \\ \xi_\downarrow^* \end{pmatrix}. \quad (3.7)$$

A sesquilinear form can then be created with this vector and its adjoint such that

$$\boldsymbol{\xi}^\dagger S \boldsymbol{\xi} = S_{11} \xi_\uparrow^* \xi_\uparrow + S_{22} \xi_\downarrow^* \xi_\downarrow + S_{12} \xi_\uparrow^* \xi_\downarrow^* + S_{21} \xi_\uparrow \xi_\downarrow. \quad (3.8)$$

This allows any action that contains spin-dependent terms of the form of the right-hand side of Eq. (3.8) to be put on sesquilinear form. Assuming this is the case, then the partition function in the field-integral representation takes the form

$$\mathcal{Z} = \int \mathcal{D}[\xi^* \xi] e^{-\int_0^\beta d\tau \boldsymbol{\xi}^\dagger S_{\gamma\delta} \boldsymbol{\xi}}. \quad (3.9)$$

In this equation, the indices γ and δ are arbitrary collections of quantum numbers needed to specify a state other than spin, for example they could be momentum indices $\gamma = \mathbf{k}, \delta = \mathbf{k}'$, and summation over these repeated indices is implicitly understood.

Splitting the integral over τ into M imaginary time-slices and expanding the path integral measure into a product of individual integrals over specific quantum numbered and time-sliced Grassmann variables such that

$$\int \mathcal{D}[\xi^* \xi] \propto \lim_{M \rightarrow \infty} \int \prod_{\tau=1}^M \prod_{\alpha} d\xi_{\alpha,\tau}^* d\xi_{\alpha,\tau}, \quad (3.10)$$

the path-integral in Eq. (3.9) can be evaluated by the Gaussian Graßmann integral identity

$$\int \prod_i (\mathrm{d}\xi_i^* \mathrm{d}\xi_i) e^{-\xi_i^* S_{ij} \xi_j} = \det S, \quad (3.11)$$

for which a derivation can be found in Ref. [76]. This identity holds for any Hermitian matrix S , even if it is not positive definite. The result is then that the partition function in Eq. (3.9) becomes $\mathcal{Z} = \det S$. To calculate this determinant one has to consider the matrix S as also a matrix with time-slice indices. This is perhaps most easily accomplished using the Matsubara formalism in which the τ dependence is substituted with a dependence on Matsubara frequencies through a Fourier-like transform. More details on this formalism can be found in Section 3.2, but first we consider what to do when a spin-dependent action cannot be written on the form in Eq. (3.8).

3.1.3 Extended Nambu Spinor

From Eq. (3.8) we see that the Nambu spinor sesquilinear product fails to accommodate terms in a Hamiltonian that mix creation and annihilation operators of differing spins, e.g. a term $\propto \hat{c}_\uparrow^\dagger \hat{c}_\downarrow$. In general, a quadratic Hamiltonian can contain any combination of spin-indices of the form $\hat{c}_{s_1} \hat{c}_{s_2}$, $\hat{c}_{s_1}^\dagger \hat{c}_{s_2}$, $\hat{c}_{s_1} \hat{c}_{s_2}^\dagger$ and $\hat{c}_{s_1}^\dagger \hat{c}_{s_2}^\dagger$. This gives in total 16 different combinations, and to accommodate them all we thus need a 4×4 matrix. Exchanging to Graßmann numbers, we define the vector

$$\boldsymbol{\xi}_\gamma = \begin{pmatrix} \xi_{\gamma,\uparrow}^* \\ \xi_{\gamma,\uparrow} \\ \xi_{\gamma,\downarrow}^* \\ \xi_{\gamma,\downarrow} \end{pmatrix}, \quad (3.12)$$

where all quantum numbers except spin is included in the index γ . Writing the elements of this vector $(\boldsymbol{\xi}_\gamma)_i = \tilde{\xi}_{\gamma,i}$ regardless of whether it is a conjugate or not, we can write all quadratic terms of a Hamiltonian on the bilinear form

$$\boldsymbol{\xi}_\gamma^\top S_{\gamma\delta} \boldsymbol{\xi}_\delta = \tilde{\xi}_{\gamma,i} S_{\gamma i; \delta j} \tilde{\xi}_{\delta,j}, \quad (3.13)$$

where $S_{\gamma\delta}$ is a 4×4 antisymmetric¹ matrix, and $S_{\gamma i; \delta j}$ denotes its elements. Let there be n number of different quantum numbers, now including spin. Then there must be $2n$ different Grassmann generators $\tilde{\xi}_{\gamma, i}$. All of these are integrated over in the discrete version of the partition function field integral

$$\mathcal{Z} = \int \mathcal{D}[\xi^* \xi] e^{-\int_0^\beta d\tau \tilde{\xi}_{\gamma, i} S_{\gamma i; \delta j} \tilde{\xi}_{\delta, j}}. \quad (3.14)$$

Even though this superficially looks like the field integral in Eq. (3.9), we now have a bilinear and not a sesquilinear form, and S is now a $2n \times 2n$ matrix and not an $n \times n$ matrix. This means that we cannot use the integral in Eq. (3.11) to evaluate the integral, but instead have to rely on the more general Gaussian Grassmann integral

$$\int \prod_i (d\tilde{\xi}_i) e^{-\frac{1}{2} \tilde{\xi}_i S_{ij} \tilde{\xi}_j} = \text{Pf}(S), \quad (3.15)$$

which applies for any antisymmetric matrix S . The right-hand side is called the Pfaffian $\text{Pf}(S)$ of the matrix S and is defined for any anti-symmetric matrix to be given by

$$\text{Pf}[S] = \frac{1}{2^n n!} \sum_{P \in S_n} (-1)^P S_{P_1 P_2} \cdots S_{P_{n-1} P_n}, \quad (3.16)$$

where P is a permutation in the finite group S_n of all possible permutations of n numbers. This matrix function is related to the determinant by the relation $\text{Pf}(S)^2 = \det(S)$.

1. To see why this matrix can always be said to be antisymmetric lets first simplify the notation and write the bilinear product as $\tilde{\xi}_i S_{ij} \tilde{\xi}_j$. Then the matrix $S = (S + S^T)/2 + (S - S^T)/2$, such that we can write it as a symmetric matrix $\mathcal{S} = (S + S^T)/2$ and an antisymmetric matrix $\mathcal{A} = (S - S^T)/2$. Considering only the symmetric part of the bilinear form we get

$$\tilde{\xi}_i \mathcal{S}_{ij} \tilde{\xi}_j = -\tilde{\xi}_j \mathcal{S}_{ij} \tilde{\xi}_i = -\tilde{\xi}_i \mathcal{S}_{ji} \tilde{\xi}_j = -\tilde{\xi}_i \mathcal{S}_{ij} \tilde{\xi}_j.$$

Hence $\tilde{\xi}_i \mathcal{S}_{ij} \tilde{\xi}_j = 0$ and all that remains is the antisymmetric bilinear form.

Applying the integral identity in Eq. (3.15) to the partition function² in Eq. (3.14) after applying the proper discretization of the imaginary time, then yields the result

$$\mathcal{Z} = \int \mathcal{D}[\xi^* \xi] e^{-\int_0^\beta d\tau \tilde{\xi}_{\gamma,i} S_{\gamma i; \delta j} \tilde{\xi}_{\delta,j}} = \sqrt{\det(S)}. \quad (3.17)$$

We have chosen the positive result in $\text{Pf}(S) = \pm \sqrt{\det(S)}$ since the partition function \mathcal{Z} needs to be positive on physical grounds. The matrix S on the right-hand side of Eq. (3.17), which we take the determinant of, is the full matrix one gets after discretizing the imaginary time into slices which is usually done through the Matsubara-frequency formalism.

Now that we know that the partition function is given in terms of the determinant of the action-matrix S , we can use this information to manipulate the definition of $\tilde{\xi}_{\gamma,i}$ so that we can still write the action as a sesquilinear form. In particular, switching the position of $\xi_{\gamma,s}^*$ and $\xi_{\gamma,s}$ for both spins in the transposed vector on the left of the bilinear form $\xi_\gamma^T S_{\gamma\delta} \xi_\delta$, the transposed vector becomes the adjoint vector. This affects the matrix S by switching two pairs of rows. Denoting the matrix where the rows are switched S' , we can thus rewrite the bilinear form such that

$$\xi_\gamma^T S_{\gamma\delta} \xi_\delta = \xi_\gamma^\dagger S'_{\gamma\delta} \xi_\delta. \quad (3.18)$$

Now, the integral over the exponent has not changed since all we have done is simply re-ordering its terms. However, since exchange of rows in a determinant at most produces a minus sign and we do this twice, we get that $\det S = \det S'$, and we can write

$$\mathcal{Z} = \int \mathcal{D}[\xi^* \xi] e^{-\int_0^\beta d\tau \xi_\gamma^\dagger S'_{\gamma\delta} \xi_\delta} = \sqrt{\det(S')}. \quad (3.19)$$

In this equation, it is important to remember that S' is the row-switched matrix of an antisymmetric matrix S .

-
2. In relating the discrete version of Eq. (3.15) to (3.14) we have to make sure that the spinor elements $\tilde{\xi}_i$ are defined in terms of ξ_i and ξ_i^* in such a way as to get a correspondence to the sequence of Grassmann generators $d\xi_i d\xi_i^*$ in the measure to avoid any sign errors. One solution is to set $\xi_i^* = \tilde{\xi}_{2i-1}$ and $\xi_i = \tilde{\xi}_{2i}$ as we have done in Eq. (3.12). With this definition, then the measure $\int \prod_i d\xi_i^* d\xi_i$, which results from the discretized version of the field-integral measure, becomes equal to $\int \prod_{i=1}^{2n} d\tilde{\xi}_i$ such that Eq. (3.15) can be directly applied.

3.2 Matsubara formalism

The Matsubara formalism³ is a way of handling the imaginary time τ dependence of the coherent state eigenvalue fields $\xi_\alpha(\tau)$, where α denotes a collection of quantum numbers that are necessary to specify a state, without having to go back to the time-sliced path-integral. It also lets us automatically satisfy the imaginary-time boundary conditions $\xi_\alpha(0) = \zeta \xi_\alpha(\beta)$, where $\zeta = +1$ for bosons and $\zeta = -1$ for fermions. Imagining that τ is a continuous variable as suggested in the path-integral notation, we define two countable infinite sets of new field-variables through the Fourier-transforms

$$\xi_{\alpha,n} = \frac{1}{\sqrt{\beta}} \int_0^\beta d\tau e^{i\omega_n \tau} \xi_\alpha(\tau), \quad (3.20a)$$

$$\xi_{\alpha,n}^* = \frac{1}{\sqrt{\beta}} \int_0^\beta d\tau e^{-i\omega_n \tau} \xi_\alpha^*(\tau). \quad (3.20b)$$

The frequencies ω_n are called Matsubara frequencies and are defined by $\omega_n = (2n + 1)\pi/\beta$ with $n \in \mathbb{Z}$ for fermions. For bosons we use instead the notation ν_n where $\nu_n = 2n\pi/\beta$. The inverse relations are given by

$$\xi_\alpha(\tau) = \sum_{n \in \mathbb{Z}} e^{-i\omega_n \tau} \xi_{\alpha,n}, \quad (3.21a)$$

$$\xi_\alpha^*(\tau) = \sum_{n \in \mathbb{Z}} e^{i\omega_n \tau} \xi_{\alpha,n}^*. \quad (3.21b)$$

3.2.1 Matsubara sums

When the Matsubara formalism $\xi_{\alpha,n}$ is used for the field variables in the action of a partition-function field-integral, we will often need to evaluate infinite sums of Matsubara frequencies of the form

$$\sum_n h(if_n), \quad (3.22)$$

where f_n is either a fermionic- or bosonic Matsubara-frequency, to evaluate the field integral. A useful strategy in such evaluations is to

3. Named after the Japanese physicist Matsubara, Takeo.

transform the sum to a complex integral by using reverse residue integration. We consider the complex contour integral along a path \mathcal{C} running counterclockwise around the complex plane infinitesimally close to the imaginary axis as shown in Fig. 3.1. The integrand we consider

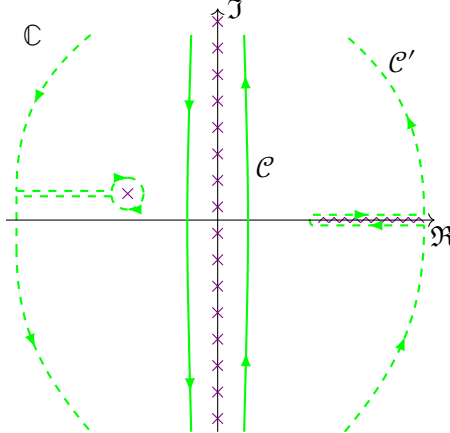


Figure 3.1: Integration contour for the Matsubara sum $\sum_n h(if_n)$. The contour is marked by a solid line and is imagined continuing to $\pm i\infty$. The crosses along the imaginary axis symbolize the simple poles of the Fermi-Dirac distribution-function. A deformed integration contour is shown with dashed lines that is imagined to cross the real axis at $\pm\infty$. This contour then encloses a simple pole on the left and a branch cut on the right belonging to the summand.

is given by the product of the summand and the complex continuation of the Fermi-Dirac- or Bose-Einstein distribution-function

$$n_\zeta(z) = (e^{\beta z} - \zeta)^{-1}, \quad z \in \mathbb{C}, \quad (3.23)$$

depending on whether the Matsubara frequency in the sum is of fermionic ($\zeta = -1$) or bosonic ($\zeta = +1$) nature. This function has simple poles⁴ at $z = if_n$ and thus integration around the contour results in a sum of residues of the integrand at these poles such that we get

$$\sum_n h(if_n) = \frac{\zeta\beta}{2\pi i} \oint_{\mathcal{C}} dz h(z) n_\zeta(z), \quad (3.24)$$

4. That the poles are simple, i.e. 1st order, is easily seen by expanding the exponential around if_n to leading order.

given that $h(z)$ does not contain any poles at these points. The contour can now be continuously deformed at will, as long as it does not cross any singularities, which can greatly facilitate the calculation of the integral. The default approach is to see if the integrand vanishes as $|z| \rightarrow \infty$, in which case it is usually useful to expand the contour as much as possible as illustrated by the deformed contour \mathcal{C}' in Figure 3.1.

Using the method outlined above, we may calculate the sums

$$\sum_{n \in \mathbb{Z}} \frac{1}{if_n - x} = -\zeta \beta n_\zeta(x), \quad (3.25a)$$

$$\sum_{n \in \mathbb{Z}} \frac{1}{(i\omega_n - x)(i\omega_n - y)} = \frac{\beta}{x - y} \left(\frac{1}{1 + e^{\beta x}} - \frac{1}{1 + e^{\beta y}} \right), \quad (3.25b)$$

$$\sum_{n \in \mathbb{Z}} \ln[\beta(i\omega_n + x)] = \ln(1 + e^{-\beta x}). \quad (3.25c)$$

3.3 Hubbard-Stratonovich transformation

The HS transformation is a transformation in the fields of a theory, where a new complex field is introduced in order to convert a term that is quadratic in an existing field variable, into a linear coupling between the existing- and new field. This is particularly useful when the existing field is Fermionic and thus a Grassmann variable, since it makes it possible to consider low energy excitations of the theory using e.g. a saddle-point approximation. It is however important to point out that the transformation itself is not in any way approximative but is an exact transformation that maintains all information of the original theory.

In technical terms, the HS transformation can be viewed simply as the solution of a complex multivariate integral. Let A have a strictly positive Hermitian part and \mathbf{J} be a vector of coefficients that could contain Grassmann- or complex variables. Then

$$e^{\mathbf{J}^\dagger A \mathbf{J}} = \det A^{-1} \int_{\mathbb{C}} \prod_i \left[\frac{dz_i^* dz_i}{2\pi i} \right] e^{-(\mathbf{z}^\dagger A^{-1} \mathbf{z} + \mathbf{z}^\dagger \mathbf{J} + \mathbf{J}^\dagger \mathbf{z})}, \quad (3.26)$$

exchanges a quadratic term in \mathbf{J} with an integration over the complex \mathbf{z} variables. Since \mathbf{J} usually represents some field in a field theory, the new \mathbf{z} is called the auxiliary- or conjugate field because of its linear

coupling to \mathbf{J} . In the less general case that A is a Hermitian matrix, this formula is proved simply by completing the square, then diagonalizing A by a unitary transformation and calculating the resulting integrals by the formula $\int dz^* dz e^{-azz^*} = 2\pi i/a$.

From Eq. (3.26), we see that what we have to do to perform the HS transformation is first to make a choice for what to interpret as part of the matrix A and what to interpret as part of \mathbf{J} . We then have to check that this definition of A leads to its Hermitian part having only positive eigenvalues. Finally, we need to know an analytical expression for its inverse. It is usually the first step that is the most difficult, since this dictates the low energy excitation a subsequent saddle point approximation or a stationary phase approximation will produce. Typically, we are interested in transforming a Fermionic interaction potential of the form

$$V = \frac{1}{2} \sum_{\alpha\beta\gamma\delta} V_{\alpha\beta\gamma\delta} \xi_\alpha^* \xi_\beta^* \xi_\delta \xi_\gamma, \quad (3.27)$$

where ξ_α are Grassmann variables, which can be sketched in the way of the single-vertex diagram in Figure 3.2. The HS-transformation is

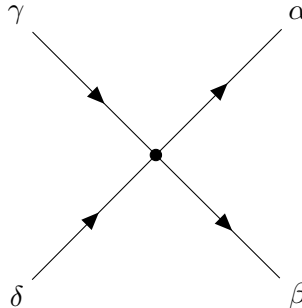


Figure 3.2: Generic two-body interaction.

classified into being done in a specific *channel* depending on which pair of Grassmann variables are considered to be part of \mathbf{J} and consequently \mathbf{J}^\dagger . The direct channel⁵ is given by the identification $J_i \sim \xi_\alpha^* \xi_\gamma$, the Cooper channel⁶ is defined by the identification $J_i \sim \xi_\delta \xi_\gamma$ while the

5. Also known as the density-density channel.

6. Also known as the particle-particle channel.

exchange channel is given by the identification $J_i \sim \xi_\alpha^* \xi_\delta$. Depending on exactly how \mathbf{J} is chosen, the Gaussian integral in Eq. (3.26) might have to be modified. For example, in the case of the direct- and exchange-channel, the exponential argument on the left side will have the form $\mathbf{J}^\top A \mathbf{J}$, which necessitates the Gaussian integral identity

$$e^{-\frac{1}{2}\mathbf{J}^\top A \mathbf{J}} = \sqrt{\det A^{-1}} \int_{\mathbb{R}} \prod_i \left[\frac{dx_i}{\sqrt{2\pi}} \right] e^{-\frac{1}{2}\mathbf{x}^\top A^{-1}\mathbf{x} - i\mathbf{J}^\top \mathbf{x}}, \quad (3.28)$$

where the auxiliary field \mathbf{x} now is a *real* conjugate field.

3.3.1 Transformation in symmetry channels

In the Cooper-channel of the HS transformation, the complex field \mathbf{z} is conjugate to some combination of pairs of annihilation operators $\hat{c}_\delta \hat{c}_\gamma$ (or their corresponding Grassmann variables). The symmetry of the specific combination in turn then determines the symmetry of any low energy field theory obtained through a subsequent stationary phase approximation. By diagonalizing the interaction potential \hat{V} into its different irreducible representations as we will do in Section 4.8, then a HS transformation in a specific symmetry channel is done by identifying \mathbf{J} with irreducible representation (IR) basis function combinations of latter operators.

Let's take the case of a BCS theory of superconductivity where the interaction can be written in terms of basis functions $d_{s_1 s_2}^{(b),m}(\mathbf{k})$ such that the diagonalized interaction takes the form

$$\hat{V} = \sum d_{s_1 s_2}^{(b),m}(\mathbf{k})^* v_{(b)} d_{s'_1 s'_2}^{(b),m}(\mathbf{k}') c_{\frac{\mathbf{q}}{2} + \mathbf{k}, s_1}^\dagger c_{\frac{\mathbf{q}}{2} - \mathbf{k}, s_2}^\dagger c_{\frac{\mathbf{q}}{2} - \mathbf{k}', s'_2} c_{\frac{\mathbf{q}}{2} + \mathbf{k}', s'_1}, \quad (3.29)$$

where \sum indicates the sum over the indices, $\mathbf{k}, \mathbf{k}', \mathbf{q}, s_1, s_2, s'_1, s'_2, b$ and m . Here b specifies the irreducible representation while m enumerates the representation basis.⁷ Identifying

$$\hat{J}_{\mathbf{q}}^{(b,m)} = \sum_{\mathbf{k} s_1 s_2} d_{s_1 s_2}^{(b),m}(\mathbf{k}) \hat{c}_{\frac{\mathbf{q}}{2} - \mathbf{k}, s_1} \hat{c}_{\frac{\mathbf{q}}{2} + \mathbf{k}, s_2}, \quad (3.30)$$

the interaction potential is simply written

$$\hat{V} = \sum_{\mathbf{q}, b, m} \hat{J}_{\mathbf{q}}^{(b,m)\dagger} v^{(b)} \hat{J}_{\mathbf{q}}^{(b,m)}. \quad (3.31)$$

7. For an exposition on the basics of irreducible representations in superconductivity theory see Chapter 4.

In the path-integral representation of the partition function, the annihilation operators become Grassmann variables which we denote by writing J instead of \hat{J} , such that the contribution from the interaction potential results in the exponential

$$\mathcal{Z}_I = e^{-\int_0^\beta d\tau \sum_{q,b,m} J_q^{(b,m)\dagger} v^{(b)} J_q^{(b,m)}}. \quad (3.32)$$

Now it is straightforward to use the HS formula

$$e^{\int_0^\beta d\tau \sum_{ij} J_i^* A_{ij} J_j} = \int \mathcal{D}[\eta_i^* \eta_i] e^{-\int_0^\beta d\tau (\eta_i^* A_{ij}^{-1} \eta_j + J_i^* \eta_i + J_i \eta_i^*)}, \quad (3.33)$$

which is a path integral version of Eq. (3.26), to transform each pair of irreducible representation basis vectors to individual conjugate fields. In the notation of Eq. (3.33) implicit summation over repeated indices is used and each index i is a collection $i = (b, m, q)$ of indices. Comparing Eq. (3.33) and (3.32) we gather that

$$A_{ij} = A_{b,m,q; b',m',q'} = -\delta_{qq'} \delta_{mm'} \delta_{bb'} v^{(b)}, \quad (3.34)$$

which is trivially Hermitian and positive definite provided $v^{(b)} < 0$. In this case we say that the irreducible representation b is an attractive channel. A is in this case also trivially invertible with $A_{ij}^{-1} = -\delta_{ij}/v^{(b)}$. Writing out all the indices, we finally arrive at the HS transformation of the interaction potential in individually attractive symmetry channels

$$\mathcal{Z}_I = \int \mathcal{D}[\eta_q^{(b,m)*} \eta_q^{(b,m)}] e^{\int_0^\beta d\tau \sum_{q,b,m} \left[\frac{|\eta_q^{(b,m)}|}{v^{(b)}} - (J_q^{(b,m)*} \eta_q^{(b,m)} + J_q^{(b,m)} \eta_q^{(b,m)}) \right]}, \quad (3.35)$$

where

$$J_q^{(b,m)} = \sum_{k s_1 s_2} d_{s_1 s_2}^{(b),m}(\mathbf{k}) \xi_{\frac{q}{2}-\mathbf{k}, s_1} \xi_{\frac{q}{2}+\mathbf{k}, s_2} \quad (3.36)$$

in terms of Grassmann variables ξ . We note that this derivation does not assume either odd or even basis functions for the irreducible representations and thus works just as well for either.

3.4 Field theory approximations

3.4.1 Stationary phase and the one loop expansion

Let Z be the partition function

$$Z(l) = \int \mathcal{D}[\eta_\alpha^* \eta_\alpha] e^{-lS(\eta_\alpha^*, \eta_\alpha)}, \quad (3.37)$$

given in terms of bosonic fields η_α^* , η_α and where l is some large parameter $l \gg 1$. In what is called the stationary phase approximation⁸ of a bosonic field integral, we create an expansion of the free energy around the field configuration $\{\eta_\alpha^c\}$ where the action S is stationary and a minimum. This configuration is the main contribution to the integral in Eq. (3.37) since it provides the maximum of the exponent and determines the leading order asymptotic behavior as $l \rightarrow \infty$. It also corresponds in a sense to a classical solution and gives in the case of the Feynman path-integral for the evolution operator of a single particle in an external potential, the classical Euler-Lagrange equations. The configuration is found in the path-integral notation by varying the fields in the action such that

$$\frac{\delta S}{\delta \eta_\alpha} = 0 \quad \wedge \quad \frac{\delta S}{\delta \eta_\alpha^*} = 0. \quad (3.38)$$

As an example, the Hubbard-model with a conventional negative- U Hubbard-potential $U \sum_{r_i} \hat{n}_{r_i,\uparrow} \hat{n}_{r_i,\downarrow}$, can be expressed as a bosonic field integral through a HS transformation. The stationary field configuration $\{\eta_q^c(\tau)\}$ is in this case given by a imaginary-time- and spatially-independent field-configuration η^c . Assuming such a solution, the action reduces to

$$S(\eta^{c*}, \eta^c) = \frac{\beta N}{U} |\eta^c|^2 - \sum_{\mathbf{q}} \ln \left[\left(1 + e^{\beta E_{\mathbf{q}}} \right) \left(1 + e^{-\beta E_{\mathbf{q}}} \right) \right], \quad (3.39)$$

where $E_{\mathbf{q}} = \sqrt{(\epsilon(\mathbf{q}) - \mu)^2 + |\eta^c|^2}$, N is the number of hopping sites, $\epsilon(\mathbf{q})$ is the Fourier transformed kinetic hopping energy, μ is the chemical potential, and U is the repulsive Hubbard interaction strength. The

8. The name is misleading in the case of the many-particle partition function since we do not have a strict phase in the exponent but in general a complex function because $\eta_\alpha \in \mathbb{C}$. Technically it is the method of steepest descent for the case of an exponent with stationary points that is used in this case.

stationary action condition in Eq. (3.38) then yields the equation

$$|\eta^c| \left(\frac{1}{U} - \frac{1}{N} \sum_{\mathbf{q}} \frac{1}{2E_{\mathbf{q}}} \tanh \frac{\beta E_{\mathbf{q}}}{2} \right) = 0, \quad (3.40)$$

which has two solutions: one given by $\eta^c = 0$, and one given by setting the terms in the parenthesis equal to 0. The last non-trivial solution is a form of the BCS solution and represents the order-parameter in an *s*-wave superconductor. Because of the parameter β , this solution will be temperature dependent and disappears at some critical temperature at which the two solutions for η_c converge.

The stationary phase expansion is then the expansion resulting from expanding the action around the stationary solution. Setting $\tilde{\eta}_\alpha = \sqrt{l}(\eta_\alpha - \eta_\alpha^c)$ we get in general the expansion

$$\begin{aligned} S(\tilde{\eta}_\alpha, \tilde{\eta}_\alpha^*) &= S_c + \frac{1}{l} \left[\frac{1}{2!} \frac{\delta^2 S}{\delta \eta_\alpha \delta \eta_\beta} \Big|_{\eta_c} \tilde{\eta}_\alpha \tilde{\eta}_\beta \right. \\ &\quad \left. + \frac{1}{2!} \frac{\delta^2 S}{\delta \eta_\alpha^* \delta \eta_\beta^*} \Big|_{\eta_c} \tilde{\eta}_\alpha^* \tilde{\eta}_\beta^* + \frac{\delta^2 S}{\delta \eta_\alpha \delta \eta_\beta^*} \Big|_{\eta_c} \tilde{\eta}_\alpha \tilde{\eta}_\beta^* \right] + \mathcal{O}\left(\frac{1}{l\sqrt{l}}\right) \\ &= \sum_{n_1+n_2 \geq 2} \frac{1}{n_1! n_2!} \frac{\delta^{n_1+n_2} S}{\delta \tilde{\eta}_\alpha^{n_1} \delta \tilde{\eta}_\beta^{n_2}} \Big|_{\eta_c} \frac{1}{l^{(n_1+n_2)/2}}. \end{aligned} \quad (3.41)$$

We have used implicit summation over repeated indices and on the last line we have assumed that new indices should be introduced and summed for each n_1 and n_2 . This is simply the multivariate Taylor expansion around η_c where we have treated η and η^* as independent variables.

A simpler expansion can be found when the bosonic fields correspond to order parameters in a system close to a phase transition. In this case we can assume the fields η_α to be small in general such that S simply can be expanded about 0. If the system is fermionic, then the bosonic field integral of the order-parameters will have resulted from a HS transformation, in which case we will have a contribution to the integral of the form

$$\sqrt{\det G^{-1}(\eta_\alpha, \eta_\alpha^*)} = e^{\frac{1}{2} \text{Tr} \ln G^{-1}}, \quad (3.42)$$

where G^{-1} is the result of the integration of a quadratic fermionic action and will in general depend on the auxiliary bosonic fields η_α and

η_α^* in a non-linear way. Then the matrix G^{-1} can be decomposed in a matrix G_0^{-1} that results purely from fermionic integration, and a matrix ϕ that is dependent on the auxiliary fields η_α and importantly vanishes as $\eta_\alpha \rightarrow 0$, such that $G^{-1} = G_0^{-1} + \phi$. When the system is close to the phase transition such that the auxiliary fields are small, then this allows for the expansion of the logarithm in Eq. (3.42) such that

$$\begin{aligned}\frac{1}{2} \text{Tr} \ln(G_0^{-1} + \phi) &= \frac{1}{2} \left(\text{Tr} \ln G_0^{-1} + \text{Tr} \ln(1 + G_0 \phi) \right) \\ &= \frac{1}{2} \left(\text{Tr} \ln G_0^{-1} - \sum_{n=1}^{\infty} \frac{\text{Tr}(-G_0 \phi)^n}{n} \right).\end{aligned}\quad (3.43)$$

This is known as the one-loop expansion since in terms of perturbation theory, G_0 is the fermionic propagator such that the sum in the last line of Eq. (3.43) corresponds to a series of propagators and interactions that are connected in a closed loop by the trace.

3.4.2 Gradient expansion

The gradient expansion rests on the assumption that the fields are sufficiently smooth, such that progressively higher order derivatives with respect to the field parameters are progressively smaller, i.e. we assume

$$l_\alpha^n |\partial_\alpha^n \eta_\alpha| \gg l_\alpha^{n+1} |\partial_\alpha^{n+1} \eta_\alpha|, \quad (3.44)$$

where l_α is some appropriate length scale such as to make $l_\alpha \partial_\alpha$ dimensionless. In practice this usually means that given a momentum-dependent action density, $S(\eta_{\mathbf{q},\alpha}^*, \eta_{\mathbf{q},\alpha}; \mathbf{q})$, we assume q_i small compared to the lattice spacing⁹ a_i . Then we expand the explicit \mathbf{q} dependence in the action density in the small parameters $a_i q_i$ as a Maclaurin series. In the following notation, we will assume the length parameter a^i is present in the notation q^i where appropriate. The momentum dependence of the fields themselves should not be expanded, as our goal is to have terms of the form $(q^i)^n (\tilde{\eta}_{\mathbf{q},\alpha})^m$. If we then let partial momentum-derivatives only act on the explicit momentum-dependence in S , and neglecting the field dependence in the notation

9. This could be the spacing between hopping sites, i.e. stationary ions in an electron model.

for S , the expanded action can be written as the series

$$S(\mathbf{q}) = S(0) + \frac{\partial S}{\partial q^i}(0) q^i + \frac{1}{2!} \frac{\partial^2 S}{\partial q^i \partial q^j}(0) q^i q^j + \mathcal{O}(q^3). \quad (3.45)$$

Usually, the linear term cancels by symmetry of the underlying lattice. In general, it is smart to here check for terms that cancel by considering any internal momentum sums that may be included in the coefficients.

Terms with products between fields $\eta_{\mathbf{q},\alpha}$ and q^i lead to gradients of the spatially dependent fields $\eta_{\mathbf{R},\alpha}$, which is why the expansion in Eq. (3.45) can be called a gradient expansion. The spatially dependent fields are defined as the coefficients in the inverse Fourier transform

$$\eta_{\mathbf{q},\alpha} = \frac{1}{\sqrt{N}} \sum_{\mathbf{R}} e^{i\mathbf{q}\cdot\mathbf{R}} \eta_{\alpha}(\mathbf{R}), \quad (3.46)$$

where N is the number of terms in the sums $\sum_{\mathbf{q}}$ and $\sum_{\mathbf{R}}$. One way of now obtaining gradients of the spatial fields is to realize that since q^i is small we can set

$$q^i \approx \sin(q^i) = \frac{1}{2i} (e^{iq^i} - e^{-iq^i}). \quad (3.47)$$

With this identification, all the momentum dependence in $S(\mathbf{q})$ exists as phases such that the sum $\sum_{\mathbf{q}} S(\mathbf{q})$ results in a series of Kronecker-delta functions which we evaluate by the $\sum_{\mathbf{R}}$ sums coming from the inverse Fourier transforms in Eq. (3.46). Grouping terms of displaced spatial fields, we can identify derivatives, such that

$$\eta_{\alpha}(\mathbf{R} + a\hat{e}_i) - \eta_{\alpha}(\mathbf{R}) \approx a \frac{\partial}{\partial R^i} \eta_{\alpha}(\mathbf{R}). \quad (3.48)$$

These identifications are justified by going to the continuum limit where $a \rightarrow 0$.

As an example, consider the sum

$$S = \sum_{\mathbf{q}} K_{\alpha\beta ij} q^i q^j \eta_{\mathbf{q},\alpha}^* \eta_{\mathbf{q},\beta}, \quad (3.49)$$

where there is an implicit summation over repeated indices i, j, α and β . Fourier transforming the fields according to Eq. (3.46) and writing

q^i as $\sin q^i$, we can group terms such that

$$\begin{aligned}
 S &= \frac{1}{N} \sum_{\mathbf{R}_1 \mathbf{R}_2} K_{\alpha\beta ij} \eta_\alpha(\mathbf{R}_1)^* \eta_\beta(\mathbf{R}_2) \frac{1}{4} \sum_{\mathbf{q}} \left[e^{i\mathbf{q} \cdot (\mathbf{R}_2 - \mathbf{R}_1 + a\hat{\mathbf{e}}_i - a\hat{\mathbf{e}}_j)} \right. \\
 &\quad \left. + e^{i\mathbf{q} \cdot (\mathbf{R}_2 - \mathbf{R}_1 + a\hat{\mathbf{e}}_j - a\hat{\mathbf{e}}_i)} - e^{i\mathbf{q} \cdot (\mathbf{R}_2 - \mathbf{R}_1 + a\hat{\mathbf{e}}_i + a\hat{\mathbf{e}}_j)} - e^{i\mathbf{q} \cdot (\mathbf{R}_2 - \mathbf{R}_1 - a\hat{\mathbf{e}}_i - a\hat{\mathbf{e}}_j)} \right] \\
 &= \sum_{\mathbf{R}} K_{\alpha\beta ij} a^2 \frac{\partial}{\partial R_i} \eta_\alpha(\mathbf{R})^* \frac{\partial}{\partial R_j} \eta_\beta(\mathbf{R}). \tag{3.50}
 \end{aligned}$$

A more conventional way of converting to gradients, is to use integration by parts. Then the product rule of partial derivatives is used to obtain

$$q^j \eta_\alpha(\mathbf{R}) e^{i\mathbf{q} \cdot \mathbf{R}} = i \frac{\partial \eta_\alpha}{\partial R^i} e^{i\mathbf{q} \cdot \mathbf{R}} - i \frac{\partial}{\partial R^i} [\eta_\alpha(\mathbf{R}) e^{i\mathbf{q} \cdot \mathbf{R}}]. \tag{3.51}$$

Summing on both sides and arguing that the boundary term vanishes because $\eta_\alpha(\mathbf{R}) \rightarrow 0$ as $R^i \rightarrow \infty$, then

$$\sum_{\mathbf{R}} q^j \eta_\alpha(\mathbf{R}) e^{i\mathbf{q} \cdot \mathbf{R}} = i \sum_{\mathbf{R}} e^{i\mathbf{q} \cdot \mathbf{R}} \nabla_i \eta_\alpha(\mathbf{R}). \tag{3.52}$$

CHAPTER 4

Group Theory

In this chapter we will introduce some basic group-theoretic framework to clarify the meaning of how a free energy can “belong” to an irreducible representation, and to show how group-theory can be applied to quantum-mechanical concepts such as operators and states.

A few words about notation. We will use the semicolon ‘;’ in equations as notation for the words ‘*such that*’, e.g., when defining sets. A colon with a trailing space ‘:’ is used when defining maps where the symbol representing the mapping itself should be on the left, while the sets being related or how the elements of the sets are related, is on the right of the colon. The colon ‘:’ is also used as a shortcut for the words ‘*applied through its representation to*’ for when group elements are applied to vectors, where the correct representation to use for this application should be implicitly understood.

The material in this section is based on the material covered in Refs. [77] and [76], specified for the use in quantum mechanical theories of unconventional superconducting states.

4.1 Irreducible representations

To know what an irreducible representation (IR) is, let’s start with what we mean by a *reducible* representation.

Def. 4.1. *A matrix representation is **reducible** if there exists a non-trivial invariant subspace of the vector space of the representation.*

The intuition is then that the vector space of the representation is reducible if a “smaller” representation is contained within it. Since there is a smaller vector space within the vector space of the original representation, and this vector space is invariant, it is possible to define another representation on this smaller vector space, i.e., *reduce* the original representation. We have now used the word “invariant” a couple of times, so let’s define what it means more precisely.

Def. 4.2. Let $D(g)$ be a representation of the group G on the vector space V such that $D(g): V \rightarrow V$. Then a subspace $U \subseteq V$ is **invariant** if

$$\forall g \in G \quad u \in U \implies D(g)u \in U. \quad (4.1)$$

In other words: a vector space is invariant if it is not possible for any vector in it to escape using the representation¹ of any group element. All representations applied to any vector in the invariant subspace must necessarily land in that same subspace from which it started.

4.2 BCS Hilbert Space

We define the BCS Hilbert space as the Hilbert space upon which BCS-type potentials operate. Specifically, this is a reduced form of the two-particle fermionic product Hilbert space $\mathcal{H}_2 = \mathcal{H} \otimes \mathcal{H}$ where $\mathcal{H} = \text{span}\{|\mathbf{k}, s\rangle\}$ and we only consider states that have opposite momentum. Thus, this Hilbert space is given by

$$\mathcal{B} = \text{span}\{|\mathbf{k}, s_1\rangle|-\mathbf{k}, s_2\rangle\}, \quad (4.2)$$

and the identity operator in this space can be written

$$\hat{\mathbb{I}} = \sum_{\mathbf{k} s_1 s_2} |\mathbf{k}, s_1\rangle|-\mathbf{k}, s_2\rangle\langle-\mathbf{k}, s_2|\langle\mathbf{k}, s_1|. \quad (4.3)$$

Acting on the arbitrary vector $|v\rangle \in \mathcal{B}$ with this identity operator, we find that in terms of this basis, the vector can be written

$$|v\rangle = \sum_{\mathbf{k} s_1 s_2} v_{s_1 s_2}(\mathbf{k})|\mathbf{k}, s_1\rangle|-\mathbf{k}, s_2\rangle, \quad (4.4)$$

1. In this language we use the word *representation* both to mean *linear transformation* that corresponds to a group element on a vector space, and the *set* of all such linear transformations together with the vector space.

where

$$v_{s_1 s_2}(\mathbf{k}) = \langle -\mathbf{k}, s_2 | \langle \mathbf{k}, s_1 | v \rangle. \quad (4.5)$$

The indices s_1 and s_2 can take on only two values each, namely $s_1, s_2 \in \{\uparrow, \downarrow\}$. In total, there are thus 4 different realizations of the pairs $s_1 s_2$, e.g., $s_1 s_2 = \uparrow\uparrow$, for $v_{s_1 s_2}(\mathbf{k})$. Putting these different realizations of $v_{s_1 s_2}(\mathbf{k})$ as elements in a 2×2 matrix, we get

$$v_{s_1 s_2}(\mathbf{k}) = \begin{pmatrix} v_{\uparrow\uparrow}(\mathbf{k}) & v_{\uparrow\downarrow}(\mathbf{k}) \\ v_{\downarrow\uparrow}(\mathbf{k}) & v_{\downarrow\downarrow}(\mathbf{k}) \end{pmatrix}. \quad (4.6)$$

Any 2×2 matrix can be written in the conventional basis of the 4 Pauli matrices $\sigma^0 = \mathbb{1}_{2 \times 2}$, σ^x , σ^y , and σ^z . This means that we *could* write the matrix in Eq. (4.6)

$$v_{s_1 s_2}(\mathbf{k}) = v_{\mathbf{k}}^0 \sigma_{s_1 s_2}^0 + v_{\mathbf{k}}^i \sigma_{s_1 s_2}^i. \quad (4.7)$$

It is, however, conventional to factor out a Pauli matrix $i\sigma^y$ to the right in the expansion, since this results in nice transformation properties of the coefficients as we shall see. With the spin-indices expanded in this basis, it is conventional to let the function of \mathbf{k} that is in front of σ^0 be called $\psi_{\mathbf{k}}$. The three others are conventionally denoted $d_{\mathbf{k},i}$ which are components of what we call the \mathbf{d} -vector.² Expanded in this conventional basis, then, $v_{s_1 s_2}(\mathbf{k})$ takes the form

$$v_{s_1 s_2}(\mathbf{k}) = (\psi_{\mathbf{k}} \sigma_{s_1 s_2}^0 + d_{\mathbf{k},i} \sigma_{s_1 s_2}^i) i\sigma_{s_1 s_2}^y, \quad (4.8)$$

and finally, the state $|v\rangle$ can be written

$$|v\rangle = \sum_{\mathbf{k} s_1 s_2} [(\psi_{\mathbf{k}} \sigma^0 + \mathbf{d}_{\mathbf{k}} \cdot \boldsymbol{\sigma}) i\sigma^y]_{s_1 s_2} |\mathbf{k}, s_1\rangle |-\mathbf{k}, s_2\rangle. \quad (4.9)$$

Going one step back and writing out the different combinations of $s_1 s_2$ in $v_{s_1 s_2}(\mathbf{k})$ as a matrix like we did in Eq. (4.6), but now multiplying out the Pauli matrices in Eq. (4.8), we get

$$\begin{pmatrix} v_{\uparrow\uparrow}(\mathbf{k}) & v_{\uparrow\downarrow}(\mathbf{k}) \\ v_{\downarrow\uparrow}(\mathbf{k}) & v_{\downarrow\downarrow}(\mathbf{k}) \end{pmatrix} = \begin{pmatrix} -d_{\mathbf{k},x} + id_{\mathbf{k},y} & \psi_{\mathbf{k}} + d_{\mathbf{k},z} \\ -\psi_{\mathbf{k}} + d_{\mathbf{k},z} & d_{\mathbf{k},x} + id_{\mathbf{k},y} \end{pmatrix}. \quad (4.10)$$

2. Note that a state in \mathcal{B} that is described by a \mathbf{d} -vector does not necessarily mean that it has d -wave symmetry, which is a symmetry of its \mathbf{k} -space argument. Rather, it tells us that the state is a spin-triplet state.

This set of linear relations is easily inverted, which yields

$$\psi_{\mathbf{k}} = \frac{1}{2}(v_{\uparrow\downarrow}(\mathbf{k}) - v_{\downarrow\uparrow}(\mathbf{k})) \quad (4.11)$$

$$d_{\mathbf{k},x} = \frac{1}{2}(v_{\downarrow\downarrow}(\mathbf{k}) - v_{\uparrow\uparrow}(\mathbf{k})) \quad (4.12)$$

$$d_{\mathbf{k},y} = -\frac{i}{2}(v_{\uparrow\uparrow}(\mathbf{k}) + v_{\downarrow\downarrow}(\mathbf{k})) \quad (4.13)$$

$$d_{\mathbf{k},z} = \frac{1}{2}(v_{\uparrow\downarrow}(\mathbf{k}) + v_{\downarrow\uparrow}(\mathbf{k})). \quad (4.14)$$

Since the space \mathcal{B} is fermionic, we have the symmetry³

$$|\mathbf{k}, s_1\rangle |-\mathbf{k}, s_2\rangle = -|-\mathbf{k}, s_2\rangle |\mathbf{k}, s_1\rangle. \quad (4.15)$$

Using this symmetry transformation on the basis vectors in the expansion of $|v\rangle$ in Eq. (4.4), then renaming indices and finally equating coefficients term by term, we see that for the coefficients of $|v\rangle$, this symmetry takes the form

$$v_{s_1 s_2}(\mathbf{k}) = -v_{s_2 s_1}(-\mathbf{k}). \quad (4.16)$$

4.3 Application of group elements

When we are talking about applying some symmetry transformation to a state, this is synonymous with applying a group element to a vector. Even more specifically, the ‘applying’ part means that we have some natural representation of the group on the vector space of the states, and we are using the linear transformation of the representation of the group element to act on the state vector. In this thesis, we will use the notation $g : |\psi\rangle$ to refer to this procedure.

Let g be an arbitrary group element in the symmetry group G and D be a representation of G on the d -dimensional vector space V . Let V have a basis $\{\mathbf{b}_i\}_{i=1}^d$. The application of a group element to a basis vector is then defined as

$$g : \mathbf{b}_i = \sum_j \mathbf{b}_j D_{ji}(g), \quad (4.17)$$

3. We are here assuming that the state is even in (time) frequency. It is also possible to have superconducting states that are odd in frequency [78], however we will not treat that possibility here.

where $D_{ji}(g)$ are the matrix elements of the linear transformation $D(g)$. The application of a group element to any vector in V is then calculated by expanding the vector in the basis and applying the representation D to each basis vector separately as a linear transformation:

$$g : \mathbf{v} = \sum_i v_i g : \mathbf{b}_i. \quad (4.18)$$

4.3.1 Active vector transformation

By the definition in Eq. (4.17), the transformation of $g :$ is viewed in a passive perspective since it is the basis vectors that change. It is often useful, and sometimes more intuitive, to consider the application of g to a vector \mathbf{v} in the basis $\{\mathbf{b}_i\}$ as an application not on the vectors themselves, but on the expansion coefficients v_i of \mathbf{v} in the basis. Given the transformation of the basis vectors in Eq. (4.17), we insert this into the transformation of \mathbf{v} in Eq. (4.18), which yields

$$g : \mathbf{v} = \sum_i v_i \sum_j \mathbf{b}_j D_{ji}(g) = \sum_i v'_i \mathbf{b}_i, \quad (4.19)$$

where we have defined the transformed coefficients

$$v'_i = \sum_j D_{ij}(g) v_j. \quad (4.20)$$

From this calculation, we see that we can consider the application of g as a transformation of the coefficients of the vector as

$$g : v_i = \sum_j D_{ij}(g) v_j. \quad (4.21)$$

Since, in this case, the basis vectors are left invariant and static, the vector \mathbf{v} can be viewed as being actively transformed in a fixed coordinate-system. Thus, the transformation $g : \mathbf{v}$ is, when viewed in this perspective, known as an active transformation. The active- and passive-perspective can be notoriously difficult to differentiate since they are, in the end, mathematically equivalent. Therefore, being consistent with a single perspective can dissuade a lot of confusion.

4.3.2 Representation on product spaces

The product space $V \otimes V$, where V is defined as before, is a vector space with a basis $\{\mathbf{b}_i \mathbf{b}_j\}_{i,j=1}^d$. A derived representation can be constructed from D on this product space called the product representation $D^{(D \times D)}(g)$. This is defined through its application on the basis by

$$g : \mathbf{b}_i \mathbf{b}_j = \sum_{kl} \mathbf{b}_k \mathbf{b}_l [D^{(D \times D)}(g)]_{kl,ij} = \sum_{kl} \mathbf{b}_k \mathbf{b}_l D_{ki}(g) D_{lj}(g). \quad (4.22)$$

To apply group theory to physical problems, we need to know how the objects we are working with in the physical theory transform under group elements. The most important vector space in quantum mechanics is arguably the Hilbert space where particle states are determined by a momentum- and spin quantum numbers. Each quantum number has its own vector space defined by the basis vectors $|\mathbf{k}\rangle$ and $|s\rangle$ in the Dirac notation. The combination of both quantum numbers in the description of a particle state, then gives a state in the product space of these vector spaces. A basis for this space is given by the vectors $|\mathbf{k}, s\rangle = |\mathbf{k}\rangle |s\rangle$. Given $\mathbf{k} \in \mathbb{R}^d$ and $s \in \{\uparrow, \downarrow\}$, these basis vectors transform according to the product representation of the representations on each vector space, given by

$$g : |\mathbf{k}', s'\rangle = \sum_{\mathbf{k}s} |\mathbf{k}, s\rangle D_{\mathbf{k}s; \mathbf{k}'s'}^{(\mathbf{k} \times s)} = \sum_{\mathbf{k}s} |\mathbf{k}, s\rangle D_{g ss'} \delta_{\mathbf{k}, g \cdot \mathbf{k}'}, \quad (4.23)$$

under a group element g . Here $g : \mathbf{k}'$ means application of g to the vector \mathbf{k}' through the standard representation of g in \mathbb{R}^d . $D_{g ss'}$ is a representation on the spin-up spin-down vector space given by the matrix

$$D_{g ss'} = \sigma_{ss'}^0 \cos(\phi/2) - i \hat{\mathbf{u}} \cdot \boldsymbol{\sigma}_{ss'} \sin(\phi/2), \quad (4.24)$$

where $\hat{\mathbf{u}}$ is the rotation axis unit vector, while ϕ is the angle that defines the proper rotation associated with g . $\boldsymbol{\sigma}$ is the vector notation for the 3 Pauli matrices and $\sigma_{ss'}^0 = \delta_{ss'}$ [79, 80].

In the BCS Hilbert space, which we discussed in more detail in Section 4.2, the basis vectors are outer products of the momentum spin basis vectors with opposite momentum: $\{|\mathbf{k}, s_1\rangle |-\mathbf{k}, s_2\rangle\}$. The product representation on this vector space then transforms the basis vectors

according to

$$g : |\mathbf{k}', s'_1\rangle |-\mathbf{k}', s'_2\rangle = \sum_{\mathbf{k} s_1 s_2} |\mathbf{k}, s_1\rangle |-\mathbf{k}, s_2\rangle D_{\mathbf{k} s_1 s_2; \mathbf{k}' s'_1 s'_2}^{(D \times D)}(g), \quad (4.25)$$

where

$$D_{\mathbf{k} s_1 s_2; \mathbf{k}' s'_1 s'_2}^{(D \times D)}(g) = D_{g s_1 s'_1} \delta_{\mathbf{k}, g; \mathbf{k}'} D_{g s_2 s'_2} \delta_{-\mathbf{k}, g; -\mathbf{k}'}. \quad (4.26)$$

Since group representations on \mathbf{k} is a linear transformation, then $\delta_{-\mathbf{k}, g; -\mathbf{k}'} = \delta_{\mathbf{k}, g; \mathbf{k}'}$, such that the last Kronecker delta function becomes superfluous.

4.3.3 Representation on ψ - \mathbf{d} functions

The coefficients of the basis expansion of a vector in the BCS Hilbert space are typically written in the conventional ψ - \mathbf{d} notation of Eq. (4.9). Taking the active view of group transformations, we can say that the expansion coefficients of arbitrary states $|v\rangle$ in the BCS Hilbert space \mathcal{B} transform like the v_i in Eq. (4.21), but where now the representation matrix D is given by the matrix $D_{\mathbf{k} s_1 s_2; \mathbf{k}' s'_1 s'_2}^{(D \times D)}$ above in Eq. (4.26). Written out then, the coefficients transform according to

$$g : v_{s_1 s_2}(\mathbf{k}) = \sum_{\mathbf{k}' s'_1 s'_2} D_{\mathbf{k} s_1 s_2; \mathbf{k}' s'_1 s'_2}^{(D \times D)} v_{s'_1 s'_2}(\mathbf{k}'). \quad (4.27)$$

Let now $|v\rangle$ be a state that is even in space, meaning that its expansion only consists of coefficients $\psi(\mathbf{k})$ in the ψ - \mathbf{d} notation. Then we see from Eq. (4.10) that $\psi(\mathbf{k})$ can be written $\psi(\mathbf{k}) = v_{\uparrow\downarrow}(\mathbf{k})$. The transformation properties of $\psi(\mathbf{k})$ are thus given by

$$\begin{aligned} g : \psi(\mathbf{k}) &= g : v_{\uparrow\downarrow}(\mathbf{k}) = \sum_{\mathbf{k}' s'_1 s'_2} D_{\mathbf{k} \uparrow\downarrow; \mathbf{k}' s'_1 s'_2}^{(D \times D)} \psi(\mathbf{k}') (i\sigma^y)_{s'_1 s'_2} \\ &= \psi(g^{-1} : \mathbf{k}) (i\sigma^y)_{\uparrow\downarrow} = \psi(g^{-1} : \mathbf{k}). \end{aligned} \quad (4.28)$$

In this calculation we inserted the expression of $D_{\mathbf{k} s_1 s_2; \mathbf{k}' s'_1 s'_2}^{(D \times D)}$ in Eq. (4.26) and used the equation $D_g i\sigma^y D_g^\top = i\sigma^y$, where D_g are the spin representation matrices given in Eq. (4.24).

To find the transformation properties of \mathbf{d}_k , the principle is the same as above for $\psi(\mathbf{k})$, but the calculations become more involved. We

assume that the spin-momentum basis expansion of a state $|v\rangle$ consists of only odd coefficients so that $v_{s_1 s_2}(\mathbf{k}) = \mathbf{d}_\mathbf{k} \cdot (\boldsymbol{\sigma} i \sigma^y)_{s_1 s_2}$. Inserting this into the active transformation of the coefficients of $|v\rangle$ in Eq. (4.27), and also inserting the expression for $D_{\mathbf{k} s_1 s_2; \mathbf{k}' s'_1 s'_2}^{(D \times D)}$ as we did before, yields

$$\begin{aligned} g : v_{s_1 s_2}(\mathbf{k}) &= \sum_{\mathbf{k}' s'_1 s'_2} \delta_{\mathbf{k}, g \cdot \mathbf{k}'} D_{g s_1 s'_1} D_{g s_2 s'_2} \mathbf{d}_{\mathbf{k}'} \cdot (\boldsymbol{\sigma} i \sigma^y)_{s'_1 s'_2} \\ &= \sum_s \left(D_g \boldsymbol{\sigma} \sigma^y D_g^\top \sigma^y \right)_{s_1 s} \cdot \mathbf{d}_{g^{-1} \cdot \mathbf{k}} i \sigma^y_{ss_2}. \end{aligned} \quad (4.29)$$

Since a group transformation (aka. the linear transformation given by a group representation) cannot transform a state that was even into being odd, or vice versa, then the resulting state given by the transformed coefficients $g : v_{s_1 s_2}(\mathbf{k})$ have to remain odd, and thus they can be expanded in terms of a new \mathbf{d}' such that

$$g : v_{s_1 s_2}(\mathbf{k}) = \sum_s \mathbf{d}'_{g^{-1} \cdot \mathbf{k}} \cdot \boldsymbol{\sigma}_{s_1 s} i \sigma^y_{ss_2}. \quad (4.30)$$

Having expanded both sides of the transformed coefficients with a common factor $i \sigma^y$ to the right, we can equate the remaining 2×2 spin matrices which gives an expression for $\mathbf{d}'_{g^{-1} \cdot \mathbf{k}} \cdot \boldsymbol{\sigma}$ by comparing Eq. (4.29) and Eq. (4.30). Furthermore, using the anti-commutation property $\{\sigma^i, \sigma^j\} = 2\delta_{ij}\sigma^0$ of Pauli matrices, we find that

$$d'_{\mathbf{k}, i} = \frac{1}{4} \text{Tr} (\{\sigma^i, \mathbf{d}'_\mathbf{k} \cdot \boldsymbol{\sigma}\}). \quad (4.31)$$

Inserting the expression for $\mathbf{d}'_{g^{-1} \cdot \mathbf{k}} \cdot \boldsymbol{\sigma}$ in terms of the $SU(2)$ spin-representation matrices D_g , and inserting these matrices full expression, which can be found in Eq. (4.24), yields after some algebra

$$\begin{aligned} d'_{g^{-1} \cdot \mathbf{k}, i} &= \frac{1}{4} \text{Tr} (\{\sigma^i, \mathbf{d}_{g^{-1} \cdot \mathbf{k}} \cdot D_g \boldsymbol{\sigma} \sigma^y D_g^\top \sigma^y\}) \\ &= R_{ij}(\hat{\mathbf{u}}, \phi) d_{g^{-1} \cdot \mathbf{k}, j}, \end{aligned} \quad (4.32)$$

where we have defined the matrix

$$\begin{aligned} R_{ij}(\hat{\mathbf{u}}, \phi) &= \delta_{ij} \cos \phi + \hat{u}_i \hat{u}_j (1 - \cos \phi) - \epsilon_{ijk} \hat{u}_k \sin \phi \\ &= \begin{pmatrix} \cos \phi + \hat{u}_x^2 (1 - \cos \phi) & \hat{u}_x \hat{u}_y (1 - \cos \phi) - \hat{u}_z \sin \phi & \hat{u}_x \hat{u}_z (1 - \cos \phi) + \hat{u}_y \sin \phi \\ \hat{u}_y \hat{u}_x (1 - \cos \phi) + \hat{u}_z \sin \phi & \cos \phi + \hat{u}_y^2 (1 - \cos \phi) & \hat{u}_y \hat{u}_z (1 - \cos \phi) - \hat{u}_x \sin \phi \\ \hat{u}_z \hat{u}_x (1 - \cos \phi) - \hat{u}_y \sin \phi & \hat{u}_z \hat{u}_y (1 - \cos \phi) + \hat{u}_x \sin \phi & \cos \phi + \hat{u}_z^2 (1 - \cos \phi) \end{pmatrix}. \end{aligned} \quad (4.33)$$

This matrix is in fact the rotation matrix of a vector in \mathbb{R}^3 by an angle ϕ about a unit vector $\hat{\mathbf{u}}$. Since the coefficients of an odd state $|v\rangle$ are fully determined by the vector \mathbf{d} , their transformation can be regarded just as a transformation of \mathbf{d} itself, which thus takes the form

$$g : d_{\mathbf{k},i} = R_{ij}(\hat{\mathbf{u}}, \phi) d_{g^{-1}(\mathbf{k}),j}, \quad (4.34)$$

where $\hat{\mathbf{u}}$ and ϕ give the unit vector and angle respectively, of the proper rotation⁴ that is associated with g . The conclusion is thus that \mathbf{d} transforms as a vector by the proper rotation associated with g .

4.3.4 Representation on ladder operators

The fermionic creation and annihilation operators $c_{\mathbf{k},s}^\dagger$ and $c_{\mathbf{k},s}$, which we will collectively refer to as $c_{\mathbf{k},s}^{(\dagger)}$, are second-quantized operators that act on multi-particle states in a fermionic Fock space [76]. To properly define how a group element g transforms these operators, we should strictly speaking first derive the representation $Q(g)$ of g on N -particle states $|\mathbf{k}_1, s_1\rangle \wedge \dots \wedge |\mathbf{k}_N, s_N\rangle$ for arbitrary N , and then use the relation $g : c_{\mathbf{k},s}^{(\dagger)} = Q(g)c_{\mathbf{k},s}^{(\dagger)}Q(g)^{-1}$ to derive their transformation properties. However, luckily, a shortcut is possible because the $Q(g)$ representation is connected with how g acts on the single-particle basis $\{|\mathbf{k}, s\rangle\}$ through the relationship

$$Q(g)c_{\mathbf{k},s}^{(\dagger)}Q(g)^{-1} = c^{(\dagger)}(g : |\mathbf{k}, s\rangle). \quad (4.35)$$

In this notation we treat the creation and annihilation operators as respectively linear and antiunitary functions of the states that they create or annihilate. If the matrix-components of the representation of g on the single-particle basis is denoted $D_{\mathbf{k}s; \mathbf{k}'s'}^{(\mathbf{k} \times s)}$, then we thus have the transformation property

$$g : c_{\mathbf{k},s}^{(\dagger)} = \sum_{\mathbf{k}'s'} c_{\mathbf{k}',s'}^{(\dagger)} [D_{\mathbf{k}'s'; \mathbf{k}s}^{(\mathbf{k} \times s)}]^{(*)}, \quad (4.36)$$

where the matrix-elements are complex conjugated only if we are transforming an annihilation operator.

4. The *proper rotation* of a group element g is the rotation obtained when writing g as this rotation followed by either the group element of inversion or identity, which can be done in all point-groups.

Given that g is an element of some point-group, such that it can be decomposed into a rotation and a parity inversion, then we may use the representation on $\{|\mathbf{k}, s\rangle\}$ given in Eq. (4.23) such that

$$g : c_{\mathbf{k},s}^{(\dagger)} = \sum_{s'} c_{g:\mathbf{k},s'}^{(\dagger)} D_{g s' s}^{(*)}, \quad (4.37)$$

where the matrix $D_{g s s'}$ is defined in Eq. (4.24). As an example, a simple parity transformation $g = \hat{P}$, then transform the operators according to $\hat{P} : c_{\mathbf{k},s}^{(\dagger)} = c_{-\mathbf{k},s}^{(\dagger)}$.

We will later need the translation transformation $g = \mathbf{R}$ as well. In real space it is defined by $\mathbf{R} : |\mathbf{r}, s\rangle = |\mathbf{r} + \mathbf{R}, s\rangle$ and given by the linear transformation $L(\mathbf{R}) = e^{i\mathbf{R} \cdot \hat{\mathbf{p}}/\hbar}$, where $\hat{\mathbf{p}}$ is the momentum operator⁵ $\hat{\mathbf{p}} = \hbar \nabla / i$. It then follows by a Fourier-transformation that the fermionic operators transform according to

$$\mathbf{R} : c_{\mathbf{k},s}^{(\dagger)} = (e^{-i\mathbf{R} \cdot \mathbf{k}})^{(*)} c_{\mathbf{k},s}^{(\dagger)}. \quad (4.38)$$

Finally, we discuss the transformation of time-reversal. This operation is traditionally denoted Θ and consists of flipping the sign of time, which implies flipping the spin and momentum. Time-reversal is special in that it is antiunitary, i.e. it transforms all linear coefficients into their complex conjugates. Because of this, any representation of time-reversal is often factorized into a normal linear part and a complex-conjugation operator \hat{K} . From its action on the spin-momentum basis vectors $|\mathbf{k}, s\rangle$, time-reversal transforms the fermionic creation and annihilation operators according to

$$\Theta : c_{\mathbf{k},s}^{(\dagger)} = \sum_{s'} c_{-\mathbf{k},s'}^{(\dagger)} (-i\sigma_y)_{s's}. \quad (4.39)$$

Note that the matrix $-i\sigma_y$ is not complex conjugated for the fermionic annihilation operators because of the antiunitarity of Θ .

4.4 Single-particle Hamiltonian symmetries

Any fermionic single-particle operator can be written in the spin-momentum basis as

$$\hat{H} = \sum_{\mathbf{k}\mathbf{k}'ss'} H_{\mathbf{k}\mathbf{k}'ss'}^{ss'} c_{\mathbf{k},s}^{\dagger} c_{\mathbf{k}',s'}^{ss'}. \quad (4.40)$$

5. The form of the linear transformation $L(\mathbf{R})$ follows directly from the multivariate Taylor expansion.

In this section we will apply the common finite symmetry-transformations discussed in the last Section and see how this reduces the degrees of freedom in \hat{H} so that it can be written in a more concise form. To begin, we reduce the notational burden by expanding the spin-matrix elements in separate coefficients in the Pauli-matrix basis just as was done for the BCS Hilbert space vector coefficients $v_{s_1 s_2}(\mathbf{k})$ in Eq. (4.7), such that

$$\hat{H} = \sum_{\mathbf{k}\mathbf{k}'ss'} [\xi_{\mathbf{k}\mathbf{k}'}\sigma^0 + \gamma_{\mathbf{k}\mathbf{k}'} \cdot \boldsymbol{\sigma}]_{ss'} c_{\mathbf{k},s}^\dagger c_{\mathbf{k}',s'}.$$
 (4.41)

The transformation of a quantum mechanical operator such as the Hamiltonian, is defined by $g : \hat{H} = Q(g)\hat{H}Q(g)^{-1}$ for some many-body representation $Q(g)$. Inserting the form of \hat{H} in Eq. (4.41) as a single-particle operator in the spin-momentum basis, yields

$$g : \hat{H} = \sum_{\mathbf{k}\mathbf{k}'ss'} [\xi_{\mathbf{k}\mathbf{k}'}\sigma^0 + \gamma_{\mathbf{k}\mathbf{k}'} \cdot \boldsymbol{\sigma}]_{ss'} (g : c_{\mathbf{k},s}^\dagger)(g : c_{\mathbf{k}',s'}),$$
 (4.42)

after inserting $Q(g)^{-1}Q(g)$ between the creation and annihilation operator. We can now use the transformation properties of these operators presented in Section 4.3.4 to derive the transformation properties and symmetric form of the Hamiltonian.

For a translation invariant system, we need a translation invariant Hamiltonian. Using the transformation of $c^{(\dagger)}$ in Eq. (4.38) under a translation \mathbf{R} , we get that the coefficients $\xi_{\mathbf{k}\mathbf{k}'}$ and $\gamma_{\mathbf{k}\mathbf{k}'}$ have to satisfy the equation

$$(e^{i\mathbf{R}\cdot(\mathbf{k}'-\mathbf{k})} - 1)[\xi_{\mathbf{k}\mathbf{k}'}\sigma^0 + \gamma_{\mathbf{k}\mathbf{k}'} \cdot \boldsymbol{\sigma}] = 0.$$
 (4.43)

Since the sigma-matrices are linearly independent and the translation \mathbf{R} is arbitrary, it follows that both $\xi_{\mathbf{k}\mathbf{k}'}$ and $\gamma_{\mathbf{k}\mathbf{k}'}$ must vanish whenever $\mathbf{k} \neq \mathbf{k}'$, i.e. these coefficients must be diagonal in \mathbf{k} . The Hamiltonian can then be written on the reduced form

$$\hat{H} = \sum_{\mathbf{k}ss'} [\xi_{\mathbf{k}}\sigma^0 + \gamma_{\mathbf{k}} \cdot \boldsymbol{\sigma}]_{ss'} c_{\mathbf{k},s}^\dagger c_{\mathbf{k},s'}.$$
 (4.44)

In the vast majority of cases, the system is Hermitian such that the Hamiltonian is self-adjoint and has real eigenvalues. Enforcing the

condition $\hat{H}^\dagger = \hat{H}$ on the translationally invariant Hamiltonian in Eq. (4.44) yields the equation

$$(\xi_{\mathbf{k}}^* - \xi_{\mathbf{k}})\sigma^0 + (\gamma_{\mathbf{k}}^* - \gamma_{\mathbf{k}}) \cdot \boldsymbol{\sigma} = 0, \quad (4.45)$$

by using the self-adjoint property of the Pauli-matrices. This implies further, by the linear independence of the sigma-matrices, that the coefficients $\xi_{\mathbf{k}}$ and $\gamma_{\mathbf{k}}$ are self-conjugate and hence real.

Time-reversal symmetry of the system implies that \hat{H} should be invariant under the transformation Θ , which transforms fermionic ladder-operators according to Eq. (4.39). Applying this transformation to the fermionic ladder-operators in the translationally invariant Hamiltonian of Eq. (4.44), and remembering that $Q(\Theta)$ is an antiunitary operator, we get the transformed Hamiltonian

$$\Theta : \hat{H} = \sum_{\mathbf{k}ss'} [\xi_{-\mathbf{k}}^* \sigma^0 - \gamma_{-\mathbf{k}}^* \cdot \boldsymbol{\sigma}]_{ss'} c_{\mathbf{k},s}^\dagger c_{\mathbf{k},s'}. \quad (4.46)$$

For the Hamiltonian to be invariant under time-reversal symmetry, its coefficients thus have to satisfy $\xi_{\mathbf{k}} = \xi_{-\mathbf{k}}^*$ and $\gamma_{\mathbf{k}} = -\gamma_{-\mathbf{k}}^*$.

Finally, we look at the transformation of the Hamiltonian under point-group elements g . Using the transformation-property of the fermionic creation and annihilation operators in Eq. (4.37), then the translation-invariant Hamiltonian in Eq. (4.44) transforms according to

$$g : \hat{H} = \sum_{\mathbf{k}ss'} [\xi_{g^{-1}:\mathbf{k}} \sigma^0 + \gamma_{g^{-1}:\mathbf{k}} \cdot D_g \boldsymbol{\sigma} D_g^\dagger]_{ss'} c_{\mathbf{k},s}^\dagger c_{\mathbf{k},s'}. \quad (4.47)$$

Using the form of the spin-rotation matrix D_g in Eq. (4.24), we find that

$$\gamma_{g^{-1}:\mathbf{k}} \cdot D_g \boldsymbol{\sigma} D_g^\dagger = \gamma'_{g^{-1}:\mathbf{k}} \cdot \boldsymbol{\sigma}, \quad (4.48)$$

for the transformed vector

$$\gamma'_{g^{-1}:\mathbf{k}} = R(\hat{\mathbf{u}}, \phi) \gamma_{g^{-1}:\mathbf{k}}, \quad (4.49)$$

where $R(\hat{\mathbf{u}}, \phi)$ is the 3×3 matrix representation of the proper-rotation associated with g given in Eq. (4.33). Symmetry of \hat{H} under point-group transformation thus implies the symmetry conditions $\xi_{g:\mathbf{k}} = \xi_{\mathbf{k}}$ and $R(\hat{\mathbf{u}}, \phi) \gamma_{g^{-1}:\mathbf{k}} = \gamma_{\mathbf{k}}$ on the coefficients of the Hamiltonian.

4.5 Projection Operators

Let us assume that we are in a vector space V that can be divided into possibly several different IRs $D^{(\alpha)}$ of some symmetry group G . Further, let the basis vectors of these IRs be denoted by $b_m^{(\alpha)}$ where m thus counts the number of basis vectors in each IR. Then, an arbitrary vector $v \in V$ can be written in terms of these basis vectors as

$$v = \sum_{\alpha} \sum_m c_m^{(\alpha)} b_m^{(\alpha)}. \quad (4.50)$$

A projection operator can be used to extract any combination of a constant $c_m^{(\alpha)}$ multiplied by a basis vector $b_n^{(\alpha)}$, where m and n can in general be different. Denoting the projection operator that picks out the m th constant multiplied by the l th basis vector in the IR β of the expansion of v : $P_{lm}^{(\beta)}$, then

$$P_{lm}^{(\beta)} v = c_m^{(\beta)} b_l^{(\beta)}. \quad (4.51)$$

This is extremely useful in finding explicit expressions for the basis vectors $b_l^{(\beta)}$ of the IRs. To achieve this, the projection operator is defined as

$$P_{l,m}^{(\beta)} = \frac{d_{\beta}}{|G|} \sum_{g \in G} D_{lm}^{(\beta)}(g)^* g :, \quad (4.52)$$

where d_{β} is the dimension of IR β , $D_{lm}^{(\beta)}(g)$ is the lm element of the matrix representation of the group element g and finally we have used the notation $g :$ to denote application on vectors by the relevant representation. An example is the application of g to the basis vectors $b_m^{(\alpha)}$. Since the relevant representation of g in this case is the IR for which $b_m^{(\alpha)}$ is a basis vector, the application becomes

$$g : b_m^{(\alpha)} = \sum_n b_n^{(\alpha)} D_{nm}^{(\alpha)}(g). \quad (4.53)$$

Usually, the full generality of the projection operators $P_{l,m}^{(\beta)}$ isn't needed and it suffices to consider the diagonal projection operators $P_{l,l}^{(\beta)} \equiv P_l^{(\beta)}$ or indeed their sum, in which case the resulting operator can be written only in terms of the IR characters $\chi^{(\alpha)}(g)$ since

$$P^{(\beta)} \equiv \sum_l P_l^{(\beta)} = \frac{d_{\beta}}{|G|} \sum_{g \in G} \sum_l D_{ll}^{(\beta)}(g)^* g := \frac{d_{\beta}}{|G|} \sum_{g \in G} \chi^{(\beta)}(g)^* g : . \quad (4.54)$$

4.6 Symmetries of the Square Lattice

The symmetry group of the square lattice is denoted C_{4v} in the Schönflies notation. It contains 8 elements in total:

e : The identity element (do nothing),

C_4 : Rotation by 90° in the positive direction (ccw),

C_4^{-1} : Rotation by 90° in the negative direction (cw),

C_4^2 : Rotation by 180° ,

σ_x : Mirror about the zy -plane,

σ_y : Mirror about the zx -plane,

σ_{d_1} : Mirror about the downwards diagonal plane,⁶

σ_{d_2} : Mirror about the upwards diagonal plane.

This results in the group multiplication table in Table 4.1. We can check that this is correct by performing the group transformations in the top row followed by the one in the left column⁷ and seeing that this results in the group transformations where these two intersect. As an example consider the vector $(x, y)^\top$. Transforming the basis by the 90° counterclockwise rotation C_4 we get $(-y, x)^\top$. Then mirroring this result about the yz -plane yields $(y, x)^\top$. We now realize that this is the same as mirroring the original basis about the axis $y = x$, hence $\sigma_x C_4 = \sigma_{d_2}$ as the multiplication table says.

4.6.1 Conjugation classes

The conjugation classes of a group are the sets of group elements that are conjugate to each other, meaning that there exists a group element g such that $gAg^{-1} = B$ between conjugate elements A and B . Since conjugation is an equivalence relation, it subdivides the group elements exactly into conjugation classes. The conjugation classes of the

-
6. We are assuming the western bias of left-to-right movement here. More precisely it is the plane containing the z axis and the line $y = -x$
 7. When combining a group-element g_c from the left column and g_r from the top row, the result should be $g_c g_r$.

Table 4.1: Group multiplication table of the group C_{4v} .

	e	C_4	C_4^2	C_4^{-1}	σ_x	σ_y	σ_{d_1}	σ_{d_2}
e	e	C_4	C_4^2	C_4^{-1}	σ_x	σ_y	σ_{d_1}	σ_{d_2}
C_4	C_4	C_4^2	C_4^{-1}	e	σ_{d_1}	σ_{d_2}	σ_y	σ_x
C_4^2	C_4^2	C_4^{-1}	e	C_4	σ_y	σ_x	σ_{d_2}	σ_{d_1}
C_4^{-1}	C_4^{-1}	e	C_4	C_4^2	σ_{d_2}	σ_{d_1}	σ_x	σ_y
σ_x	σ_x	σ_{d_2}	σ_y	σ_{d_1}	e	C_4^2	C_4^{-1}	C_4
σ_y	σ_y	σ_{d_1}	σ_x	σ_{d_2}	C_4^2	e	C_4	C_4^{-1}
σ_{d_1}	σ_{d_1}	σ_x	σ_{d_2}	σ_y	C_4	C_4^{-1}	e	C_4^2
σ_{d_2}	σ_{d_2}	σ_y	σ_{d_1}	σ_x	C_4^{-1}	C_4	C_4^2	e

group C_{4v} are $e = \{e\}$, $2C_4 = \{C_4, C_4^{-1}\}$, $C_4^2 = \{C_4^2\}$, $2\sigma_d = \{\sigma_{d_1}, \sigma_{d_2}\}$ and $2\sigma_v = \{\sigma_x, \sigma_y\}$. The character $\chi^\Gamma(g)$ of a representation Γ is the trace of the representation matrix $D^\Gamma(g)$ of a certain group element g . Since the trace is cyclic, then for conjugate group elements A and B

$$\begin{aligned} \chi^\Gamma(B) &= \text{Tr} \left(D^\Gamma(g) D^\Gamma(A) D^\Gamma(g^{-1}) \right) \\ &= \text{Tr} \left(D^\Gamma(g^{-1}) D^\Gamma(g) D^\Gamma(A) \right) \\ &= \text{Tr} \left(D^\Gamma(g^{-1}g) D^\Gamma(A) \right) = \chi^\Gamma(A). \end{aligned} \quad (4.55)$$

This means that the representations of all group elements in a certain conjugation class have the same character.

It is useful to list the characters of the different conjugation classes in a table according to the different IRs of a group. This is because the number of conjugation classes of a finite group is the same as the number of IRs of that group. This table is known as the character table of the group. The character table of the group C_{4v} is shown in Table 4.2. This table can be derived without knowing the details of the irreducible representations, but instead using character relations from basic group theory.⁸ Because of this, the character table can be of immense help, and is typically the first step in determining the irreducible representations of a group.

8. Many of these relations are derived from the great orthogonality theorem which can be found e.g. in [77].

Table 4.2: Character table of the group C_{4v} .

C_{4v}	e	$2C_4$	C_4^2	$2\sigma_v$	$2\sigma_d$
Γ_1	1	1	1	1	1
Γ_2	1	1	1	-1	-1
Γ_3	1	-1	1	1	-1
Γ_4	1	-1	1	-1	1
Γ_5	2	0	-2	0	0

4.6.2 Irreducible representations

The dimensionality of the IR can be found in Table 4.2 by looking up the first column, i.e. the column giving the character of the conjugation class $\{e\}$. Since the group element e maps to the identity transformation in all representations, then its trace gives the dimension of the representation. From the table, we see that all the IRs are 1-dimensional except for Γ_5 which is 2-dimensional. All the 1-dimensional IR matrices are then completely determined by the character table since they are just given by the characters themselves, e.g. $D^{\Gamma_2}(\sigma_x) = -1$.

To find a 2-dimensional representation of C_{4v} , we can imagine how a normal 2D vector $(x, y)^T \in \mathbb{R}^2$ behaves under its transformations. We take again the example of a counterclockwise rotation by 90° of the basis which transforms a vector

$$C_4 : \begin{pmatrix} x \\ y \end{pmatrix} = \begin{pmatrix} -y \\ x \end{pmatrix} = \begin{pmatrix} 0 & -1 \\ 1 & 0 \end{pmatrix} \begin{pmatrix} x \\ y \end{pmatrix}. \quad (4.56)$$

Obviously, the matrix

$$D^{(\Gamma_5)}(C_4) = \begin{pmatrix} 0 & -1 \\ 1 & 0 \end{pmatrix}, \quad (4.57)$$

is the representation matrix of a two-dimensional representation of C_4 . Continuing in this way for all the group transformations, yields the

matrices

$$D^{(\Gamma_5)}(e) = \begin{pmatrix} 1 & 0 \\ 0 & 1 \end{pmatrix}, \quad D^{(\Gamma_5)}(C_4) = \begin{pmatrix} 0 & -1 \\ 1 & 0 \end{pmatrix}, \quad (4.58a)$$

$$D^{(\Gamma_5)}(C_4^{-1}) = \begin{pmatrix} 0 & 1 \\ -1 & 0 \end{pmatrix}, \quad D^{(\Gamma_5)}(C_4^2) = \begin{pmatrix} -1 & 0 \\ 0 & -1 \end{pmatrix}, \quad (4.58b)$$

$$D^{(\Gamma_5)}(\sigma_x) = \begin{pmatrix} -1 & 0 \\ 0 & 1 \end{pmatrix}, \quad D^{(\Gamma_5)}(\sigma_y) = \begin{pmatrix} 1 & 0 \\ 0 & -1 \end{pmatrix}, \quad (4.58c)$$

$$D^{(\Gamma_5)}(\sigma_{d_1}) = \begin{pmatrix} 0 & -1 \\ -1 & 0 \end{pmatrix}, \quad D^{(\Gamma_5)}(\sigma_{d_2}) = \begin{pmatrix} 0 & 1 \\ 1 & 0 \end{pmatrix}. \quad (4.58d)$$

Taking the trace of these matrices, we see that this representation's characters are the same as the ones for the IR Γ_5 in the character table (Table 4.2). This implies that $\sum_g |\chi^{\Gamma_5}(g)|^2 = |C_{4v}|$, which implies in turn that the representation given by the matrices in Eq. (4.58) is irreducible. Thus, this is indeed the Γ_5 IR as advertised, and we have completed the description of the representation matrices of all the IRs of C_{4v} .

4.6.3 Proper rotations of the odd BCS function d_k

When discussing the representation of general group elements on states in the BCS Hilbert space in Section 4.3.3, we learned from Eq. (4.34) that the coefficient $\mathbf{d}_k \in \mathbb{R}^3$ of odd states transforms by a proper rotation $R(\hat{\mathbf{u}}, \phi)$. As mentioned before, a proper rotation of a group element g is the rotation obtained when writing g as a rotation followed by an inversion P or the identity transformation. We thus obtain the representation matrices of the 3D-representations of group elements $g \in C_{4v}$ directly from the 3D rotation matrix $R(\hat{\mathbf{u}}, \phi)$, by envisioning the combination of a rotation and $C_4^2 = P$ or e that leads to g . Because of this, we denote the representation matrices of this representation $R(g)$. As an example $\sigma_x = C_4^2 R(\hat{\mathbf{x}}, \pi)$, such that the representation $R(\sigma_x) = R(\hat{\mathbf{x}}, \pi)$. Written out in its full matrix form, this yields the

representation matrices

$$R(C_4) = \begin{pmatrix} 0 & -1 & 0 \\ 1 & 0 & 0 \\ 0 & 0 & 1 \end{pmatrix}, \quad R(C_4^{-1}) = \begin{pmatrix} 0 & 1 & 0 \\ -1 & 0 & 0 \\ 0 & 0 & 1 \end{pmatrix}, \quad (4.59a)$$

$$R(e) = \begin{pmatrix} 1 & 0 & 0 \\ 0 & 1 & 0 \\ 0 & 0 & 1 \end{pmatrix}, \quad R(C_4^2) = \begin{pmatrix} -1 & 0 & 0 \\ 0 & -1 & 0 \\ 0 & 0 & 1 \end{pmatrix}, \quad (4.59b)$$

$$R(\sigma_x) = \begin{pmatrix} 1 & 0 & 0 \\ 0 & -1 & 0 \\ 0 & 0 & -1 \end{pmatrix}, \quad R(\sigma_y) = \begin{pmatrix} -1 & 0 & 0 \\ 0 & 1 & 0 \\ 0 & 0 & -1 \end{pmatrix}, \quad (4.59c)$$

$$R(\sigma_{d_1}) = \begin{pmatrix} 0 & 1 & 0 \\ 1 & 0 & 0 \\ 0 & 0 & -1 \end{pmatrix}, \quad R(\sigma_{d_2}) = \begin{pmatrix} 0 & -1 & 0 \\ -1 & 0 & 0 \\ 0 & 0 & -1 \end{pmatrix}. \quad (4.59d)$$

4.7 Square Lattice Harmonics

Since $\psi(\mathbf{k})$ and $\mathbf{d}_\mathbf{k}$ are invariant with respect to translation by any reciprocal lattice vector \mathbf{Q} , $\psi(\mathbf{k} + \mathbf{Q}) = \psi(\mathbf{k})$, they can be expanded in a discrete Fourier transform over the real lattice, such that

$$\psi(\mathbf{k}) = \frac{1}{\sqrt{N}} \sum_{\mathbf{R}} \psi_{\mathbf{R}} \cos \mathbf{R} \cdot \mathbf{k}, \quad (4.60)$$

and

$$\mathbf{d}_{\mathbf{k}} = \frac{1}{\sqrt{N}} \sum_{\mathbf{R}} \mathbf{d}_{\mathbf{R}} \sin \mathbf{R} \cdot \mathbf{k}, \quad (4.61)$$

where the exponential of the Fourier transform has been reduced to trigonometric functions by the parity assumed of the functions.

We are interested in the basis vectors $|\Gamma, q, m\rangle$ of the representations of the symmetry group C_{4v} of the 2D square lattice. In this ket notation, Γ gives the irreducible representation, m enumerates the basis vectors in case the IR is multi-dimensional, while q gives the version of the IR in case the space of possible $|v\rangle$ permits multiple versions of the same IR. In the active view of group transformations, the question of finding the basis vectors translates to finding the basis-functions of the functions $\psi(\mathbf{k})$ and $\mathbf{d}_\mathbf{k}$ for even and odd bases, respectively. In Section 4.3.3, we saw how these functions transformed under group

transformations. In Section 4.5, we saw how the projection operators could be used to extract individual basis vectors. We will now use these operators on the Fourier expansions of $\psi(\mathbf{k})$ and $\mathbf{d}_\mathbf{k}$ to extract possible basis-functions given the symmetry group of the square lattice.

4.7.1 Even basis-functions

We remember from Eq. (4.28) that the function $\psi(\mathbf{k})$ transforms as

$$g : \psi(\mathbf{k}) = \psi(g^{-1} : \mathbf{k}), \quad (4.62)$$

under a group transformation g . Operating on the Fourier expansion of $\psi(\mathbf{k})$ in Eq. (4.60) with the projection operator defined in Eq. (4.52) by an arbitrary IR Γ , yields

$$\begin{aligned} P_{l,l}^{(\Gamma)} \psi(\mathbf{k}) &= \frac{d_\Gamma}{8\sqrt{N}} \sum_{\mathbf{R}} \psi_{\mathbf{R}} \left[(D_{ll}^{(\Gamma)}(e) + D_{ll}^{(\Gamma)}(C_4^2)) \cos(\mathbf{R} \cdot \mathbf{k}) \right. \\ &\quad + (D_{ll}^{(\Gamma)}(C_4) + D_{ll}^{(\Gamma)}(C_4^{-1})) \cos(R_x k_y - R_y k_x) \\ &\quad + (D_{ll}^{(\Gamma)}(\sigma_x) + D_{ll}^{(\Gamma)}(\sigma_y)) \cos(R_x k_x - R_y k_y) \\ &\quad \left. + (D_{ll}^{(\Gamma)}(\sigma_{d_1}) + D_{ll}^{(\Gamma)}(\sigma_{d_2})) \cos(R_x k_y + R_y k_x) \right]. \end{aligned} \quad (4.63)$$

Since $\mathbf{k} \in \mathbb{R}^2$, we have in this calculation used the natural 2D representation given by the matrices in Eq. (4.58) of the group elements in C_{4v} to calculate the expressions $g^{-1} : \mathbf{k}$ inside the cosine functions. Inserting the matrix elements of the different IRs of C_{4v} which we discussed in Section 4.6, we get the projected functions

$$\begin{aligned} P_{1,1}^{(\Gamma_1)} \psi(\mathbf{k}) &\propto \sum_{\mathbf{R}} \psi_{\mathbf{R}} [\cos R_x k_x \cos R_y k_y + \cos R_x k_y \cos R_y k_x], \\ P_{1,1}^{(\Gamma_2)} \psi(\mathbf{k}) &\propto \sum_{\mathbf{R}} \psi_{\mathbf{R}} [\sin R_x k_y \sin R_y k_x - \sin R_x k_x \sin R_y k_y], \\ P_{1,1}^{(\Gamma_3)} \psi(\mathbf{k}) &\propto \sum_{\mathbf{R}} \psi_{\mathbf{R}} [\cos R_x k_x \cos R_y k_y - \cos R_x k_y \cos R_y k_x], \\ P_{1,1}^{(\Gamma_4)} \psi(\mathbf{k}) &\propto \sum_{\mathbf{R}} \psi_{\mathbf{R}} [\sin R_x k_x \sin R_y k_y + \sin R_x k_y \sin R_y k_x], \\ P_{1,1}^{(\Gamma_5)} \psi(\mathbf{k}) &\propto 0, \\ P_{2,2}^{(\Gamma_5)} \psi(\mathbf{k}) &\propto 0. \end{aligned} \quad (4.64)$$

Since the projection operators $P_{ll}^{(\Gamma)}$ projects onto the subspace of vectors belonging to the IR Γ , if we let the different basis-functions of the IRs Γ be denoted $\psi^{(\Gamma),q,m}(\mathbf{k})$, then we expect the projection to produce the result

$$P_{l,l}^{(\Gamma)}\psi(\mathbf{k}) = \sum_q c_{q,l}\psi^{(\Gamma),q,l}(\mathbf{k}), \quad (4.65)$$

by the property of projection operators in Eq. (4.51). Here q again enumerates the version of the basis of Γ possible in the space of different $\psi(\mathbf{k})$, and $c_{q,l}$ are the coefficients of $\psi(\mathbf{k})$ in the basis of the IR basis-functions. Comparing Eqs. (4.65) and (4.64), we see that different sets of basis vectors can be obtained for the IRs by including different order terms in the \mathbf{R} -sum, i.e. different lattice neighbour sites. It is also worth noting that the IR Γ_5 does not exist in the space of possible $\psi(\mathbf{k})$, since it is an odd representation.

Including on-site, nearest neighbour and next-nearest neighbour sites in the \mathbf{R} sum of the projected arbitrary function $\psi(\mathbf{k})$ on the Γ_1 subspace in Eq. (4.65), we see that any such function can be constructed from the three basis-functions

$$\psi^{(\Gamma_1),1}(\mathbf{k}) = \frac{1}{2\pi}, \quad (4.66a)$$

$$\psi^{(\Gamma_1),2}(\mathbf{k}) = \frac{1}{2\pi}(\cos k_x + \cos k_y), \quad (4.66b)$$

$$\psi^{(\Gamma_1),3}(\mathbf{k}) = \frac{1}{\pi} \cos k_x \cos k_y. \quad (4.66c)$$

Each of these functions give a complete basis-function set of the Γ_1 IR which can be checked by calculating how they transform under group elements $g \in C_{4v}$. In this case, since this is the trivial Γ_1 representation, the functions are symmetric under all group elements g which produces the character 1 for all conjugation classes (compare with the first row in Table 4.2).

These basis-functions are automatically mutually orthogonal since they belong to different IR version subspaces and their normalization coefficients have been chosen such that they are normal on the 1st Brillouin zone, i.e.

$$\int_{-\pi}^{\pi} \int_{-\pi}^{\pi} dk_x dk_y \psi^{(\Gamma_1),q}(\mathbf{k})^* \psi^{(\Gamma_1),q'}(\mathbf{k}) = \delta_{qq'}. \quad (4.67)$$

Inserting up to next-nearest neighbor sites for \mathbf{R} in the projected functions under the remaining IRs, we find the orthonormal basis-functions

$$\psi^{(\Gamma_3)}(\mathbf{k}) = \frac{1}{2\pi}(\cos k_x - \cos k_y), \quad (4.68a)$$

$$\psi^{(\Gamma_4)}(\mathbf{k}) = \frac{1}{\pi} \sin k_x \sin k_y, \quad (4.68b)$$

of the representations Γ_3 and Γ_4 , respectively. The Γ_3 basis is found by expansion of \mathbf{R} to nearest neighbor, while the one for Γ_4 is found at the next-nearest neighbor. To get a basis vector for the representation Γ_2 , we would need to expand beyond the next-nearest neighbor site.

The basis-functions in Eqs. (4.68) and (4.66) are also known as square lattice harmonics. The set of square lattice harmonic functions includes the set of functions found when expanding \mathbf{R} to arbitrary sites. As we have seen, they can be grouped and found through consideration of the IRs of the symmetry group of the square lattice. We have so far only considered even-in- \mathbf{k} basis-functions. In the next section we will complete our discussion of square lattice harmonics with the inclusion of odd functions.

4.7.2 Odd basis-functions

Any state made from exclusively odd basis-functions, is fully determined by the coefficients \mathbf{d}_k . As we derived in Section 4.3.3, these coefficients transform as⁹ $g : \mathbf{d}_k = R(g)\mathbf{d}_{g^{-1}\cdot k}$ under group elements $g \in C_{4v}$, where $R(g)$ are the representation matrices in Eq. (4.59). Otherwise, finding bases for irreducible representations can be done by following the same procedure as that outlined for even functions in the last Section.

As an example, we consider finding a basis for the Γ_5 irreducible representation of the group C_{4v} in the space of odd functions \mathbf{d}_k . Acting on the Fourier expansion of the arbitrary function \mathbf{d}_k in Eq. (4.61) with the projection operators Eq. (4.52) down on the subspace of the

9. See Eq. (4.34).

IR Γ_5 of the symmetry group C_{4v} , yields the results

$$P_{1,1}^{(\Gamma_5)} \mathbf{d}_k = \frac{\hat{\mathbf{z}}}{\sqrt{N}} \sum_{\mathbf{R}} d_{\mathbf{R},z} \cos R_x k_x \sin R_y k_y, \quad (4.69a)$$

$$P_{2,2}^{(\Gamma_5)} \mathbf{d}_k = \frac{\hat{\mathbf{z}}}{\sqrt{N}} \sum_{\mathbf{R}} d_{\mathbf{R},z} \sin R_x k_y \cos R_y k_y, \quad (4.69b)$$

for the two basis-functions of Γ_5 .¹⁰ As in the spin-singlet case, we get different versions of the Γ_5 basis vectors depending on the order of our expansion in \mathbf{R} . Expanding to nearest neighbor sites and normalizing such that the states are orthonormal, produces the basis-functions

$$\mathbf{d}_k^{(\Gamma_5),1} = -\frac{\hat{\mathbf{z}}}{2\pi} \sin k_y, \quad (4.70a)$$

$$\mathbf{d}_k^{(\Gamma_5),2} = \frac{\hat{\mathbf{z}}}{2\pi} \sin k_x, \quad (4.70b)$$

of the two-dimensional IR Γ_5 .

4.8 Decomposition of the Potential

Let at first \hat{V} be a general two-body operator that acts on an N -particle state which is a vector in $\mathcal{H}_N = \otimes_{i=1}^N \mathcal{H}$. The single particle Hilbert space \mathcal{H} in question, is quantified by momentum and spin, such that $\mathcal{H} = \text{span}\{|\mathbf{k}, s\rangle\}$. Denoting for the moment the specific combinations of \mathbf{k} and s as α as a shorthand, then \hat{V} acts on basis vectors in \mathcal{H}_N such that

$$\hat{V}|\alpha_1\rangle \dots |\alpha_N\rangle = \sum_{1 \leq i < j \leq N} \hat{V}_{ij} |\alpha_1\rangle \dots |\alpha_N\rangle, \quad (4.71)$$

by definition of being a two-body operator [76]. Here, \hat{V}_{ij} is an operator that only acts on the i th and j th ket. Even though \hat{V} acts on \mathcal{H}_N , because of how it can be written in terms of \hat{V}_{ij} , and this only acts on two states at a time, it follows that \hat{V} is completely determined by its action on the reduced two-particle Hilbert space \mathcal{H}_2 . This implies that \hat{V} is fully described by its matrix elements

$$\langle \alpha | \langle \alpha' | \hat{V} | \beta \rangle | \beta' \rangle. \quad (4.72)$$

10. Since Γ_5 is two-dimensional as opposed to the other IRs in C_{4v} , any complete basis for Γ_5 requires two basis functions that can be related through transformation by a group element.

Inserting back the $|\mathbf{k}, s\rangle$ notation, these matrix elements are referred to as

$$V_{\mathbf{k}_1 \mathbf{k}_2 \mathbf{k}_3 \mathbf{k}_4; s_1 s_2 s_3 s_4} = \langle \mathbf{k}_1 s_1 | \langle \mathbf{k}_2 s_2 | \hat{V} | \mathbf{k}_4 s_4 \rangle | \mathbf{k}_3 s_3 \rangle. \quad (4.73)$$

When \hat{V} is a BCS operator acting on the BCS Hilbert space described in Section 4.2, these matrix elements are denoted

$$V_{\mathbf{k}\mathbf{k}'; s_1 s_2 s_3 s_4} = \langle \mathbf{k} s_1 | \langle -\mathbf{k} s_2 | \hat{V} | \mathbf{k}' s_4 \rangle | -\mathbf{k}' s_3 \rangle. \quad (4.74)$$

Since \hat{V} is Hermitian, it must be diagonalizable in some basis of eigenfunctions. Barring accidental degeneracy, a basis for a d -degenerate eigenvalue is also a basis for an IR of the symmetry group G of the Hamiltonian [77]. In the case of accidental degeneracy, then this d -dimensional vector space consists of several non-intersecting subspaces, where each subspace is a basis for a (possibly different) IR. Note that this does not mean that (barring accidental degeneracy) there exists one separate eigenvalue for each IR of G , since there might be several different eigenvalues with different eigenspace bases but where all of them are bases for the same IR. Regardless of these details, the connection between IRs and the eigenvalues of \hat{V} is a great help in finding the bases for which it is diagonal.

Let the basis for a d_Γ -dimensional IR Γ be denoted $\{|\Gamma, q_\Gamma, m\rangle\}_{m=1}^{d_\Gamma}$, where \hat{V} has an eigenvalue V_{Γ, q_Γ} for the vectors in this basis, and q_Γ is an index enumerating the different versions of bases of Γ that \hat{V} might have in its set of eigenspace bases. Since \hat{V} is diagonal in this set of bases, then

$$\hat{V} = \sum_{\Gamma q_\Gamma} V_{\Gamma, q_\Gamma} \sum_{m=1}^{d_\Gamma} |\Gamma, q_\Gamma, m\rangle \langle \Gamma, q_\Gamma, m|. \quad (4.75)$$

Because of the potential for accidental degeneracy,¹¹ we cannot guarantee that $V_{\Gamma, q_\Gamma} \neq V_{\Gamma', q_{\Gamma'}}$ for different Γ and Γ' . Inserting this expression for \hat{V} into the matrix elements in Eq. (4.74) lets us write them in

11. A degeneracy of an eigenvalue is *accidental* if two degenerate eigenvectors belong to different IR vector spaces, while a non-accidental degeneracy of an eigenvalue happens when the eigenvectors in the eigen-space belong to a several-dimensional IR.

terms of IR basis vectors in the momentum spin function representation:

$$V_{\mathbf{k}\mathbf{k}'; s_1 s_2 s_3 s_4} = \sum_{\Gamma} V_{\Gamma, q_{\Gamma}} \sum_{m=1}^{d_{\Gamma}} \Psi_{s_1 s_2}^{\Gamma, q_{\Gamma}}(\mathbf{k}) \Psi_{s_3 s_4}^{\Gamma, q_{\Gamma}}(-\mathbf{k}')^{\dagger}, \quad (4.76)$$

where

$$\Psi_{s_1 s_2}^{\Gamma, q_{\Gamma}}(\mathbf{k}) = \langle \mathbf{k}, s_1 | \langle -\mathbf{k}, s_2 | \Gamma, q_{\Gamma}, m \rangle. \quad (4.77)$$

We can separate the set of different IR bases into bases that have vectors that transform either symmetrically or anti-symmetrically with respect to the group element of space inversion P . We call the representations of such bases even or odd representations. Even representations are those that map P to the identity operator $\mathbb{1}$ and as a consequence have functions with the symmetry $\Psi_{s_1 s_2}^{\Gamma, q_{\Gamma}, m}(-\mathbf{k}) = \Psi_{s_1 s_2}^{\Gamma, q_{\Gamma}, m}(\mathbf{k})$. Writing the spin-indices of these functions in terms of Pauli matrices by using the expansion in Eq. (4.8), and using the fermionic symmetry following the same logic as Section 4.2, then functions of even representations a can be written

$$\Psi_{s_1 s_2}^{a, q_a, m}(\mathbf{k}) = \psi_{\mathbf{k}}^{a, q_a, m} i \sigma_{s_1 s_2}^y. \quad (4.78)$$

Odd representations b map P to the inversion operator I such that $\Psi_{s_1 s_2}^{b, q_b, m}(-\mathbf{k}) = -\Psi_{s_1 s_2}^{b, q_b, m}(\mathbf{k})$. Expanding in Pauli matrices, then yields

$$\Psi_{s_1 s_2}^{b, q_b, m}(\mathbf{k}) = \mathbf{d}_{\mathbf{k}}^{b, q_b, m} \cdot (\boldsymbol{\sigma} i \sigma^y)_{s_1 s_2}. \quad (4.79)$$

Separating the sum over IRs Γ into sums over even (a) and odd (b) representations in the potential operator matrix elements in Eq. (4.76), we arrive at the fully expanded expression

$$\begin{aligned} V_{\mathbf{k}\mathbf{k}'; s_1 s_2 s_3 s_4} &= \sum_{aq_a} V_{a, q_a} \sum_{m=1}^{d_a} \psi_{\mathbf{k}}^{a, q_a, m} i \sigma_{s_1 s_2}^y (\psi_{-\mathbf{k}'}^{a, q_a, m} i \sigma_{s_3 s_4}^y)^{\dagger} \\ &+ \sum_{bq_b} V_{b, q_b} \sum_{m=1}^{d_b} (\mathbf{d}_{\mathbf{k}}^{b, q_b, m} \cdot \boldsymbol{\sigma} i \sigma^y)_{s_1 s_2} \left[(\mathbf{d}_{-\mathbf{k}'}^{b, q_b, m} \cdot \boldsymbol{\sigma} i \sigma^y)_{s_3 s_4} \right]^{\dagger}. \end{aligned} \quad (4.80)$$

In this use of the dagger notation, the adjoint acts on both the spin- and momentum matrix indices, such that $\mathbf{d}_{-\mathbf{k}}^{\dagger} = \mathbf{d}_{\mathbf{k}}^*$ and $\sigma_{s_1 s_2}^{\dagger} = \sigma_{s_2 s_1}^*$.

On a square lattice, the functions $\psi_{\mathbf{k}}^{a,q_a,m}$ and $d_{\mathbf{k}}^{b,q_b,m}$ of the eigenspace basis vectors $|\Gamma, q_\Gamma, m\rangle$ are given by the square lattice harmonics. Given an interaction potential \hat{V} with a known form of $V_{\mathbf{k}\mathbf{k}'; s_1s_2s_3s_4'}$, to decompose it into the form of Eq. (4.80), we can first find the eigenvalues by calculating the matrix elements

$$\langle \Gamma, q_\Gamma, m | \hat{V} | \Gamma, q_\Gamma, m \rangle = V_{\Gamma, q_\Gamma}. \quad (4.81)$$

Then we can simply insert these eigenvalues and the known form of $\psi_{\mathbf{k}}^{a,q_a,m}$ and $d_{\mathbf{k}}^{b,q_b,m}$ into Eq. (4.80), and we have a symmetry-decomposed potential!

Writing the potential on this form, easily lets us see if there are any attractive symmetric channels in the potential, which could lead to an instability and thus a phase-transition by pairing of the electrons according to the specified symmetry. A low energy effective theory can then be found in the unstable symmetry-channel by using the channel's square-lattice harmonics in determining the \mathbf{J}_s in the Hubbard-Stratonovich transformation in Eq. (3.26), and then performing a saddle-point approximation.

CHAPTER 5

Lattice Models

When we have a model for the free energy of a statistical mechanical system that is too complicated to calculate analytically, one approach is to utilize computers and Monte-Carlo (MC) techniques to gain quantitative answers to questions about the system's behaviour. Such techniques often require the discretization of a continuous model down on a numerical lattice. The lattice can in principle be of any form as long as the continuum limit reproduces the original theory, however in this thesis we will exclusively focus on a square (cubic) numerical lattice due to its simplicity.

In this chapter we will introduce different aspects of discretizing a continuous free-energy model down on a square numerical lattice. If starting with a continuous model with a spatially dependent field $f(\mathbf{r})$, then the discretized model will have a corresponding field f_r only defined on the numerical lattice sites at

$$\mathbf{r} = \sum_{\mu} r_{\mu} \hat{\mu} = \sum_{\mu} a_{\mu} n_{\mu} \hat{\mu} \quad (5.1)$$

where a_{μ} is the distance between lattice sites, $n_{\mu} \in [0, 1, \dots, N_{\mu} - 1]$ and N_{μ} is the total number of sites in the μ -direction. The length of the numerical lattice in this direction is $L_{\mu} = a_{\mu} N_{\mu}$. The cubic numerical lattice is specified by $a_{\mu} = a \ \forall \mu$ and $\mu \in \{x, y, z\}$. Any integrals $\int d^3r F[f(\mathbf{r})]$ will in such a discretization have to be replaced with

sums such that

$$\int d^3r \mapsto a^3 \sum_{r_\mu=a}^{Na}. \quad (5.2)$$

If we are interested in bulk properties of the model in the thermodynamic limit, then specifying realistic boundary conditions of the numerical lattice are of less importance. In this case, periodic boundary conditions are from a computational- and theoretical perspective a convenient choice. We define periodic boundary conditions by the requirement that $f_{\mathbf{r}+L_\mu \hat{\mu}} = f_{\mathbf{r}}$ for any direction $\hat{\mu}$.

5.1 Discretizing derivatives

In a model where fields only are defined at discrete points in space, any spatial gradient of the fields must take the form of discrete differences of the field values at these points. In a cubic grid of points with defined field-values, such differences can be denoted by the forward-difference operator Δ_μ . This operator acts on a spatially discrete function $f_{\mathbf{r}}$ as a forward-difference in the direction of $\hat{\mu}$ such that

$$\Delta_\mu f_{\mathbf{r}} = f_{\mathbf{r}+a\hat{\mu}} - f_{\mathbf{r}}, \quad (5.3)$$

where a is the distance between lattice points. In a Euclidean geometry, the natural discretization of a derivative ∂_μ is $\partial_\mu \mapsto \Delta_\mu/a$, which reproduces the continuum derivative in the limit $a \rightarrow 0$ with a fixed grid-size. Using an appropriate set of units, we in most cases can set $a = 1$.

5.1.1 Covariant derivatives

When discretizing continuous gauge theories, some extra care must be taken when discretizing a covariant derivative. Because of the gauge field, the geometry is no longer naively Euclidean. Then we need to rotate a field-value at one point by a gauge group element to parallel-transport it to another point, such that the field values at these spatially separate points can be compared. Given a $U(1)$ gauge symmetry with gauge field components $A_\mu(\mathbf{r})$, the appropriate way of discretizing a covariant derivative is the identification [81]

$$D_\mu f(\mathbf{r}) = [\partial_\mu + igA_\mu(\mathbf{r})]f(\mathbf{r}) \mapsto \frac{1}{a}(f_{\mathbf{r}+a\hat{\mu}} U_{\mathbf{r},\mu} - f_{\mathbf{r}}). \quad (5.4)$$

The value of f at $\mathbf{r} + a\hat{\mu}$ is parallel transported back to \mathbf{r} by the $U(1)$ group element [82]

$$U_{\mathbf{r},\mu} = e^{igA_{\mathbf{r},\mu}}, \quad (5.5)$$

where g is the coupling constant between f and the gauge field A , and

$$A_{\mathbf{r},\mu} \equiv \int_{\mathbf{r}}^{\mathbf{r}+a\hat{\mu}} d\mathbf{r} \cdot \mathbf{A}(\mathbf{r}), \quad (5.6)$$

is a link-variable, linking \mathbf{r} to its nearest neighbors.

In the limit of $a \rightarrow 0$, this identification reproduces the covariant derivative.¹ Furthermore, it produces terms that transform in an analogous way to the continuum version under gauge transformations, such that gauge invariant terms remain invariant after discretization. In the continuous fields, a gauge transformation is defined by

$$\begin{aligned} f(\mathbf{r}) &\rightarrow f(\mathbf{r})e^{i\phi(\mathbf{r})}, \\ A_\mu(\mathbf{r}) &\rightarrow A_\mu(\mathbf{r}) - \frac{1}{g}\partial_\mu\phi(\mathbf{r}). \end{aligned} \quad (5.7)$$

Then the covariant derivative transforms as $D_\mu f(\mathbf{r}) \rightarrow e^{i\phi(\mathbf{r})}D_\mu f(\mathbf{r})$, such that terms such as $|D_\mu f(\mathbf{r})|^2$ are invariant under gauge-transformations. Inserting the gauge transformation into the discretized field f_r and the definition of the link-variables $A_{\mathbf{r},\mu}$, we see that these discretized fields transform as

$$\begin{aligned} f_r &\rightarrow f_r e^{i\phi_r}, \\ A_{\mathbf{r},\mu} &\rightarrow A_{\mathbf{r},\mu} - \frac{1}{g}\Delta_\mu\phi_r, \end{aligned} \quad (5.8)$$

where the field ϕ_r is discretely defined on the same lattice points as f_r . Inserting this into the discretization of the covariant derivative on the right-hand side of Eq. (5.4), we see that indeed the right-hand side transforms in the same way as the left, i.e. by picking up an overall factor $e^{i\phi_r}$. This means that the discretized version of terms such as $|D_\mu f(\mathbf{r})|^2$, which were originally gauge-invariant, will be invariant under the gauge-transformation in Eq. (5.8) after discretization.

1. To show this, we see from Eq. (5.6) that $A_{\mathbf{r},\mu} \rightarrow aA_\mu(\mathbf{r})$. Then we expand the exponential in $U_{\mathbf{r},\mu}$ to first order and insert on the right-hand side of Eq. (5.4).

5.1.2 Discretized symmetry

One word of caution when discretizing continuous expressions is that discretized gradient terms will not in general have all the same spatial symmetries as the originating continuous terms. This is because the bias of the forward direction in the forward-difference operator and the cubic structure of the numerical lattice will in general break such symmetries.

The effects of the cubic symmetry of the numerical lattice can be thought of as caused by implicit lattice potentials that increases in influence towards lower temperatures and higher field strengths when the model contains an external field [83]. Such lattice potentials can e.g., cause topological defects to have preferred positions in discretizations of theories with translational symmetry.² As an example, consider again the discretization of the term $\int d^3r |Df(\mathbf{r})|^2$ with discretized scalar field $f_{\mathbf{r}} = \rho_{\mathbf{r}} e^{i\theta_{\mathbf{r}}}$. The density term is rotationally symmetric³ in 3D, however the discretized version can be written

$$2 \sum_{\mathbf{r}} \sum_{\mu} \rho_{\mathbf{r}}^2 [1 - \cos(\Delta_{\mu} \theta_{\mathbf{r}} + g A_{\mathbf{r},\mu})]. \quad (5.9)$$

From this form, we can see that the term is only symmetric by rotation by 90° in the planes normal to the x , y and z directions. The discretized term contains cubic distortions when rotating in directions in-between these, hence the $SO(3)$ rotational symmetry is broken down to the octahedral point group O .

The forward bias of the forward-difference discretization scheme can also lead to breaking of symmetries that both the continuous model and the numerical lattice have in common when the scalar field consists of multiple components. Consider a density term of the form

$$\Re[D_x \eta_x D_y \eta_y], \quad (5.10)$$

where η_x and η_y are two scalar fields that transform as components of spin and \Re extracts the real part of the complex number. Under an active $90^\circ \hat{z}$ -rotation (which is called a C_4 transformation), then

-
2. More on this in Section 7.
 3. By rotationally symmetric we mean that if we were to rotate the field configurations of $f(\mathbf{r})$ and $\mathbf{A}(\mathbf{r})$ in any direction, by any amount, the term would still yield the same value.

$D_x \rightarrow D_y$, $D_y \rightarrow -D_x$, $\eta_x \rightarrow \eta_y$ and $\eta_y \rightarrow -\eta_x$. Inserting this into the continuous density term in Eq. (5.10), we see that it remains precisely the same, i.e. invariant. Now consider the discretization of this term by the discretization procedure detailed above. This would read

$$\begin{aligned} & \rho_{r+\hat{x}}^x \rho_{r+\hat{y}}^y \cos [\theta_{r+\hat{x}}^x - \theta_{r+\hat{y}}^y + g(A_{r,x} - A_{r,y})] \\ & - \rho_{r+\hat{x}}^x \rho_r^y \cos (\theta_{r+\hat{x}}^x - \theta_r^y + gA_{r,x}) \\ & - \rho_r^x \rho_{r+\hat{y}}^y \cos (\theta_r^x - \theta_{r+\hat{y}}^y - gA_{r,y}) \\ & + \rho_r^x \rho_r^y \cos (\theta_r^x - \theta_r^y), \end{aligned} \quad (5.11)$$

where we have used the notation $\eta_r^a = \rho_r^a e^{i\theta_r^a}$ for the discrete scalar fields. In terms of these scalar fields and link-variables, a C_4 transformation consists of the mappings $\eta_r^x \rightarrow \eta_{C_4 r}^y$ and $\eta_r^y \rightarrow -\eta_{C_4 r}^x$, such that e.g., $\rho_{r+\hat{x}}^x \rightarrow \rho_{r'+\hat{y}}^y$. The link-variables transform as $A_{r,\mu} \rightarrow A_{C_4 r, C_4 \mu'}$ such that e.g., $A_{r,y} \rightarrow A_{r',-x} = -A_{r'-\hat{x},x}$. Using these transformations, and shifting the summation index of the external r -sum, then the rotated discrete terms take the form

$$\begin{aligned} & -\rho_{r-\hat{x}}^x \rho_{r+\hat{y}}^y \cos [\theta_{r-\hat{x}}^x - \theta_{r+\hat{y}}^y - g(A_{r,y} + A_{r-\hat{x},x})] \\ & + \rho_r^x \rho_{r+\hat{y}}^y \cos (\theta_r^x - \theta_{r+\hat{y}}^y - gA_{r,y}) \\ & + \rho_{r-\hat{x}}^x \rho_r^y \cos (\theta_{r-\hat{x}}^x - \theta_r^y - gA_{r-\hat{x},x}) \\ & - \rho_r^x \rho_r^y \cos (\theta_r^x - \theta_r^y), \end{aligned} \quad (5.12)$$

which certainly is not the same as Eq. (5.11), i.e. the discretization of Eq. (5.10) is not invariant under a C_4 rotation. A more immediate way of seeing the problem is to recognize that the first term in Eq. (5.11) is a next-nearest neighbor coupling on the numeric lattice that only couples sites along one diagonal, but not the other as illustrated in Figure 5.1, thus rotational symmetry is broken by the discretization.

One remedy for this kind of problem is to re-establish the broken symmetry by an average over symmetry-transformed terms. In the case of the discretization of $\Re[D_x \eta_x D_y \eta_y]$ in Eq. (5.11), the C_4 symmetry can thus be re-established by taking the average of Eq. (5.11), Eq. (5.12), as well as the terms obtained by transforming the discretization in Eq. (5.11) by the rotations C_4^2 and C_4^3 . Let \mathcal{F}_r denote the density terms in Eq. (5.11) and let $\mathcal{T}\mathcal{F}_r$ be the terms that result when

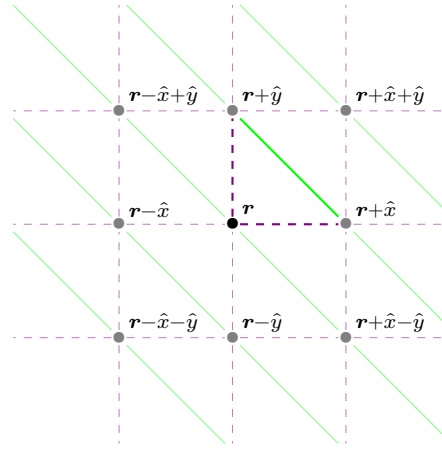


Figure 5.1: Couplings between sites on a single z -layer of the numerical lattice from the discretization in Eq. (5.11) of the term $\Re[D_x \eta_x D_y \eta_y]$. On-site terms are illustrated by a point (\bullet), while nearest neighbor and next-nearest neighbor couplings are illustrated by dashed and solid lines, respectively. The couplings obtained by evaluating Eq. (5.11) at a point r are slightly emphasized compared to the other lines.

transforming \mathcal{F} by a symmetry transformation \mathcal{T} . The average of symmetry-transformed terms, which re-establishes the C_4 rotational symmetry, can then be written

$$\begin{aligned} \mathcal{F}_r^{\text{sym}} &= \frac{1}{4} \sum_{\mathcal{T} \in \{1, C_4, C_4^2, C_4^3\}} \mathcal{T} \mathcal{F}_r \\ &= \frac{1}{4} \sum_{hh'=\pm 1} hh' \rho_{r+h\hat{x}}^x \rho_{r+h'\hat{y}}^y \cos [\theta_{r+h\hat{x}}^x - \theta_{r+h'\hat{y}}^y + g(A_{r,hx} - A_{r,h'y})]. \end{aligned} \quad (5.13)$$

In this expression, the next-nearest neighbour couplings are along all diagonals around the point r such that it is rotationally symmetric under C_4 and thus does not explicitly break symmetries that both the original theory and the numerical lattice have in common. Such breaking of symmetries can, as we have shown above, result from the naive application of a forward-difference discretization scheme⁴ when discretizing terms with multiple gradient-directions and components. In

4. The symmetric expression in Eq. (5.13) can be more easily obtained by the use of a different discretization procedure than the discretization of the covariant

models with such terms, the symmetry averaged expression can then be useful in diminishing the effect of meta-stable states and faster convergence when investigating such models by means of numerical computation. Finally, we would like to stress that both versions yield the same theory in the continuum limit.

5.2 Including an external field

The interaction between superconductors and magnetic fields is an essential aspect in the study of superconductors and thus we will need to be able to add external magnetic fields to our models to study this interaction. An external field is usually included as a constant homogeneous magnetic field in a certain direction and is a parameter of the problem rather than a variable. In other words, we assume the magnetic flux to be the same everywhere and unchanging, and rather than ask what consequence the existence of a superconductor has on this field, we are interested in the effects the field has on the superconducting state. Physically this situation is relevant, e.g., if a relatively small and thin sheet of superconducting material is placed in between two strong electromagnets as illustrated in Figure 5.2.

One way to introduce a constant magnetic field in a lattice model, is simply to figure out what kind of vector potential $\mathbf{A}(\mathbf{r})$ would give a constant magnetic field $\mathbf{B}(\mathbf{r})$ through $\mathbf{B} = \nabla \times \mathbf{A}$, and then set the link-variables $A_{\mathbf{r},\mu}$ of Eq. (5.6) accordingly, with the only caveat being that for a lattice-model with periodic boundary conditions, the factor $e^{igA_{\mathbf{r},\mu}}$ has to satisfy periodic boundary conditions as well. This implies the condition

$$\forall \nu \quad A_{\mathbf{r},\mu} = A_{\mathbf{r}+L_\nu \hat{\mu},\mu} + 2\pi m_\nu / g, \quad (5.14)$$

where $m_\nu \in \mathbb{Z}$ and ν gives a direction on the lattice. For $m_\nu \neq 0$ this condition is called a twisted boundary-condition.

derivative in Eq. (5.4). Taking the average of a forward and backward difference that respects gauge-transformations we get the discretization mapping

$$D_\mu f(\mathbf{r}) \mapsto (e^{igA_{\mathbf{r},\mu}} f_{\mathbf{r}+\hat{\mu}} - e^{igA_{\mathbf{r},-\mu}} f_{\mathbf{r}-\hat{\mu}})/2.$$

Applying this symmetrized covariant discretization mapping to the density term in Eq. (5.10), yields Eq. (5.13).

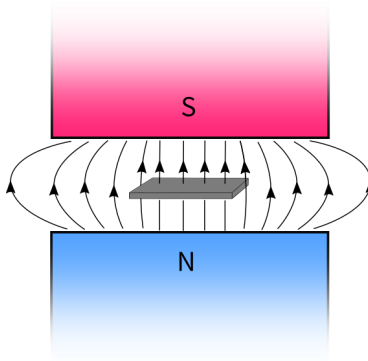


Figure 5.2: A thin sheet of superconducting material in the magnetic field produced by two magnets pointing in the same direction above and below the superconductor.

5.2.1 Landau Gauge

As an example, let's say we are interested in having an external field in the \hat{z} -direction with magnitude B . The vector-potential components A_x and A_y then have to satisfy the equation

$$\partial_x A_y - \partial_y A_x = B. \quad (5.15)$$

One configuration of the vector potential, which is called the *Landau gauge*, that satisfies this condition is $A_y = Bx$, with the other vector potential components set to zero. Inserting this into the definition of the link-variables in Eq. (5.6) yields $A_{r,\mu} = ar_x B \delta_{\mu,y}$. Here x is a continuous variable while r_x is the x -component of a lattice vector. Periodic boundary conditions on the lattice implies the condition $A_{r,y} = A_{r+L_x \hat{x},y} - 2\pi m/g$, which finally restricts the value of the field B such that the link-variables in the Landau gauge must take the form

$$A_{r,\mu} = \delta_{\mu,y} r_x \frac{2\pi m}{gL_x}, \quad m \in \mathbb{Z}, \quad (5.16)$$

where $L_x = N_x a$ and N_x is the number of lattice sites in the x -direction. With this link-variable configuration, the field strength becomes $B = 2\pi f/ga^2$, where we have defined the filling fraction $f = m/N_x$, which in terms of vortices gives the number of magnetic single-quanta vortices pr. plaquette of the numerical lattice.

5.2.2 Symmetric Landau gauge

The Landau gauge has the disadvantage that it singles out a direction in the xy -plane, since the vector potential is set to $\mathbf{A}(\mathbf{r}) = Bx\hat{\mathbf{y}}$, and thus is only spatially dependent in the x -direction. It could, because of this, be argued to break a rotational symmetry of the model in the xy -plane given that Aharenov-Bohm-like effects are significant to the results. To mitigate any such concern, one can consider a symmetric gauge given by the choice $\mathbf{A}(\mathbf{r}) = -\mathbf{r} \times B\hat{\mathbf{z}}/2$, which is rotationally symmetric in the xy -plane, and like the Landau gauge, produces the field $\mathbf{B} = B\hat{\mathbf{z}}$. Inserting this choice of vector potential into the link-variables, yields, using implicit summation over repeated indices, $A_{\mathbf{r},\mu} = \epsilon_{\mu z\nu} r_\nu a B / 2$. Periodic boundary conditions in this case implies two restrictions on the field value B because the vector potential varies in both the x - and y -direction. Implementing these conditions, we can write the link-variables as

$$A_{\mathbf{r},\mu} = \epsilon_{\mu z\nu} r_\nu \frac{2\pi m}{gL_x}, \quad (5.17)$$

where m is a number $m \in \mathbb{Z}$ chosen such that there exists some $n \in \mathbb{Z}$ such that $mN_y = nN_x$, i.e. m is some multiple of N_x/N_y . Then the field value is given by $B = 2\pi f/ga^2$ for filling fraction $f = 2m/N_x$.

This gauge is a specification of the more general extended Landau gauge [69, 84], which is borne purely out of the assumptions of a field $\mathbf{B} \parallel \hat{\mathbf{z}}$, $\mathbf{A}(\mathbf{r})$ linear in \mathbf{r} , and twisted periodic boundary conditions.

5.2.3 Fluctuating field

For a normal strongly type-II superconductor, the London penetration depth λ is much larger than the superconducting coherence length ξ . In this regime, it is valid to neglect spatial fluctuations in the gauge field since any deviation around the extremal field configuration is strongly suppressed. This is called the frozen gauge approximation and makes the vector potential act only as a constraint on the value of the uniform magnetic induction given by one of the gauges presented in the above sections [69]. When the superconducting state consists of multiple components, on the other hand, it becomes difficult to classify it simply in terms of type-I or type-II based solely on λ and ξ [85]. With multiple components, it becomes essential to fluctuate the gauge

field, because it mediates a significant indirect interaction between the components [71, 86].

Fluctuations of the gauge field imparts an energy cost on the system given in SI-units by the free energy⁵

$$F_A = \frac{1}{2\mu_0} (\nabla \times \mathbf{A})^2. \quad (5.18)$$

There are a couple of different ways of discretizing this energy for inclusion in a lattice model depending on whether one defines the link-variables compactly, i.e. $gA_{\mathbf{r},\mu} \in (-\pi, \pi)$, or non-compactly, i.e. $gA_{\mathbf{r},\mu} \in (-\infty, \infty)$. Both versions belong to the same universality class and thus produce the same results in a renormalization group sense, provided that the fluctuations are sufficiently small [81]. For noncompact link-variables, we simply replace the gradient with the lattice difference operator from Eq. (5.3) divided by the lattice spacing a , and the gauge-field components by their corresponding link-variables such that

$$\begin{aligned} \partial_\mu &\mapsto \Delta_\mu/a_\mu, \\ A_\mu(\mathbf{r}) &\mapsto A_{\mathbf{r},\mu}/a_\mu. \end{aligned} \quad (5.19)$$

The discretized free energy pr. lattice site then becomes

$$F_{A,\mathbf{r}} = \frac{(\Delta \times \mathbf{A}_\mathbf{r})^2}{2\mu_0 a^4} = \frac{1}{2\mu_0 a^4} \sum_\mu (A_{\mathbf{r},\mu}^\square)^2, \quad (5.20)$$

where we have defined the link-variable plaquette-sum vector, with components given by

$$A_{\mathbf{r},\mu}^\square = \epsilon_{\mu\alpha\beta} \Delta_\alpha A_{\mathbf{r},\beta} = \oint_{\square_\mu} d\mathbf{r}' \cdot \mathbf{A}(\mathbf{r}'). \quad (5.21)$$

In the line-integral on the right-hand side, the curve \square_μ is given by a plaquette⁶ normal to the vector $\hat{\mu}$, starting at the lattice point at \mathbf{r} , and

5. One way of deriving said energy is to start with the sourceless Maxwell Lagrangian for a massless vector field $\mathcal{L}_M = -F^{\mu\nu}F_{\mu\nu}/4\mu_0$. In this relativistic notation $F^{\mu\nu} = \partial^\mu A^\nu - \partial^\nu A^\mu$, $A^0 = V$, $\partial_0 = \partial_t/c$ and we use the metric $g^{\mu\nu} = \text{diag}(1, -1, -1, -1)$. Assuming time-independence and neglecting terms consisting only of V since they do not couple to the Higgs fields (e.g. the superconducting components) in minimal coupling, then the Lagrangian reduces to $\mathcal{L}_M \rightarrow -(\nabla \times \mathbf{A})^2/2\mu_0$ and the free energy in Eq. (5.18) results.
6. In this context, a plaquette is a square given by 4 neighboring lattice points contained in some plane.

moving along the square following the right-hand rule. The integration curve given by the plaquette \square_z is shown in Figure 5.3.

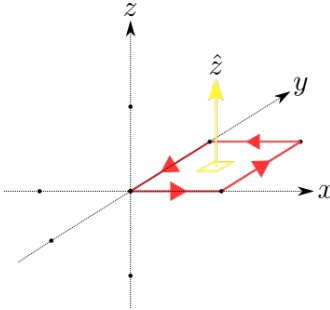


Figure 5.3: Integration path defined as \square_z along a plaquette of the numerical lattice in the xy -plane.

To impose an external field on a system with a fluctuating field, we divide the link-variables into a fluctuating part $A_{r,\mu}^f$ with periodic boundary conditions, and a constant part $A_{r,\mu}^0$, such that $A_{r,\mu} = A_{r,\mu}^f + A_{r,\mu}^0$. The field is then imposed by setting the constant part such that there is a net field induction through the system, e.g. by setting it to one of the gauges in Section 5.2.1 or 5.2.2.

CHAPTER 6

Monte-Carlo Techniques

In this chapter, we discuss some techniques useful in MC simulations of systems in statistical physics. In such systems, these techniques will be used to calculate thermal averages using random numbers. Let Z denote the partition function and \mathcal{H} the Hamiltonian of the system. Then the thermal average of an observable \mathcal{O} is defined as

$$\langle \mathcal{O} \rangle = \frac{1}{Z} \sum_{\psi} \mathcal{O}(\psi) e^{-\beta \mathcal{H}(\psi)}, \quad (6.1)$$

where ψ denotes states of the system, and we thus sum over all possible states. In the case of a quantum many-particle system, this sum turns into a multi-dimensional integral over quantum coherent states. Now, any attempt at estimating these integrals through an interpolation scheme is destined to fail because if we divide a 1-dimensional integral into M pieces and the error of the interpolation scheme scales as $\sim M^{-\kappa}$, then applied to a d -dimensional integral, its error will scale as $M^{-\kappa/d}$. What MC techniques then provides is a way of using random numbers in calculating Eq. (6.1) without actually summing over all the states. We do this by drawing random states ψ_i from a carefully selected probability distribution and using statistics to estimate how close the resulting thermal average is likely to be to the true thermal average. Letting M be the number of samples, then the error scales as $M^{-1/2}$ and is independent of the number of dimensions of the integral.

As in the case of the stationary phase approximation, the calculation of the sum in Eq. (6.1) can be made much more effective by considering which terms give large contributions. If we have a probability distribution $\pi(\psi)$ of sampled states ψ that is peaked around states that give large contributions to $\langle \mathcal{O} \rangle$, then our estimate will converge much quicker towards the true value than if we were to sample states uniformly. In a sense, we are interested in sampling only the important states, and hence this is called importance sampling. Let $\{\tilde{\psi}_i\}$ be a set of states that are uniformly sampled, while $\{\psi_i\}$ are sampled with probability distribution $\pi(\psi_i)$. The statistical estimator $\langle \bar{\mathcal{O}} \rangle$ of the thermal average of the observable \mathcal{O} is then

$$\langle \bar{\mathcal{O}} \rangle = \sum_i \mathcal{O}(\tilde{\psi}_i) \frac{e^{-\beta \mathcal{H}(\tilde{\psi}_i)}}{Z(\{\tilde{\psi}_i\})} = \sum_i \mathcal{O}(\psi_i) \frac{e^{-\beta \mathcal{H}(\psi_i)}}{\pi(\psi_i) Z(\{\psi_i\})}. \quad (6.2)$$

Now, assuming that the state-dependence of the observable is less important than the exponential, then the largest contributions to the sum will come from states that are such that $e^{-\beta \mathcal{H}}/Z$ is large. We thus want to pick states such that

$$\pi(\psi_i) = e^{-\beta \mathcal{H}(\psi_i)} / Z. \quad (6.3)$$

Then, given M states sampled according to this probability distribution, the statistical estimator reduces to the arithmetic average

$$\langle \bar{\mathcal{O}} \rangle = \frac{1}{M} \sum_i \mathcal{O}(\psi_i). \quad (6.4)$$

6.1 Markov-Chain Monte-Carlo method

The Markov-Chain Monte-Carlo (MCMC) method is a strategy of obtaining a sample of random states ψ_k , where the states are drawn sequentially in such a way that the probability $P_k(\psi)$ of drawing a new state $\psi_k = \psi$ is only dependent on what the last state ψ_{k-1} was. The chain developed by drawing states in this way, thus has no memory of the rest of the content of the chain, except for its last link ψ_{k-1} . A chain with this property is called a Markov-Chain, hence the name.

We want the sampled states to be drawn according to the probability distribution $\pi(\psi_k)$ discussed above. This is assured with the criteria of ergodicity and detailed balance. Ergodicity means in this context that

the states are drawn in such a way that if we were to draw infinitely many states, then we would have drawn all possible states ψ in the original sum in Eq. (6.1).

The criterion of detailed balance comes from the idea that we want the probability that a certain state is drawn at any given point, to be independent of when/where that point is located in the chain. Let $P_k(\psi)$ be the probability that ψ is drawn at the k th point in the chain. Because of the Markov-chain property, this probability is fully determined by the probability that the previous state in the chain transitions into the state ψ . Let $\mathcal{T}(\psi' \rightarrow \psi)$ denote the probability that state ψ' transitions into state ψ , i.e. that the state ψ is drawn given a previously drawn state ψ' . Then the probability that the state drawn at the point $k + 1$ in the chain is ψ , is given by

$$\begin{aligned} P_{k+1}(\psi) &= \sum_{\psi'} P(\psi_k = \psi' \wedge \psi' \text{ transitions to } \psi) \\ &= \sum_{\psi'} P_k(\psi') \mathcal{T}(\psi' \rightarrow \psi) \\ &= P_k(\psi) + \sum_{\psi'} \left[P_k(\psi') \mathcal{T}(\psi' \rightarrow \psi) - P_k(\psi) \mathcal{T}(\psi \rightarrow \psi') \right], \end{aligned} \tag{6.5}$$

where we have used that $\sum_{\psi'} \mathcal{T}(\psi \rightarrow \psi') = 1$ since the state must transition to some state. Now since we want the probability $P_k(\psi)$ to be invariant of the point's position in the chain k and be given by our desired probability density $\pi(\psi)$, we demand that $P_{k+1}(\psi) = P_k(\psi) = \pi(\psi)$. This implies that the last sum in Eq. (6.5) vanishes. Because the probability density \mathcal{T} is arbitrary, the sum needs to vanish term-wise, yielding the condition of detailed balance:

$$\pi(\psi') \mathcal{T}(\psi' \rightarrow \psi) = \pi(\psi) \mathcal{T}(\psi \rightarrow \psi'). \tag{6.6}$$

This states that for the selection process of choosing states for points in the Markov-chain to be invariant of the relative locations of the points in the chain, the process must be reversible.

6.2 Metropolis-Hastings method

The Metropolis-Hastings (MH) method is an algorithm for drawing states in a Markov-Chain that specifies a transition probability $\mathcal{T}(\psi \rightarrow$

$\psi')$ between states ψ and ψ' that satisfies the detailed balance criterion. The algorithm proceeds as follows:

1. Given a state ψ_k , generate a new state ψ_p where the process of generating this state has an, as of now, arbitrary probability distribution denoted $q(\psi_p | \psi_k)$ with the only requirement being that it leads to ergodic selection.
2. Accept this new proposed state ψ_p , with the probability $\alpha(\psi_p | \psi_k)$, defined as

$$\alpha(\psi_p | \psi_k) = \min \left\{ 1, \frac{\pi(\psi_p)q(\psi_k | \psi_p)}{\pi(\psi_k)q(\psi_p | \psi_k)} \right\}. \quad (6.7)$$

3. If ψ_p is accepted, we set $\psi_{k+1} = \psi_p$. If not, then $\psi_{k+1} = \psi_k$. Finally return to 1. to pick the next state in the chain.

By this procedure, then the probability of transitioning between a state ψ at point k to a state ψ' at point $k + 1$ is given by the probability that the state ψ' is picked and that ψ' is accepted, such that

$$\mathcal{T}(\psi \rightarrow \psi') = \alpha(\psi' | \psi) q(\psi' | \psi). \quad (6.8)$$

This transition probability satisfies detailed balance since inserting Eq. (6.8) and (6.7) yields

$$\begin{aligned} \pi(\psi')\mathcal{T}(\psi' \rightarrow \psi) &= \min\{\pi(\psi)q(\psi' | \psi), \pi(\psi')q(\psi | \psi')\} \\ &= \pi(\psi)\mathcal{T}(\psi \rightarrow \psi'). \end{aligned} \quad (6.9)$$

6.2.1 Practical considerations

Usually, the above is a bit too general for practical implementation since we would have to calculate or know the probability distribution $q(\psi' | \psi)$ used in picking new proposed states. If we assume q to be symmetric, such that

$$q(\psi' | \psi) = q(\psi | \psi'), \quad (6.10)$$

then we do not need to calculate it explicitly since it cancels out of the equation for α in Eq. (6.7).

A further simplification can be achieved by inserting the expression for $\pi(\psi)$ in Eq. (6.3) into the q symmetric version of α , which in this case reduces to

$$\alpha(\psi' | \psi) = \min \left\{ 1, e^{-\beta[\mathcal{H}(\psi') - \mathcal{H}(\psi)]} \right\}. \quad (6.11)$$

This form has the merit that the acceptance probability is only dependent on the difference between the energy of the updated and original state. If the state of the system ψ is a collection of site-dependent sub-states $\phi(r_j)$, e.g., how the state of an Ising-chain is given by a collection of site-dependent spins, then the calculation of $\mathcal{H}(\psi)$ must include all the sites. If we update only a single site r_j of ψ to get ψ' , which we call a local MC update, then all the sites that do not have an interaction with r_j cancels out in the difference $\mathcal{H}(\psi') - \mathcal{H}(\psi)$. Then we only need to calculate the difference in the sub-states that are affected by r_j to calculate the energy-difference. This is an essential property to have when creating a parallelized version of this algorithm, since different parts of the lattice of sites then can be updated in an asynchronous manner without affecting each other. In other words: by simplifying to the energy difference, the update scheme becomes local, which makes local MC updates grid-parallelizable.

To use pseudo-random numbers to accept a new state ψ' with probability α , we pick a uniformly distributed number $r \in (0, 1]$. Then we use the fact that

$$P[r \leq \alpha(\psi' | \psi)] = \alpha(\psi' | \psi), \quad (6.12)$$

which implies that updating the state if $r \leq \alpha$, is equivalent to updating the state with probability α . Given the form of α in Eq. (6.11), then

$$r \leq \alpha(\psi' | \psi) \Leftrightarrow \ln r \leq -\beta[\mathcal{H}(\psi') - \mathcal{H}(\psi)]. \quad (6.13)$$

To update the state with probability α , we thus simply take the natural logarithm of r , and update the state if the right-hand side of Eq. (6.13) is true.

To obtain good statistics, we want, as a rule of thumb, the acceptance rate to be about 30 – 60% for high temperature states.¹ The

1. High temperature states refers to states that are well above any transition temperature of the system.

acceptance rate is defined as the number of proposed states ψ' that are accepted, divided by the total number of proposed states, within some finite time-interval, and will in general be proportional to the acceptance probability $\alpha(\psi' | \psi)$. The acceptance rate can be adjusted by changing the way new states ψ' are proposed. Let ψ be composed of site-specific sub-states $\phi(\mathbf{r}_j)$ and let a state ψ' be proposed by changing the values of the sub-state $\phi(\mathbf{r}_0)$. Choosing values closer to the original sub-state $\phi(\mathbf{r}_0)$, the difference $\mathcal{H}(\psi') - \mathcal{H}(\psi)$ decreases such that $\alpha(\psi' | \psi)$ in Eq. (6.11) approaches 1 and thus the acceptance rate increases.

Proposing states such that the acceptance rate is very high by using this technique, can lead to new states not changing very much with each MC update. This can lead to freezing of the simulation, where the measurements do not change even after a significant number of MC updates because a large number of updates in the same direction is needed to significantly change the measurements. On the other hand, too low of an acceptance rate will also freeze the simulation since then obviously states are very unlikely to change, leading to the same measurements repeatedly. Ultimately, whether the acceptance rate should be considered too high or too low, should be guided by the physics of the system since in the case that the system has reached a global minimum in the energy-landscape and has low temperature, the proper statistics is obtained by an update scheme that gives a low acceptance rate. It is not advisable to change the acceptance rate during a measurement-run over decreasing temperatures, as this has tended to freeze the measurements at varying temperatures leading to confusion when trying to find a transition point.

6.3 Thermalization procedures

Thermalization in a MCMC simulation, refers to the process of discarding a set number of MC updates before starting to measure the states in the Markov-chain. The reason for doing this is because the first states in the chain will usually be very unlikely in the ensemble of states, and thus including them will give these states an artificially high statistical weight, unless we measure long enough. That time could be very long indeed if the starting states are very unlikely, thus, to get

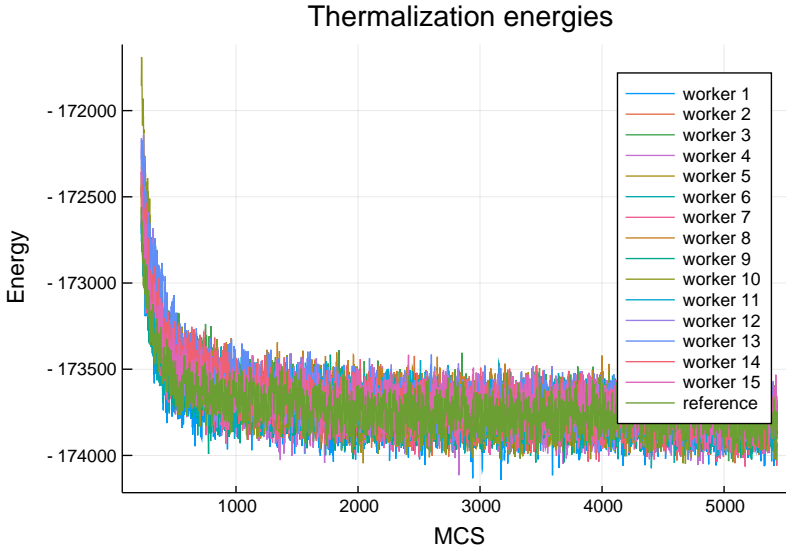


Figure 6.1: Thermalization of a 64^3 single-component XY -system from random initial states to a numerical temperature $T = 0.5$. The different curves represent the energy of different realizations of the same system initialized at different random states over several MCSs. The random initial states have a relatively high energy that stabilizes to the same value for all realizations in an exponential fashion.

measurements in a reasonable time, these unlikely starting states are discarded.

How many states to discard, is usually estimated with the help of an energy vs. Monte-Carlo sweep (MCS)² plot as shown in Figure 6.1. Since the initial state usually has a different energy than the average energy in the Markov-chain, the energy can be seen to rapidly stabilize to the average value in such a plot.

Whether the energy stabilizes from above or below will depend on what the initial state is, and what the temperature of the simulation has been set to. An ab-initio state in which the values of the sub-states are set to uniformly distributed random values within their validity range, normally corresponds to a high temperature and high energy

2. A Monte-Carlo sweep is a term used for attempting to update all the different sites of a system once.

state, hence thermalizing from such a state will have the energy stabilize from above. Another possibility for an ab-initio state, is some kind of mean-field minimal solution of the Hamiltonian, where sub-states at different sites are correlated. In this case, the energy will usually be low, and the thermalization energy will thus stabilize from below. This option has the disadvantage that if the mean field solution lies inside some local energy minimum, then simulations that start in this state might not be able to get out and find the global minimum. In contrast, simulations that are thermalized from random high energy states will have the possibility of finding the global minimum, even if some simulations also fall down in the local minimum of the mean-field solution. In general, it is recommended to thermalize several independent systems from different initial conditions and check that they yield quantitatively similar results to make it less likely that the results come from a local minimum or meta-stable state.

A last suggestion for an initial state of the system is the last state of a previous simulation. In this case, the thermalization will stabilize depending on the relative temperature of the two simulations. To be sure that the measurements are not correlated with the measurements of the last simulation, one should discard a number of states equal to the *auto-correlation time* of the system. The continuation from a previous simulation is a useful practice if gathering results over an extended temperature range where the systems need a large thermalization time in order to stabilize. One would then typically start measuring at a high temperature, and then decrease the temperature successively in steps with a separate thermalization- and measure-period for each step.

For systems prone to fall into local minima, it was found that a more careful thermalization process analogous to the measurement procedure described above, decreased the probability of freezing into such minima. Instead of thermalizing from a high energy / high temperature state directly down to the desired temperature, which we call quenching, a cooldown period was added. During the cooldown period, the temperature was lowered stepwise from a high temperature T_0 to a target temperature T , with intermediate temperatures

$$T_k = \left(\frac{T}{T_0} \right)^{\frac{k}{N}} T_0. \quad (6.14)$$

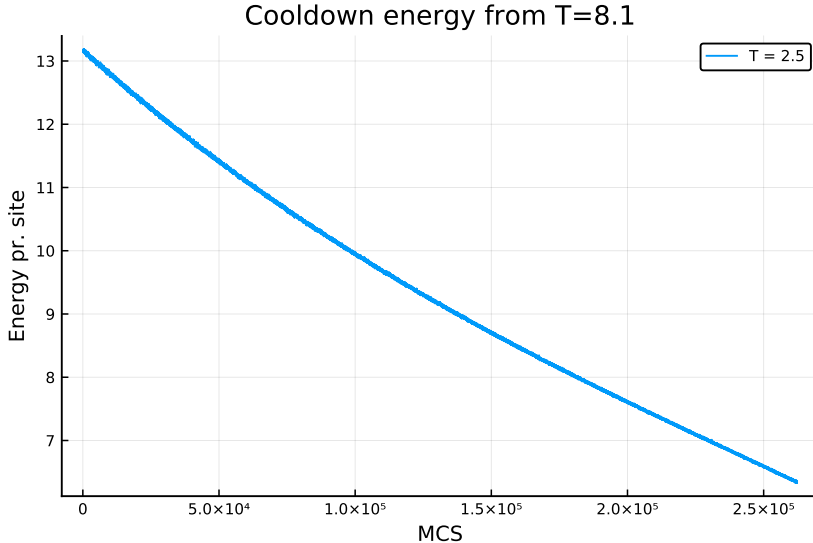


Figure 6.2: Energy pr. site of a 64^3 site model system of a $p + ip$ chiral superconductor during the cooldown stage. The temperature is lowered as a geometric sequence and a fixed number of MCSs are done at each temperature step. Comparing with the thermalization in Figure 6.1, we see that the cooldown period gives a significantly more gradual thermalization.

The intermediate temperatures were geometrically distributed over the cooldown region to ensure a higher density of intermediate steps towards lower temperatures. At each temperature step, a fixed number of MCSs were performed such that more MCSs were done towards the lower temperature than higher. This was done because the simulations in general took longer to thermalize when the temperature decreased. An example of how the energy changed during such a thermalization period is shown in Figure 6.2.

The cooldown period was then followed by a conventional thermalization stage where the temperature was held constant at T . In most cases, the energy had already stabilized at this point, such that the energy measurements during this extra thermalization stage typically only showed fluctuations around the mean.

6.4 Parallel tempering

Parallel tempering is a method of simulating multiple systems over a range of different temperatures where the systems can exchange positions with their neighbors in this temperature range according to a MH-like update step. Since the different systems all have the same parameters except for temperature, when viewed from the perspective of a single temperature, this leads to a normal Metropolis-Hastings MCMC simulation with an occasional global update of all sites of the system, whenever the system at that temperature exchanges with the system at a neighboring temperature. From the dual perspective of a single system, parallel tempering (PT) allows the system to make a random walk in temperature space.

This global updating, or movement in temperature space, has the advantage that it can prevent systems from getting stuck in local minima, by allowing them to move to a higher temperature where it is easier to fluctuate to a more favorable configuration. In systems that have a jagged energy-landscape with lots of local minima, this can be of great benefit and can reduce the required time it takes to measure observables with a certain accuracy by several orders of magnitude [87].

To implement parallel tempering MCMC in a temperature-centric perspective, let $\{T_i\}_{i=1}^M$ be a sorted list of M ascending temperatures, and let $\{\lambda_i\}_{i=1}^M$ be a list of indices λ , that identify replica states $\{\psi_\lambda\}_{\lambda=1}^M$ of the system such that the replica with temperature T_i is given by ψ_{λ_i} and its energy is given by E_{λ_i} . The simulation then proceeds according to the algorithm

1. Perform Δt normal MC updates on all replica states, e.g., using the MH method.
2. For each replica state ψ_λ , calculate the corresponding energy E_λ .
3. For each pair of neighboring temperatures T_i and T_{i+1} where $T_i < T_{i+1}$:
 - a) Calculate the quantity

$$\Delta = (E_{\lambda_{i+1}} - E_{\lambda_i}) \left(\frac{1}{T_{i+1}} - \frac{1}{T_i} \right). \quad (6.15)$$

- b) Then swap the indices $\lambda_i \leftrightarrow \lambda_{i+1}$ with probability $\min\{1, e^\Delta\}$. This can as in the MH method be done by generating a random number $r \in [0, 1)$ and then swapping indices if $\ln r \leq \Delta$.
4. If the replicas ψ_λ have internal knowledge of their temperatures, then distribute T_i to ψ_{λ_i} , for all temperatures T_i .
 5. Sample observables and return to 1.

This algorithm is easily parallelizable since the bulk of computing time will be going to doing the Δt MC-updates, which can be performed in parallel by having each replica state ψ_λ be assigned to a separate thread / processor. If each thread in addition keeps track of the replica's energy at the end of the MC updates, the only information that needs to be transferred between worker processes and the process doing the PT update step, is the values of the energies to the PT process, and afterwards: the set of new temperatures back to the worker processes. The PT process itself only needs to calculate $M - 1$ simple expressions and move around the indices in an array.

For the PT method to generate good statistics efficiently, some care should be taken in the distribution of the temperatures T_i . A rule of thumb is to distribute them geometrically, i.e. according to

$$T_i = \left(\frac{T_M}{T_1} \right)^{\frac{k-1}{M-1}} T_1, \quad (6.16)$$

with the argument that lower temperatures generally have a lower relaxation rate. With geometric distribution, the temperatures are denser towards the low end such that the acceptance rate of swaps of replicas at neighboring temperatures would in general become flatter and more independent of temperature. Should the specific heat diverge at some point T_c in the temperature range, as in the case of a phase transition, then this distribution would no longer be optimal since the acceptance probability of temperature swaps is inversely proportional to C_v , and thus the acceptance rate would no longer be flat. In this case, more temperatures should be distributed around T_c in order for systems to be able to random walk from one side of T_c to the other.

From the perspective of an individual replica, the overall goal with the distribution of temperatures is to maximize the number of times

the replica moves from the lowest temperature T_1 , up to the highest temperature T_M , and back to the lowest temperature again. This will then maximize the number of statistically independent visits of the system to each temperature. The hope is that a flat acceptance rate with respect to the distributed temperatures will facilitate a good number of such roundtrips. The number of roundtrips can be optimized with more advanced methods such as the *feedback-optimized parallel-tempering MC method*, which models the movement of replicas by parallel tempering as a diffusion process [88].

6.5 Grid parallelization

A simple way of utilizing multiple processor cores (or cpus) on a multi-processor system, is to run independent MC simulation on each processor. This is usually very efficient if a parameter of the system such as temperature is to be varied over some interval. Then, each simulation could have a different value of this parameter. In this case, it is recommended to also implement PT since the extra overhead is minimal and the speedup of the simulations can be significant.

Alternatively, all the simulations can run with the same value on different processes, and the samples from the individual simulations can then be combined to a super-sample. This is often referred to as “dummy-parallelization”. It has the advantages that the individual sampling-runs can be shortened, and the implementation of the parallelization is straight-forward. A drawback with this method is however that separate simulations have to be thermalized individually, such that the more the super-sample is split on different processes, the more processor time is wasted on thermalization. Additionally, if the individual simulation-runs depend on some sort of freezing, like how vortices freeze to the numeric lattice, then individual simulations could freeze at different angles such that they cannot be combined to form good statistics.

A solution to the above issues with this simple parallelization, is provided by grid-parallelization. This parallelization method is suited for simulations that consist of interacting sites either in 2D or 3D where local MC updates are to be performed. We will focus on the case of a 3D simulation where the sub-sites are organized in a numerical cubic lattice. The idea is to split the cube into different sub-cuboids as illus-

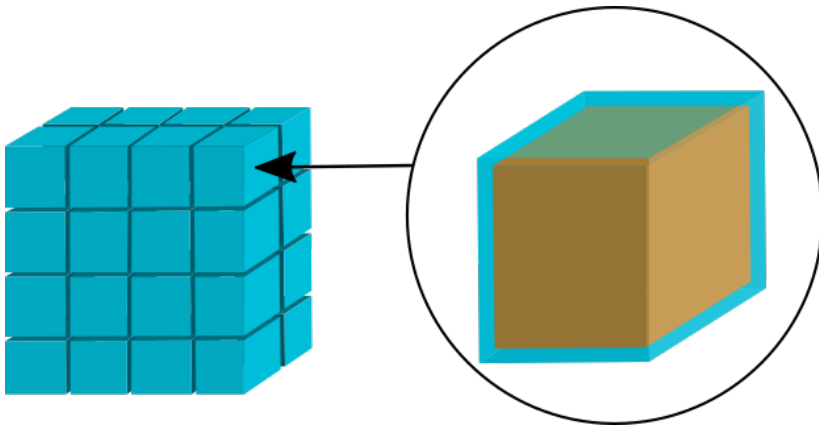


Figure 6.3: Illustration of the subdivision of the numerical grid into sub-cuboids. The right side illustrates that the sites in each sub-cuboid can be categorized as either internal sites, which can be updated asynchronously on different sub-cuboids and is illustrated in the figure by the internal orange cube, or sites in a border region.

trated on the left side of Figure 6.3. Each sub-cuboid's internal sites can then be updated in the normal MC fashion, in parallel with the internal sites of other sub-cuboids. If the individual sites of the original system interacts with neighboring sites,³ then it will be necessary for each sub-cuboid to have a border whose thickness depends on the range of the interaction. The sites in this border-region will then have an interaction with sites in the border-region of other sub-cuboids, such that care must be taken not to update a site based on the value of a neighboring site that is no longer valid. One solution to this is simply updating all the sites in the border-regions serially, i.e. update the border sites in a single sub-cuboid, communicate the updated values to the affected neighboring sub-cuboids, then move to the next sub-cuboid, etc. Or it could be even more effective to parallelize the updates of the border sites as well by further subdividing the border-sites into different categories. As an example, one could define *internal* border-sites on the face of a sub-cuboid to be the border-sites that only depend on sites in

3. In the case of a local MH update this can take the form of an energy-difference of the system at a proposed update-site that depends on the value of fields at neighboring sites.

the single neighboring sub-cuboid that is in the direction of the face-plane normal vector. Then all the right-facing internal border-sites can be done in parallel on all sub-cuboids, followed by all the top-facing internal border-sites, etc. The specifics of how the border-categories should be defined in order to achieve full parallelization, will in general depend on the specifics of the interaction between the sites.

6.6 Reweighting

Reweighting techniques are methods for finding estimates of parameter-dependent observables based on previously obtained samples of these observables from MC-simulations that have been done at parameter values independent of the ones we are interested in. Given a set of samples of some observable $\{o_i\}_{i=1}^M$ from previous MC simulation(s), these techniques provide a set of weights $\{w(\beta')_i\}_{i=1}^M$ that can be used to estimate the observable at a parameter value β' by the reweighting

$$\hat{o}(\beta') = \sum_i w(\beta')_i o_i. \quad (6.17)$$

This is very useful when estimating some observable over a temperature-range, since then a single simulation can yield results not only for a single temperature, but for an extended region. If this region is close to a phase-transition, then this can be used as a way of avoiding the critical slowing down of simulations at phase transitions by instead simulating at temperatures *close* to the critical temperature T_c , and then using reweighting techniques to estimate results *at* T_c . All this is possible because a simulation at a given temperature⁴ produces an extended statistical distribution of energy values for the sampled states. This energy distribution will in general overlap with the energy-distribution produced when simulating at a temperature that is sufficiently close to the original. Because of this overlap, it is possible to statistically extrapolate the value of observables at the neighboring temperature.

Reweighting techniques are categorized as single-histogram and multi-histogram reweighting-techniques depending on whether they use statistical information from a single histogram or can combine histograms generated at multiple parameter values. The single-histogram techniques are used to estimate values of the observables at neighboring

4. It is possible to use reweighting techniques on other parameters of the simulation as well, as long as they are, like inverse-temperature, linear in the action.

temperature-values and has the virtue of being comparatively simple to implement and understand. The multi-histogram techniques, on the other hand, have the advantage that the additional statistical information in general gives better estimates, and can even give better estimates at the original temperatures that the simulations were performed at, but have a more involved implementation.

In our simulations we used a Julia implementation⁵ of the multi-histogram technique originally developed by Bojesen, a technique which they used in [89], and which was updated for the current Julia release and modified by us.

6.6.1 Ferrenberg-Swendsen single-histogram method

To derive the Ferrenberg-Swendsen single-histogram reweighting technique, let o_i be samples of an observable \mathcal{O} from sample states ψ_i sampled at parameter value β of a system with a Hamiltonian \mathcal{H} , such that $\mathcal{O}(\psi_i) = o_i$. Then, from our discussion of importance sampling, the estimate of the average of the observable when the states are sampled according to a probability distribution $\pi(\psi_i)$, is given by

$$\langle \hat{\mathcal{O}} \rangle_\beta = \frac{\sum_i o_i e^{-\beta \mathcal{H}(\psi_i)} / \pi(\psi_i)}{\sum_i e^{-\beta \mathcal{H}(\psi_i)} / \pi(\psi_i)}. \quad (6.18)$$

Using a simulation with importance sampling at parameter-value β to generate the sampled states, the probability distribution was

$$\pi(\psi_i) = \frac{e^{-\beta \mathcal{H}(\psi_i)}}{Z_\beta} = \frac{e^{-\beta \mathcal{H}(\psi_i)}}{\sum_\psi e^{-\beta \mathcal{H}(\psi)}}, \quad (6.19)$$

where the sum in the denominator is over all possible states ψ and not only sampled states. Inserting $\pi(\psi_i)$ into $\langle \mathcal{O} \rangle_\beta$ in Eq. (6.18), this equation reduces to the arithmetic average, however if we now imagine wanting an estimate of $\langle \mathcal{O} \rangle_{\beta'}$ at an arbitrary parameter value β' , then insertion yields

$$\langle \hat{\mathcal{O}} \rangle_{\beta'} = \frac{\sum_i o_i e^{-(\beta' - \beta) \mathcal{H}(\psi_i)}}{\sum_i e^{-(\beta' - \beta) \mathcal{H}(\psi_i)}}. \quad (6.20)$$

5. This implementation is available at https://github.com/Sleort/FerrenbergSwendsenReweighting.jl/tree/1.0.3_update

This expression then gives an estimate of the average of the observable \mathcal{O} at an arbitrary parameter value β' using states ψ_i that were sampled at a specific parameter value β . This is called the Ferrenberg-Swendsen single-histogram reweighting technique [90], and in terms of the reweighting expression in Eq. (6.17) we can read off that the weights of this technique are given by

$$w(\beta')_i = \exp \left[-\ln \left(\sum_j e^{-(\beta' - \beta)[\mathcal{H}(\psi_j) - \mathcal{H}(\psi_i)]} \right) \right]. \quad (6.21)$$

Although simple, this technique's ability to extract information about observables around the simulated parameter-value, makes it extremely valuable in for instance the study of scaling relations, and to accurately calculate the peak of thermodynamic variables at phase-transitions where the MC-simulations themselves take a significant amount of computing time.

6.6.2 Numeric evaluation of exponential sums

The reason for introducing the extra exponential in the form of $w(\beta')_i$ in Eq. (6.21) is because sums of exponential numbers generally are hard to do numerically using finite-precision floating point numbers, however the logarithm of such a sum can be found using an iterative scheme. Let $S^{(k)}$ be a sum of k exponential numbers decreasing in magnitude that presumably are too large to be stored individually, such that

$$S^{(k)} = e^{a_1} + e^{a_2} + \dots + e^{a_k}, \quad (6.22)$$

with $a_{i+1} \leq a_i$, is numerically hard to do. Assuming however that fractions of the numbers can be stored, then we can numerically calculate

$$\ln S^{(2)} = a_1 + \ln \left(1 + e^{a_2 - a_1} \right). \quad (6.23)$$

Following the iteration

$$\ln S^{(k)} = \ln S^{(k-1)} + \ln \left(1 + e^{a_k - \ln S^{(k-1)}} \right), \quad (6.24)$$

then $\ln S^{(k)}$ can be found for arbitrary k without ever storing a single exponential number, only fractions of such numbers that are close to each other.

6.6.3 Multi-histogram Ferrenberg-Swendsen method

Let $\{\psi_i^k\}_{i=1}^{N_k}$ be sets of states sampled at the N_0 inverse temperatures $\{\beta_k\}_{k=1}^{N_0}$ of a system with Hamiltonian \mathcal{H} . The energy of these states is then given by E_i^k , and samples of an observable \mathcal{O} at these states are given by $\mathcal{O}(\psi_i^k) = o_i^k$. The energy-samples can then be used to construct N_0 histograms

$$h_k(E) = \sum_{i=1}^{N_k} \delta_{E, E_i^k}, \quad (6.25)$$

giving the number of sampled states at a certain energy in the simulation with parameter value β_k . The goal is to use these histograms to estimate the density of states of the system which we for the purpose of the derivation of this method will define $n(E) = \sum_{\psi} \delta_{E, \mathcal{H}(\psi)}$. The essential steps in this derivation can be found in the original paper in Ref. [91], as well as Ref. [92] and [93]. With these definitions, the energetic probability distribution of the system at an inverse temperature β is given by

$$W(\beta, E) = n(E) e^{-\beta E} / Z_{\beta}, \quad (6.26)$$

where $Z_{\beta} = \sum_{\psi} e^{-\beta \mathcal{H}(\psi)}$ is the partition function. Based on the sampled histograms, $W(\beta_k, E)$ at temperature β_k can be estimated by $\hat{p}_k(E) = h_k(E)/N_k$, i.e. $\langle \hat{p}_k(E) \rangle = W(\beta_k, E)$. This implies that $\langle h_k(E) \rangle = N_k W(\beta_k, E)$, and assuming for now that the samples of states ψ_i^k and ψ_j^k are statistically independent, it can be shown by, among other things, insertion of the definition of $h_k(E)$ in Eq. (6.25), that

$$\langle h_k(E)^2 \rangle = N_k W(\beta_k, E) [1 + (N_k - 1) W(\beta_k, E)]. \quad (6.27)$$

Inserting these cumulants of the histograms into the variance, we get

$$\delta^2 h_k(E) = \langle h_k(E)^2 \rangle - \langle h_k(E) \rangle^2 \approx g_k N_k W(\beta_k, E), \quad (6.28)$$

by assuming $W(\beta_k, E) \ll 1$. The factor $g_k = 1 + 2\tau_k$, where τ_k is the autocorrelation time of the samples at β_k , is included to generalize the result to samples where ψ_i^k and ψ_j^k are not statistically independent.

By solving Eq. (6.26) w.r.t. $n(E)$ and inserting the estimator of $W(\beta_k, E)$, an estimator of the density of states is given by

$$\hat{n}_k(E) = \hat{p}_k(E) Z_{\beta_k} e^{\beta_k E}, \quad (6.29)$$

where Z_{β_k} is assumed known, an assumption we will have to reconcile later. By the error propagation formula, then the variance of this estimator is given by

$$\delta^2 \hat{n}_k(E) = (Z_{\beta_k} e^{\beta_k E} / N_k)^2 \delta^2 h_k(E). \quad (6.30)$$

The estimator $\hat{n}_k(E)$ is an estimator of $n(E)$ using only a single histogram. We combine the estimators of single histograms using a weighted sum

$$\hat{n}(E) = \sum_k r_k \hat{n}_k(E), \quad (6.31)$$

where the coefficients r_k must satisfy the condition $\sum_k r_k = 1$ for the expectation value of $\hat{n}(E)$ to give the density of states. The coefficients r_k are determined by minimizing the variance $\delta^2 \hat{n}_k(E)$ subject to the constraint $\sum_k r_k = 1$ using a Lagrange multiplier, which yields the estimator

$$\hat{n}(E) = \frac{\sum_{k=1}^{N_0} g_k^{-1} h_k(E)}{\sum_{l=1}^{N_0} N_l g_l^{-1} e^{-\beta_l E} Z_{\beta_l}^{-1}}. \quad (6.32)$$

The assumption that Z_{β_k} is known is now reconciled. Since we can write the partition function using the density of states through

$$Z_\beta = \sum_\psi e^{-\beta \mathcal{H}(\psi)} = \sum_E n(E) e^{-\beta E}, \quad (6.33)$$

then we use the density of states estimator to estimate the partition function and use this estimate of the partition function \hat{Z}_{β_k} in the density of states estimator. This then creates an implicit equation for \hat{Z}_{β_k} that must be solved self-consistently. Inserting the definition of $h_k(E)$ and exchanging sums to remove the histograms, this equation takes the form

$$\hat{Z}_\beta = \sum_{k=1}^{N_0} \sum_{i=1}^{N_k} \frac{g_k^{-1} e^{-\beta E_i^k}}{\sum_{l=1}^{N_0} N_l g_l^{-1} e^{-\beta_l E_i^k} \hat{Z}_{\beta_l}^{-1}}, \quad (6.34)$$

which gives N_0 equations for N_0 unknowns \hat{Z}_{β_k} when evaluated at the different $\beta = \beta_m$.

Solving Eq. (6.34) is usually done with the help of an iterative solution method for non-linear equations such as the Newton-Raphson method. To numerically calculate a solution, it is inconvenient to work

with the full quantities \hat{Z}_{β_m} since these are usually extremely large. Instead, it is sufficient to calculate the variables

$$L_m \equiv \ln \hat{Z}_{\beta_m} - \ln \hat{Z}_{\beta_1}, \quad (6.35)$$

since the weights in the reweighting of observables can be written in terms of them. Dividing Eq. (6.34) by Z_{β_1} , we get that the $N_0 - 1$ equations we need to solve self consistently for the $N_0 - 1$ variables L_m , are given by

$$L_m = \ln \left\{ \sum_{k=1}^{N_0} \sum_{i=1}^{N_k} \frac{g_k^{-1} e^{-\beta_m E_i^k}}{\sum_{l=1}^{N_0} g_l^{-1} e^{-\beta_l E_i^k - L_l}} \right\}. \quad (6.36)$$

This form has the big advantage that the overall logarithm allows us to not have to calculate the exponential sums directly, but instead only calculate logarithms of these sums. For each sum $\sum_i e^{a_i}$ containing exponentials, which are potentially too large to be stored numerically, we simply re-exponentiate the entire sum to $\exp \ln \sum_i e^{a_i}$ and then use the method outlined in Section 6.6.2 to calculate $\ln \sum_i e^{a_i}$. Because of the overall logarithm, the exponential drops out in the last re-exponentiation such that we never have to store a single exponential number.

After finding self-consistent values for the $N_0 - 1$ variables L_m , the weights w_i^k for reweighting the observable \mathcal{O} can be found. In terms of the density of states $n(E)$, the thermal average of the observable is written

$$\langle \mathcal{O} \rangle_\beta = \frac{\sum_E \mathcal{O}(E) n(E) e^{-\beta E}}{\sum_E n(E) e^{-\beta E}}. \quad (6.37)$$

Inserting the reweighting estimate of $\hat{n}(E)$ in Eq. (6.32) for $n(E)$, we get the reweighting estimate

$$\langle \hat{\mathcal{O}} \rangle_\beta = \frac{\hat{Z}_{\beta_1}}{\hat{Z}_\beta} \sum_{k=1}^{N_0} \sum_{i=1}^{N_k} \frac{o_i^k g_k^{-1} e^{-\beta E_i^k}}{\sum_{l=1}^{N_0} N_l g_l^{-1} e^{-\beta_l E_i^k - L_l}}, \quad (6.38)$$

where $\hat{Z}_{\beta_1}/\hat{Z}_\beta$ is given by

$$\frac{\hat{Z}_\beta}{\hat{Z}_{\beta_1}} = \sum_{k=1}^{N_0} \sum_{i=1}^{N_k} \frac{g_k^{-1} e^{-\beta E_i^k}}{\sum_{l=1}^{N_0} N_l g_l^{-1} e^{-\beta_l E_i^k - L_l}}, \quad (6.39)$$

through Eq. (6.34). The two equations for $\langle \hat{\mathcal{O}} \rangle_\beta$ in Eqs. (6.38) and (6.39) together with the self-consistency equation in Eq. (6.36), is sufficient to describe the multi-histogram method. Notice that in these equations the histograms on which the method was derived do not figure but have been replaced by the more fundamental energy samples. This form makes the method more convenient to implement for systems with continuous energy distributions since it removes the need for a sum over all possible energies.

When calculating the exponential sums in the weights implied by Eqs. (6.38) and (6.39), numerical overflow can be avoided by first using logarithms to calculate the logarithm of a set of related un-normalized weights as before, then subtracting the maximum logarithmic value for each weight such that each weight is $\lesssim 1$ and then using the sum of these weights to properly normalize in the end.

6.6.4 Initial guess

An iterative non-linear solver usually needs an initial guess at the solution. In the case of the multi-histogram method equations, a good initial guess can be provided by the single-histogram Ferrenberg-Swendsen method. Since only fractions of partition function values are needed, we may set that $\hat{Z}_{\beta_1} = 1$ and use the Ferrenberg-Swendsen method based on the β_1 energies to estimate the value $\hat{Z}_{\beta_2}^0$ of \hat{Z}_{β_2} at neighboring inverse-temperature β_2 by the formula

$$\hat{Z}_{\beta_2}^0 = \sum_{i=1}^{N_1} e^{-(\beta_2 - \beta_1)E_i^1}. \quad (6.40)$$

In terms of the numerically convenient variables L_m , then this first guess L_2^0 takes the form

$$L_2^0 = \ln \left[\frac{1}{N_1} \sum_{i=1}^{N_1} e^{-(\beta_2 - \beta_1)E_i^1} \right]. \quad (6.41)$$

Continuing to estimate the partition function \hat{Z}_{β_m} through the single-histogram Ferrenberg-Swendsen method based on the data at β_{m-1} , then we may find all subsequent L_m^0 by applying the iteration scheme

$$L_m^0 = L_{m-1}^0 + \ln \left[\frac{1}{N_{m-1}} \sum_{i=1}^{N_{m-1}} e^{-(\beta_m - \beta_{m-1})E_i^{m-1}} \right]. \quad (6.42)$$

Vortices in superconductors

In conventional type-I superconductors, the Meissner effect prevents any magnetic field from penetrating the superconductor when it is in the superconducting state. In a type-II superconductor, the transition between the normal- and superconducting state is more gradual than in the type-I case due to an intermediate transitional state where topological defects in the superconducting field becomes stable, allowing quanta of magnetic field to pass through the material. The transitional value of the external field strength below which no magnetic field penetrates the superconductor is called B_{c1} . The upper transitional field strength above which the material stops being superconducting altogether is called B_{c2} . The state with regions of topological defects through which magnetic field quanta can penetrate, which are interspersed in a sea of superconducting state, exists between these values. It is important to note that the Meissner effect is still present in this transitional state — preventing magnetic field lines from penetrating the superconducting state. However, at topological defects, the material switches to the normal state and thus allows magnetic field-lines to penetrate at these points. The final continuous transition to the normal state at B_{c2} is then caused by the proliferation of vortex-loops, sending the whole material to the normal state.

The regions of normal state containing a topological defect of the superconducting state and through which magnetic field quanta can penetrate are known as superconducting vortices because they are sur-

rounded by a circulating superconducting current. This current is set up by the presence of the magnetic field and shields the rest of the superconducting condensate from its influence.

Whether a superconductor is type-I or type-II can conventionally be predicted by examination of the relative value of the magnetic field penetration depth λ and the superconducting coherence length ξ , which together form the GL parameter $\kappa = \lambda/\xi$. These parameters come out of the description of the superconducting state given by the GL theory of a single-component complex field minimally coupled to a gauge field. If $\kappa \gg 1$, then we say we have a strongly type-II superconductor, while if $\kappa \ll 1$, the superconductor is strongly type-I. The transitional value between type-I and type-II has a theoretical mean-field value of $\kappa = 1/\sqrt{2}$, however numerical calculations have given it the value $\kappa = (0.76 \pm 0.04)/\sqrt{2}$ all within the conventional GL formalism.

In a type-II conventional superconductor without any structural defects, as we increase the field strength, we introduce more vortices into the material in order to carry the required number of magnetic field quanta. At first these vortices behave like a liquid where they mutually repel each other if they get close. As more vortices are introduced to the system, the inter-vortex repulsion leads to them forming a two-dimensional lattice with equidistant lattice spacing. Since the triangular lattice is the lattice with the highest packing fraction, i.e. the lattice that has the highest density of sites at a given lattice spacing, the lattice formed will be triangular. Such a triangular (hexagonal) lattice of single quanta vortices is known as the Abrikosov lattice since it consists of single quanta vortices which are known as Abrikosov vortices.

7.1 Vorticity observables

A condensate described by a complex field ψ with phase θ can have topological defects given by discontinuities in the field θ due to its compact nature ($\theta \in [0, 2\pi)$). Such topological defects can be quantified by a non-zero winding-number N_v , which measures how the phase $\theta(\mathbf{r})$ moves around the unit circle as we change the position \mathbf{r} in a closed loop around the defect. These topological defects then lead to singularities in the field $\nabla\theta$ which allows a nonzero value of $\nabla \times \nabla\theta$ at

these points.¹ Integrating over a surface S with surface normal vector \hat{s} of the system and using Stokes' theorem then yields

$$\int_S d^2r (\nabla \times \nabla \theta) \cdot \hat{s} = \oint_{\partial S} \nabla \theta \cdot dr = 2\pi N_v, \quad N_v \in \mathbb{Z}, \quad (7.1)$$

where ∂S is a path around the boundary of S traversed counterclockwise. The last equality comes from the observation that ∂S is far away from the singularity such that $\nabla \theta$ is continuous along the path and N_v thus counts the number of times the vector θ rotates counterclockwise back to its initial position. If there is no topological defect inside the boundary ∂S then θ will increase as much as it decreases along the path, such that $N_v = 0$. If a topological defect in the form of a vortex is present, then $N_v \neq 0$ [94]. N_v can then be interpreted as the total vorticity of the field θ over the surface S . Since N_v is the total vorticity, which can consist of several individual defects, then from Eq. (7.1) we see that

$$\mathbf{n}_v = \frac{\nabla \times \nabla \theta}{2\pi} \quad (7.2)$$

must be interpreted as a vector of the local density of vorticity.

If the system described above contains a gauge field that is coupled to ψ , then any meaningful observable needs to be gauge-invariant. We clearly see that the expression in Eq. (7.2) is gauge-dependent by sending $\theta \rightarrow \theta + \phi$. To make a gauge-invariant observable under the gauge-transformation in Eq. (5.7), we see that we need to modify the definition to

$$\mathbf{n}_v = \frac{\nabla \times (\nabla \theta + g\mathbf{A})}{2\pi}. \quad (7.3)$$

This expression then defines \mathbf{n}_v as a gauge invariant vector of local vorticity density of the compact field θ .

In lattice models we want to discretize the vorticity density in Eq. (7.3) in order to effectively calculate it in MC simulations of the lattice model. In such a discrete model we have to take care to re-compactify the quantity $\nabla \theta + g\mathbf{A}$ to only be defined on some interval of length 2π . Using the discretization mapping of ∂_μ and $A_\mu(\mathbf{r})$ from Eq. (5.19), we want $\Delta_\mu \theta + gA_{\mathbf{r},\mu} \in [-\pi, \pi]$. Defining the operator

$$\hat{C}_\pi x = \text{mod}(x + \pi, 2\pi) - \pi, \quad (7.4)$$

1. From vector calculus we know that for a continuously differentiable field $f(\mathbf{r})$, it is the case that $\nabla \times \nabla f = 0 \forall \mathbf{r}$.

the discretized vorticity density can be written

$$\begin{aligned}\mathbf{n}_{v,r} &= \frac{\hat{e}_\mu \epsilon_{\mu\nu\lambda} \Delta_\nu \hat{C}_\pi (\Delta_\lambda \theta_r + g A_{r,\lambda})}{2\pi a^2} \\ &= \frac{1}{2\pi a^2} \sum_\mu \hat{e}_\mu \sum_{\square_\mu} \hat{C}_\pi (\Delta_\lambda \theta_r + g A_{r,\lambda}).\end{aligned}\quad (7.5)$$

Implicit summation over repeated indices is used on the first line, while on the second, the components of the vector $\mathbf{n}_{v,r}$ are written as plaquette-sums. Plaquette sums are sums of direction dependent quantities along a path \square_μ , which is described below Eq. (5.21) and illustrated in Figure 5.3. In the plaquette-sum, the directional quantity is always chosen along the path, and the path is traversed according to the right-hand rule with normal vector \hat{e}_μ [81, 95].

If the lattice system has an external field that yields a filling fraction f , e.g. produced by one of the gauges in Section 5.2, then each plaquette-sum in Eq. (7.5) will have a contribution f/a^2 . To motivate this assume, e.g., that θ_r is the same everywhere such that $\Delta_\lambda \theta_r = 0$ and insert the Landau gauge from Eq. (5.16) into the z -component of $\mathbf{n}_{v,r}$. This yields f/a^2 . Hence, to assure that the vortex observable yields the actual vortex quanta integer values when evaluated on a lattice with a uniform external field in the z direction with filling fraction f , we have to use the lattice function

$$n_r^z = (\mathbf{n}_{v,r})_z - \frac{f}{a^2}. \quad (7.6)$$

If the system consists of multiple condensate components $\psi^h = \rho^h e^{i\theta^h}$, then we can define a separate vorticity flux density $n_r^{z,h}$ for each component h by letting $\theta \mapsto \theta^h$ in the definitions of n_r^z in Eqs. (7.5) - (7.6).

7.2 Unconventional vortices

In a conventional superconductor, the isotropic (i.e. s -wave) nature of the superconducting state implies that stable vortices can only contain a single quanta of magnetic flux. In other words, if through some random thermal fluctuation, a defect appears that contains n quanta of magnetic flux, this will soon decay into n individual vortices that each contains a single magnetic flux quantum. We call these n individual

vortices: single-quanta vortices. For the individual stable topological defects to contain multiple quanta of magnetic flux, the superconducting state has to be unconventional in some way. One way in which a superconductor can host stable vortices with multiple quanta is if the superconducting state for some reason has an unconventional symmetry. This could, e.g., be caused by unconventional (i.e. non-phononic) mechanisms of Cooper-pair formation such as Van der Waals or spin-mediated interaction [66]. In this case, multiple components might be needed in order to describe the symmetry, which can result in the stabilization of vortices with double as well as fractionalized quanta [96].

A more specific example is that this can happen when a magnetic field penetrates a sample of material that is in a $p+ip$ superconducting state, i.e. a state where the pairing function is described by two components that each have a $k_x \pm ik_y$ dependence on the crystal momentum \mathbf{k} in the continuum limit. The linear k -dependence implies a finite angular momentum of the Cooper pairs with $l = 1$, and that the phases of the components are locked by an angular momentum difference $\Delta l = 2$ in the ground state. This has the consequence $n_+ = n_- + 2$ on any non-trivial winding numbers n_+ and n_- of the two different components, which implies that if a vortex exists some place where the sub-dominant component has winding number $n_- = 0$, then the dominant component must have $n_+ = 2$ and thus the vortex must be a double quantum vortex.²

In the type of superconductor described above, the winding numbers n_+ and n_- fully determine the structure of possible vortices. In the following we will use the notation (n_+, n_-) to specify these types of vortices, and assume that '+' is the dominant component. The possibilities for single-quanta vortices in this notation are thus the vortices $(1, -1)$ and $(-1, -3)$. The latter type has a higher winding number in the sub-dominant component, which implies a more complex core structure and has a higher energy cost pr. vortex [97]. This means that

2. It is the winding number of the dominant component that determines the number of magnetic flux quanta that the vortex is allowed to contain because the sub-dominant component is zero in locations far away from the vortex core by the nature of being sub-dominant. Thus, it doesn't contribute to the closed loop integral in Eq. (7.1) when integrating the supercurrent in a circle around the vortex.

of the two, it is the $(1, -1)$ variety that will be expected to be stable in experiments.

It is also possible to have double quanta vortices, which are either of the $(2, 0)$ or $(-2, -4)$ variety. Again, the type of vortex with the higher winding number in the sub-dominant component exhibits a more complex core structure. For the choices of various internal parameters of such systems that we have studied, it is the $(2, 0)$ type of vortex that is associated with the lowest energy cost and thus the one that is stable [97–99].

As we have mentioned, the different types of vortices will in general have different types of core-structures even though they may permit the same number of magnetic flux quanta to penetrate. One diagnostic tool to separate different kinds of vortices, is thus to observe the structure of the vortex core. Aside from plotting the actual vorticity n_{\pm} of the component through Eq. (7.6), this can be done by e.g., plotting the amplitudes of the dominant and sub-dominant component, plotting the phase-difference $\theta_+ - \theta_-$ of the different components, or plotting the magnetic field in the region of the vortex core. A rendition of the essential features of plots of dominant component vorticity density n_+ and phase-difference is shown in Figure 7.1 for the two vortex types $(1, -1)$ and $(2, 0)$. We see from the figure that the double quanta vortex type $(2, 0)$ can be distinguished from the single quanta vortex by having an extended ring of vorticity density, as well as having a core region in the phase difference plot that is rotated by $\pi/2$ radians from the asymptotic value of this phase difference. These features were used in our work to identify double and single quanta vortices in MC simulations.

7.3 Ensembles of vortices

With increasing field strength, more quanta of magnetic flux will penetrate the mixed phase and thus it will contain an increasing number of vortices that form flux-lines through the system. If any structural defects are present in the system, then this leads to local suppression of the superconducting condensate such that vortices are less energetically costly, and vortices will thus be predominantly located in such regions. This is called pinning of vortices because these regions attract vortices, and since their location is determined by external factors and

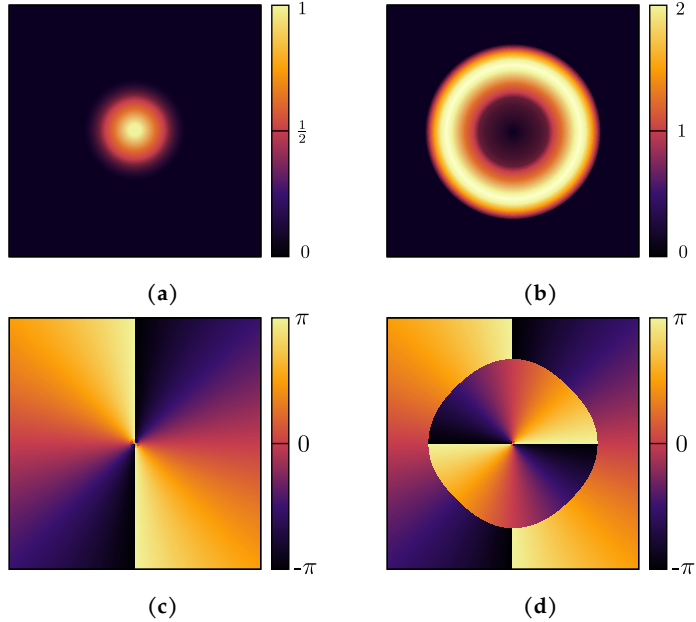


Figure 7.1: Schematic of vorticities and corresponding phase difference signature $\theta_+ - \theta_-$ of vortices in a system with external magnetic field $\mathbf{B} = B\hat{z}$. **a** and **c** show vorticity and phase-difference respectively for a singly quantized vortex with winding number $n_+ = 1$ and $n_- = -1$. **b** and **d** show vorticity and phase-difference respectively for a doubly quantized vortex with winding number $n_+ = 2$ and $n_- = 0$. The figures are directly based on the ones presented in Ref. [98].

not by the inter-vortex interactions themselves. Free vortices are mobile in response to an electric current and this leads to energy-loss and resistance in the mixed phase. Pinning-regions have the effect of resisting such movement and thus can contribute to increasing the amount of resistance-free current [100].

In the absence of such pinning, vortex tubes that run through the material in the direction of an external magnetic field can be ordered in a lattice according to their mutual interaction. Such a lattice is called an Abrikosov lattice or a flux line lattice since the vortex lines/tubes carry quanta of flux of the external magnetic field. The Abrikosov lattice then exists in the mixed phase of type-II superconductors and is destroyed when either the temperature or magnetic field strength is

increased beyond a certain level $B_{c2}(T)$ where the material enters the normal non-superconducting phase. This transition can be characterized in terms of a proliferations of unbound vortex loops which destroys the phase-coherence of the superconducting state [101].

If the interaction between the flux-lines is weak compared to entropic forces such as thermal fluctuations, then fluctuations of the vortex flux-lines can cause melting of the vortex lattice. In this molten state, the vortex flux-lines still interact repulsively which yields an average preferred inter-vortex distance given by the balance between inter-vortex repulsion, and the inclusion of the necessary number of vortices to carry the external magnetic field. However, any directionally dependent long-range correlation is lost. This corresponds to the behavior of particles in a liquid, and the molten state is thus called a vortex liquid. Such states are commonly found in high- T_c superconductors such as $\text{YBa}_2\text{Cu}_3\text{O}_{7-\delta}$. The transition between an ordered lattice of vortices and a vortex liquid is known as a vortex lattice melting transition. This transition can also be achieved by tuning the strength of the magnetic field. This implies a magnetic field strength B_{c1} , below which the Meissner effect completely excludes all magnetic fields, and a strength $B_M > B_{c1}$ above which the vortices behave as a liquid, i.e. without any long range correlations except that of an average distance. Finally, superconductivity is destroyed at $B_{c2} > B_M$ when a proliferation of vortex loops destroys all vortex correlations, and the material enters the normal state. These different states of the vortex lattice map out a region in the $B - T$ parameter space such as the one shown in Figure 7.2. There can also exist intermediate glassy phases of vortex matter between the extremes of a completely ordered lattice and a liquid when pinning of vortices is combined with low temperature in an external magnetic field [102, 103].

The structure and behavior of a flux-line lattice in the mixed phase of a type-II superconductor is dependent on the symmetry and nature of the superconducting phase. In conventional single-component superconductors with *s*-wave symmetry, the vortices interact asymptotically³ through isotropic repulsion that can be modeled by a modified Bessel function of the second kind [28, 105, 106]. In a clean ma-

3. In this context “asymptotically” means in the asymptotic limit of large separation between vortices.

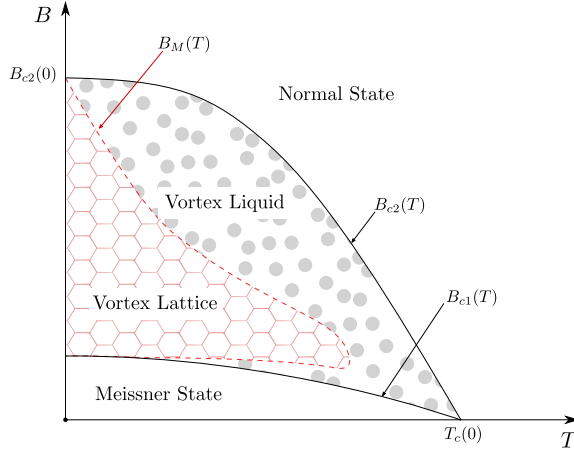


Figure 7.2: Simplified phase diagram of the states of vortex matter in a type-II superconductor in the B – T phase space. This is based on the Lindemann criterion [104].

terial, this interaction leads experimentally to a triangular (hexagonal) lattice of vortices due to this lattice symmetry having the largest packing-fraction of any two-dimensional lattice, i.e. it is the lattice that gives the highest density of vortices given a set inter-vortex distance and thus gives the lowest energy configuration [107, 108]. Theory predicts that also a square lattice of single quanta vortices should be possible at higher fields for $\kappa \gtrsim 1/\sqrt{2}$ [105], however in the London-approximation, which is valid at $\kappa \gg 1$, the triangular symmetry is the most stable for all fields [109]. Interestingly, the vortex lattice symmetry can be incommensurate to the underlying crystal lattice structure.

In theoretical models of unconventional superconductors, such as superconductors with multiple components and non-isotropic symmetry, even more complex behavior of the mixed phase is predicted. We have already mentioned the appearance of a vortex-liquid state separate from the vortex lattice state in high- T_c superconductors, which are overwhelmingly of the extreme type-II category and described by a single component unconventional d -wave symmetry. In superconductors with multiple components where each component can be modeled by a conventional London-approximation, a phase transition from the superconducting state to a superfluid state is possible in the mixed

phase by melting of a composite Abrikosov vortex lattice into a state with a remaining ordered neutral mode [70].

7.3.1 Vortex matter in $p_x + ip_y$ -superconductors

In our work we have been specifically interested in the vortex matter of superconductors with p -wave symmetry. These types of superconductors are described by two components that are intrinsically coupled and give rise to unconventional composite vortices as described in Section 7.2. The stable single-quanta composite vortices, which are denoted as vortex type $(1, -1)$ in the notation of Section 7.2, are theoretically predicted to form lattices with square symmetry [110–112]. Such symmetry has been observed in the vortex lattice of the unconventional superconductor Sr_2RuO_4 [113–116] and is thus part of the body of evidence supporting a p -wave symmetry of the superconducting state of this material. The theoretical predictions are supported by numerical calculations that also show that at lower fields a triangular vortex lattice consisting of double-quanta $(2, 0)$ -vortices is the preferred configuration [98]. Since these calculations did not account for thermal fluctuations in a convincing way, we used large-scale MC simulations to consider this effect on the vortex matter. Our results support the transition of a triangular vortex lattice consisting of double-quanta vortices to a square vortex lattice consisting of single-quanta vortices at higher fields and temperatures. These results are presented in Paper II.

7.4 Observables of lattice symmetry

In this section we discuss two tools usable in lattice theories for considering the symmetry of vortex line lattices. These tools are based on the observables of vortex flux density discussed in Section 7.1, but in this case, we are interested in measuring the structural correlations of a collection of vortex lines.

7.4.1 Structure function

The structure function of a discrete cuboid system of N_μ lattice sites along the $\hat{\mu}$ direction and with local vorticity n_r^z , as defined in Eq. (7.6),

is defined as

$$S(\mathbf{k}_\perp) = \frac{1}{(fN_x N_y N_z)^2} \left\langle \left| \sum_{\mathbf{r}} a^2 n_{\mathbf{r}}^z e^{i\mathbf{k}_\perp \cdot \mathbf{r}_\perp} \right|^2 \right\rangle, \quad (7.7)$$

where a is the lattice spacing, \mathbf{r}_\perp is the projected lattice vector $\mathbf{r}_\perp = \mathbf{r} - (\mathbf{r} \cdot \hat{\mathbf{z}})\hat{\mathbf{z}}$ down on the xy -plane, and f is the filling fraction, i.e. the number of vortex quanta pr. plaquette in the xy -plane. The filling fraction f relates to the inclusion of an external magnetic field in the z -direction as described in Section 7.1. This function takes a reciprocal 2D momentum vector as an argument and measures the structural correlation of the vortex lattice at this Bragg-point with normalization such that $S(0) = 1$.

To motivate this expression, consider a continuous cuboid system with a uniform field in the z -direction with average flux density of the number of magnetic flux quanta: \tilde{f} , which gives rise to a lattice of vortex lines along the z -direction. Let $n^z(\mathbf{r})$ be a flux density distribution of local vorticity in the z -direction such that if a vortex line with winding number $n \in \mathbb{Z}$ goes through the point \mathbf{r}_0 , then $\int_A d^2r n^z(\mathbf{r}_0) = n$, where A is an area that contains the vortex line. Taking the average over the z -direction keeps the value n of any vortex flux-lines since they will be coherent over this dimension of the system. In contrast, any contributions from vortex loops, which could result from random thermal fluctuations, will vanish in the limit of a large system size, hence

$$w(\mathbf{r}_\perp) = \int_0^{L_z} dr_z n^z(\mathbf{r})/L_z, \quad (7.8)$$

contributes to filtering out the vortex lines from the thermal noise. This w produces a distribution of vortex lines over the extent of the system in the xy plane. Since we are interested in structural correlations in this system, we perform the 2D Fourier transform and look at its amplitude through

$$\tilde{S}(\mathbf{k}_\perp) = \left| \int d^2r w(\mathbf{r}_\perp) e^{i\mathbf{k}_\perp \cdot \mathbf{r}_\perp} \right|^2. \quad (7.9)$$

This function then produces a reciprocal lattice of the 2D lattice of vortex lines where Bragg-points that correspond to structural correlations have increased value. To arrive at the structure-function, we need only now to take the thermal average to average over thermal fluctuations

of the vortex lattice lines and normalize such that $S(0) = 1$. To find this normalization constant, we need to calculate the integral

$$\int d^2r n^z(\mathbf{r}) = ?, \quad (7.10)$$

over the systems extent in the xy plane. However, from the definition of $n^z(\mathbf{r})$, the answer is given to us. Since $n^z(\mathbf{r})$ measures the flux density of vorticity in the xy -plane, then the integral is simply the total vorticity, which can be written as $\tilde{f}L_xL_y$ by the definition of \tilde{f} . Finally then, we arrive at the normalized dimensionless quantity

$$S(\mathbf{k}_\perp) = \frac{1}{(\tilde{f}L_xL_yL_z)^2} \left\langle \left| \int d^3r n^z(\mathbf{r}) e^{i\mathbf{k}_\perp \cdot \mathbf{r}_\perp} \right|^2 \right\rangle. \quad (7.11)$$

Discretizing this expression through the method in Section 5, i.e. by letting $\int dr \mapsto a \sum_{\mathbf{r}'} n^z(\mathbf{r}) \mapsto n_{\mathbf{r}}^z$ and $L_\mu = aN_\mu$, then we find that the filling fraction f , which is the number of vortex quanta pr. plaquette of the lattice,⁴ is related to \tilde{f} through $f = a^2\tilde{f}$, and we reproduce the expression in Eq. (7.7).

As an example of how the structure function singles out specific structural correlations, consider Figure 7.3. Figure 7.3b shows a plot of the structure function for all crystal momenta \mathbf{k}_\perp in the 1st Brillouin zone. The 6 yellow points surrounding the origin corresponds to correlations in the structure of the vortex lattice in these 6 directions, which implies a hexagonal lattice. The hexagonal lattice is shown directly in Fig. 7.3a, which in this case is a hexagonal lattice of double-quanta vortices. Choosing specific points in the plot of Fig. 7.3b and plotting the structure function's value at different values of a parameters of the system, e.g., temperature, is a common method for evaluating different phases of the structure of the vortex lattice, for example for measuring when the vortex lattice melts into a vortex liquid (see e.g. [70, 71, 117–119]).

7.4.2 Angular histogram

Building on the idea of measuring a specific point in the structure function to signify a structural transition, we developed an angular

4. We note that by the definitions here, f is a dimensionless quantity, while \tilde{f} has dimension inverse length square.

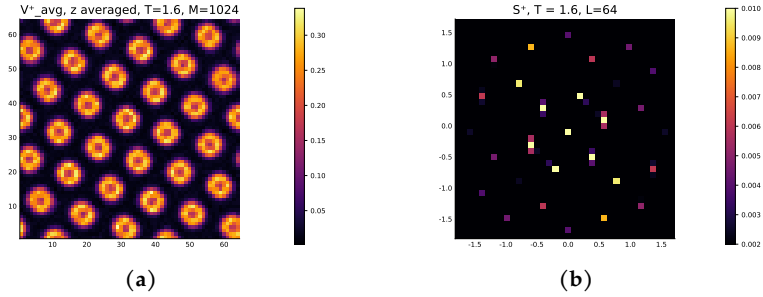


Figure 7.3: Plots of vorticity of the $+$ -component of a $p + ip$ superconductor system. Figure **a** shows a plot of the real space vorticity, which corresponds to a thermal average of a discretized version of $w(\mathbf{r}_\perp)$ from Eq. (7.9). Fig. **b** shows the corresponding structure function, which shows a hexagonal structure of the vortex line lattice.

histogram approach that is robust towards rotations of the vortex lattice. We found this to be important in measuring the transition from a hexagonal to a square vortex lattice since the angular symmetry of the model allowed the hexagonal vortex lattice to freeze in various directions. To combat this rotation, we built a histogram of the angular distance between peaks in the structure function over several MC steps. For a hexagonal lattice, such a histogram is peaked at the bin containing the angular distance $\pi/3$, while a square lattice would be peaked at $\pi/2$. Plotting these bins of angular distance over various temperatures, we were able to measure the transition from the square to the hexagonal lattice as seen in Figure 7.4.

The histogram was constructed algorithmically by creating a set of angular distances between peaks of the structure function for each MC step. We first found the radius where the peaks were located, by searching the average structure function over the entire MC series within a specified radius interval for the radius ρ_m that produced the largest value of the discretization of the integral

$$\int_0^{2\pi} d\theta S(\rho, \theta), \quad (7.12)$$

where $S(\rho, \theta)$ is the structure function given in polar coordinates about the Bragg-point $\mathbf{k}_\perp = 0$. The entire series of MC data was then di-

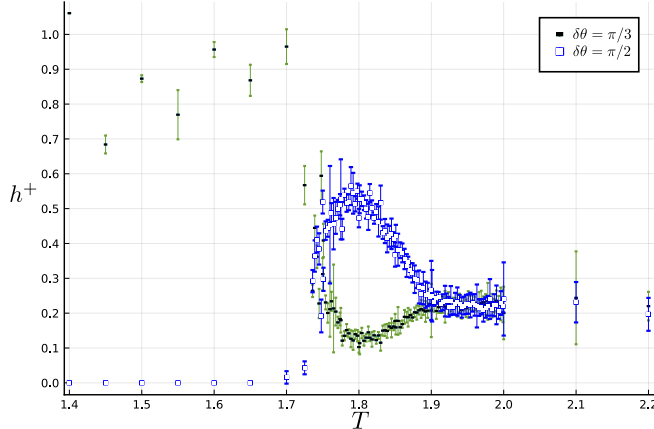


Figure 7.4: Plot of the bins of angular distance $\delta\theta = \pi/3$ and $\delta\theta = \pi/2$, as a function of simulation temperature.

vided into blocks containing $\Delta\tau$ numbers of individual MC measurements of the structure function. Each such interval of structure function measurements was then averaged over to yields separate averaged measurements of the structure function. The averaging over sufficient number of measurements $\Delta\tau$ is absolutely necessary in order to reveal the hidden vortex lattice from the noise. From each block t , a structure function ring $S^t(\theta)$ was then created by selecting the highest value of the blocked structure function over a ribbon centered at radius ρ_m such that

$$S^t(\theta) = \max_{\rho_m - \delta\rho \leq \rho \leq \rho_m + \delta\rho} \{S^t(\rho, \theta)\}. \quad (7.13)$$

A collection of n peak positions $P^t = \{\theta^p\}$ was then found for each block by finding the highest possible S_m such that $S^t(\theta)$ crossed the line at S_m a number of times equal to $2n$. From this set of peaks, then all possible distances between these peak positions were constructed by

$$\Theta^t = \{\delta\theta_{ij} = |\theta_i^p - \theta_j^p| \mid i \neq j, \theta_i^p, \theta_j^p \in P^t\}. \quad (7.14)$$

Let $\Theta = \bigcup_t \Theta^t$ be the union of all block sets of mutual angular peak distances. The final histogram h was then constructed based on all the distances in Θ . Let the bin in this histogram of the interval $[0, 2\pi)$ that

contains the angular distance $\delta\theta$ be denoted $\Delta\delta\theta$ such that

$$\Delta\delta\theta = [\delta\theta - \delta\theta_-, \delta\theta + \delta\theta_+], \quad (7.15)$$

for some non-negative $\delta\theta_-$ and $\delta\theta_+$. The value of the histogram $h(\Delta\delta\theta)$ at this bin was then calculated by

$$h(\Delta\delta\theta) = \frac{1}{|\Delta\delta\theta||\Theta|} \sum_{\delta\theta' \in \Theta} \delta_{\delta\theta' \in \Delta\delta\theta}, \quad (7.16)$$

where $|\Delta\delta\theta|$ is the size of bin $\Delta\delta\theta$, $|\Theta|$ is the number of mutual distances $\delta\theta'$ in Θ and $\delta_{\delta\theta' \in \Delta\delta\theta}$ is the Kronecker delta function defined as

$$\delta_{\delta\theta' \in \Delta\delta\theta} = \begin{cases} 1 & : \delta\theta' \in \Delta\delta\theta \\ 0 & : \delta\theta' \notin \Delta\delta\theta \end{cases}. \quad (7.17)$$

An example of the resulting histogram from calculating $h(\Delta\delta\theta)$, given equal size of the $\Delta\delta\theta$ intervals is shown in Figure 7.5. In this figure we observe a large peak at $\delta\theta = \pi/2 \approx 1.6$. This correlation comes from the fact that there are 4 peaks in the structure function that are equidistant to each other in angular distance from the origin. From this we draw the conclusion that the histogram represents a signature of a square vortex lattice. The even larger peak at $\delta\theta = \pi$ comes from a mathematical symmetry of the 2D Fourier transform that says that $\mathcal{F}(\mathbf{k}) = \mathcal{F}(-\mathbf{k})^*$. The small peak at $\delta\theta = 3\pi/2$ is a remnant of the peak at $\pi/2$, while the peak at low $\delta\theta$ is an artifact coming from noise in the data.

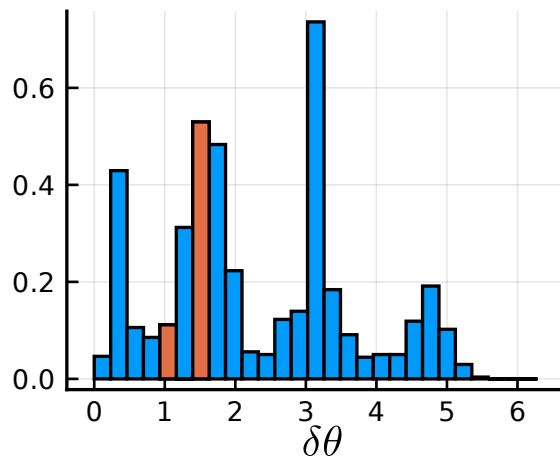


Figure 7.5: Plot of the bins of h in Eq. (7.16) for a simulation of a square vortex lattice. The bins corresponding to $\delta\theta = \pi/3$ and $\delta\theta = \pi/2$ are colored orange to mark the main contributions from a triangular- and square lattice, respectively.

CHAPTER 8

Outlook

In this thesis we have introduced some of the fundamental techniques we employed in our theoretical investigations into the nature of unconventional superconductivity with p -wave pairing symmetry. These investigations have resulted in three papers.

In Paper I we used a group-theoretical approach to motivate the form of the effective interaction potential between electrons whose low energy excitations could be described in terms of Cooper-pairs with p -wave symmetry. This potential was then used as a basis for deriving the effective free energy for such a superconductor when it was influenced by explicit spin-orbit interaction. We found that the effective free energy had the expected form given by its group-theoretical constraints, but that previous assumptions about its coefficients needed revision because of the effect of spin-orbit coupling.

In Paper II we used large-scale Monte-Carlo simulations to investigate the vortex matter of a p -wave superconductor with a free energy similar to the one derived in Paper I. We found a transition between a square vortex-lattice of single-quanta vortices and a hexagonal vortex lattice consisting of double quanta vortices as the temperature was lowered in a finite field parallel to the crystallographic c -axis.

In Paper III we investigated this same superconductor when exposed to zero external magnetic field and found an Ising phase transition in the neutral sector of the theory. This transition did not separate from the phase-transition of the charged sector in contrast to other models

of two-component superconductors. The reason for the connection between the charged and neutral modes seemed to be because of their group-theoretical nature as components of a single irreducible representation. This identification implies equal stiffness for both components and an explicit coupling through mixed gradient and mixed-component terms in the effective free energy.

Looking towards the future, it now seems less likely that the unconventional superconductor Sr_2RuO_4 should be theoretically modeled as a $p + ip$ superconductor despite the strong evidence for its spontaneous time-reversal-symmetry breaking nature [120–122] and the good agreement between theory and experiment for the qualitative nature of its vortex lattices [98, 115]. Rather, the prevailing view based on the current evidence has shifted to suggesting a degeneracy between a $d_{x^2-y^2}$ and a $g_{xy(x^2-y^2)}$ superconducting state [123, 124]. It might in this regard be interesting to use Monte-Carlo simulations to investigate the vortex lattice behavior of such a superconductor and see how it matches with experiments on Sr_2RuO_4 .

In the exploration of such a novel symmetry state it might be beneficial to utilize more modern forms of Monte-Carlo analysis such as those offered by the advances in machine-learning to yield convincing results in an efficient manner [125–127].

Building on the results of Paper I, it would be of interest to investigate numerically how the kinetic dimensionless phenomenological parameters in the Ginzburg-Landau model depend on the microscopic parameters, especially spin-orbit coupling strength and spin-orbit coupling spin z -component.

Bibliography

1. **F.N. Krohg, A. Sudbø.**
Derivation of a Ginzburg-Landau free energy density of a $p + ip$ superconductor from spin-orbit coupling with mixed gradient terms.
Phys. Rev. B 98, 014510 (1 July 2018).
DOI: [10.1103/physrevb.98.014510](https://doi.org/10.1103/physrevb.98.014510)
2. **F.N. Krohg, E. Babaev, J. Garaud, H.H. Haugen, A. Sudbø.**
Thermal fluctuations and vortex lattice structures in chiral p -wave superconductors: Robustness of double-quanta vortices.
Phys. Rev. B 103, 214517 (21 June 2021).
DOI: [10.1103/physrevb.103.214517](https://doi.org/10.1103/physrevb.103.214517)
3. **H.H. Haugen, E. Babaev, F.N. Krohg, A. Sudbø.**
First order superconducting phase transition in chiral $p + ip$ system.
arXiv: Superconductivity (June 2021).
arXiv: [2106.01007 \[cond-mat.supr-con\]](https://arxiv.org/abs/2106.01007).

4. M. Allen et al.

IPCC, 2018. Summary for Policymakers.

in

Global Warming of 1.5°C. An IPCC Special Report on the impacts of global warming of 1.5°C above pre-industrial levels and related global greenhouse gas emission pathways, in the context of strengthening the global response to the threat of climate change, sustainable development, and efforts to eradicate poverty

(eds V. Masson-Delmotte et al.)

(World Meteorological Organization, Geneva, Switzerland, 2018).

5. UNFCCC Secretariat.

Nationally determined contributions under the Paris Agreement: Synthesis report.

Tech. rep.

(United Nations Framework Conventions on Climate Change, Glasgow, 2021).

6. M. Corduan et al.

Topology Comparison of Superconducting AC Machines for Hybrid Electric Aircraft.

IEEE Transactions on Applied Superconductivity 30, 1–10 (2020).

dor: [10.1109/tasc.2019.2963396](https://doi.org/10.1109/tasc.2019.2963396)

7. Y. Cheng et al.

Design and Analysis of 10 MW HTS Double-Stator Flux-Modulation Generators for Wind Turbines.

IEEE Transactions on Applied Superconductivity, 1–1 (2021).

dor: [10.1109/tasc.2021.3061928](https://doi.org/10.1109/tasc.2021.3061928)

8. Y. Liu et al.

Measurement of Magnetic Materials at Room and Cryogenic Temperature for Their Application to Superconducting Wind Generators.

IEEE Transactions on Applied Superconductivity 28, 1–6 (2018).

dor: [10.1109/tasc.2018.2799163](https://doi.org/10.1109/tasc.2018.2799163)

9. **P. Tixador et al.**
Status of the European Union Project FASTGRID.
IEEE Transactions on Applied Superconductivity 29, 1–5 (2019).
doi: [10.1109/tasc.2019.2908586](https://doi.org/10.1109/tasc.2019.2908586)
10. **M. Stemmle, F. Merschel, M. Noe, A. Hobl.**
AmpaCity — Advanced superconducting medium voltage system for urban area power supply.
in 2014 IEEE PES T D Conference and Exposition (2014), 1–5.
doi: [10.1109/tdc.2014.6863566](https://doi.org/10.1109/tdc.2014.6863566)
11. **Z.S. Hartwig et al.**
VIPER: an industrially scalable high-current high-temperature superconductor cable.
Superconductor Science and Technology 33, 11LT01 (Oct. 2020).
doi: [10.1088/1361-6668/abb8c0](https://doi.org/10.1088/1361-6668/abb8c0)
12. **D. Whyte.**
Small, modular and economically attractive fusion enabled by high temperature superconductors.
Philosophical Transactions of the Royal Society A: Mathematical, Physical and Engineering Sciences 377, 20180354 (2019).
doi: [10.1098/rsta.2018.0354](https://doi.org/10.1098/rsta.2018.0354)
eprint: <https://royalsocietypublishing.org/doi/pdf/10.1098/rsta.2018.0354>.
13. **M. Mentink et al.**
Evolution of the Conceptual FCC-hh Baseline Detector Magnet Design.
IEEE Transactions on Applied Superconductivity 28, 1–10 (2018).
doi: [10.1109/tasc.2017.2782708](https://doi.org/10.1109/tasc.2017.2782708)
14. **J.D.S. Bommer et al.**
Spin-Orbit Protection of Induced Superconductivity in Majorana Nanowires.
Phys. Rev. Lett. 122, 187702 (18 May 2019).
doi: [10.1103/physrevlett.122.187702](https://doi.org/10.1103/physrevlett.122.187702)

15. **P. Bernstein, J. Noudem.**
Superconducting magnetic levitation: principle, materials, physics and models.
Superconductor Science and Technology 33, 033001 (Jan. 2020).
doi: [10.1088/1361-6668/ab63bd](https://doi.org/10.1088/1361-6668/ab63bd)
16. **J.R. Alonso, T.A. Antaya.**
Superconductivity in Medicine.
Reviews of Accelerator Science and Technology 05, 227–263 (2012).
doi: [10.1142/s1793626812300095](https://doi.org/10.1142/s1793626812300095)
eprint: <https://doi.org/10.1142/S1793626812300095>.
17. **H.K. Onnes.**
The disappearance of the resistivity of mercury.
Commun. Phys. Lab. Univ. Leiden (May 1911).
18. **W. Meissner, R. Ochsenfeld.**
Ein neuer Effekt bei Eintritt der Supraleitfähigkeit.
Naturwissenschaften 21, 787–788 (Nov. 1933).
doi: [10.1007/bf01504252](https://doi.org/10.1007/bf01504252)
19. **F. London, H. London, F.A. Lindemann.**
The electromagnetic equations of the supraconductor.
Proceedings of the Royal Society of London. Series A - Mathematical and Physical Sciences 149, 71–88 (1935).
doi: [10.1098/rspa.1935.0048](https://doi.org/10.1098/rspa.1935.0048)
eprint: <https://royalsocietypublishing.org/doi/pdf/10.1098/rspa.1935.0048>.
20. **V.L. Ginzburg, L.D. Landau.**
On the theory of superconductivity.
Zh. Eksper. Teor. Fiz. 20, 1064–82 (1950).
eprint: https://link.springer.com/chapter/10.1007/978-3-540-68008-6_4.
21. **L.D. Landau.**
On the theory of phase transitions. II.
Phys. Z. der Sowjet Union 11, 545 (1937).
22. **A.A. Abrikosov.**
Doklady Akademii Nauk SSSR 86 (1952).

23. **H. Fröhlich.**
Theory of the Superconducting State. I. The Ground State at the Absolute Zero of Temperature.
Phys. Rev. 79, 845–856 (5 Sept. 1950).
doi: [10.1103/physrev.79.845](https://doi.org/10.1103/physrev.79.845)
24. **A.B. Pippard, W.L. Bragg.**
An experimental and theoretical study of the relation between magnetic field and current in a superconductor.
Proceedings of the Royal Society of London. Series A. Mathematical and Physical Sciences 216, 547–568 (1953).
doi: [10.1098/rspa.1953.0040](https://doi.org/10.1098/rspa.1953.0040)
eprint: <https://royalsocietypublishing.org/doi/pdf/10.1098/rspa.1953.0040>.
25. **L.D. Landau.**
The Theory of a Fermi Liquid.
J. Exptl. Theoret. Phys. 3, 920 (Mar. 1956).
eprint: <http://www.jetp.ac.ru/cgi-bin/e/index/r/30/6/p1058?a=list>.
26. **J. Bardeen, L.N. Cooper, J.R. Schrieffer.**
Microscopic Theory of Superconductivity.
Phys. Rev. 106, 162–164 (1 Apr. 1957).
doi: [10.1103/physrev.106.162](https://doi.org/10.1103/physrev.106.162)
27. **J. Bardeen, L.N. Cooper, J.R. Schrieffer.**
Theory of Superconductivity.
Phys. Rev. 108, 1175–1204 (5 Dec. 1957).
doi: [10.1103/physrev.108.1175](https://doi.org/10.1103/physrev.108.1175)
28. **A.A. Abrikosov.**
On the Magnetic properties of superconductors of the second group.
Zh. Eksper. Teor. Fiz. 32, 1442 (Dec. 1957).
eprint: http://www.jetp.ac.ru/cgi-bin/dn/e_005_06_1174.pdf.
29. **N.N. Bogoliubov.**
A new method in the theory of superconductivity I.
Zh. Eksper. Teor. Fiz. 34, 58 (July 1958).
eprint: http://www.jetp.ac.ru/files/Bogolubov_007_01_0041.pdf.

30. **N.N. Bogoliubov.**
A new method in the theory of superconductivity III.
Zh. Eksper. Teor. Fiz. 34, 73 (July 1958).
eprint: http://www.jetp.ac.ru/files/Bogolubov_007_01_0051.pdf.
31. **N.N. Bogolyubov, V.V. Tolmachev, D.V. Shirkov.**
A New method in the theory of superconductivity.
Fortsch. Phys. 6, 605–682 (1958).
DOI: [10.1002/prop.19580061102](https://doi.org/10.1002/prop.19580061102)
32. **P.G. de Gennes, P.A. Pincus.**
Superconductivity of metals and alloys (ed **D. Pines**) (1966).
ISBN: [0-7382-0101-4](#)
33. **L.P. Gor'kov.**
On the energy spectrum of superconductors.
Zh. Eksper. Teor. Fiz. 34, 735 (Sept. 1958).
eprint: <http://www.jetp.ac.ru/cgi-bin/e/index/e/7/3/p505?a=list>.
34. **L.P. Gor'kov.**
Microscopic derivation of the Ginzburg-Landau equations in the theory of superconductivity.
Zh. Eksper. Teor. Fiz. 36, 1918 (Dec. 1959).
eprint: <http://www.jetp.ac.ru/cgi-bin/e/index/e/9/6/p1364?a=list>.
35. **G.M. Éliashberg.**
Interaction between electrons and lattice vibrations in a superconductor.
Zh. Eksper. Teor. Fiz. 38, 966 (Sept. 1960).
eprint: http://www.jetp.ac.ru/cgi-bin/dn/e_011_03_0696.pdf.
36. **P.W. Anderson.**
Knight Shift in Superconductors.
Phys. Rev. Lett. 3, 325–326 (7 Oct. 1959).
DOI: [10.1103/physrevlett.3.325](https://doi.org/10.1103/physrevlett.3.325)
37. **A.V. Balatsky, I. Vekhter, J.-X. Zhu.**
Impurity-induced states in conventional and unconventional superconductors.
Rev. Mod. Phys. 78, 373–433 (2 May 2006).
DOI: [10.1103/revmodphys.78.373](https://doi.org/10.1103/revmodphys.78.373)

38. **I. Giaever.**
Energy Gap in Superconductors Measured by Electron Tunneling.
Phys. Rev. Lett. 5, 147–148 (4 Aug. 1960).
doi: [10.1103/physrevlett.5.147](https://doi.org/10.1103/physrevlett.5.147)
39. **B. Josephson.**
Possible new effects in superconductive tunnelling.
Physics Letters 1, 251–253 (1962).
doi: [10.1016/0031-9163\(62\)91369-0](https://doi.org/10.1016/0031-9163(62)91369-0)
40. **G. Eilenberger.**
Transformation of Gorkov's equation for type II superconductors into transport-like equations.
Zeitschrift für Physik A Hadrons and nuclei 214, 195–213 (Apr. 1968).
doi: [10.1007/bf01379803](https://doi.org/10.1007/bf01379803)
41. **K.D. Usadel.**
Generalized Diffusion Equation for Superconducting Alloys.
Phys. Rev. Lett. 25, 507–509 (8 Aug. 1970).
doi: [10.1103/physrevlett.25.507](https://doi.org/10.1103/physrevlett.25.507)
42. **A.J. Leggett.**
A theoretical description of the new phases of liquid ^3He .
Rev. Mod. Phys. 47, 331–414 (2 Apr. 1975).
doi: [10.1103/revmodphys.47.331](https://doi.org/10.1103/revmodphys.47.331)
43. **F. Steglich *et al.***
Superconductivity in the Presence of Strong Pauli Paramagnetism: $\text{Ce}\text{Si}_2\text{Si}_2$.
Phys. Rev. Lett. 43, 1892–1896 (25 Dec. 1979).
doi: [10.1103/physrevlett.43.1892](https://doi.org/10.1103/physrevlett.43.1892)
44. **B. White, J. Thompson, M. Maple.**
Unconventional superconductivity in heavy-fermion compounds.
Physica C: Superconductivity and its Applications 514. Superconducting Materials: Conventional, Unconventional and Undetermined, 246–278 (2015).
doi: [10.1016/j.physc.2015.02.044](https://doi.org/10.1016/j.physc.2015.02.044)

45. **J.G. Bednorz, K.A. Müller.**
Possible highT_c superconductivity in the Ba–La–Cu–O system.
Zeitschrift für Physik B Condensed Matter 64, 189–193 (June 1986).
doi: [10.1007/bf01303701](https://doi.org/10.1007/bf01303701)
46. **M.K. Wu et al.**
Superconductivity at 93 K in a new mixed-phase Y-Ba-Cu-O compound system at ambient pressure.
Phys. Rev. Lett. 58, 908–910 (9 Mar. 1987).
doi: [10.1103/physrevlett.58.908](https://doi.org/10.1103/physrevlett.58.908)
47. **V.J. Emery.**
Theory of high-T_c superconductivity in oxides.
Phys. Rev. Lett. 58, 2794–2797 (26 June 1987).
doi: [10.1103/physrevlett.58.2794](https://doi.org/10.1103/physrevlett.58.2794)
48. **P. Monthoux, A.V. Balatsky, D. Pines.**
Toward a theory of high-temperature superconductivity in the antiferromagnetically correlated cuprate oxides.
Phys. Rev. Lett. 67, 3448–3451 (24 Dec. 1991).
doi: [10.1103/physrevlett.67.3448](https://doi.org/10.1103/physrevlett.67.3448)
49. **P. Monthoux, D. Pines.**
Spin-fluctuation-induced superconductivity in the copper oxides: A strong coupling calculation.
Phys. Rev. Lett. 69, 961–964 (6 Aug. 1992).
doi: [10.1103/physrevlett.69.961](https://doi.org/10.1103/physrevlett.69.961)
50. **P. Monthoux, D.J. Scalapino.**
Self-consistent d_x^2 - y^2 pairing in a two-dimensional Hubbard model.
Phys. Rev. Lett. 72, 1874–1877 (12 Mar. 1994).
doi: [10.1103/physrevlett.72.1874](https://doi.org/10.1103/physrevlett.72.1874)
51. **B. Keimer, S.A. Kivelson, M.R. Norman, S. Uchida, J. Zaanen.**
From quantum matter to high-temperature superconductivity in copper oxides.
Nature 518, 179–186 (Feb. 2015).
doi: [10.1038/nature14165](https://doi.org/10.1038/nature14165)

52. **M. Sigrist, K. Ueda.**
Phenomenological theory of unconventional superconductivity.
Rev. Mod. Phys. 63, 239–311 (2 Apr. 1991).
doi: [10.1103/revmodphys.63.239](https://doi.org/10.1103/revmodphys.63.239)
53. **D.A. Wollman, D.J. Van Harlingen, W.C. Lee, D.M. Berg, A.J. Leggett.**
Experimental determination of the superconducting pairing state in YBCO from the phase coherence of YBCO-Pb dc SQUIDS.
Phys. Rev. Lett. 71, 2134–2137 (13 Sept. 1993).
doi: [10.1103/physrevlett.71.2134](https://doi.org/10.1103/physrevlett.71.2134)
54. **C.C. Tsuei, J.R. Kirtley.**
Pairing symmetry in cuprate superconductors.
Rev. Mod. Phys. 72, 969–1016 (4 Oct. 2000).
doi: [10.1103/revmodphys.72.969](https://doi.org/10.1103/revmodphys.72.969)
55. **Y. Maeno *et al.***
Superconductivity in a layered perovskite without copper.
Nature 372, 532–534 (Dec. 1994).
doi: [10.1038/372532a0](https://doi.org/10.1038/372532a0)
56. **H. Ding *et al.***
Spectroscopic evidence for a pseudogap in the normal state of underdoped high-T_c superconductors.
Nature 382, 51–54 (July 1996).
doi: [10.1038/382051a0](https://doi.org/10.1038/382051a0)
57. **Y. Kamihara, T. Watanabe, M. Hirano, H. Hosono.**
Iron-Based Layered Superconductor La[O_{1-x}F_x]FeAs ($x = 0.05–0.12$) with T_c = 26K.
Journal of the American Chemical Society 130, 3296–3297 (Mar. 2008).
doi: [10.1021/ja800073m](https://doi.org/10.1021/ja800073m)
58. **R.M. Fernandes, A.V. Chubukov, J. Schmalian.**
What drives nematic order in iron-based superconductors?
Nature Physics 10, 97–104 (Feb. 2014).
doi: [10.1038/nphys2877](https://doi.org/10.1038/nphys2877)

59. **J. Paglione, R.L. Greene.**
High-temperature superconductivity in iron-based materials.
Nature Physics 6, 645–658 (Sept. 2010).
doi: [10.1038/nphys1759](https://doi.org/10.1038/nphys1759)
60. **D.V. Semenok *et al.***
Superconductivity at 161 K in thorium hydride ThH_{10} : Synthesis and properties.
Materials Today 33, 36–44 (2020).
doi: [10.1016/j.mattod.2019.10.005](https://doi.org/10.1016/j.mattod.2019.10.005)
61. **E. Snider *et al.***
Room-temperature superconductivity in a carbonaceous sulfur hydride.
Nature 586, 373–377 (Oct. 2020).
doi: [10.1038/s41586-020-2801-z](https://doi.org/10.1038/s41586-020-2801-z)
62. **W. Wang *et al.***
Evidence for an edge supercurrent in the Weyl superconductor MoTe_2 .
Science 368, 534–537 (2020).
doi: [10.1126/science.aaw9270](https://doi.org/10.1126/science.aaw9270)
eprint: <https://science.sciencemag.org/content/368/6490/534.full.pdf>.
63. **J.M. Park, Y. Cao, K. Watanabe, T. Taniguchi, P. Jarillo-Herrero.**
Tunable strongly coupled superconductivity in magic-angle twisted trilayer graphene.
Nature 590, 249–255 (Feb. 2021).
doi: [10.1038/s41586-021-03192-0](https://doi.org/10.1038/s41586-021-03192-0)
64. **P.W. Anderson, P. Morel.**
Generalized Bardeen-Cooper-Schrieffer States and the Proposed Low-Temperature Phase of Liquid He^3 .
Phys. Rev. 123, 1911–1934 (6 Sept. 1961).
doi: [10.1103/physrev.123.1911](https://doi.org/10.1103/physrev.123.1911)
65. **P.W. Anderson, W.F. Brinkman.**
Anisotropic Superfluidity in ${}^3\text{He}$: A Possible Interpretation of Its Stability as a Spin-Fluctuation Effect.
Phys. Rev. Lett. 30, 1108–1111 (22 May 1973).
doi: [10.1103/physrevlett.30.1108](https://doi.org/10.1103/physrevlett.30.1108)

66. **M. Sigrist.**
Introduction to Unconventional Superconductivity.
AIP Conference Proceedings 789, 165–243 (2005).
doi: [10.1063/1.2080350](https://doi.org/10.1063/1.2080350)
eprint: <http://aip.scitation.org/doi/pdf/10.1063/1.2080350>.
67. **M. Sigrist.**
Introduction to unconventional superconductivity in non-centrosymmetric metals.
AIP Conference Proceedings 1162, 55–96 (2009).
doi: [10.1063/1.3225489](https://doi.org/10.1063/1.3225489)
eprint: <http://aip.scitation.org/doi/pdf/10.1063/1.3225489>.
68. **A.J. Leggett.**
Superfluid 3-He: The early days as seen by a theorist.
Nobel Lecture, December 8, 2003.
eprint: <https://www.nobelprize.org/uploads/2018/06/leggett-lecture.pdf>.
69. **A.K. Nguyen, A. Sudbø.**
Topological phase fluctuations, amplitude fluctuations, and criticality in extreme type-II superconductors.
Phys. Rev. B 60, 15307–15331 (22 Dec. 1999).
doi: [10.1103/physrevb.60.15307](https://doi.org/10.1103/physrevb.60.15307)
70. **J. Smiseth, E. Smørgrav, E. Babaev, A. Sudbø.**
Field- and temperature-induced topological phase transitions in the three-dimensional N-component London superconductor.
Phys. Rev. B 71, 214509 (21 June 2005).
doi: [10.1103/physrevb.71.214509](https://doi.org/10.1103/physrevb.71.214509)
71. **E. Smørgrav, J. Smiseth, E. Babaev, A. Sudbø.**
Vortex Sublattice Melting in a Two-Component Superconductor.
Phys. Rev. Lett. 94, 096401 (9 Mar. 2005).
doi: [10.1103/physrevlett.94.096401](https://doi.org/10.1103/physrevlett.94.096401)
72. **T.A. Bojesen, E. Babaev, A. Sudbø.**
Phase transitions and anomalous normal state in superconductors with broken time-reversal symmetry.
Phys. Rev. B 89, 104509 (10 Mar. 2014).
doi: [10.1103/physrevb.89.104509](https://doi.org/10.1103/physrevb.89.104509)

73. **P.N. Galteland, E. Babaev, A. Sudbø.**
Fluctuation effects in rotating Bose-Einstein condensates with broken $SU(2)$ and $U(1) \times U(1)$ symmetries in the presence of intercomponent density-density interactions.
Phys. Rev. A 91, 013605 (1 Jan. 2015).
doi: [10.1103/physreva.91.013605](https://doi.org/10.1103/physreva.91.013605)
74. **N. Metropolis.**
The beginning of the Monte Carlo method.
Los Alamos Science 15, 125 (Jan. 1987).
doi: [10.2172/1054744](https://doi.org/10.2172/1054744)
75. **H. Nishimori, G. Ortiz.**
Elements of Phase Transitions and Critical Phenomena (2015).
ISBN: [9780198754084](#)
76. **J.W. Negele, H. Orland.**
Quantum Many-Particle Systems 1st ed. (ed **D. Pines**) (1998).
ISBN: [0-7382-0052-2](#)
doi: <https://doi.org/10.1201/9780429497926>
77. **T. Inui, Y. Tanabe, Y. Onodera.**
Group Theory and Its Applications in Physics (1990).
doi: [10.1007/978-3-642-80021-4](https://doi.org/10.1007/978-3-642-80021-4)
78. **A. Pal, J.A. Ouassou, M. Eschrig, J. Linder, M.G. Blamire.**
Spectroscopic evidence of odd frequency superconducting order.
Scientific Reports 7, 40604 (Jan. 2017).
doi: [10.1038/srep40604](https://doi.org/10.1038/srep40604)
79. **I.A. Sergienko, S.H. Curnoe.**
Order parameter in superconductors with nondegenerate bands.
Phys. Rev. B 70, 214510 (21 Dec. 2004).
doi: [10.1103/physrevb.70.214510](https://doi.org/10.1103/physrevb.70.214510)
80. **E. Merzbacher.**
Quantum Mechanics 3rd (1999).
ISBN: [9788126533176](#)

-
81. **A. Shimizu, H. Ozawa, I. Ichinose, T. Matsui.**
Lattice Ginzburg-Landau model of a ferromagnetic p -wave pairing phase in superconducting materials and an inhomogeneous coexisting state.
Phys. Rev. B 85, 144524 (14 Apr. 2012).
doi: [10.1103/physrevb.85.144524](https://doi.org/10.1103/physrevb.85.144524)
 82. **G. Münster, M. Walzl.**
Lattice Gauge Theory - A short Primer.
arXiv: High Energy Physics (Dec. 2000).
arXiv: [hep-lat/0012005 \[hep-lat\]](https://arxiv.org/abs/hep-lat/0012005).
 83. **Y.-H. Li, S. Teitel.**
Vortex-line fluctuations in model high-temperature superconductors.
Phys. Rev. B 47, 359–372 (1 Jan. 1993).
doi: [10.1103/physrevb.47.359](https://doi.org/10.1103/physrevb.47.359)
 84. **A.K. Nguyen, A. Sudbø.**
A new broken $U(1)$ -symmetry in extreme type-II superconductors.
Eur. Phys. Lett. 46, 780–786 (6 June 1999).
doi: [10.1209/epl/i1999-00332-7](https://doi.org/10.1209/epl/i1999-00332-7)
 85. **E. Babaev, M. Speight.**
Semi-Meissner state and neither type-I nor type-II superconductivity in multicomponent superconductors.
Phys. Rev. B 72, 180502 (18 Nov. 2005).
doi: [10.1103/physrevb.72.180502](https://doi.org/10.1103/physrevb.72.180502)
 86. **J. Smiseth, E. Smørgrav, A. Sudbø.**
Critical Properties of the N -Color London Model.
Phys. Rev. Lett. 93, 077002 (7 Aug. 2004).
doi: [10.1103/physrevlett.93.077002](https://doi.org/10.1103/physrevlett.93.077002)
 87. **H.G. Katzgraber.**
Introduction to Monte Carlo Methods.
arXiv: Statistical Mechanics (May 2011).
arXiv: [0905.1629v3 \[cond-mat.stat-mech\]](https://arxiv.org/abs/0905.1629v3).
 88. **H.G. Katzgraber, S. Trebst, D.A. Huse, M. Troyer.**
Feedback-optimized parallel tempering Monte Carlo.
Journal of Statistical Mechanics: Theory and Experiment 2006, P03018–P03018 (Mar. 2006).
doi: [10.1088/1742-5468/2006/03/p03018](https://doi.org/10.1088/1742-5468/2006/03/p03018)

89. **T.A. Bojesen.**
Multihistogram reweighting for nonequilibrium Markov processes using sequential importance sampling methods.
Phys. Rev. E 87, 045302 (4 Apr. 2013).
doi: [10.1103/physreve.87.045302](https://doi.org/10.1103/physreve.87.045302)
90. **A.M. Ferrenberg, R.H. Swendsen.**
New Monte Carlo technique for studying phase transitions.
Phys. Rev. Lett. 61, 2635–2638 (23 Dec. 1988).
doi: [10.1103/physrevlett.61.2635](https://doi.org/10.1103/physrevlett.61.2635)
91. **A.M. Ferrenberg, R.H. Swendsen.**
Optimized Monte Carlo data analysis.
Phys. Rev. Lett. 63, 1195–1198 (12 Sept. 1989).
doi: [10.1103/physrevlett.63.1195](https://doi.org/10.1103/physrevlett.63.1195)
92. **M. Newman, G. Barkema.**
Monte Carlo Methods in Statistical Physics (1999).
ISBN: [9780198517979](https://doi.org/10.1103/physrevlett.63.1195)
93. **K. Rummukainen.**
Monte Carlo simulation methods.
University of Helsinki lecture notes.
eprint: https://www.mv.helsinki.fi/home/rummukai/lectures/montecarlo_oulu/.
94. **E. Smørgårv.**
Critical properties of effective gauge theories for novel quantum fluids.
:179.
PhD thesis (NTNU, 2005).
eprint: <https://ntnuopen.ntnu.no/ntnu-xmlui/handle/11250/246193>.
95. **S. Kragset, E. Babaev, A. Sudbø.**
Effects of boundaries and density inhomogeneity on states of vortex matter in Bose-Einstein condensates at finite temperature.
Phys. Rev. A 77, 043605 (4 Apr. 2008).
doi: [10.1103/physreva.77.043605](https://doi.org/10.1103/physreva.77.043605)

96. **E. Babaev.**
Vortices with Fractional Flux in Two-Gap Superconductors and in Extended Faddeev Model.
Phys. Rev. Lett. 89, 067001 (6 July 2002).
doi: [10.1103/physrevlett.89.067001](https://doi.org/10.1103/physrevlett.89.067001)
97. **J. Garaud, E. Babaev.**
Properties of skyrmions and multi-quanta vortices in chiral p -wave superconductors.
Scientific Reports 5, 17540 (Dec. 2015).
doi: [10.1038/srep17540](https://doi.org/10.1038/srep17540)
98. **J. Garaud, E. Babaev, T.A. Bojesen, A. Sudbø.**
Lattices of double-quanta vortices and chirality inversion in $p_x + ip_y$ superconductors.
Phys. Rev. B 94, 104509 (10 Oct. 2016).
doi: [10.1103/physrevb.94.104509](https://doi.org/10.1103/physrevb.94.104509)
99. **J.A. Sauls, M. Eschrig.**
Vortices in chiral, spin-triplet superconductors and superfluids.
New Journal of Physics 11, 075008 (July 2009).
doi: [10.1088/1367-2630/11/7/075008](https://doi.org/10.1088/1367-2630/11/7/075008)
100. **S. Ishida et al.**
Unique defect structure and advantageous vortex pinning properties in superconducting $\text{CaKFe}_4\text{As}_4$.
npj Quantum Materials 4, 27 (June 2019).
doi: [10.1038/s41535-019-0165-0](https://doi.org/10.1038/s41535-019-0165-0)
101. **K. Fossheim, A. Sudbø.**
Superconductivity: physics and applications 1st ed. (June 2004).
ISBN: [0-470-84452-3](#)
102. **J. Aragón Sánchez et al.**
Unveiling the vortex glass phase in the surface and volume of a type-II superconductor.
Communications Physics 2, 143 (Nov. 2019).
doi: [10.1038/s42005-019-0243-4](https://doi.org/10.1038/s42005-019-0243-4)
103. **R.H. Koch et al.**
Experimental evidence for vortex-glass superconductivity in Y-Ba-Cu-O .
Phys. Rev. Lett. 63, 1511–1514 (14 Oct. 1989).
doi: [10.1103/physrevlett.63.1511](https://doi.org/10.1103/physrevlett.63.1511)

104. J.E. Sonier.

The Magnetic Penetration Depth and the Vortex Core Radius in Type-II Superconductors.

PhD thesis (University of British Columbia, Apr. 1998).

doi: [10.14288/1.0085673](https://doi.org/10.14288/1.0085673)

105. L. Kramer.

Thermodynamic Behavior of Type-II Superconductors with Small κ near the Lower Critical Field.

Phys. Rev. B 3, 3821–3825 (11 June 1971).

doi: [10.1103/physrevb.3.3821](https://doi.org/10.1103/physrevb.3.3821)

106. A. Chaves, F.M. Peeters, G.A. Farias, M.V. Milošević.

Vortex-vortex interaction in bulk superconductors: Ginzburg-Landau theory.

Phys. Rev. B 83, 054516 (5 Feb. 2011).

doi: [10.1103/physrevb.83.054516](https://doi.org/10.1103/physrevb.83.054516)

107. D. Cribier, B. Jacrot, B. Farnoux, L.M. Rao.

Study of the Lattice of Vortex Lines in Superconducting Niobium by Neutron Diffraction.

Journal of Applied Physics 37, 952–952 (1966).

doi: [10.1063/1.1708536](https://doi.org/10.1063/1.1708536)

108. U. Essmann, H. Träuble.

The direct observation of individual flux lines in type II superconductors.

Physics Letters A 24, 526–527 (1967).

doi: [10.1016/0375-9601\(67\)90819-5](https://doi.org/10.1016/0375-9601(67)90819-5)

109. J. Matricon.

Energy and elastic moduli of a lattice of vortex lines.

Physics Letters 9, 289–291 (1964).

doi: [10.1016/0031-9163\(64\)90365-8](https://doi.org/10.1016/0031-9163(64)90365-8)

110. D. Agterberg et al.

Vortex lattice structures and pairing symmetry in Sr_2RuO_4 .

Physica C: Superconductivity 341–348, 1643–1646 (2000).

doi: [10.1016/s0921-4534\(00\)01492-1](https://doi.org/10.1016/s0921-4534(00)01492-1)

111. R. Heeb, D.F. Agterberg.

Ginzburg-Landau theory for a p -wave Sr_2RuO_4 superconductor: Vortex core structure and extended London theory.

Phys. Rev. B 59, 7076–7082 (10 Mar. 1999).

doi: [10.1103/physrevb.59.7076](https://doi.org/10.1103/physrevb.59.7076)

112. **D.F. Agterberg.**
Vortex Lattice Structures of Sr₂RuO₄.
Phys. Rev. Lett. 80, 5184–5187 (23 June 1998).
doi: [10.1103/physrevlett.80.5184](https://doi.org/10.1103/physrevlett.80.5184)
113. **T.M. Riseman *et al.***
Observation of a square flux-line lattice in the unconventional superconductor Sr₂RuO₄.
Nature 396, 242–245 (Nov. 1998).
doi: [10.1038/24335](https://doi.org/10.1038/24335)
114. **C.M. Aegerter *et al.***
Evidence for a square vortex lattice in from muon-spin-rotation measurements.
Journal of Physics: Condensed Matter 10, 7445–7451 (Aug. 1998).
doi: [10.1088/0953-8984/10/33/013](https://doi.org/10.1088/0953-8984/10/33/013)
115. **S.J. Ray *et al.***
Muon-spin rotation measurements of the vortex state in Sr₂RuO₄: Type-1.5 superconductivity, vortex clustering, and a crossover from a triangular to a square vortex lattice.
Phys. Rev. B 89, 094504 (9 Mar. 2014).
doi: [10.1103/physrevb.89.094504](https://doi.org/10.1103/physrevb.89.094504)
116. **P.J. Curran *et al.***
Vortex imaging and vortex lattice transitions in superconducting Sr₂RuO₄ single crystals.
Phys. Rev. B 84, 104507 (10 Sept. 2011).
doi: [10.1103/physrevb.84.104507](https://doi.org/10.1103/physrevb.84.104507)
117. **A.K. Nguyen, A. Sudbø.**
Phase coherence and the boson analogy of vortex liquids.
Phys. Rev. B 58, 2802–2815 (5 Aug. 1998).
doi: [10.1103/physrevb.58.2802](https://doi.org/10.1103/physrevb.58.2802)
118. **A.K. Nguyen, A. Sudbø, R.E. Hetzel.**
Vortex-Loop Unbinding and Flux-Line Lattice Melting in Superconductors.
Phys. Rev. Lett. 77, 1592–1595 (8 Aug. 1996).
doi: [10.1103/physrevlett.77.1592](https://doi.org/10.1103/physrevlett.77.1592)

119. **A.K. Nguyen, A. Sudbø.**
Onsager loop transition and first-order flux-line lattice melting in high- T_c superconductors.
Phys. Rev. B 57, 3123–3143 (5 Feb. 1998).
doi: [10.1103/physrevb.57.3123](https://doi.org/10.1103/physrevb.57.3123)
120. **G.M. Luke *et al.***
Time-reversal symmetry-breaking superconductivity in Sr_2RuO_4 .
Nature 394, 558–561 (Aug. 1998).
doi: [10.1038/29038](https://doi.org/10.1038/29038)
121. **J. Xia, Y. Maeno, P.T. Beyersdorf, M.M. Fejer, A. Kapitulnik.**
High Resolution Polar Kerr Effect Measurements of Sr_2RuO_4 : Evidence for Broken Time-Reversal Symmetry in the Superconducting State.
Phys. Rev. Lett. 97, 167002 (16 Oct. 2006).
doi: [10.1103/physrevlett.97.167002](https://doi.org/10.1103/physrevlett.97.167002)
122. **V. Grinenko *et al.***
Split superconducting and time-reversal symmetry-breaking transitions, and magnetic order in Sr_2RuO_4 under uniaxial stress.
arXiv: Superconductivity (Jan. 22, 2020).
arXiv: [2001.08152 \[cond-mat.supr-con\]](https://arxiv.org/abs/2001.08152).
123. **S.A. Kivelson, A.C. Yuan, B. Ramshaw, R. Thomale.**
A proposal for reconciling diverse experiments on the superconducting state in Sr_2RuO_4 .
npj Quantum Materials 5, 43 (June 2020).
doi: [10.1038/s41535-020-0245-1](https://doi.org/10.1038/s41535-020-0245-1)
124. **S. Ghosh *et al.***
Thermodynamic evidence for a two-component superconducting order parameter in Sr_2RuO_4 .
Nature Physics 17, 199–204 (Feb. 2021).
doi: [10.1038/s41567-020-1032-4](https://doi.org/10.1038/s41567-020-1032-4)
125. **T.A. Bojesen.**
Policy-guided Monte Carlo: Reinforcement-learning Markov chain dynamics.
Phys. Rev. E 98, 063303 (6 Dec. 2018).
doi: [10.1103/physreve.98.063303](https://doi.org/10.1103/physreve.98.063303)

126. **Y. Nagai, M. Okumura, A. Tanaka.**
Self-learning Monte Carlo method with Behler-Parrinello neural networks.
Phys. Rev. B 101, 115111 (11 Mar. 2020).
DOI: [10.1103/physrevb.101.115111](https://doi.org/10.1103/physrevb.101.115111)
127. **E. Bedolla, L.C. Padierna, R. Castañeda-Priego.**
Machine learning for condensed matter physics.
Journal of Physics: Condensed Matter 33, 053001 (Nov. 2020).
DOI: [10.1088/1361-648x/abb895](https://doi.org/10.1088/1361-648x/abb895)

Paper I

Fredrik Nicolai Krohg and Asle Sudbø

*Derivation of a Ginzburg-Landau free energy density of a $p + ip$ superconductor
from spin-orbit coupling with mixed gradient terms*

Physical Review B **98**, 014510 (2018)

Derivation of a Ginzburg-Landau free energy density of a $p + ip$ superconductor from spin-orbit coupling with mixed gradient terms

Fredrik Nicolai Krohg and Asle Sudbø

*Department of Physics, Norwegian University of Science and Technology, NO-7491 Trondheim, Norway
and Department of Physics, Center for Quantum Spintronics, Norwegian University of Science and Technology, NO-7491 Trondheim, Norway*



(Received 27 March 2018; published 13 July 2018)

A Ginzburg-Landau free energy for a superconducting chiral p -wave order parameter is derived from a two-dimensional tight-binding lattice model with weak spin-orbit coupling included as a general symmetry-breaking field. Superconductivity is accounted for by a BCS-type nearest-neighbor opposite-spin interaction where we project the potential onto the p -wave irreducible representation of the square lattice symmetry group and assume this to be the dominating order. The resulting free energy contains kinetic terms that mix components of the order parameter as well as directional gradients—so-called mixed gradient terms—as a virtue of the symmetry of the order parameter. Spin-orbit coupling and electron-hole anisotropy lead to additional contributions to the coefficients of these terms, increasing the number of necessary phenomenological parameters by one compared to previous work and leading to an increase in the coefficient measuring Fermi-surface anisotropy for Rashba spin-orbit coupling in the continuum limit.

DOI: [10.1103/PhysRevB.98.014510](https://doi.org/10.1103/PhysRevB.98.014510)

I. INTRODUCTION

Spin-orbit coupling (SOC) couples the spin of the electron to its momentum which splits spin-degenerate electronic bands and is a recurring theme in many novel superconducting systems. If SrTiO_3 is slightly doped with Ca, there is a region in the temperature-versus-carrier concentration phase diagram where superconductivity and ferroelectricity coexist and where the material has broken spatial inversion symmetry—a key cause of SOC [1,2]. When SOC is a significant factor, the associated symmetry of the superconductivity is often of an unconventional character. In this context, unconventional means superconductivity where the order parameter does not have the usual spin-singlet s -wave pairing symmetry [3]. One example is the one-atom layer of the Tl-Pb compound on a Si(111) surface studied in Ref. [4]. This system exhibits two-dimensional (2D) superconductivity at a critical temperature of $T_c \sim 2.25$ K followed by a Berezinskii-Kosterlitz-Thouless transition and has Rashba SOC leading to a maximum splitting of spin bands by ~ 250 meV. In this case the superconductivity is argued to be nonconventional because the average distance between Cooper pairs is longer than the Ginzburg-Landau (GL) coherence length.

Another example is the 2D electron liquid in the celebrated $\text{LaAlO}_3/\text{SrTiO}_3$ interface (for a review see Ref. [5]). By using a back gate to apply an electric potential across the interface, which tunes the carrier density, T_c can be increased to ~ 300 mK [6]. In a certain region, tuning this gate voltage affects the Rashba spin-orbit coupling dramatically—reaching values of 10 meV. This region also seems to be correlated to where superconductivity develops [7]. The unconventional symmetry resulting from large Rashba SOC is evident from the critical field parallel to the interface being much larger than what would be expected from the Pauli limit [8].

Finally, it should be mentioned that it was initially the discovery of superconductivity in the heavy fermion system

CePt_3Si [9,10] that helped intensify research efforts into noncentrosymmetric superconductors. This system exhibits an increase in critical magnetic field compared to the Pauli limit as well as suppression of superconductivity by nonmagnetic impurities. Other lines of evidence for the unconventional character of the order parameter include indications of line nodes in the superconducting gap from penetration depth [11], thermal conductivity measurements [12], among others. For a more thorough overview of noncentrosymmetric systems, see Ref. [13].

In this paper, the Ginzburg-Landau free energy density is derived for a 2D square lattice with spin-orbit coupling where a chiral $p_x + ip_y$ symmetry is assumed to describe the dominating pairing channel. This particular pairing state has attracted much attention because of its topological properties, which include the existence of topologically protected Majorana edge states as well as Majorana bound states in the core regions of half-integer vortices [14]. In the context of superfluidity, p -wave pairing is realized as the A phase in ${}^3\text{He}$ [15] and has long been hypothesized to be the dominant superconducting pairing symmetry in Sr_2RuO_4 [16–18].

The vortex structure of a phenomenological Ginzburg-Landau theory for a 2D chiral p -wave pairing symmetry [3,19] was studied using numerical simulations in Ref. [20]. A magnetic field breaks the degeneracy between the two components of the order parameter so that one becomes dominant whereas the other only exists close to topological defects, such as vortices. The simulations found that the superconducting vortices tend to arrange themselves in a square lattice of single-quantized vortices when the magnetic field is very close to the upper critical field, however for slightly lower field strengths the phase diagram is dominated by a triangular lattice consisting of double-quanta vortices, which are coreless. The relative angular momentum between the dominant and the subdominant components of the order parameter determines

the kinds of vortices possible in the system and originates in the structure of the mixed gradient terms in the GL free energy. These terms also drive the subdominant component [21]. An interesting question is therefore what physical parameters influence the phenomenological coefficients of these types of terms. Mixed gradient terms have also been found in a multicomponent GL theory for a $s + is$ pairing state derived through the Eilenberger equations for quasiclassical propagators [22]. This state breaks time-reversal symmetry, similar to the chiral p -wave state, and is found to exist in a doped four-band model for iron pnictides [23]. In this GL theory however, the terms could be eliminated by a simple spin rotation in contrast to the p -wave case.

Expressions for Ginzburg-Landau theory coefficients for general order parameters have previously been derived assuming either pairing in the normal BCS spin basis and ignoring spin-orbit coupling or by pairing in a single spin-orbit split nondegenerate band [24]. Additionally, GL theory has been derived for a superconductor with p -wave symmetry and a coexistent ferromagnetic state [25]. The derivations in this paper will largely follow the methods used in these two references.

The difference between the current paper and Ref. [24] is that spin-orbit coupling is considered a symmetry-breaking field on the ordered state when deriving the GL theory. The spin-orbit coupling strength is assumed to be small compared to the Debye cutoff frequency. A similar system was considered in Ref. [26] where the spin-orbit coupling strength was assumed to be small relative to a Zeeman field. A pairing state with p -wave symmetry in the diagonalized bands was discovered as a result of a Kohn-Luttinger-type interaction coming from the transformation of a repulsive U Hubbard model to the new bands. In the present case, the interaction is assumed to give rise to a chiral $p + ip$ pairing symmetry in the nondiagonal spin bands. This leads to a number of additional terms in the generalized effective mass compared to the limit of zero spin-orbit coupling.

The paper is organized as follows: In Sec. II the model is introduced, first in terms of the single-particle properties in Sec. II A, and then in Sec. II B the pairing interaction is presented with a brief justification. A sketch of how the Ginzburg-Landau free energy was derived is given in Sec. III and its form reduced to the same as in Ref. [20]. The contributions from spin-orbit coupling to the phenomenological coefficients are finally discussed in Sec. IV. Details of the calculations are relegated to the Appendices. Units are chosen throughout the papers such that $k_B = \hbar = a = 1$ for lattice spacing a .

II. TIGHT-BINDING MODEL

A. Single-particle problem

The system is modeled as a two-dimensional square lattice, which has symmetry group C_{4v} , where fermions can exist at each lattice site. In the clean limit there is no disorder in the system implying that the Fourier-transformed single-particle Hamiltonian is diagonal in wave-vectors \mathbf{k} . Including antisymmetric spin-orbit coupling [13] by spin-dependent hopping between lattice sites, the single-particle Hamiltonian can be

written

$$\hat{H}_0 = \sum_{\substack{s_1 s_2 \\ \mathbf{k}}} [\epsilon(\mathbf{k}) + \boldsymbol{\gamma}(\mathbf{k}) \cdot \boldsymbol{\sigma}]_{s_1 s_2} c_{\mathbf{k} s_1}^\dagger c_{\mathbf{k} s_2}, \quad (1)$$

where $\boldsymbol{\sigma}$ consists of Pauli matrices, $c_{\mathbf{k}s}$ is the annihilation operator for a fermion with wave-vector \mathbf{k} and spin s , and the sum over \mathbf{k} runs over the first Brillouin zone. Hermiticity of the Hamiltonian implies that $\epsilon(\mathbf{k})$ and $\boldsymbol{\gamma}(\mathbf{k})$ are real. Time-reversal symmetry implies the restrictions $\epsilon(\mathbf{k}) = \epsilon(-\mathbf{k})$ and $\boldsymbol{\gamma}(\mathbf{k}) = -\boldsymbol{\gamma}(-\mathbf{k})$. If parity symmetry is enforced, $\boldsymbol{\gamma}(\mathbf{k})$ vanishes, and this vector is hence identified with the parity breaking antisymmetric spin-orbit coupling. The Hamiltonian in Eq. (1) becomes diagonal by a unitary transformation to the helicity basis given by

$$\mathbf{a}_{\mathbf{k}} = \frac{1}{\sqrt{2}} \begin{pmatrix} \frac{i\hat{\gamma}^y - \hat{\gamma}^x}{\sqrt{1-\hat{\gamma}^z}} e^{i\phi_+} & \frac{i\hat{\gamma}^y - \hat{\gamma}^x}{\sqrt{1+\hat{\gamma}^z}} e^{i\phi_-} \\ -\sqrt{1-\hat{\gamma}^z} e^{i\phi_+} & \sqrt{1+\hat{\gamma}^z} e^{i\phi_-} \end{pmatrix}^\dagger \mathbf{c}_{\mathbf{k}}, \quad (2)$$

where ϕ_\pm are arbitrary phases and $\hat{\gamma}^i = \gamma^i(\mathbf{k})/|\boldsymbol{\gamma}(\mathbf{k})|$, assuming $\boldsymbol{\gamma}$ has some nonzero component on the xy plane in spin space, or a similar transformation if $\boldsymbol{\gamma} \parallel \hat{e}_z$ (cf. Appendix B). The dispersion relations of the eigenvalues of the single-particle Hamiltonian are given by

$$\epsilon_{\mathbf{k}}^h = \epsilon(\mathbf{k}) + h|\boldsymbol{\gamma}(\mathbf{k})|, \quad (3)$$

where $h \in \{\pm\}$ enumerates the two different helicity bands when written in exponentials and is used as ± 1 when written as a factor.

B. Pairing interaction

To include p -wave superconductivity in the model, an attractive BCS-type weak-coupling interaction is introduced between electrons given by

$$\hat{V} = -\frac{1}{2} \sum_{\mathbf{k}\mathbf{k}'\mathbf{q}} \sum_{s_1 s_2 s'_1 s'_2} V_{\mathbf{k}\mathbf{k}', s_1 s_2 s'_1 s'_2} \times c_{(\mathbf{q}/2)+\mathbf{k}s_1}^\dagger c_{(\mathbf{q}/2)-\mathbf{k}s_2}^\dagger c_{(\mathbf{q}/2)-\mathbf{k}'s'_2} c_{(\mathbf{q}/2)+\mathbf{k}'s'_1} \quad (4)$$

for

$$V_{\mathbf{k}\mathbf{k}', s_1 s_2 s'_1 s'_2} = V_b \sum_{m=1}^{d_b} d_{\mathbf{k}, s_1 s_2}^{(b_m)} (d_{\mathbf{k}', s'_1 s'_2}^{(b_m)})^*, \quad (5)$$

where $d_{\mathbf{k}, s_1 s_2}^{(b_m)}$ are coefficients for basis vectors for the d_b -dimensional irreducible representation b . These basis vectors are odd and linear in \mathbf{k} , i.e., a p -wave-like momentum dependence in the continuum limit. Since superconductivity is introduced in the spin basis, it is assumed that the spin-orbit coupling is sufficiently weak compared to the superconducting energy scale for this pairing between opposite momentum fermions to be valid, i.e., spin-orbit coupling is treated as a symmetry-breaking field on the superconducting state [13].

The exact forms of the basis vectors are found in the process of proving that such an interaction exists for the square lattice. This is performed by finding the possible eigenvectors for a general two-particle Hermitian operator \hat{V} that has eigenvectors consisting of pairs of particles with opposite momentum. The eigenspace of a Hermitian operator can be separated into

irreducible spaces that are representations of the symmetry group of the lattice. By expanding in the spin-momentum basis of the two-particle Hilbert space, any such eigenvector $|d\rangle$ can be written

$$|d\rangle = \sum_{\mathbf{k}, s_1 s_2} d_{s_1 s_2}(\mathbf{k}) |\mathbf{k}, s_1\rangle |-\mathbf{k}, s_2\rangle. \quad (6)$$

The eigenvectors will also include a cutoff function $f_c(\epsilon_{\mathbf{k}})$ since the attractive interaction is assumed to only exist on the Fermi surface. This cutoff function is implicit in the notation for $d_{s_1 s_2}(\mathbf{k})$. If the coefficient $d_{s_1 s_2}(\mathbf{k})$ is odd in \mathbf{k} , then because of the fermionic particle exchange symmetry and because it is periodic in reciprocal lattice vectors it can be expanded in terms of lattice vectors \mathbf{R} as

$$d_{s_1 s_2}(\mathbf{k}) = \frac{1}{\sqrt{N}} \sum_{\mathbf{R}} [\beta_{\mathbf{R}} \sin(\mathbf{R} \cdot \mathbf{k}) \cdot \sigma i \sigma^y]_{s_1 s_2}. \quad (7)$$

These general vectors are then projected down on the space consisting of basis vectors of a particular irreducible representation (irrep.) b of interest by the projection operators [27,28],

$$P_{ll}^{(b)} = \frac{d_b}{|C_{4v}|} \sum_{g \in C_{4v}} D_{ll}^{(b)}(g)^* g, \quad (8)$$

where $D_{ll}^{(b)}$ are matrices of the irrep., g : denotes transformation of a vector by the group element g , and the index l runs over the dimension d_b of the irrep. The group C_{4v} contains one two-dimensional irrep. E . Projecting down on this irrep. and assuming the eigenspace of \hat{V} only is constructed from nearest-neighbor sites yields a vector space constructed from the orthonormal basis vectors given by the spin-momentum coefficients,

$$d_{s_1 s_2}^{(E_y)}(\mathbf{k}) = -\frac{\hat{\mathbf{z}}}{\sqrt{N}} \sin k_y \cdot (\sigma i \sigma^y)_{s_1 s_2} \quad (9a)$$

$$\equiv \mathbf{d}^{(E_y)}(\mathbf{k}) \cdot (\sigma i \sigma^y)_{s_1 s_2}, \quad (9b)$$

$$d_{s_1 s_2}^{(E_x)}(\mathbf{k}) = \frac{\hat{\mathbf{z}}}{\sqrt{N}} \sin k_x \cdot (\sigma i \sigma^y)_{s_1 s_2} \quad (9c)$$

$$\equiv \mathbf{d}^{(E_x)}(\mathbf{k}) \cdot (\sigma i \sigma^y)_{s_1 s_2}. \quad (9d)$$

These are p -wave basis vectors since they are linear in \mathbf{k} in the continuum limit. Note that the assumptions of a single 2D square lattice implies that basis vectors that have \mathbf{k} dependencies with components in the \hat{e}_z direction are neglected. When \hat{V} is expanded in its eigenvector basis, it is therefore possible that it has a channel consisting of the eigenvectors in Eq. (9) and it has been proved that Eq. (4) is a possible interaction.

This p -wave channel interaction could originate as the dominant channel of a simpler interaction. As an example, consider the attractive nearest-neighbor interaction,

$$\hat{V} = -\frac{V}{2} \sum_{\langle i, j \rangle} \sum_{s=\uparrow\downarrow} c_{i,s}^\dagger c_{j,-s}^\dagger c_{j,-s} c_{i,s}, \quad (10)$$

which could be considered an effective one-band model from a reduction of a multiband system [29]. Finding basis vectors in the eigenspace of nearest-neighbor interactions analogous

to the irrep. E , \hat{V} becomes diagonal in this basis and can be written in the form of Eq. (4) but with coefficient,

$$V_{\mathbf{k}\mathbf{k}', s_1 s_2 s'_1 s'_2} = V \left[\sum_{a=A_1, B_1} \psi_{s_1 s_2}^{(a)}(\mathbf{k}) [\psi_{s'_1 s'_2}^{(a)}(\mathbf{k}')]^* + \sum_{m=x, y} d_{s_1 s_2}^{(E_m)}(\mathbf{k}) [d_{s'_1 s'_2}^{(E_m)}(\mathbf{k}')]^* \right], \quad (11)$$

where a runs over the one-dimensional irreps. A_1 and B_1 which has basis vectors given by

$$\psi_{s_1 s_2}^{(A_1)}(\mathbf{k}) = \frac{1}{\sqrt{2N}} (\cos k_x + \cos k_y) (i \sigma^y)_{s_1 s_2}, \quad (12)$$

$$\psi_{s_1 s_2}^{(B_1)}(\mathbf{k}) = \frac{1}{\sqrt{2N}} (\cos k_x - \cos k_y) (i \sigma^y)_{s_1 s_2}, \quad (13)$$

and give the extended s -wave channel and d -wave channel, respectively. Note that these basis vectors are normalized on the first Brillouin zone and even though they have the same coupling constant V , the critical temperature T_c of the different channels is affected by physical parameters in the single-particle part of the Hamiltonian, such as doping level and spin-orbit coupling strength and is thus in general different. The channel with the highest critical temperature will then completely dominate as the relevant order for temperatures immediately below T_c . This temperature can be calculated by solving the linearized gap equation by, e.g., the method used in Ref. [26] but is considered outside the scope of this paper.

III. DERIVATION OF GINZBURG-LANDAU FREE ENERGY

The Ginzburg-Landau coefficients are calculated by deriving the free energy F of the system described in Sec. II. This free energy is defined as $F = -\frac{1}{\beta} \ln Z$, where Z is the partition function and β is inverse temperature. The partition function is defined as $Z = \text{Tr } e^{-\beta(\hat{H}-\mu\hat{N})}$, where $\hat{H} = \hat{H}_0 + \hat{V}$ is the Hamiltonian of the system, μ is the chemical potential, and \hat{N} is the number operator. Calculating the trace in the path-integral formalism where the annihilation and creation operators get replaced by Graßmann fields ξ and ξ^* , the Hubbard-Stratonovich transformation is preformed on the p -wave subspace of the potential \hat{V} , whereas the other subspaces are neglected. It is assumed that there exists some region in the doping level and SOC strength parameter space where the p -wave coupling is associated with the highest critical temperature such that neglecting the other subspaces of the interaction is justified. Given the potential in Eq. (11), the p -wave subspace is two dimensional, and its contribution to the partition function can thus be written in terms of a path integral over the two complex fields $\eta^{(x)}$ and $\eta^{(y)}$ as

$$e^{S_{\text{int}}} = \int \mathcal{D}[\eta, \eta^*] \exp \left\{ - \int_0^\beta d\tau \sum_{\mathbf{q} m} \left[\frac{2|\eta_q^{(m)}|^2}{V} + (J_q^{m*} \eta_q^{(m)} + J_q^m \eta_q^{(m)*}) \right] \right\}, \quad (14)$$

where J_q^m is defined as

$$J_q^m = \sum_{\mathbf{k}s_1s_2} [d_{s_1s_2}^{(E_m)}(\mathbf{k})]^* \xi_{(\mathbf{q}/2)-\mathbf{k}, s_2} \xi_{(\mathbf{q}/2)+\mathbf{k}, s_1}, \quad (15)$$

and

$$S_{\text{int}} = \frac{V}{2} \int_0^\beta d\tau \sum_{\mathbf{q}m} J_q^{m*} J_q^m. \quad (16)$$

In these equations both the Graßmann fields ξ and the complex fields η are dependent on imaginary time. The time dependence in the complex fields η , which are the order parameters of the system, is neglected since the goal is a time-independent Ginzburg-Landau theory, whereas the time dependence in the Graßmann fields are converted to sums over Matsubara frequencies. The system is assumed to be close to the transition temperature T_c so that the free energy can be expanded to second order in the order parameters after integrating out the fermionic degrees of freedom. The integration itself is performed by expressing the part of the exponent with quadratic dependence on fermionic fields as an Hermitian form $\xi^\dagger \check{G}^{-1} \xi$ using four-component Matsubara vectors ξ such that the result depends on the determinant of \check{G}^{-1} by

$$\begin{aligned} Z_{\text{ferm}} &= \int \mathcal{D}[\xi, \xi^*] \exp \left(-\frac{1}{2} \sum \xi^\dagger \check{G}^{-1} \xi \right) \\ &= \sqrt{\det \check{G}^{-1}} = \exp \left(\frac{1}{2} \text{Tr} \ln \check{G}^{-1} \right). \end{aligned} \quad (17)$$

The expansion to second order in the order parameter is preformed by splitting \check{G}^{-1} into a diagonal matrix \check{G}_0^{-1} independent of η and a matrix $\check{\phi}$ for which each element is proportional to the order parameter components $\eta^{(a)}$. The logarithm in Eq. (17) is then expanded by

$$\text{Tr} \ln \check{G}^{-1} = \text{Tr} \ln \check{G}_0^{-1} + \text{Tr} \check{G}_0 \check{\phi} - \frac{1}{2} \text{Tr} \check{G}_0 \check{\phi} \check{G}_0 \check{\phi}. \quad (18)$$

The first term is absorbed into the normalization of the path integral over η , whereas the second term vanishes trivially which leaves the contribution of the third term. The single-particle problem in Eq. (1) and thus the spin-orbit coupling are included in this integration over fermionic degrees of freedom. The order parameter is assumed to be slowly varying in real space, which justifies a gradient expansion. Given these assumptions and approximations, the free energy density in momentum space takes the form

$$f_{\mathbf{q}} = A_{ab} (\eta_{\mathbf{q}}^{(a)})^* \eta_{\mathbf{q}}^{(b)} + K_{ab,ij} (\eta_{\mathbf{q}}^{(a)})^* \eta_{\mathbf{q}}^{(b)} q^i q^j, \quad (19)$$

where the Einstein summation convention has been used to drop the summation over directions $i, j = x, y$ and dimensions of the subspace $a, b = x, y$. We denote A_{ab} as the potential-energy tensor whereas $K_{ab,ij}$ is the generalized effective mass tensor [24]. It is worth noting that the same expression is obtained regardless of what choice is made for the phases ϕ_\pm in Eq. (2), and whether γ has a component on the xy plane or not.

Note that Eq. (19) does not contain terms linear in \mathbf{q} . Such terms, Lifshitz invariants, are in general allowed by symmetry when the crystal does not contain an inversion center [13]. When the order parameter only has a single component, these terms exist only in the presence of an external magnetic

field and give rise to a helical nonuniform superconducting state. However for a multiple-component order parameter, symmetry allows Lifshitz invariants also in the absence of any external field [30,31]. In Eq. (E29) in Appendix E, we give an expression for the partition function that holds for a general odd-momentum order parameter, which do exhibit terms linear in \mathbf{q} . These terms can be shown to be proportional to $\mathbf{d}^{(b_{m'})}(\mathbf{k})^* \times \mathbf{d}^{(b_m)}(\mathbf{k})$ and thus disappear for unitary odd-momentum pairing states, such as the pairing state given by the basis vectors in Eq. (E29).

A. Form of the free energy density tensors

The potential-energy tensor derived in Eq. (19) is given by

$$A_{ab} = \frac{2\delta_{ab}}{V} - \sum_{\mathbf{k}hh'} d^{ab} \{1 - hh'[1 - 2(\hat{\gamma}^z)^2]\} \chi^{hh'}, \quad (20)$$

where $\chi^{hh'}$ is the Matsubara-frequency sum over Green's functions given by

$$\chi^{hh'} = \frac{1}{\beta} \sum_n \frac{1}{(i\omega_n - \epsilon_{\mathbf{k}}^h)(-i\omega_n - \epsilon_{\mathbf{k}}^{h'})}, \quad (21)$$

and

$$d^{ab} = [\mathbf{d}^{(E_a)}(\mathbf{k})]^* \cdot \mathbf{d}^{(E_b)}(\mathbf{k}). \quad (22)$$

In Eq. (21) the chemical potential has been absorbed into the definition of $\epsilon_{\mathbf{k}}^h$. As in Eq. (3), $h, h' \in \{\pm\}$'s enumerate the helicity bands and are used as ± 1 when written as factors. Since the only \mathbf{k} dependencies in this sum are in the Fermi energies, it is invariant with respect to symmetry transformations. This means that the momentum sum vanishes if $a \neq b$ since the summand then becomes odd with respect to each of the components of \mathbf{k} [cf. definition of $\mathbf{d}^{(E_a)}(\mathbf{k})$ in Eq. (9)].

The generalized effective mass tensor in Eq. (19) can be expressed as

$$\begin{aligned} K_{ab,ij} &= \frac{1}{8} \sum_{\mathbf{k}hh'} d^{ab} \{hh'[1 - 2(\hat{\gamma}^z)^2] - 1\} \chi_{ij}^{hh'} \\ &\quad + 2h'h \chi^{hh'} g_{ij}, \end{aligned} \quad (23)$$

where

$$\begin{aligned} g_{ij} &= \partial_i \hat{\gamma} \cdot \partial_j \hat{\gamma} - 2 \partial_i \hat{\gamma}^z \partial_j \hat{\gamma}^z \\ &\quad - (\hat{\gamma} \cdot \partial_i \partial_j \hat{\gamma} - 2 \hat{\gamma}^z \partial_i \partial_j \hat{\gamma}^z), \end{aligned} \quad (24)$$

and

$$\begin{aligned} \chi_{ij}^{hh'} &= -\frac{1}{\beta} \sum_n \left\{ \frac{\partial}{\partial \epsilon} \frac{1}{i\omega_n - \epsilon_{\mathbf{k}}^h} \frac{\partial}{\partial \epsilon} \frac{1}{-i\omega_n - \epsilon_{\mathbf{k}}^{h'}} v_i^h v_j^{h'} \right. \\ &\quad - \left(\frac{\partial^2}{\partial \epsilon^2} \frac{1}{i\omega_n - \epsilon_{\mathbf{k}}^h} \right) \frac{1}{-i\omega_n - \epsilon_{\mathbf{k}}^{h'}} v_i^h v_j^{h'} \\ &\quad - \left. \left(\frac{\partial}{\partial \epsilon} \frac{1}{i\omega_n - \epsilon_{\mathbf{k}}^h} \right) \frac{1}{-i\omega_n - \epsilon_{\mathbf{k}}^{h'}} m_{hij}^{-1} \right\} \\ &\quad + h \leftrightarrow h'. \end{aligned} \quad (25)$$

The inverse effective mass of the h band is given by

$$m_{hij}^{-1} = \frac{\partial^2 \epsilon_{\mathbf{k}}^h}{\partial k^i \partial k^j} = m_{ij}^{-1} + h \partial_i \partial_j |\boldsymbol{\gamma}|, \quad (26)$$

whereas the h -band Fermi velocity is given by

$$v_i^h = \frac{\partial}{\partial k^i} \epsilon_{\mathbf{k}}^h = v_i + h \partial_i |\boldsymbol{\gamma}|. \quad (27)$$

B. Approximation of free energy density tensors in terms of Fermi-surface averages

More useful expressions can be obtained for A_{ab} and $K_{ab,ij}$ by expressing the sums over momenta \mathbf{k} as averages over energy surfaces defined as

$$\langle (\cdot) \rangle_{\xi} \equiv \frac{1}{N_0(\xi)} \sum_{\mathbf{k}} (\cdot) \delta[\epsilon(\mathbf{k}) - \xi], \quad (28)$$

where $N_0(\xi)$ is the density of states at energy ξ . Including the chemical potential in the definition of $\epsilon(\mathbf{k})$, the Fermi surface is obtained at $\xi = 0$. Let $h[\mathbf{k}, \epsilon(\mathbf{k})]$ be a generic summand in one of the \mathbf{k} sums with an explicit $\epsilon(\mathbf{k})$ dependence. The momentum sum is exchanged for a Fermi-surface average by inserting an energy integral over a δ function such that

$$\begin{aligned} \sum_{\mathbf{k}} h[\mathbf{k}, \epsilon(\mathbf{k})] &= \int_{-\epsilon_c}^{\epsilon_c} d\xi N_0(\xi) \langle h(\mathbf{k}, \xi) \rangle_{\xi} \\ &\approx \left\langle \int_{-\epsilon_c}^{\epsilon_c} d\xi N_0(\xi) h(\mathbf{k}, \xi) \right\rangle_0. \end{aligned} \quad (29)$$

The integral is cut off at ϵ_c because of the assumption that the interaction potential only allows pairing to happen within some energy shell around the Fermi surface. The energy average is assumed to be constant over this energy shell such that only the value at $\xi = 0$ is considered. To simplify the resulting integrals, it is assumed that the critical temperature is small compared to the energy cutoff such that

$$e_c \equiv \frac{\epsilon_c \beta}{\pi} \gg 1. \quad (30)$$

The spin-orbit coupling is additionally assumed to be small compared to the pairing energy range such that $\epsilon_c \gg |\boldsymbol{\gamma}| \forall \mathbf{k}$. With these approximations A_{ab} becomes

$$\begin{aligned} A_{ab} &= \delta_{ab} \left[\frac{2}{V} - 8N_F \ln(2e_c e^C) \langle d^{ab} \rangle_0 \right. \\ &\quad \left. - 16N_F \langle d^{ab} [1 - 2(\hat{\gamma}^z)^2] f(\rho_{\mathbf{k}}) \rangle_0 \right], \end{aligned} \quad (31)$$

whereas $K_{ab,ij}$ becomes

$$\begin{aligned} K_{ab,ij} &= \frac{N_F \beta^2 7\zeta(3)}{(2\pi)^2} \langle d^{ab} v_i v_j \rangle_0 + N'_F \frac{\ln(2e_c e^C)}{2} \langle d^{ab} m_{ij}^{-1} \rangle_0 \\ &\quad + N_F \left\{ -2 \frac{\beta^2}{\pi^2} \langle d^{ab} (\hat{\gamma}^z)^2 f_3(\rho_{\mathbf{k}}) v_i v_j \rangle_0 \right. \\ &\quad \left. + \frac{\beta^2 7\zeta(3)}{(2\pi)^2} \langle d^{ab} [1 + (\hat{\gamma}^z)^2] \partial_i |\boldsymbol{\gamma}| \partial_j |\boldsymbol{\gamma}| \rangle_0 \right. \\ &\quad \left. + \frac{\beta}{\pi} \left\langle d^{ab} \left[\frac{\rho_{\mathbf{k}}}{2e_c^2} [1 + (\hat{\gamma}^z)^2] - (\hat{\gamma}^z)^2 f_2(\rho_{\mathbf{k}}) \right] \partial_i \partial_j |\boldsymbol{\gamma}| \right\rangle_0 \right\} \end{aligned}$$

$$\begin{aligned} &+ \langle d^{ab} f(\rho_{\mathbf{k}}) g_{ij} \rangle_0 \Big\} \\ &+ N'_F \left\{ \frac{\beta}{\pi} \left\langle d^{ab} \left[f_2(\rho_{\mathbf{k}}) (\hat{\gamma}^z)^2 + \rho_{\mathbf{k}} \frac{7\zeta(3)}{4} [1 + (\hat{\gamma}^z)^2] \right] \right. \right. \\ &\quad \times (v_i \partial_j |\boldsymbol{\gamma}| + \partial_i |\boldsymbol{\gamma}| v_j) \Big\rangle_0 \\ &\quad \left. - \langle d^{ab} (\hat{\gamma}^z)^2 f(\rho_{\mathbf{k}}) m_{ij}^{-1} \rangle_0 \right\}. \end{aligned} \quad (32)$$

The energy range $[-\epsilon_c, \epsilon_c]$ is assumed to be sufficiently small such that $N_0(\xi) \approx N_F + N'_F \xi$ is a good approximation. $N_F = N_0(0)$ is the value of the density of states at the Fermi level, whereas $N'_F = N'_0(0)$ is a measure of the particle-hole asymmetry (PHA). The f functions are all convergent sums that vanish in the limit of no spin-orbit coupling defined as

$$f(\rho) = \text{Re} \sum_{n=0}^{\infty} \left(\frac{1}{2n+1+i\rho} - \frac{1}{2n+1} \right), \quad (33)$$

$$f_2(\rho) = \text{Im} \sum_{n=0}^{\infty} \frac{1}{(2n+1+i\rho)^2}, \quad (34)$$

$$f_3(\rho) = \text{Re} \sum_{n=0}^{\infty} \left(\frac{1}{(2n+1+i\rho)^3} - \frac{1}{(2n+1)^3} \right). \quad (35)$$

The dimensionless spin-orbit coupling $\rho_{\mathbf{k}} = \beta |\boldsymbol{\gamma}| / \pi$. $\zeta(\cdot)$ is the Riemann- f function and C in e^C is the Euler-Mascheroni constant. In Eq. (32) the terms are grouped such that the first is independent of both SOC and PHA, then comes a term only dependent on PHA, the bracket proportional to N_F consists of terms caused by SOC whereas the bracket proportional to N'_F consists of terms dependent on both PHA and SOC.

C. The limit of zero spin-orbit coupling

In the limit of zero spin-orbit coupling, the unit vectors $\hat{\boldsymbol{\gamma}}$ become indeterminate, however the expressions for the free energy tensors A_{ab} and $K_{ab,ij}$ still have a well-defined limit since all the unit-vector dependencies vanish. To see this, first consider the limit of $|\boldsymbol{\gamma}| \rightarrow 0$ of $\chi^{hh'}$. In this limit, the band-energies $\epsilon_{\mathbf{k}}^h \rightarrow \epsilon$ such that, after performing the sum over Matsubara frequencies, Eq. (21) becomes

$$\lim_{|\boldsymbol{\gamma}| \rightarrow 0} \chi^{hh'} = \frac{\tanh \frac{\beta \epsilon}{2}}{2\epsilon} \equiv S[\epsilon(\mathbf{k})]. \quad (36)$$

Since $\chi^{hh'}$ becomes independent of h , $\hat{\gamma}^z$ vanishes under the sum over h and h' in Eq. (20) and leaves

$$\begin{aligned} \lim_{|\boldsymbol{\gamma}| \rightarrow 0} A_{ab} &= \frac{2\delta_{ab}}{V} - 4 \sum_{\mathbf{k}} d^{ab} S[\epsilon(\mathbf{k})] \\ &= \delta_{ab} \left[\frac{2}{V} - 8I \langle d^{ab} \rangle_0 \right], \end{aligned} \quad (37)$$

for the energy integral,

$$I = \int_{-\epsilon_c}^{\epsilon_c} d\xi N_0(\xi) S[\xi] \approx N_F \ln(2e_c e^C). \quad (38)$$

This corresponds to the A_{ab} calculated in Ref. [24] if $V \rightarrow 2V$ and $8d^{ab} = \text{tr}[\Psi_a^\dagger \Psi_b]$.

In $\chi_{ij}^{hh'}$, the limit reduces $v_i^h \rightarrow v_i$ and $m_{h ij}^{-1} \rightarrow m_{ij}^{-1}$ as well as the previously mentioned limit of Fermi energies $\epsilon_{\mathbf{k}}^h \rightarrow \epsilon$ such that

$$\begin{aligned} \lim_{|\gamma| \rightarrow 0} \chi_{ij}^{hh'} &= v_i v_j \frac{1}{\epsilon} \frac{\partial^2}{\partial \epsilon^2} (\epsilon S[\epsilon]) + m_{ij}^{-1} \frac{\partial}{\partial \epsilon} S[\epsilon] \\ &\equiv 4S_2[\epsilon] v_i v_j + 2S_1[\epsilon] m_{ij}^{-1}. \end{aligned} \quad (39)$$

Since $\chi_{ij}^{hh'}$ is independent of h and h' in the zero spin-orbit limit, the second line in Eq. (23) as well as the parentheses in the first line vanish under the hh' sum. Inserting the above expression for $\lim_{|\gamma| \rightarrow 0} \chi_{ij}^{hh'}$ into $K_{ab,ij}$ and converting to Fermi-surface averages yields

$$\begin{aligned} \lim_{|\gamma| \rightarrow 0} K_{ab,ij} &= - \sum_{\mathbf{k}} d^{ab} (2S_2[\epsilon] v_i v_j + S_1[\epsilon] m_{ij}^{-1}) \\ &= -2 \langle v_i v_j d^{ab} \rangle_0 I_2 - \langle m_{ij}^{-1} d^{ab} \rangle_0 I_1 \end{aligned} \quad (40)$$

for the integrals [24],

$$I_1 = \int_{-\epsilon_c}^{\epsilon_c} d\xi N_0(\xi) S_1[\xi] \approx -\frac{N'_F}{2} \ln(2e_c e^C), \quad (41)$$

$$I_2 = \int_{-\epsilon_c}^{\epsilon_c} d\xi N_0(\xi) S_2[\xi] \approx -N_F \frac{7\beta^2 \zeta(3)}{8\pi^2}. \quad (42)$$

This corresponds to the result for $K_{ab,ij}$ found in Ref. [24] if $8d^{ab} = \text{tr}[\Psi_a^\dagger \Psi_b]$.

D. Reduction by symmetries

By considering the symmetry of the coefficients $K_{ab,ij}$ and A_{ab} , the form of the free energy density $f_{\mathbf{q}}$ in Eq. (19) can be further restricted. Assuming we have chosen a proper pseudospin representation [13], the spin-orbit coupling vector $\gamma(\mathbf{k})$ has the property,

$$\gamma(\mathbf{k}) = \tilde{R}_g \gamma(R_g^{-1} \mathbf{k}) \quad (43)$$

for proper and improper rotations g where R_g is the 3×3 rotation matrix and $\tilde{R}_g = -R_g$ for improper rotations. This relationship leads to the conclusion that $[\hat{\gamma}(\mathbf{k})^z]^2$ and $\hat{\gamma}(\mathbf{k})^2$ are invariant under all C_{4v} symmetries. This implies that $K_{aa,ii}$ and $K_{a\bar{a},ii}$ are both odd with respect to each of the components of \mathbf{k} and thus vanish under the \mathbf{k} sum. Here the notation \bar{a} means

$$\bar{a} = \begin{cases} y, & \text{if } a = x, \\ x, & \text{if } a = y. \end{cases} \quad (44)$$

Remember that $a, b, i, j \in \{x, y\}$. Using the symmetries $K_{a\bar{a},ij} = K_{\bar{a}a,ij}$ and $K_{ab,ij} = K_{ab,ji}$, the free energy density can be expressed as [3]

$$\begin{aligned} f_{\mathbf{q}} &= -\alpha(|\eta_{\mathbf{q}}^{(x)}|^2 + |\eta_{\mathbf{q}}^{(y)}|^2) \\ &+ \kappa_1 (|q^x \eta_{\mathbf{q}}^{(x)}|^2 + |q^y \eta_{\mathbf{q}}^{(y)}|^2) \\ &+ \kappa_2 (|q^y \eta_{\mathbf{q}}^{(x)}|^2 + |q^x \eta_{\mathbf{q}}^{(y)}|^2) \\ &+ \kappa_3 [(q^x \eta_{\mathbf{q}}^{(x)}) (q^y \eta_{\mathbf{q}}^{(y)})^* + \text{H.c.}] \\ &+ \kappa_4 [(q^y \eta_{\mathbf{q}}^{(x)}) (q^x \eta_{\mathbf{q}}^{(y)})^* + \text{H.c.}] \end{aligned} \quad (45)$$

for coefficients $\alpha = -A_{xx}$, $\kappa_1 = K_{xx,xx}$, $\kappa_2 = K_{xx,yy}$, and $\kappa_3 = \kappa_4 = K_{xy,xy}$. Rotating the coordinate system such that

$$\begin{pmatrix} q^x \\ q^y \end{pmatrix} = \begin{pmatrix} \cos \theta & -\sin \theta \\ \sin \theta & \cos \theta \end{pmatrix} \begin{pmatrix} \tilde{q}^x \\ \tilde{q}^y \end{pmatrix}, \quad (46)$$

defining the chiral basis of the order parameters as

$$\begin{pmatrix} \eta^+ \\ \eta^- \end{pmatrix} = \frac{1}{\sqrt{2}} \begin{pmatrix} 1 & i \\ 1 & -i \end{pmatrix} \begin{pmatrix} \eta^{(E_y)} \\ \eta^{(E_x)} \end{pmatrix}, \quad (47)$$

as well as using dimensionless variables [19], the free energy density can be further reduced to the form

$$\begin{aligned} f_{\mathbf{q}} &= -(|\eta_{\mathbf{q}}^+|^2 + |\eta_{\mathbf{q}}^-|^2) + |\tilde{\eta}_{\mathbf{q}}^+|^2 + |\tilde{\eta}_{\mathbf{q}}^-|^2 \\ &+ \text{Re}\{[e^{i2\theta}(v + \Delta) + e^{-i2\theta}(1 - \Delta)][\tilde{q}^x \eta_{\mathbf{q}}^+ (\tilde{q}^y \eta_{\mathbf{q}}^-)^* \\ &- \tilde{q}^y \eta_{\mathbf{q}}^+ (\tilde{q}^y \eta_{\mathbf{q}}^-)^*]\} \\ &+ \text{Im}\{[e^{-i2\theta}(v + \Delta) - e^{i2\theta}(1 - \Delta)][\tilde{q}^x \eta_{\mathbf{q}}^- (\tilde{q}^y \eta_{\mathbf{q}}^+)^* \\ &+ \tilde{q}^y \eta_{\mathbf{q}}^- (\tilde{q}^x \eta_{\mathbf{q}}^+)^*]\}. \end{aligned} \quad (48)$$

Here the dimensionless parameters are $\Delta = 2(\kappa_2 - \kappa_3)/(\kappa_1 + \kappa_2)$ and $v = (\kappa_1 - 3\kappa_2)/(\kappa_1 + \kappa_2)$ [19]. In the above expression, the parameter Δ is new compared to the expression in Ref. [19] and is necessary because of the additional contributions to $K_{ab,ij}$ in Eq. (32) as will be discussed below. Dimensionless variables were introduced by the substitution,

$$\begin{pmatrix} \eta \\ \tilde{\eta} \end{pmatrix} \rightarrow \begin{pmatrix} \eta/\sqrt{\alpha} \\ \sqrt{\frac{2\alpha}{\kappa_1 + \kappa_2}} \tilde{\eta} \end{pmatrix}. \quad (49)$$

Choosing $\theta = 0$ and transforming to real space yields a free energy density of the form

$$\begin{aligned} f_{\text{GL}} &= -(|\eta^+|^2 + |\eta^-|^2) + |\mathbf{D}\eta^+|^2 + |\mathbf{D}\eta^-|^2 + (v + 1) \\ &\times \text{Re}\{[D_x \eta^+ (D_x \eta^-)^* - D_y \eta^+ (D_y \eta^-)^*]\} \\ &+ (v - 1 + 2\Delta) \text{Im}\{[D_x \eta^- (D_y \eta^+)^* \\ &+ D_y \eta^- (D_x \eta^+)^*]\}. \end{aligned} \quad (50)$$

Here D_i stands for a dimensionless gradient in the i direction in real space, and the space dependence of the order parameter is implicit.

IV. SUMMARY

Mixed gradient terms in a Ginzburg-Landau free energy are defined as terms of the form $(D_x \eta^+)^* D_y \eta^-$ [21], i.e., terms mixing different components and directional gradients. These terms drive the subdominant component of a chiral p -wave superconductor that exists in the core of topological defects, such as vortices when a magnetic field breaks the degeneracy between the superconducting components. The core structures of vortices are also influenced by these terms in that the structures of the terms determine the relative phase of the two order parameters and thus the different kinds of vortices possible [20,21]. It is evident from the definition that the order parameter needs multiple components for such terms to be present. The number of components of the order parameter depends on the number of dimensions of the irreducible representations that the pairing interaction furnishes. If the symmetry group contains a two-dimensional irreducible representation and the

interaction contains this irrep. as a subspace of its eigenvalue space, then the order parameter associated with this subspace has two components. In the weak-coupling BCS framework this discussion is based on, on-site Hubbard interaction on a square 2D lattice in the clean limit only consists of the one-dimensional *s*-wave representation. If spin-orbit coupling is included as a symmetry-breaking field, then the gap function is rotated in the new basis so that it gains a momentum dependence determined by the SOC spin texture [13,32]. In the case of Rashba spin-orbit coupling, the transformation is such that the intracomponent elements of the gap function and thus the pairing amplitude in the spin-orbit split bands and gains a *p*-wave-like momentum dependence. Such systems could thus be called effective *p*-wave superconductors [33], however their topological properties are different from those of true triplet *p*-wave superconductors and, importantly, the order parameter does not gain additional components. For the 2D square lattice, this means that a pairing interaction that acts at least as far as nearest-neighbor lattice sites is necessary for a multicomponent order parameter to be present. This type of interaction was also found to be sufficient to contain a two-dimensional subspace given by the *p*-wave irreducible representation basis vectors.

The two mixed gradient terms found in the Ginzburg-Landau free energy f_{GL} are determined by two phenomenological parameters $\Delta = 2(\kappa_2 - \kappa_3)/(\kappa_1 + \kappa_2)$ and $v = (\kappa_1 - 3\kappa_2)/(\kappa_1 + \kappa_2)$ where $\kappa_1 = K_{xx,xx}$, $\kappa_2 = K_{xx,yy}$, and $\kappa_3 = K_{xy,xy}$ for the generalized effective mass tensor $K_{ab,ij}$.

If both SOC and the particle-hole asymmetry are set to zero, and we assume nearest-neighbor hopping, $K_{ab,ij}$ reduces to

$$K_{ab,ij} = \zeta_{ab} \frac{N_F \beta^2 7\zeta(3)}{(4\pi)^2 N_F t^2} \langle v_a v_b v_i v_j \rangle_0, \quad (51)$$

where $\zeta_{ab} = (-1)^{\delta_{ab}-1}$. With this reduction, v can be written as

$$v = \frac{\langle v_x^4 \rangle_0 - 3\langle v_x^2 v_y^2 \rangle_0}{\langle v_x^4 \rangle_0 + \langle v_x^2 v_y^2 \rangle_0}, \quad (52)$$

as in Refs. [19,20] and is thus a measure of the Fermi-surface anisotropy. The coefficient in front of the last mixed gradient term becomes ≥ 0 and proportional to $\langle v_x^2 v_y^2 \rangle_0$. It will therefore exist as long as there is superconducting order, and the Fermi velocity does not vanish. The coefficient in front of the first mixed gradient term is, on the other hand, $(v+1)$. From Eq. (52) we see that for a completely anisotropic square Fermi-surface $v = -1$ such that this term vanishes. The remaining term can in this case be rotated away by a rotation of the order parameter components as in Refs. [22].

With the simplification of $K_{ab,ij}$ in Eq. (51), the parameter Δ becomes $\Delta = -(v-1)$ and the form of f_{GL} reduces to that of Ref. [19] except for a minus sign. This discrepancy originates with the choice made for the basis of the *p*-wave subspace. To get equality, you would simply choose both eigenvectors positive in Eq. (9), which would yield an irreducible representation equivalent to E . Then $K_{ab,ij}$ would reduce in the same way except missing the factor ζ_{ab} such that $\Delta = 0$ and f_{GL} would reduce to the same form.

If the particle-hole asymmetry given by N'_F is present, $K_{ab,ij}$ gains a contribution from the Fermi-surface average $\langle v_a v_b m_{ij}^{-1} \rangle_0$. For nearest-neighbor hopping, m_{ij}^{-1} is diagonal such that κ_3 is not affected by it, however because of its contribution to κ_1 and κ_2 the terms get rescaled. In the continuum limit this leads to increasing coefficients for the mixed gradient terms compared to the normal kinetic terms in the free energy.

In the continuum limit v is expected to vanish by Eq. (52) since the Fermi surface becomes isotropic. However, including Rashba spin-orbit coupling with a SOC vector of the form $\gamma = \alpha(\mathbf{k}_y \hat{e}_x - \mathbf{k}_x \hat{e}_y)$ leads to

$$v \approx \frac{1}{2} \left(\frac{\alpha}{k_F} \right)^2, \quad (53)$$

where $t > 0$ is the nearest-neighbor hopping amplitude and k_F is the Fermi wave-vector magnitude because of the contribution to the κ coefficients from the term $N_F \langle d^{ab} g_{ij} \rangle_0$ in $K_{ab,ij}$. From this result we conclude that v is no longer only a measure of Fermi-surface anisotropy, but also a measure of spin-orbit coupling strength. The coefficient in front of the last mixed gradient term in Eq. (50) now becomes $1/(1-v)$, whereas the other mixed gradient term coefficient is $1+v$ for the choice $\theta = 0$. This shows that, in the continuum limit, the mixed gradient terms become more prominent compared to the normal gradient terms as the Rashba spin-orbit coupling strength increases.

ACKNOWLEDGMENTS

F.N.K. was supported by a NTNU University grant and thanks S. Rex for useful discussions. A.S. was supported by the Research Council of Norway through Grant No. 250985, “Fundamentals of Low-dissipative Topological Matter,” and Center of Excellence Grant No. 262633, Center for Quantum Spintronics.

APPENDIX A: SYMMETRIES OF THE SINGLE-PARTICLE PROBLEM

Combining the two different spin options for the annihilation operators in Eq. (1) in a vector $\hat{\mathbf{c}}_{\mathbf{k}}$, then under time-reversal $\hat{\theta}$, the operators transform as [34]

$$\hat{\theta} \hat{\mathbf{c}}_{\mathbf{k}} \hat{\theta}^{-1} = i\sigma^y \hat{\mathbf{c}}_{-\mathbf{k}}, \quad (A1a)$$

$$\hat{\theta} \hat{\mathbf{c}}_{\mathbf{k}}^\dagger \hat{\theta}^{-1} = \hat{\mathbf{c}}_{-\mathbf{k}}^\dagger (-i\sigma^y). \quad (A1b)$$

Since $\hat{\theta}$ contains a conjugation operator, the time-reversal of the single-particle Hamiltonian in Eq. (1) becomes

$$\begin{aligned} \hat{\theta} \hat{H}_0 \hat{\theta}^{-1} &= \sum_{\mathbf{k}} \hat{\theta} \hat{\mathbf{c}}_{\mathbf{k}}^\dagger \hat{\theta}^{-1} [\epsilon(\mathbf{k})^* + \gamma(\mathbf{k})^* \cdot \boldsymbol{\sigma}^*] \hat{\theta} \hat{\mathbf{c}}_{\mathbf{k}} \hat{\theta}^{-1} \\ &= \sum_{\mathbf{k}} \hat{\mathbf{c}}_{-\mathbf{k}}^\dagger [\epsilon(\mathbf{k})^* + \gamma(\mathbf{k})^* \cdot (-i\sigma^y) \boldsymbol{\sigma}^* (i\sigma^y)] \hat{\mathbf{c}}_{-\mathbf{k}} \\ &= \sum_{\mathbf{k}} \hat{\mathbf{c}}_{\mathbf{k}}^\dagger [\epsilon(-\mathbf{k})^* - \gamma(-\mathbf{k})^* \cdot \boldsymbol{\sigma}] \hat{\mathbf{c}}_{\mathbf{k}}. \end{aligned} \quad (A2)$$

If the Hamiltonian should be time-reversal invariant, then the coefficients must have the symmetries $\epsilon(\mathbf{k}) = \epsilon(-\mathbf{k})^*$ and

TABLE I. Character table for the group C_{4v} . The first row gives the conjugation classes, whereas the first column denotes the different irreducible representations. Note that E is the only two-dimensional irreducible representation.

C_{4v}	e	C_4^2	$2C_4$	$2\sigma_v$	$2\sigma_d$
A_1	1	1	1	1	1
A_2	1	1	1	-1	-1
B_1	1	1	-1	1	-1
B_2	1	1	-1	-1	1
E	2	-2	0	0	0

$\gamma(\mathbf{k}) = -\gamma(-\mathbf{k})^*$. Since the Pauli matrices are self-adjoint, taking the adjoint of \hat{H}_0 yields

$$\hat{H}_0^\dagger = \sum_{\mathbf{k}} \hat{\mathbf{c}}_{\mathbf{k}}^\dagger [\epsilon(\mathbf{k})^* + \gamma(\mathbf{k})^* \cdot \boldsymbol{\sigma}] \hat{\mathbf{c}}_{\mathbf{k}}. \quad (\text{A3})$$

If the Hamiltonian should be Hermitian, then the coefficients must satisfy $\epsilon(\mathbf{k}) = \epsilon(\mathbf{k})^*$ and $\gamma(\mathbf{k}) = \gamma(\mathbf{k})^*$. Time-reversal invariance together with Hermiticity thus implies that the coefficients are real, that $\epsilon(\mathbf{k})$ is even in \mathbf{k} , and that $\gamma(\mathbf{k})$ is odd in \mathbf{k} , which were the symmetries mentioned in Sec. II A.

APPENDIX B: DIAGONALIZATION OF THE SINGLE-PARTICLE PROBLEM

It is easily verified through substitution that the basis defined in Eq. (2) diagonalizes the Hamiltonian in Eq. (1) as long as $|\hat{\gamma}^z| \neq 1$, regardless of whether \hat{H}_0 is Hermitian or time-reversal invariant. This means that the same diagonalization is used when γ represents spin-orbit coupling (time-reversal invariant but not parity invariant), and when it represents an external magnetic field (parity invariant but not time-reversal invariant). The matrix determining the basis in Eq. (2) is found by solving the characteristic equation of the corresponding linear-algebra problem and finding the normal eigenvectors that correspond to each eigenvalue.

In the case that $\gamma(\mathbf{k}) \parallel \hat{e}_z$ the basis transformation instead reads

$$\mathbf{a}_{\mathbf{k}} = \frac{1}{2} \begin{pmatrix} (1 + \hat{\gamma}^z)e^{i\phi_+} & (1 - \hat{\gamma}^z)e^{i\phi_-} \\ (1 - \hat{\gamma}^z)e^{i\phi_+} & (1 + \hat{\gamma}^z)e^{i\phi_-} \end{pmatrix}^\dagger \mathbf{c}_{\mathbf{k}}. \quad (\text{B1})$$

This results in the same expression for the eigenvalues $\epsilon_{\mathbf{k}}^h = \epsilon(\mathbf{k}) + h|\gamma(\mathbf{k})|$ as is obtained from the basis transformation in Eq. (1).

APPENDIX C: BASIS VECTOR FOR THE IRREDUCIBLE REPRESENTATION E OF C_{4v}

The group of symmetry transformations of the two-dimensional square lattice is denoted C_{4v} in the Schönflies notation or $4mm$ in the abbreviated Hermann-Mauguin notation [27]. In Ref. [27] the character table of C_{4v} is as shown in Table I. For the one-dimensional irreps. the matrix elements of the representation are the characters themselves. For the two-dimensional irrep. E , the matrix elements of the

representation are given by

$$\begin{aligned} D^{(E)}(e) &= \begin{pmatrix} 1 & 0 \\ 0 & 1 \end{pmatrix}, \\ D^{(E)}(C_4^2) &= \begin{pmatrix} -1 & 0 \\ 0 & -1 \end{pmatrix}, \\ D^{(E)}(C_4) &= \begin{pmatrix} 0 & -1 \\ 1 & 0 \end{pmatrix}, \\ D^{(E)}(C_4^{-1}) &= \begin{pmatrix} 0 & 1 \\ -1 & 0 \end{pmatrix}, \\ D^{(E)}(\sigma_x) &= \begin{pmatrix} -1 & 0 \\ 0 & 1 \end{pmatrix}, \\ D^{(E)}(\sigma_y) &= \begin{pmatrix} 1 & 0 \\ 0 & -1 \end{pmatrix}, \\ D^{(E)}(\sigma_{d_1}) &= \begin{pmatrix} 0 & -1 \\ -1 & 0 \end{pmatrix}, \\ D^{(E)}(\sigma_{d_2}) &= \begin{pmatrix} 0 & 1 \\ 1 & 0 \end{pmatrix}. \end{aligned} \quad (\text{C1})$$

This can be verified by calculating the traces of the matrices $\chi^{(E)}(g)$ and showing that they satisfy the condition,

$$\sum_{g \in C_{4v}} |\chi^{(E)}(g)|^2 = |C_{4v}|, \quad (\text{C2})$$

which imply that this is an irreducible representation as well as showing that the matrices satisfy the group multiplication relations for group elements in C_{4v} .

Since the goal is to find a basis for this representation E consisting of eigenvectors of the Hermitian operator \hat{V} , these basis vectors can be written in the form of Eq. (6), repeated here for convenience,

$$|d\rangle = \sum_{\mathbf{k}, s_1 s_2} d_{s_1 s_2}(\mathbf{k}) |\mathbf{k}, s_1\rangle |-\mathbf{k}, s_2\rangle. \quad (\text{C3})$$

This eigenvector space is projected down on the irreducible subspace of the irreducible representation by the projection operator in Eq. (8). This operator includes the symbol g : which means that the state should be transformed by the group-element g . For spin-momentum eigenstates, the transformation law is given by [34]

$$g: |\mathbf{k}', s'\rangle = \sum_s |g\mathbf{k}', s\rangle D_{gss'} \quad (\text{C4})$$

for the matrix,

$$D_{gss'} = \delta_{ss'} \cos(\phi/2) - i \hat{\mathbf{u}} \cdot \boldsymbol{\sigma}_{ss'} \sin(\phi/2), \quad (\text{C5})$$

where the rotation given by the angle and normal vector $(\phi, \hat{\mathbf{u}})$ is given by the proper rotation associated with g . The transformation of vectors in the product space of two spin-momentum eigenstates is thus given by

$$g: |\mathbf{k}'_1, s'_1\rangle |\mathbf{k}'_2, s'_2\rangle = \sum_{s_1 s_2} |g\mathbf{k}'_1, s_1\rangle |g\mathbf{k}'_2, s_2\rangle D_{gs_1 s'_1} D_{gs_2 s'_2}. \quad (\text{C6})$$

Writing this as an active transformation where the transformation acts on the coefficients of the eigenvectors in Eq. (C3)

results in

$$g \cdot d_{s_1 s_2}(\mathbf{k}) = \sum_{s'_1 s'_2} D_{gs_2 s'_2} D_{gs_1 s'_1} d_{s'_1 s'_2}(g^{-1}\mathbf{k}). \quad (\text{C7})$$

Coefficients that are odd in \mathbf{k} can be written as

$$d_{s_1 s_2}(\mathbf{k}) = \mathbf{d}(\mathbf{k}) \cdot (\sigma i \sigma^y)_{s_1 s_2}, \quad (\text{C8})$$

because of fermionic particle exchange asymmetry. The transformation rule in Eq. (C7) is then simplified to

$$g \cdot \mathbf{d}(\mathbf{k}) = R(\hat{\mathbf{u}}, \phi) \mathbf{d}(g^{-1}\mathbf{k}), \quad (\text{C9})$$

where R is the conventional 3×3 rotation matrix, which shows that \mathbf{d} transforms as a vector. Since the \mathbf{k} dependency of $\mathbf{d}(\mathbf{k})$ must be such that it is invariant with respect to translations by reciprocal lattice vectors it can be expanded as a Fourier series in the fundamental lattice vectors \mathbf{R} such that

$$\mathbf{d}(\mathbf{k}) = \frac{1}{\sqrt{N}} \sum_{\mathbf{R}} \beta_{\mathbf{R}} \sin \mathbf{R} \cdot \mathbf{k}. \quad (\text{C10})$$

Applying the projection operators in Eq. (8) onto $\mathbf{d}(\mathbf{k})$ using the transformation law in Eq. (C9) and the matrix elements of the representation given in Eq. (C2), the \hat{x} and \hat{y} components of β vanish leaving

$$P_{ll}^{(E)} \mathbf{d}(\mathbf{k}) = \frac{\hat{\mathbf{z}}}{2\sqrt{N}} \sum_{\mathbf{R}} \beta_{\mathbf{R}}^z [\sin(\mathbf{R} \cdot \mathbf{k}) + (-1)^l \sin(\hat{\mathbf{z}} \cdot \mathbf{R} \times \mathbf{k})]. \quad (\text{C11})$$

This expression implies immediately that the simplest potential that contains a nonvanishing representation E is a nearest-neighbor potential where $\mathbf{R} \in \{(0, \pm 1), (\pm 1, 0)\}$. Inserting these possible lattice vectors \mathbf{R} in the sum $\sum_{\mathbf{R}}$ in Eq. (C11), vectors in the projected space can be written

$$P_{ll}^{(E)} \mathbf{d}(\mathbf{k}) = \frac{\hat{\mathbf{z}}}{2\sqrt{N}} \{ (\beta_{(1,0)}^z - \beta_{(-1,0)}^z) [\sin k_x + (-1)^l \sin k_y] + (\beta_{(0,1)}^z - \beta_{(0,-1)}^z) [\sin k_y - (-1)^l \sin k_x] \}. \quad (\text{C12})$$

Such vectors can clearly all be written using the basis vectors made up of

$$\mathbf{d}_{\pm}(\mathbf{k}) = \hat{\mathbf{z}} (\sin k_x \pm \sin k_y). \quad (\text{C13})$$

Although this is a basis for the irreducible vector space associated with the irreducible representation E , it does not transform as the matrices given in Eq. (C2). Recall that a basis $\{b_i\}$ for a representation D transforms according to

$$g \cdot b_i = \sum_j b_j D_{ji}(g). \quad (\text{C14})$$

Instead $\{\mathbf{d}_{\pm}\}$ transforms like an equivalent representation to the matrices in Eq. (C2). This is simply solved by rotating the basis into new basis vectors,

$$\mathbf{d}^{(E_y)}(\mathbf{k}) = -\hat{\mathbf{z}} \sin k_y, \quad (\text{C15a})$$

$$\mathbf{d}^{(E_x)}(\mathbf{k}) = +\hat{\mathbf{z}} \sin k_x, \quad (\text{C15b})$$

which when properly normalized gives the basis set in Eq. (9).

APPENDIX D: SPECTRAL DECOMPOSITION OF NEAREST-NEIGHBOR INTERACTION

To find the representations the potential in Eq. (10) consists of, first it is Fourier transformed into

$$\hat{V} = - \sum_{\mathbf{q} \mathbf{k} \mathbf{k}' s} \tilde{V}(\mathbf{k} - \mathbf{k}') \times c_{(\mathbf{q}/2) + \mathbf{k}, s}^\dagger c_{(\mathbf{q}/2) - \mathbf{k}, -s}^\dagger c_{(\mathbf{q}/2) - \mathbf{k}', -s} c_{(\mathbf{q}/2) + \mathbf{k}', s} \quad (\text{D1})$$

for

$$\tilde{V}(\mathbf{k} - \mathbf{k}') = \frac{V}{2N} \sum_{\delta} e^{\delta \cdot (\mathbf{k} - \mathbf{k}')}, \quad (\text{D2})$$

where δ sums over nearest-neighbor lattice vectors. The spectral decomposition of \hat{V} is found by expressing \hat{V} in terms of its eigenvectors. Since \hat{V} is a two-body operator, it is completely determined by the matrix elements $\langle \alpha \beta | \hat{V} | \alpha' \beta' \rangle$ where $|\alpha \beta\rangle$ are states in the two-particle Hilbert space. For BCS-type potentials this two-particle Hilbert space consists of states where the particles have opposite momentum and any eigenvector can thus be expanded as in Eq. (6). This means that in terms of spin-momentum eigenstates, the potential can be written as

$$\hat{V} = \frac{1}{2} \sum_{\mathbf{q} \mathbf{k} \mathbf{k}' s_1 s_2 s_3 s_4} V_{\mathbf{k}, \mathbf{k}'; s_1 s_2 s_3 s_4} \times c_{(\mathbf{q}/2) + \mathbf{k}, s_1}^\dagger c_{(\mathbf{q}/2) - \mathbf{k}, s_2}^\dagger c_{(\mathbf{q}/2) - \mathbf{k}', s_4} c_{(\mathbf{q}/2) + \mathbf{k}', s_3} \quad (\text{D3})$$

for the matrix elements,

$$V_{\mathbf{k}, \mathbf{k}'; s_1 s_2 s_3 s_4} = \langle \mathbf{k}, s_1 | \langle -\mathbf{k}, s_2 | \hat{V} | \mathbf{k}', s_3 \rangle | -\mathbf{k}', s_4 \rangle = -2 \tilde{V}(\mathbf{k} - \mathbf{k}') \delta_{s_1 s_3} \delta_{s_2 s_4} \sigma_{s_1 s_2}^x. \quad (\text{D4})$$

The space associated with a single eigenvalue can in general be written as a sum of irreducible spaces where each irreducible space consists of basis vectors forming a basis for an irreducible representation of the symmetry group [27]. If the space consists of several irreducible representations, these are said to have accidental symmetry since the fact that vectors belonging to two different irreducible spaces have the same eigenvalue is not necessary by symmetry and thus, in a sense, accidental. Writing the basis vectors for an irreducible representation Γ as $|\Gamma, m_\Gamma\rangle$ where m_Γ enumerates the dimensions of the irrep., this implies that $\{|\Gamma, m_\Gamma\rangle\}$ is a complete orthonormal basis set. Inserting this complete set on either side of the potential operator, in the space of two-particle states the potential can be represented by

$$\hat{V} = \sum_{\Gamma} V_{\Gamma} \sum_{m=1}^{d_{\Gamma}} |\Gamma, m_{\Gamma}\rangle \langle \Gamma, m_{\Gamma}| \quad (\text{D5})$$

for the eigenvectors,

$$V_{\Gamma} = \langle \Gamma, m_{\Gamma} | \hat{V} | \Gamma, m_{\Gamma} \rangle. \quad (\text{D6})$$

Note that it does not matter which of the d_{Γ} different basis vectors one inserts for m_{Γ} since all will give the same eigenvalue as long as they are basis vectors in the same irreducible space. These eigenvalues can then be evaluated by inserting a

complete set of spin-momentum eigenstates as

$$V_\Gamma = \sum_{\mathbf{k}\mathbf{k}'} \sum_{s_1 s_2 s_3 s_4} V_{\mathbf{k}, \mathbf{k}'; s_1 s_2 s_3 s_4} \\ \times (d_{\mathbf{k}, s_1 s_2}^{(\Gamma, m_\Gamma)})^* d_{\mathbf{k}', s_3 s_4}^{(\Gamma, m_\Gamma)}. \quad (\text{D7})$$

Inserting the irreducible representation basis vectors in Eqs. (13), (12), and (9) yield the eigenvalues,

$$V_{A_1} = V_{B_1} = V_{E_x} = V_{E_y} = -V. \quad (\text{D8})$$

Conversely, Eq. (D5) may be inserted into Eq. (D4) such that the spin-momentum eigenstate matrix elements can be written as

$$V_{\mathbf{k}, \mathbf{k}'; s_1 s_2 s_3 s_4} = \sum_{\Gamma} V_\Gamma \sum_{m_\Gamma=1}^{d_\Gamma} d_{\mathbf{k}, s_1 s_2}^{(\Gamma, m_\Gamma)} (d_{\mathbf{k}', s_3 s_4}^{(\Gamma, m_\Gamma)})^*. \quad (\text{D9})$$

If all the eigenvectors given by irreducible representations have been accounted for, this must reproduce Eq. (D1). Inserting the singlet irreducible irreducible representations with even functions $\psi^{(a)}(\mathbf{k})$ as well as the triplet irreducible basis vectors with odd vector functions $\mathbf{d}^{(E_i)}(\mathbf{k})$ from Eqs. (13), (12), and (9) yield

$$\hat{V} = -V \sum_{\mathbf{q} \mathbf{k} \mathbf{k}' s} \left(\sum_{a=A_1, B_1} \psi^{(a)}(\mathbf{k}) \psi^{(a)}(\mathbf{k}')^* \right. \\ \left. + \sum_{i=x, y} d_z^{(E_i)}(\mathbf{k}) d_z^{(E_i)}(\mathbf{k}')^* \right) \\ \times c_{(\mathbf{q}/2)+\mathbf{k}, s}^\dagger c_{(\mathbf{q}/2)-\mathbf{k}, -s}^\dagger c_{(\mathbf{q}/2)-\mathbf{k}', -s} c_{(\mathbf{q}/2)+\mathbf{k}', s} \\ = -\frac{V}{N} \sum_{\mathbf{q} \mathbf{k} \mathbf{k}' s} \tilde{V}(\mathbf{k} - \mathbf{k}') \\ \times c_{(\mathbf{q}/2)+\mathbf{k}, s}^\dagger c_{(\mathbf{q}/2)-\mathbf{k}, -s}^\dagger c_{(\mathbf{q}/2)-\mathbf{k}', -s} c_{(\mathbf{q}/2)+\mathbf{k}', s}, \quad (\text{D10})$$

which indeed is the initial potential presented in Eq. (D1). This shows that Eq. (11) is the diagonalized form of Eq. (10) and the nearest-neighbor interaction thus consists of the irreducible representations A_1 , B_1 , and E which correspond to the extended s -wave, d -wave, and p -wave channels, respectively.

APPENDIX E: INTEGRATION OVER FERMIONS

The single-particle problem Hamiltonian \hat{H}_0 defined in Eq. (1) and interaction potential \hat{V} defined in Eq. (4) for b equal to the two-dimensional irreducible representation E of C_{4v} with eigenvectors given in Eq. (9) defines the relevant system. The finite temperature partition function for this system can then be written as a path integral over Grassmann fields ξ and ξ^* as

$$Z = \int \mathcal{D}[\xi^* \xi] e^{-S}, \quad (\text{E1})$$

for the action,

$$S = \int_0^\beta d\tau \left\{ \sum_{\mathbf{k} s s'} \xi_{\mathbf{k}, s}^* \{ \delta_{ss'} [\partial_\tau + \epsilon(\mathbf{k})] + \boldsymbol{\gamma} \cdot \boldsymbol{\sigma}_{ss'} \} \xi_{\mathbf{k}, s'} \right. \\ \left. - \frac{V}{2} \sum_{\mathbf{q} m} J_{\mathbf{q}}^{m*} J_{\mathbf{q}}^m \right\}, \quad (\text{E2})$$

where $J_{\mathbf{q}}^m$'s are defined in Eq. (15). By Hubbard-Stratonovich transforming the interaction potential exponential at the expense of introducing new auxiliary complex fields $\eta_{\mathbf{q}}^{(m)}$ and $\eta_{\mathbf{q}}^{(m)*}$ as in Eq. (14), the partition function can be factorized into a path integral over the auxiliary fields and a path integral over the quadratic fermionic Grassmann fields by

$$Z = \int \mathcal{D}[\eta^* \eta] \exp \left[- \int_0^\beta d\tau \sum_{\mathbf{q} m} \frac{2|\eta_{\mathbf{q}}^{(m)}|^2}{V} \right] Z_F, \quad (\text{E3})$$

such that

$$Z_F = \int \mathcal{D}[\xi^* \xi] e^{-S_F}. \quad (\text{E4})$$

Because of the Hubbard-Stratonovich transformation, the fermionic action S_F now consists of only quadratic combination of Grassmann fields where one part of it comes from the single-particle problem on the first line of Eq. (E2) and the other is proportional with the new complex fields η . To simplify the calculation, the Grassmann fields are transformed through Eq. (2) to the helicity basis in which the single-particle Hamiltonian is diagonal. Denoting the unitary matrix in the transformation in Eq. (2), $U(\mathbf{k})_{sh}$ such that

$$\xi_{\mathbf{k}s} = \sum_h U(\mathbf{k})_{sh} \zeta_{\mathbf{k}h}, \quad (\text{E5})$$

the fermionic action S_F can be written

$$S_F = \int_0^\beta d\tau \left\{ \sum_{\mathbf{k} h} \zeta_{\mathbf{k}h}^* (\partial_\tau + \epsilon_{\mathbf{k}}^h) \zeta_{\mathbf{k}h} \right. \\ \left. + \sum_{\substack{\mathbf{k}_1 \mathbf{k}_2 \\ h_1 h_2 m}} [\eta_{\mathbf{k}_1 + \mathbf{k}_2}^{(m)} \tilde{d}_{\mathbf{k}_1 \mathbf{k}_2; h_1 h_2}^{(E_m)} \zeta_{\mathbf{k}_1 h_1}^* \zeta_{\mathbf{k}_2 h_2}^* \right. \\ \left. + \eta_{\mathbf{k}_1 + \mathbf{k}_2}^{(m)*} (\tilde{d}_{\mathbf{k}_1 \mathbf{k}_2; h_1 h_2}^{(E_m)})^* \zeta_{\mathbf{k}_2 h_2} \zeta_{\mathbf{k}_1 h_1}] \right\}, \quad (\text{E6})$$

where in the last equality we have inserted the helicity basis and defined the helicity transformed irrep. basis vectors,

$$\tilde{d}_{\mathbf{k}_1 \mathbf{k}_2; h_1 h_2}^{(E_m)} = \sum_{s_1 s_2} d_{s_1 s_2}^{(E_m)} \left(\frac{\mathbf{k}_1 - \mathbf{k}_2}{2} \right) U(\mathbf{k}_2)_{s_2 h_2}^* U(\mathbf{k}_1)_{s_1 h_1}^*. \quad (\text{E7})$$

The imaginary-time dependence of the ζ fields is expanded in a series of Matsubara frequencies through the unitary transformation,

$$\zeta_{\mathbf{k}h}(\tau) = \frac{1}{\sqrt{\beta}} \sum_n e^{-i\tau\omega_n} \zeta_{\mathbf{k}hn}, \quad (\text{E8})$$

for $\omega_n = (2n+1)\pi/\beta$. This expansion results in a remaining time dependence in the auxiliary complex fields $\eta(\tau)$ which is itself transformed into a bosonic Matsubara-frequency dependence through the identification,

$$\frac{1}{\beta} \int_0^\beta d\tau \eta_{\mathbf{k}_1 + \mathbf{k}_2}^{(m)}(\tau) e^{i\tau(\omega_{n_1} + \omega_{n_2})} = \eta_{\mathbf{k}_1 + \mathbf{k}_2, n_1 + n_2 + 1}^{(m)}. \quad (\text{E9})$$

In the single-particle Hamiltonian, this transformation exchanges the ∂_τ for $-i\omega_{n_2}$. The fermionic action is now written

as a bilinear form

$$S_F = \frac{1}{2} \sum_{\substack{\mathbf{k}_1 \mathbf{k}_2 \\ n_1 n_2}} \zeta_{\mathbf{k}_1 n_1}^T \check{A}_{\mathbf{k}_1 \mathbf{k}_2, n_1 n_2} \zeta_{\mathbf{k}_2 n_2}, \quad (\text{E10})$$

through the 4×4 matrix \check{A} by collecting the fermionic fields in four-component vectors,

$$\zeta_{\mathbf{k}n}^T = (\zeta_{\mathbf{k}+n}, \zeta_{\mathbf{k}-n}, \zeta_{\mathbf{k}+n}^*, \zeta_{\mathbf{k}-n}^*). \quad (\text{E11})$$

Since each vector contains all the different Grassmann fields (both fields ζ and ζ^*), the integral becomes the Pfaffian of the antisymmetric component of \check{A} [35]. Reusing the notation \check{A} for this antisymmetric component, the fact that the Pfaffian of an antisymmetric matrix can be expressed as the square root of the determinant of this matrix [36], is used to write

$$Z_F = \text{Pf}(\check{A}) = \pm \sqrt{\det(\check{A})} = \exp\left(\frac{1}{2} \text{Tr} \ln \check{A}\right). \quad (\text{E12})$$

The limit of zero spin-orbit coupling is used to argue that $+$ should be used in front of the square root. The fact that exchanging two rows of a matrix leaves the determinant invariant is then used to write S_F as the familiar sesquilinear form

$$S_F = \frac{1}{2} \sum_{\substack{\mathbf{k}_1 \mathbf{k}_2 \\ n_1 n_2}} \zeta_{\mathbf{k}_1 n_1}^\dagger (\check{G}^{-1})_{\mathbf{k}_1 \mathbf{k}_2, n_1 n_2} \zeta_{\mathbf{k}_2 n_2}, \quad (\text{E13})$$

where the inverse Gor'kov Green's-function \check{G}^{-1} is expressed as

$$\check{G}^{-1} = \check{G}_0^{-1} + \check{\phi}. \quad (\text{E14})$$

The two terms represent the inverse mean-field Green's function,

$$(\check{G}_0^{-1})_{\mathbf{k}_1 \mathbf{k}_2, n_1 n_2} = \delta_{\mathbf{k}_1 \mathbf{k}_2} \delta_{n_1 n_2} \times \begin{pmatrix} -i\omega_{n_1} + \epsilon_{\mathbf{k}_1}^+ & 0 \\ 0 & -i\omega_{n_1} + \epsilon_{\mathbf{k}_1}^- \end{pmatrix} \otimes \sigma^z, \quad (\text{E15})$$

and the order-parameter-dependent 4×4 matrix,

$$(\check{\phi})_{\mathbf{k}_1 \mathbf{k}_2, n_1 n_2} = 2 \sum_m \sum_n \delta_{n, n_1 + n_2 + 1} \times \begin{pmatrix} 0 & \eta_{\mathbf{k}_1 + \mathbf{k}_2, n}^{(m)} D_{\mathbf{k}_2 \mathbf{k}_1}^{(m)\dagger} \\ \eta_{\mathbf{k}_1 + \mathbf{k}_2, n}^{(m)*} D_{\mathbf{k}_2 \mathbf{k}_1}^{(m)} & 0 \end{pmatrix}, \quad (\text{E16})$$

where the 2×2 matrix $D_{\mathbf{k}_1 \mathbf{k}_2}^{(m)}$ consists of the transformed irrep. basis vectors,

$$(D_{\mathbf{k}_1 \mathbf{k}_2}^{(m)})_{h_1 h_2} = \tilde{d}_{\mathbf{k}_1 \mathbf{k}_2; h_1 h_2}^{(E_m)}. \quad (\text{E17})$$

The result in Eq. (E12) is then expanded to second order in the order parameter through Eq. (18). The first term is independent of η and is thus absorbed in the normalization constant of the η path integral. The second term vanishes when taking the trace, leaving the third term such that

$$Z_F = \exp\left(-\frac{1}{4} \text{Tr } \check{G}_0 \check{\phi} \check{G}_0 \check{\phi}\right). \quad (\text{E18})$$

Since \check{G}_0^{-1} is a completely diagonal matrix, its inverse is trivial to find. By simple matrix multiplication and summing over the momentum and Matsubara-frequency indices for the trace, it is found that

$$\text{Tr } \check{G}_0 \check{\phi} \check{G}_0 \check{\phi} = 8 \sum_{\substack{mm' \mathbf{k} \mathbf{k}' \\ hh' n_1 n_2}} \eta_{\mathbf{k}+ \mathbf{k}', n_1}^{(m)} \eta_{\mathbf{k}+ \mathbf{k}', n_1}^{(m')*} \frac{\tilde{d}_{\mathbf{k} \mathbf{k}'; hh'}^{(E_m)} \tilde{d}_{\mathbf{k} \mathbf{k}'; hh'}^{(E_{m'})*}}{(i\omega_{n_2} - i\nu_{n_1} + \epsilon_{\mathbf{k}}^h)(i\omega_{n_2} - \epsilon_{\mathbf{k}'}^h)}. \quad (\text{E19})$$

Since the goal is a time-independent Ginzburg-Landau theory, the order parameter is assumed to be time independent such that $\eta_{\mathbf{k}, n}^{(m)} = \delta_{n0} \eta_{\mathbf{k}}^{(m)}$. Inserting this assumption back into Eq. (E19) which is inserted into Z_F in Eq. (E18) and then inserting this back into the expression for Z in Eq. (E3) yields the expression,

$$Z = \int \mathcal{D}[\eta^* \eta] \exp \left\{ - \sum_{\mathbf{q} m} \beta \frac{2|\eta_{\mathbf{q}}^{(E_m)}|^2}{V} - 2 \sum_{\substack{mm' \mathbf{k} \mathbf{k}' \\ hh' n}} \eta_{\mathbf{k}+ \mathbf{k}', n}^{(E_m)} \eta_{\mathbf{k}+ \mathbf{k}', n}^{(E_{m'})*} \frac{\tilde{d}_{\mathbf{k} \mathbf{k}'; hh'}^{(E_m)} \tilde{d}_{\mathbf{k} \mathbf{k}'; hh'}^{(E_{m'})*}}{(i\omega_n + \epsilon_{\mathbf{k}}^h)(i\omega_n - \epsilon_{\mathbf{k}'}^h)} \right\}. \quad (\text{E20})$$

After shifting the momentum indices in the second term by

$$\begin{aligned} \mathbf{k} &\rightarrow \mathbf{q}/2 + \mathbf{k}, \\ \mathbf{k}' &\rightarrow \mathbf{q}/2 - \mathbf{k}, \end{aligned} \quad (\text{E21})$$

inserting the expression for $\tilde{d}_{\mathbf{k}_1 \mathbf{k}_2; hh'}^{(E_m)}$ from Eq. (E7) as well as the elements of the transformation matrices $U(\mathbf{k})_{sh}$ from Eq. (2), Z can be rewritten in terms of the gap function [24],

$$\Delta^{s_1 s_2}(\mathbf{k}, \mathbf{q}) = \sum_m \eta_{\mathbf{q}}^{(m)} d_{s_1 s_2}^{(E_m)}(\mathbf{k}), \quad (\text{E22})$$

the spin-orbit-dependent matrix,

$$u(\mathbf{k})_{ss'}^h = (\sigma^0 + h \hat{\boldsymbol{\gamma}} \cdot \boldsymbol{\sigma})_{ss'}, \quad (\text{E23})$$

and Green's functions,

$$G^h(\mathbf{k}, i\omega_n) = (i\omega_n - \epsilon_{\mathbf{k}}^h)^{-1}, \quad (\text{E24})$$

as

$$\begin{aligned} Z = & \int \mathcal{D}[\eta^* \eta] \exp \left\{ - \sum_{\mathbf{q}m} \beta \frac{2|\eta_{\mathbf{q}}^{(E_m)}|^2}{V} + \frac{1}{2} \sum_{\substack{\mathbf{k}\mathbf{q}s_1s_2 \\ s'_1s'_2}} \Delta^{s_1s_2}(\mathbf{k}, \mathbf{q}) \Delta^{s'_1s'_2}(\mathbf{k}, \mathbf{q})^* \sum_{n hh'} G^h\left(\frac{\mathbf{q}}{2} + \mathbf{k}, -i\omega_n\right) u\left(\frac{\mathbf{q}}{2} + \mathbf{k}\right)_{s'_1s_1}^h \right. \\ & \times G^{h'}\left(\frac{\mathbf{q}}{2} - \mathbf{k}, i\omega_n\right) u\left(\frac{\mathbf{q}}{2} - \mathbf{k}\right)_{s'_2s_2}^{h'} \Bigg\}. \end{aligned} \quad (\text{E25})$$

For further development, the center-of-mass momentum \mathbf{q} of the Cooper pairs is assumed to be small compared to the fundamental lattice constant so that the momentum dependencies in Eq. (E25) can be expanded to second order by

$$u\left(\frac{\mathbf{q}}{2} \pm \mathbf{k}\right)^h \approx \sigma^0 + h\boldsymbol{\sigma} \cdot \left(\pm \hat{\mathbf{y}} + \frac{\mathbf{q}^i}{2} \partial_i \hat{\mathbf{y}} \pm \frac{\mathbf{q}^i \mathbf{q}^j}{8} \partial_i \partial_j \hat{\mathbf{y}} \right), \quad (\text{E26})$$

and

$$\sum_n G^h\left(\frac{\mathbf{q}}{2} + \mathbf{k}, -i\omega_n\right) G^{h'}\left(\frac{\mathbf{q}}{2} - \mathbf{k}, i\omega_n\right) = \beta \left(\chi^{hh} + \frac{\mathbf{q}^i}{2} \chi_i^{h'h} + \frac{\mathbf{q}^i \mathbf{q}^j}{8} \chi_{ij}^{h'h} \right), \quad (\text{E27})$$

where the Einstein-summation convention notation has been used for repeated indices and $\partial_i = \partial/\partial \mathbf{k}^i$. $\chi^{hh'}$ and $\chi_{ij}^{hh'}$ are defined as in Eqs. (21) and (25), whereas

$$\chi_i^{h'h} = \lim_{\mathbf{q} \rightarrow 0} \frac{\partial}{\partial \mathbf{q}^i} \frac{1}{\beta} \sum_n G^h(\mathbf{q} + \mathbf{k}, -i\omega_n) G^{h'}(\mathbf{q} - \mathbf{k}, i\omega_n). \quad (\text{E28})$$

Inserting these expansions, the resulting expression for Z becomes

$$\begin{aligned} Z = & \int \mathcal{D}[\eta^* \eta] \exp \left\{ - \beta \sum_{\mathbf{q}m} \frac{2|\eta_{\mathbf{q}}^{(m)}|^2}{V} - \frac{\beta}{2} \sum_{\substack{\mathbf{k}\mathbf{q}mm' \\ hh'}} \eta_{\mathbf{q}}^{(m)} \eta_{\mathbf{q}}^{(m')*} \left\{ \text{tr} [d_{\mathbf{k}}^{(E_{m'})\dagger} (hh' \hat{\mathbf{y}} \cdot \boldsymbol{\sigma} d_{\mathbf{k}}^{(E_m)}) \hat{\mathbf{y}} \cdot \boldsymbol{\sigma}^T - d_{\mathbf{k}}^{(E_m)}] \right. \right. \chi^{h'h} \\ & - \frac{\mathbf{q}^i}{2} \text{tr} [d_{\mathbf{k}}^{(E_{m'})\dagger} \boldsymbol{\sigma} d_{\mathbf{k}}^{(E_m)}] \cdot [\hat{\mathbf{y}}(h-h') \chi_i^{h'h} + \partial_i \hat{\mathbf{y}}(h+h') \chi^{h'h}] + \frac{\mathbf{q}^i \mathbf{q}^j}{8} \left\{ \text{tr} [d_{\mathbf{k}}^{(E_{m'})\dagger} (hh' \hat{\mathbf{y}} \cdot \boldsymbol{\sigma} d_{\mathbf{k}}^{(E_m)}) \hat{\mathbf{y}} \cdot \boldsymbol{\sigma}^T - d_{\mathbf{k}}^{(E_m)}] \right\} \chi_{ij}^{h'h} \\ & \left. \left. + 2hh' \chi^{h'h} \text{tr} [d_{\mathbf{k}}^{(E_{m'})\dagger} (\hat{\mathbf{y}} \cdot \boldsymbol{\sigma} d_{\mathbf{k}}^{(E_m)}) \partial_i \partial_j \hat{\mathbf{y}} \cdot \boldsymbol{\sigma}^T - \partial_i \hat{\mathbf{y}} \cdot \boldsymbol{\sigma} d_{\mathbf{k}}^{(E_m)} \partial_j \hat{\mathbf{y}} \cdot \boldsymbol{\sigma}^T] \right\} \right\}, \end{aligned} \quad (\text{E29})$$

where $\text{tr}[\cdot]$ is a trace over the spin indices and $d_{\mathbf{k}}^{(E_m)}$ is the matrix in spin space whose matrix elements are given by $d_{s_1s_2}^{(E_m)}(\mathbf{k})$. The specific form of $d_{s_1s_2}^{(E_m)}(\mathbf{k})$ given in Eq. (9) leads to considerable simplifications of Eq. (E29) since the corresponding spin-vectors $\mathbf{d}^{(E_m)}(\mathbf{k})$ are parallel and only retain the $\hat{\mathbf{z}}$ component. Inserting this fact, the partition function reduces to

$$\begin{aligned} Z = & \int \mathcal{D}[\eta^* \eta] \exp \left\{ - \beta \sum_{\mathbf{q}m} \frac{2|\eta_{\mathbf{q}}^{(m)}|^2}{V} - \frac{\beta}{2} \sum_{\substack{\mathbf{k}\mathbf{q}mm' \\ hh'}} \eta_{\mathbf{q}}^{(m)} \eta_{\mathbf{q}}^{(m')*} \text{tr} [d_{\mathbf{k}}^{(E_m)} d_{\mathbf{k}}^{(E_{m'})\dagger}] \right. \\ & \times \left. \left[\{hh'[1 - 2(\hat{\mathbf{y}}^z)^2] - 1\} \chi^{h'h} + \frac{q^i q^j}{8} (\{hh'[1 - 2(\hat{\mathbf{y}}^z)^2] - 1\} \chi_{ij}^{h'h} - 2h'h \chi^{h'h} g_{ij}) \right] \right\}. \end{aligned} \quad (\text{E30})$$

Since the spin trace in Eq. (E30) can be written

$$\text{tr} [d_{\mathbf{k}}^{(E_{m'})\dagger} d_{\mathbf{k}}^{(E_m)}] = 2(\mathbf{d}^{(E_m)})^* \cdot \mathbf{d}^{(E_{m'})}, \quad (\text{E31})$$

the free energy tensors A_{ab} and $K_{ab,ij}$ can now be identified from Eq. (E30) since their relation to the partition function is given by

$$Z = \int \mathcal{D}[\eta^* \eta] \exp \left\{ - \beta \sum_{\mathbf{q}} \left[A_{ab} (\eta_{\mathbf{q}}^{(a)})^* \eta_{\mathbf{q}}^{(b)} + K_{ab,ij} (\eta_{\mathbf{q}}^{(a)})^* \eta_{\mathbf{q}}^{(b)} \mathbf{q}^i \mathbf{q}^j \right] \right\}. \quad (\text{E32})$$

APPENDIX F: ENERGY INTEGRALS IN FERMI-SURFACE AVERAGES

The details of how to obtain the explicit expression for $K_{ab,ij}$ and A_{ab} in Eqs. (31) and (32) from Eqs. (20) and (23) were in a large part left out. In this Appendix, one of the integrals is worked out in detail, and the others needed to obtain these expressions will be listed.

To see clearly what part of the generalized mass tensor $K_{ab,ij}$ is dependent on spin-orbit coupling and which is not, the summation over h' in Eq. (23) is performed to yield the expression,

$$K_{ab,ij} = \frac{1}{4} \sum_{kh} d^{ab} \{ \chi_{ij}^{hh} + (\hat{\gamma}^z)^2 (\chi_{ij}^{hh} - \chi_{ij}^{h,-h}) + (\chi^{hh} - \chi^{h,-h}) g_{ij} \}. \quad (\text{F1})$$

Inserting $\chi_{ij}^{hh'}$ from Eq. (25) into this expression and performing the approximation outlined in Eq. (29) for converting to Fermi-surface averages yields the expression,

$$K_{ab,ij} = \frac{1}{2} \sum_h \langle d^{ab} \{ [I_2^h v_i^h v_j^h - I_1^h m_{hij}^{-1}] + (\hat{\gamma}^z)^2 [(I_2^h + I_4^h) v_i^h v_j^h - I_3^h v_i^{-h} v_j^h - (I_1^h - I_5^h) m_{hij}^{-1}] - \frac{1}{2} [I^h - I_0^h] g_{ij} \} \rangle_0. \quad (\text{F2})$$

Here the I 's represent energy integrals across the energy shell around the Fermi energy of varying combinations of Green's functions as well as the density of states $N_0(\epsilon)$. As an example, consider the integral,

$$I_5^h = \int_{-\epsilon_c}^{\epsilon_c} d\xi \frac{N_0(\xi)}{\beta} \sum_n \frac{1}{i\omega_n - \xi - h|\boldsymbol{\gamma}|} \frac{\partial}{\partial \xi} \frac{1}{-i\omega_n - \xi + h|\boldsymbol{\gamma}|}. \quad (\text{F3})$$

First the approximation $N_0(\xi) \approx N_F + N'_F \xi$ is used to split the integral in two: $I_5^h = I_{5,1}^h + I_{5,2}^h$ such that $I_{5,1}^h$ is the part that is proportional to N_F , whereas $I_{5,2}^h$ is proportional to N'_F . The integrand of $I_{5,1}^h$ is then split using partial fractions such that

$$\begin{aligned} I_{5,1}^h &= \frac{N_F}{\beta} \sum_n \frac{1}{2(i\omega_n - h|\boldsymbol{\gamma}|)} \int_{-\epsilon_c}^{\epsilon_c} d\xi \left[\frac{1}{(-i\omega_n - \xi + h|\boldsymbol{\gamma}|)^2} - \frac{1}{\xi^2 + (\omega_n + ih|\boldsymbol{\gamma}|)^2} \right] \\ &= \frac{N_F}{\beta} \sum_n \frac{1}{2(i\omega_n - h|\boldsymbol{\gamma}|)} \left[-\frac{2\epsilon_c}{\epsilon_c^2 + (\omega_n + ih|\boldsymbol{\gamma}|)^2} - \frac{2}{\omega_n + ih|\boldsymbol{\gamma}|} \tan^{-1} \left(\frac{\epsilon_c}{\omega_n + ih|\boldsymbol{\gamma}|} \right) \right] \\ &= \frac{N_F}{\pi} \sum_n \frac{1}{i(\omega_n + ih|\boldsymbol{\gamma}|)} \left[-\frac{e_c}{e_c^2 + (2n+1+ih\rho)^2} - \frac{1}{2n+1+ih\rho} \tan^{-1} \left(\frac{e_c}{2n+1+ih\rho} \right) \right] \\ &\approx -\frac{N_F \beta}{i\pi^2} \sum_n \frac{1}{(2n+1+ih\rho)^2} \tan^{-1} \left(\frac{e_c}{2n+1+ih\rho} \right) \\ &\approx -\frac{\beta N_F h}{\pi} \operatorname{Im} \sum_{n=0}^{\infty} \frac{1}{(2n+1+i\rho)^2} \\ &= -\frac{\beta N_F h}{\pi} f_2(\rho). \end{aligned} \quad (\text{F4})$$

On the third line the dimensionless variables $e_c = \beta\epsilon_c/\pi$ and $\rho = \beta|\boldsymbol{\gamma}|/\pi$ were introduced. It was assumed that the critical temperature was low compared to the Debye frequency such that $e_c \gg 1$ and the first term on the third line could be ignored since it goes as $\sim 1/e_c$ whereas the arctan goes like $\sim \pi/2$. On the last line, the sum over n was separated into the sum over positive and negative n , resulting in the imaginary component of the first sum by shifting the summation index. For $n \in [0, n_c]$, $e_c/(2n+1) \gg 1$ such that \tan^{-1} is approximately $\pi/2$. n_c depends on e_c and since $e_c \gg 1$ then $n_c \gg 1$ as well such that adding the terms in the sum for $n > n_c$ does not change the limiting behavior.

Similarly, the integrand of $I_{5,2}^h$ is split using partial fractions, albeit in a slightly different way which produces

$$\begin{aligned} I_{5,2}^h &= -\frac{N'_F}{2\beta} \sum_n \int_{-\epsilon_c}^{\epsilon_c} d\xi \left[\frac{1}{(-i\omega_n - \xi + h|\boldsymbol{\gamma}|)^2} + \frac{1}{\xi^2 + (\omega_n + ih|\boldsymbol{\gamma}|)^2} \right] \\ &= -\frac{N'_F}{\pi} \sum_n \left[\frac{1}{2n+1+ih\rho} \tan^{-1} \left(\frac{e_c}{2n+1+ih\rho} \right) - \frac{e_c}{(2n+1+ih\rho)^2 + e_c^2} \right] \\ &\approx -\frac{2N'_F}{\pi} \operatorname{Re} \sum_{n=0}^{\infty} \left[\frac{\tan^{-1} \left(\frac{e_c}{2n+1+i\rho} \right)}{2n+1+i\rho} - \frac{\tan^{-1} \left(\frac{e_c}{2n+1} \right)}{2n+1} + \frac{\tan^{-1} \left(\frac{e_c}{2n+1} \right)}{2n+1} \right] \\ &\approx -N'_F f(\rho) - \frac{N'_F}{2} \ln(2e_c e^C). \end{aligned} \quad (\text{F5})$$

Inserting these results back into Eq. (F3) then yields

$$I_5^h \approx -\frac{N_F \beta h}{\pi} f_2(\rho) - N'_F f(\rho) - \frac{N'_F}{2} \ln(2e_c e^C). \quad (\text{F6})$$

The remaining integrals are calculated in a similar manner. In the cases where ρ/e_c remains in the expression after integrating, this is expanded to first order in $O(\rho/e_c)$, e.g., in I_0^h . Terms proportional to e^{-e_c} are also neglected, such as in I_2^h . With these approximations the integrals become

$$I^h = \int_{-\epsilon_c}^{\epsilon_c} d\xi \frac{N_0(\xi)}{\beta} \sum_n \frac{1}{\omega_n^2 + (\xi + h|\gamma|)^2} \approx N_F \ln(2e_c e^C) + h N'_F |\gamma| [1 - \ln(2e_c e^C)], \quad (\text{F7a})$$

$$I_0^h = \int_{-\epsilon_c}^{\epsilon_c} d\xi \frac{N_0(\xi)}{\beta} \sum_n \frac{1}{\xi^2 + (\omega_n + ih|\gamma|)^2} \approx N_F \ln(2e_c e^C) + 2N_F f(\rho), \quad (\text{F7b})$$

$$\begin{aligned} I_1^h &= \int_{-\epsilon_c}^{\epsilon_c} d\xi \frac{N_0(\xi)}{\beta} \sum_n \frac{1}{i\omega_n - \xi - h|\gamma|} \frac{\partial}{\partial \xi} \frac{1}{-i\omega_n - \xi - h|\gamma|} \\ &\approx -\frac{N_F h |\gamma|}{2\epsilon_c^2} - \frac{N'_F \ln(2e_c e^C)}{2}, \end{aligned} \quad (\text{F7c})$$

$$\begin{aligned} I_2^h &= \int_{-\epsilon_c}^{\epsilon_c} d\xi \frac{N_0(\xi)}{\beta} \sum_n \left(\frac{\partial}{\partial \xi} \frac{1}{i\omega_n - \xi - h|\gamma|} \frac{\partial}{\partial \xi} \frac{1}{-i\omega_n - \xi - h|\gamma|} - \frac{1}{i\omega_n - \xi - h|\gamma|} \frac{\partial^2}{\partial \xi^2} \frac{1}{-i\omega_n - \xi - h|\gamma|} \right) \\ &\approx \frac{7\zeta(3)\beta^2}{4\pi^2} (N_F - h|\gamma|N'_F), \end{aligned} \quad (\text{F7d})$$

$$\begin{aligned} I_3^h &= \int_{-\epsilon_c}^{\epsilon_c} d\xi \frac{N_0(\xi)}{\beta} \sum_n \frac{\partial}{\partial \xi} \frac{1}{i\omega_n - \xi - h|\gamma|} \frac{\partial}{\partial \xi} \frac{1}{-i\omega_n - \xi + h|\gamma|} \\ &\approx \frac{N_F \beta^2}{\pi^2} \left[f_3(\rho) + \frac{7\zeta(3)}{8} \right], \end{aligned} \quad (\text{F7e})$$

$$\begin{aligned} I_4^h &= \int_{-\epsilon_c}^{\epsilon_c} d\xi \frac{N_0(\xi)}{\beta} \sum_n \frac{1}{i\omega_n - \xi - h|\gamma|} \frac{\partial^2}{\partial \xi^2} \frac{1}{-i\omega_n - \xi + h|\gamma|} \\ &\approx -\frac{N_F \beta^2}{\pi^2} \left(f_3(\rho) + \frac{7\zeta(3)}{8} \right) + \frac{N'_F \beta h}{\pi} f_2(\rho), \end{aligned} \quad (\text{F7f})$$

$$\begin{aligned} I_5^h &= \int_{-\epsilon_c}^{\epsilon_c} d\xi \frac{N_0(\xi)}{\beta} \sum_n \frac{1}{i\omega_n - \xi - h|\gamma|} \frac{\partial}{\partial \xi} \frac{1}{-i\omega_n - \xi + h|\gamma|} \\ &\approx -\frac{N_F \beta h}{\pi} f_2(\rho) - \frac{N'_F \ln(2e_c e^C)}{2} - N'_F f(\rho). \end{aligned} \quad (\text{F7g})$$

The expression for $K_{ab,ij}$ in Eq. (32) is then obtained by inserting these integrals into Eq. (F2) and summing over h . The integrals I^h and I_0^h are used to obtain the expression for A_{ab} in Eq. (31).

-
- [1] M. Gabay and J.-M. Triscone, *Nat. Phys.* **13**, 624 (2017).
 - [2] C. W. Rischau, X. Lin, C. P. Grams, D. Finck, S. Harms, J. Engelmayer, T. Lorenz, Y. Gallais, B. Fauqué, J. Hemberger, and K. Behnia, *Nat. Phys.* **13**, 643 (2017).
 - [3] M. Sigrist and K. Ueda, *Rev. Mod. Phys.* **63**, 239 (1991).
 - [4] A. V. Matetskiy, S. Ichinokura, L. V. Bondarenko, A. Y. Tupchaya, D. V. Gruznev, A. V. Zotov, A. A. Saranin, R. Hobara, A. Takayama, and S. Hasegawa, *Phys. Rev. Lett.* **115**, 147003 (2015).
 - [5] S. Gariglio, M. Gabay, and J.-M. Triscone, *APL Mater.* **4**, 060701 (2016).
 - [6] A. D. Caviglia, S. Gariglio, N. Reyren, D. Jaccard, T. Schneider, M. Gabay, S. Thiel, G. Hammerl, J. Mannhart, and J.-M. Triscone, *Nature (London)* **456**, 624 (2008).
 - [7] A. D. Caviglia, M. Gabay, S. Gariglio, N. Reyren, C. Cancelleri, and J.-M. Triscone, *Phys. Rev. Lett.* **104**, 126803 (2010).
 - [8] N. Reyren, S. Gariglio, A. D. Caviglia, D. Jaccard, T. Schneider, and J.-M. Triscone, *Appl. Phys. Lett.* **94**, 112506 (2009).
 - [9] E. Bauer, G. Hilscher, H. Michor, M. Sieberer, E. Scheidt, A. Gribanov, Y. Seropegin, P. Rogl, W. Song, J.-G. Park, D. Adroja, A. Amato, M. Nicklas, G. Sparn, M. Yogi, and Y. Kitaoka, *Czech. J. Phys.* **54**, 401 (2004).
 - [10] E. Bauer, G. Hilscher, H. Michor, C. Paul, E. W. Scheidt, A. Gribanov, Y. Seropegin, H. Noël, M. Sigrist, and P. Rogl, *Phys. Rev. Lett.* **92**, 027003 (2004).
 - [11] I. Bonalde, W. Brämer-Escamilla, and E. Bauer, *Phys. Rev. Lett.* **94**, 207002 (2005).

- [12] K. Izawa, Y. Kasahara, Y. Matsuda, K. Behnia, T. Yasuda, R. Settai, and Y. Onuki, *Phys. Rev. Lett.* **94**, 197002 (2005).
- [13] M. Smidman, M. B. Salamon, H. Q. Yuan, and D. F. Agterberg, *Rep. Prog. Phys.* **80**, 036501 (2017).
- [14] S. Das Sarma, C. Nayak, and S. Tewari, *Phys. Rev. B* **73**, 220502 (2006).
- [15] A. J. Leggett, *Rev. Mod. Phys.* **47**, 331 (1975).
- [16] G. M. Luke, Y. Fudamoto, K. M. Kojima, M. I. Larkin, J. Merrin, B. Nachumi, Y. J. Uemura, Y. Maeno, Z. Q. Mao, Y. Mori, H. Nakamura, and M. Sigrist, *Nature (London)* **394**, 558 (1998).
- [17] A. P. Mackenzie and Y. Maeno, *Rev. Mod. Phys.* **75**, 657 (2003).
- [18] B. Kim, S. Khmelevskyi, I. I. Mazin, D. F. Agterberg, and C. Franchini, *npj Quantum Materials* **2**, 37 (2017).
- [19] D. F. Agterberg, *Phys. Rev. B* **58**, 14484 (1998).
- [20] J. Garaud, E. Babaev, T. A. Bojesen, and A. Sudbø, *Phys. Rev. B* **94**, 104509 (2016).
- [21] R. Heeb and D. F. Agterberg, *Phys. Rev. B* **59**, 7076 (1999).
- [22] J. Garaud, M. Silaev, and E. Babaev, *Physica C* **533**, 63 (2017).
- [23] J. Böker, P. A. Volkov, K. B. Efetov, and I. Eremin, *Phys. Rev. B* **96**, 014517 (2017).
- [24] K. V. Samokhin, *Phys. Rev. B* **70**, 104521 (2004).
- [25] E. K. Dahl and A. Sudbø, *Phys. Rev. B* **75**, 144504 (2007).
- [26] H. G. Hugdal and A. Sudbø, *Phys. Rev. B* **97**, 024515 (2018).
- [27] T. Inui, Y. Tanabe, and Y. Onodera, *Group Theory and Its Applications in Physics*, Springer Series in Solid-State Sciences Vol. 78 (Springer-Verlag, Berlin, Heidelberg, 1990) (original Japanese edition published by Shokabo, Tokyo, 1976).
- [28] E. Otnes, Symmetrien til ordensparameteren i en høy- T_c superleder, Master's thesis, NTNU, 1996.
- [29] E. Otnes and A. Sudbø, *Int. J. Mod. Phys. B* **13**, 1579 (1999).
- [30] K. V. Samokhin, E. S. Zijlstra, and S. K. Bose, *Phys. Rev. B* **69**, 094514 (2004).
- [31] K. V. Samokhin and V. P. Mineev, *Zh. Eksp. Teor. Fiz.* **105**, 747 (1994) [JETP **78**, 401 (1994)].
- [32] I. A. Sergienko and S. H. Curnoe, *Phys. Rev. B* **70**, 214510 (2004).
- [33] F. Loder, A. P. Kampf, T. Kopp, and D. Braak, *Phys. Rev. B* **96**, 024508 (2017).
- [34] G. A. H. Schober, K.-U. Giering, M. M. Scherer, C. Honerkamp, and M. Salmhofer, *Phys. Rev. B* **93**, 115111 (2016).
- [35] D. Serre, *Matrices; Theory and Applications* (Springer, New York, 2002).
- [36] M. Wimmer, *ACM Trans. Math. Softw.* **38**, 30 (2012).

Paper II

**Fredrik Nicolai Krohg, Håvard Homleid Haugen, Egor Babaev,
Julien Garaud, and Asle Sudbø**

*Thermal fluctuations and vortex lattice structures in chiral p-wave superconductors:
Robustness of double-quanta vortices*

Physical Review B **103**, 214517 (2021)

Thermal fluctuations and vortex lattice structures in chiral p -wave superconductors: Robustness of double-quanta vortices

Fredrik Nicolai Krogh^{1,2}, Egor Babaev,³ Julien Garaud,⁴ Håvard Homleid Haugen^{1,2}, and Asle Sudbø^{1,2}

¹Department of Physics, Norwegian University of Science and Technology, NO-7491 Trondheim, Norway

²Center for Quantum Spintronics, Department of Physics, Norwegian University of Science and Technology, NO-7491 Trondheim, Norway

³Department of Physics, KTH-Royal Institute of Technology, Stockholm SE-10691, Sweden

⁴Institut Denis Poisson CNRS-UMR 7013, Université de Tours, 37200 Tours, France



(Received 26 June 2020; accepted 8 June 2021; published 22 June 2021)

We use large-scale Monte-Carlo simulations to study thermal fluctuations in chiral p -wave superconductors in an applied magnetic field in three dimensions. We consider the thermal stability of previously predicted unusual double-quanta flux-line lattice ground states in such superconductors. In previous works it was shown that, neglecting thermal fluctuations, a chiral p -wave superconductor forms a hexagonal lattice of doubly-quantized vortices, except extremely close to the vicinity of H_{c2} where double-quanta vortices split apart. We find dissociation of double-quanta vortices driven by thermal fluctuations. However, our calculations also show that the previous predictions of hexagonal doubly-quantized vortices, where thermal fluctuations were ignored, are very robust in the considered model.

DOI: [10.1103/PhysRevB.103.214517](https://doi.org/10.1103/PhysRevB.103.214517)

I. INTRODUCTION

Higher angular momentum odd-parity chiral superfluid and superconducting states are highly nontrivial pairing symmetries that result in novel topological as well as thermodynamic properties. Examples are chiral p -wave and chiral f -wave states. A prominent example of a condensed matter system where such a phase is firmly established is within the very rich phase diagram of superfluid ^3He , where the so-called A phase is a chiral p -wave superfluid. This unconventional superfluid phase was first discovered in seminal works of Osheroff *et al.* [1–4]. It is the interplay between spin and orbital degrees of freedom, with the multicomponent nature of the matter field of the superfluid or superconducting states, that makes the physics of such condensates much richer than the corresponding physics in simple superfluids like ^4He [5]. The A phase of ^3He has been used to explain exotic phenomena such as a nonvanishing orbital angular momentum in thermal equilibrium and unconventional dissipation behavior due to coreless vortex textures [6–8].

On the other hand, chiral p -wave pairing in solid state systems, i.e., superconductors, has remained less well established. One candidate superconductor with such chiral pairing that has been intensely investigated since its discovery is the superconducting phase of Sr_2RuO_4 [9]. The crystallographic structure of this compound is a perovskite, similar to the high T_c cuprates. The normal metallic phase features transport properties consistent with a 2D strongly correlated Fermi liquid phase [10], and superconductivity arises out of this normal state at $T \approx 1.5$ K. Contrary to the high- T_c cuprates however, Sr_2RuO_4 is a weak-coupling superconductor. For an early review of the basics physics and superconductivity of Sr_2RuO_4 , see Ref. [11].

Conventional pairing is excluded in Sr_2RuO_4 by the many unusual experimental properties of Sr_2RuO_4 . Early works

revealed a number of unusual features and gave indication of chiral p -wave superconductivity. The early experimental results included the indication of suppression of superconductivity by nonmagnetic impurities [12–14]. A conventional superconductor is expected to have a T_c independent of addition of small fractions of such impurities but rather depend only on the number of magnetic impurities. Early NMR Knight shift experiments showed a temperature-independent Knight shift and thus a residual spin susceptibility as $T \rightarrow 0$, which is a hallmark of spin-triplet pairing [15,16]. Instead of being isotropic, the gap in Sr_2RuO_4 is indicated to contain line nodes or near nodes by both the temperature dependence of the specific heat and thermal conductivity as well as scanning tunneling microscopy measurements of the density of states. Other early works on the anisotropy of the thermal conductivity also were interpreted in favor of chiral p -wave pairing state [17–19]. Evidence for unconventional pairing in Sr_2RuO_4 is provided by the combination of evidence for spontaneous breaking of time-reversal symmetry and spin-triplet pairing. Muon spin-relaxation experiments find spontaneous magnetization in the superconducting state. Kerr effect experiments find a temperature dependent Kerr twisting angle [20–22] which, significantly, depends on the sign of the magnetic field.

One of the main predictions of theories of superconductors with chiral p -wave symmetry is the existence of domains of different chiralities of the superconducting order parameter, and as a result of this, the existence of chiral edge currents between domains of different chirality. These chiral edge currents should produce magnetic signatures observable by scanning Hall probe microscopy. No experimental proof of such chiral edge currents exists, in spite of several attempts to detect them [23]. Another issue is that recent ^{17}O Knight shift results have seen a substantial reduction of spin susceptibility at low temperatures, which led to recently

strengthened arguments against the hypothesis of spin-triplet pairing [24]. However, the evidence for spontaneous symmetry breaking [21,22], ultrasound [25], thermodynamics [26], and unconventional vortex physics [27] strongly indicates a multicomponent order parameter. Recent works suggested the possibility of chiral d -wave, $s + id$, and $s + ig$ order parameters for the superconducting state of Sr_2RuO_4 [26,28,29]. The intense experimental pursuit and controversies associated with chiral p -wave pairing motivates the current work focused on magnetic response of such systems. Moreover, the model we consider is consistent with a certain chiral d -wave order parameter [28] that is presently discussed in connection with Sr_2RuO_4 .

Furthermore, UPt_3 is a heavy fermion topological type-II superconductor with an unconventional superconducting state believed to be a chiral f -wave pairing state with E_{2u} irreducible representation. At a phenomenological level, it can be described by a Ginzburg-Landau (GL) theory of a two-component complex matter field with the components related by a time-reversal transformation and oppositely directed internal orbital angular momentum [30]. The experimental evidence for such a two-component description of the superconducting state of UPt_3 was recently strengthened when its time-reversal symmetry breaking character was demonstrated by showing that the energy of the vortex lattice state depends on the relative direction of the external magnetic field [31]. The theoretical description we will use is thus relevant to this system.

Early numerical work showed that such a two-component GL theory for UPt_3 admits anisotropic vortices with nontrivial core structures and a hexagonal vortex lattice consisting of doubly-quantized vortices at field strengths $H < 0.3H_{c2}$ in the ground state [32]. At higher field strengths $H > 0.3H_{c2}$, the doubly-quantized vortices were found to dissociate into singly-quantized vortices. However, the lattice symmetry of the resulting singly-quantized aggregate vortex state was not determined.

The GL theory used in this paper, which posits a chiral symmetry of the superconducting state, is based on the (two-dimensional) Γ_{5u}^- representation of the D_{4h} symmetry group [33]. Lowest Landau-level calculations based on this GL theory have predicted a square lattice of vortices when the external magnetic field is applied parallel to the c axis for high field strengths close to upper critical H_{c2} [34]. For fields parallel to the c axis close to the lower critical field H_{c1} , an extended London theory predicted a singly-quantized rectangular vortex lattices continuously deforming to singly-quantized square vortex lattices as the magnetic field strength was increased [35]. (Below we will define precisely what is meant by singly-quantized and doubly-quantized vortices.) Numerical energy minimization of the free energy has shown that isolated doubly-quantized vortices are generically stable and actually are energetically favorable compared to two isolated single-quanta vortices [36,37]. In a part of parameter space, this is corroborated by calculations of isolated topological defects based on Eilenberger's equation where a Γ_{5u}^- symmetry was assumed [38]. This led to the expectation that double-quanta vortices form hexagonal lattices, while the single-quanta vortices form square lattices based on the symmetry of the current distribution of the isolated vortices.

The numerical studies of isolated vortices were extended to a finite ensemble of vortices in Ref. [39], where a finite-element method was used to minimize the GL free energy when increasing the external magnetic field strength. These computations found a robust hexagonal lattice of doubly-quantized vortices at field strengths up to a very close vicinity of H_{c2} when the field was parallel to the c axis. This is inconsistent with the vortex phase diagram of Sr_2RuO_4 [27]. To examine the vortex structure at fields close to H_{c2} , a temperature dependence was inserted into the quadratic coefficient of the free energy which allowed the system to be moved horizontally in the T - H phase space. Extremely close to H_{c2} , the double-quanta vortices were seen to dissociate into single-quanta vortices that arranged themselves in a square lattice through a mixed phase where both single and double quanta vortices were present. This type of behavior was, on one hand, quite robust, but on the other hand has never been observed in the materials that are candidates for chiral superconductivity.

The manner in which thermal effects were included in Ref. [39] was at a mean field level, i.e., entropic effects were not fully accounted for. This then leaves open the question of whether these unusual vortex states and the field-induced transitions between them are actually stable when thermal fluctuations are included. In particular, a weak binding energy as well as different entropic contributions of different lattices can alter the conclusion of the dominant character of two-quanta vortex lattice.

In other words, we will investigate in this paper whether the predicted field regime of a transition from a doubly-quantized hexagonal to a square singly-quantized vortex lattice with increasing temperature [39] is dramatically over- or underestimated by not fully accounting for entropic effects. This is particularly important in this system because the mean-field-based Ginzburg-Landau model in an external field gives two different vortex-lattice states that are close in free energy. Moreover, the mean-field results found the transition from one vortex lattice to the other at a temperature of about 80% of the zero-field critical temperature T_c . At such elevated temperatures it is by no means obvious that thermal entropic effects can be neglected, even though the thermal fluctuations are not critical. Thus, an assessment of whether the conclusion based on a mean-field analysis is robust against more accurate estimates of the entropy of the system is required. Specifically, we attempt to answer if the double-quanta vortex lattice survives inclusion of thermal fluctuations since there is more entropy in a single-quanta vortex lattice, opening the possibility that it may be entropically stabilized at substantially lower fractions of T_c than the mean-field calculation would predict. Our approach is related in spirit to that of Ref. [40], where a decay of single-quanta vortex lattice into a half-quanta lattice was considered at elevated temperatures.

The purpose of the present paper is therefore to consider the stability of doubly-quantized hexagonal vortex lattices and singly-quantized square vortex lattices when all thermal fluctuation effects are included in gauge fields and phases of the complex matter fields. In strongly type-II one-component superconductors, a good approximation is to neglect amplitude fluctuations [41–46]. In chiral superconductors, the situation is more subtle because of a number of massive normal modes that are linear combinations of phase modes, magnetic modes,

and amplitude modes [47]. Then the London-like approximation amounts to dropping the most massive modes and neglecting some of the mixing.

We present the results of extensive Monte-Carlo simulations of a chiral p -wave GL theory with an external field parallel to the c axis. This paper is organized as follows. In Sec. II, we present in detail the model we will consider, along with a discussion of its parametrization. We then discuss a subtle point on the discretization of this model on a numerical grid and the choice of basis for the two-component matter field. In Sec. III, we present details of the Monte-Carlo simulations along with definitions of the observables we will use. In Sec. IV, we present results of our detailed Monte-Carlo simulations at a filling fraction f of field-induced vortices of $f = 1/64$ at various temperatures, starting from high temperatures and proceeding to lower temperatures. We find two types of stable vortex lattices and an interesting transition region where the vortex lattices thermally reconstruct. Conclusions are presented in Sec. VI. Some mathematical details are relegated to appendices.

II. GINZBURG-LANDAU MODEL

A. Dimensionless units and reduction of parameters

We consider the clean limit of the Ginzburg-Landau energy density of the two-dimensional Γ_{5u} irreducible representation of the tetragonal D_{4h} symmetry group which in the chiral basis using dimensionless variables and units reads [35,39]

$$\mathcal{F} = g^{-2} |\nabla \times \mathbf{A}|^2 + |D_x \boldsymbol{\eta}|^2 + |D_y \boldsymbol{\eta}|^2 + 2\tilde{\kappa}_5 |D_z \boldsymbol{\eta}|^2 \quad (1a)$$

$$+ (1 + \nu) \operatorname{Re}[(D_x \eta_+)^* D_x \eta_- - (D_y \eta_+)^* D_y \eta_-] \quad (1b)$$

$$- (1 - \nu) \operatorname{Im}[(D_x \eta_+)^* D_y \eta_- + (D_y \eta_+)^* D_x \eta_-] \quad (1c)$$

$$+ 2|\eta_+ \eta_-|^2 + \nu \operatorname{Re}(\eta_+^{*2} \eta_-^2) + \sum_{h=\pm} (-|\eta_h|^2 + \frac{1}{2} |\eta_h|^4). \quad (1d)$$

The two dimensions of the representation are spanned by the complex fields η_{\pm} . The covariant derivative $D_a = \nabla_a - iA_a$, and ν and g are dimensionless material parameters with the restriction that $|\nu| < 1$. Deriving the effective Ginzburg-Landau energy from a microscopic model [48], it is seen that $\nu = ((v_x^4) - 3(v_x^2 v_y^2)) / ((v_x^4) + (v_x^2 v_y^2))$, where v_a is the a component of the Fermi velocity and the brackets: $\langle \cdot \rangle$ indicate an average over the Fermi surface. ν thus parameterizes the anisotropy of the Fermi surface in that $\nu = 0$ for a cylindrical surface, while $\nu \neq 0$ for a Fermi surface distorted by fourfold anisotropy.

The model in Eq. (1) is a restricted version of the full Γ_{5u} free energy which in SI units can be written [33,35,49]

$$\begin{aligned} \mathcal{F} = & -\alpha |\boldsymbol{\eta}|^2 + \frac{\beta_1}{2} |\boldsymbol{\eta}|^4 + \frac{\beta_2}{2} (\eta_x \eta_y^* - \eta_y \eta_x^*)^2 + \beta_3 |\eta_x \eta_y|^2 \\ & + \kappa_1 (|D_x \eta_x|^2 + |D_y \eta_y|^2) + \kappa_2 (|D_y \eta_x|^2 + |D_x \eta_y|^2) \\ & + \kappa_3 [(D_x \eta_x)^* D_y \eta_y + (D_y \eta_y)^* D_x \eta_x] \\ & + \kappa_4 [(D_x \eta_y)^* D_y \eta_x + (D_y \eta_x)^* D_x \eta_y] \\ & + \kappa_5 (|D_z \eta_x|^2 + |D_z \eta_y|^2) + \frac{|\nabla \times \mathbf{A}|^2}{2\mu_0}, \end{aligned} \quad (2)$$

TABLE I. Name, mean-field energy density, and solution modulo an overall phase of the mean field minimization of \mathcal{F} in Eq. (4). The A phase is the phase that exhibits spontaneous time-reversal symmetry breaking in zero magnetic field and is the one we focus on in this paper. The B and C phases are time-reversal symmetric odd-parity superconducting states with line nodes in the gap on the Fermi surface.

Name	\mathcal{F}	(η_+, η_-)	u^2
A phase	$-\frac{\alpha^2}{2(\beta_1 - \beta_2) + \beta_3}$	$u(0, 1) \vee u(1, 0)$	$\frac{2\alpha}{2(\beta_1 - \beta_2) + \beta_3}$
B phase	$-\frac{\alpha^2}{2\beta_1 + \beta_3}$	$u(\pm i, 1)$	$\frac{\alpha}{2\beta_1 + \beta_3}$
C phase	$-\frac{\alpha^2}{2\beta_1}$	$u(\pm 1, 1)$	$\frac{\alpha}{2\beta_1}$

where $D_a = \nabla_a - i(g/\hbar)A_a$, q is the charge of the Cooper pair, \hbar is Planck's reduced constant, and μ_0 is the vacuum permeability. In this expression, the conventional xy basis is used for the complex fields η_x and η_y . Rotating this to the chiral basis through the transformation

$$\eta_{\pm} = \frac{1}{\sqrt{2}} (\eta_x \pm i\eta_y) \quad (3)$$

yields the energy density

$$\begin{aligned} \mathcal{F} = & -\alpha |\boldsymbol{\eta}|^2 + (2(\beta_1 - \beta_2) + \beta_3) \frac{|\eta_+|^4 + |\eta_-|^4}{4} \\ & + (\beta_1 + \beta_2) |\eta_+ \eta_-|^2 - \frac{\beta_3}{2} \operatorname{Re} \eta_+^2 \eta_-^2 \\ & + \frac{\kappa_1 + \kappa_2}{2} (|D_x \boldsymbol{\eta}|^2 + |D_y \boldsymbol{\eta}|^2) + \kappa_5 |D_z \boldsymbol{\eta}|^2 \\ & + (\kappa_1 - \kappa_2) \operatorname{Re}[D_x \eta_+ (D_x \eta_-)^* - D_y \eta_+ (D_y \eta_-)^*] \\ & + (\kappa_4 - \kappa_3) \operatorname{Im}[D_x \eta_+ (D_y \eta_+)^* + D_y \eta_+ (D_x \eta_-)^*] \\ & + (\kappa_4 + \kappa_3) \operatorname{Im}[D_x \eta_+ (D_y \eta_-)^* + D_y \eta_+ (D_x \eta_-)^*] \\ & + \frac{|\nabla \times \mathbf{A}|^2}{2\mu_0}. \end{aligned} \quad (4)$$

Taking the mean field limit and looking at the fourth-order terms yields the constraint that for the mean field energy to be bounded from below, $\beta_1 > 0$, $\beta_3 > -2\beta_1$, and $\beta_3 > 2(\beta_2 - \beta_1)$. Minimizing \mathcal{F} w.r.t. η_{\pm} yields the three distinct mean field solutions in Table I. The regions of the β_3/β_1 , β_2/β_1 -parameter space for which each of these solutions minimizes \mathcal{F} is shown in Fig. 1. One of these solutions, known as the A phase, exhibits spontaneous time-reversal symmetry breaking. This is the phase we are interested in examining.

We now focus on the A phase. To write \mathcal{F} on a dimensionless form, we scale the dimensionless energy density $\tilde{\mathcal{F}}$ and dimensionless fields $\tilde{\eta}_{\pm}$ by their mean field values in the A phase such that $\mathcal{F} = 2\alpha^2/[2(\beta_1 - \beta_2) + \beta_3]\tilde{\mathcal{F}}$ and $\eta_{\pm} = \sqrt{2\alpha}/[2(\beta_1 - \beta_2) + \beta_3]\tilde{\eta}_{\pm}$. We also choose the length scale such that the coefficient in front of the first term in the kinetic part of \mathcal{F} becomes trivial in dimensionless units, i.e., $\nabla_a = \sqrt{2\alpha}/(\kappa_1 + \kappa_2)\tilde{\nabla}_a$. Finally we scale the gauge field $A_a = \hbar\sqrt{2\alpha}/(\kappa_1 + \kappa_2)/q\tilde{A}_a$ such that $\tilde{D}_a = \tilde{\nabla}_a - i\tilde{A}_a$. To simplify the notation, we neglect the tilde in the dimensionless variables in the following. With these choices of units, \mathcal{F} takes

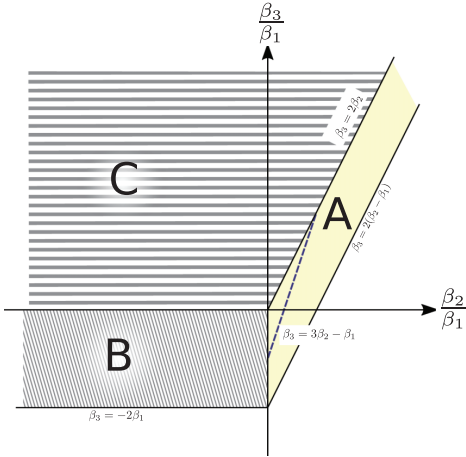


FIG. 1. Mean field phase diagram spanned by the fourth order material constants β_i . The A , B , and C regions correspond to the mean field solutions given in Table I. The white region below the phases give unbounded mean field energy and is unphysical. The blue line $\beta_3 = 3\beta_2 - \beta_1$ gives the values of parameter space spanned by the parameter choices used in the reduced free energy density. This line can be parametrized in terms of the single dimensionless parameter v for $-1 < v < 1$.

the dimensionless form

$$\begin{aligned} \mathcal{F} = & -|\boldsymbol{\eta}|^2 + \frac{|\eta_+|^4 + |\eta_-|^4}{2} + \frac{2}{1 + \Delta\tilde{\beta}} |\eta_+ \eta_-|^2 + v \operatorname{Re} \eta_+^2 \eta_-^{*2} \\ & + |D_x \boldsymbol{\eta}|^2 + |D_y \boldsymbol{\eta}|^2 + 2\tilde{\kappa}_5 |D_z \boldsymbol{\eta}|^2 + \frac{|\nabla \times \mathbf{A}|^2}{g^2} \\ & + (1 + v_k) \operatorname{Re} [D_x \eta_+ (D_x \eta_-)^* - D_y \eta_+ (D_y \eta_-)^*] \\ & + \Delta\tilde{\kappa} \operatorname{Im} [D_x \eta_+ (D_y \eta_+)^* + D_y \eta_- (D_x \eta_-)^*] \\ & + (v_k - 1 - 2\Delta) \operatorname{Im} [D_x \eta_- (D_y \eta_+)^* + D_y \eta_- (D_x \eta_+)^*], \end{aligned} \quad (5)$$

for dimensionless parameters

$$\Delta\tilde{\beta} = \frac{\beta_3 - 3\beta_2 + \beta_1}{\beta_1 + \beta_2}, \quad (6a)$$

$$v = \frac{\beta_3}{2(\beta_2 - \beta_1) - \beta_3}, \quad (6b)$$

$$v_k = \frac{\kappa_1 - 3\kappa_2}{\kappa_1 + \kappa_2}, \quad (6c)$$

$$\Delta\tilde{\kappa} = 2 \frac{\kappa_4 - \kappa_3}{\kappa_1 + \kappa_2}, \quad (6d)$$

$$\Delta = \frac{\kappa_3 + \kappa_4 - 2\kappa_2}{\kappa_1 + \kappa_2}, \quad (6e)$$

$$\tilde{\kappa}_5 = \frac{\kappa_5}{\kappa_1 + \kappa_2}, \quad (6f)$$

$$g = \frac{q}{\hbar} \sqrt{\mu_0 \frac{(\kappa_1 + \kappa_2)^2}{2(\beta_1 - \beta_2) + \beta_3}}. \quad (6g)$$

So far, no assumptions have been made about the values of the material parameters α , β_i , and κ_i . Based on microscopic derivations of the kinetic constants in the weak coupling and clean limit [48], we have that $\kappa_2 = \kappa_3 = \kappa_4 \propto \langle v_x^2 v_y^2 \rangle$ and $\kappa_1 \propto \langle v_x^4 \rangle$. For the case of a cylindrical Fermi surface, another microscopic derivation of the Ginzburg-Landau coefficients [50] shows that in the weak coupling approximation the relations $\beta_2/\beta_1 = \kappa_2/\kappa_1$ and $\beta_3 = 3\beta_2 - \beta_1$ hold. The validity of these constraints has been extended to noncylindrical Fermi surfaces in Refs. [34,49]. Using these relationships, we see that $\Delta\tilde{\beta} = \Delta\tilde{\kappa} = \Delta = 0$, $g = q/\sqrt{\mu_0 \kappa_1^2 (1 + \kappa_2/\kappa_1)/\beta_1/\hbar}$, and $v = v_k$, such that Eq. (5) reduces to Eq. (1) with the previously mentioned interpretation of v as measuring the Fermi surface anisotropy.

The weak coupling relationship $\beta_3 = 3\beta_2 - \beta_1$ constrains the system to be along the blue dashed line in parameter space in Fig. 1. This line can in turn be parametrized in terms of v such that $\beta_2/\beta_1 = (1 - v)/(v + 3)$ and $\beta_3/\beta_1 = -4v/(v + 3)$. From the discussion in the last paragraph, we can show that v can be expressed in terms of Fermi-surface averages over Fermi velocities as described below Eq. (1). From this interpretation it follows that a cylindrical, i.e., isotropic Fermi surface is equivalent with $v = 0$, while a square, i.e., anisotropic Fermi surface is equivalent with $v = \pm 1$. Going back to the interpretation of v as given in terms of the β parameters, we thus see that the Fermi surface is cylindrically symmetric for $3\beta_2 = \beta_1$, which is where the blue line crosses the x axis in Fig. 1. As v approaches 1, where the Fermi surface must be square, the system approaches the B phase. As v approaches -1 , the system approaches the C phase instead.

B. Lattice Ginzburg Landau model

The GL energy $E = \int \mathcal{F} d^3r$ in Eq. (1) is discretized on a 3D cubic lattice of points \mathbf{r} containing values for the complex fields $\eta_{\mathbf{r}}^{\pm}$ as well as link variables

$$A_{\mathbf{r},\mu} = \int_{\mathbf{r}}^{\mathbf{r} + l\hat{\mu}} A_{\mu}(\mathbf{r}) dr_{\mu} \quad (7)$$

between the points at \mathbf{r} and $\mathbf{r} + l\hat{\mu}$, where l is the lattice point separation spacing. On the lattice, $E = \int \mathcal{F} d^3r$ is written as a lattice sum over the discretized energy density

$$E = l^3 \sum_{\mathbf{r}} \mathcal{F}_{\mathbf{r}}, \quad (8)$$

where \mathbf{r} runs over the sites of the numerical lattice and the lattice energy density $\mathcal{F}_{\mathbf{r}}$ is given by

$$\mathcal{F}_{\mathbf{r}} = \mathcal{F}_{\mathbf{K}}^{\mathbf{r}} + \mathcal{F}_{\mathbf{An}}^{\mathbf{r}} + \mathcal{F}_{\mathbf{MG}}^{\mathbf{r}} + \mathcal{F}_{\mathbf{V}}^{\mathbf{r}} + \mathcal{F}_{\mathbf{A}}^{\mathbf{r}}. \quad (9)$$

This defines an effective lattice gauge theory derived from the continuum theory in Eq. (1). In Eq. (9), $\mathcal{F}_{\mathbf{r}}$ is split into various gradient terms, a potential-energy term $\mathcal{F}_{\mathbf{V}}^{\mathbf{r}}$, and a magnetic field energy density term $\mathcal{F}_{\mathbf{A}}^{\mathbf{r}}$, respectively. The gradient terms have been written as a sum of three different terms to be detailed below, namely a standard isotropic term $\mathcal{F}_{\mathbf{K}}^{\mathbf{r}}$, a term contributing to anisotropy in the kinetic energy $\mathcal{F}_{\mathbf{An}}^{\mathbf{r}}$, and a mixed gradient term $\mathcal{F}_{\mathbf{MG}}^{\mathbf{r}}$.

In the discretized energy density, covariant derivatives are treated by a forward difference scheme

$$D_\mu \eta^h = (\partial_\mu - iA_\mu) \eta^h \mapsto l^{-1}(\eta_{\mathbf{r}+l\hat{\mu}}^h e^{-ilA_{\mathbf{r},\mu}} - \eta_{\mathbf{r}}^h), \quad (10)$$

where the field value $\eta_{\mathbf{r}+l\hat{\mu}}^h$ has been parallel transported back to the point \mathbf{r} via the Abelian U(1) parallel transporter $U_{\mathbf{r},\mu} = e^{-ilA_{\mathbf{r},\mu}}$ [51]. In the following, we set the lattice spacing $l = 1$.

Writing the complex fields $\eta_{\mathbf{r}}^h$ in terms of their amplitudes $\rho_{\mathbf{r}}^h$ and phases $\theta_{\mathbf{r}}^h$, the discretized expression derived from the kinetic part of \mathcal{F} given by the covariant derivatives in Eq. (1a) is written on the standard cosine form [52]

$$\mathcal{F}_{\text{K}}^t = 2 \sum_{\mu,h} [\rho_{\mathbf{r}}^{h2} - \rho_{\mathbf{r}}^h \rho_{\mathbf{r}+\hat{\mu}}^h \cos(\theta_{\mathbf{r}+\hat{\mu}}^h - \theta_{\mathbf{r}}^h - A_{\mathbf{r},\mu})]. \quad (11)$$

Here, h denotes the two chiral components $h \in \{\pm\}$, while $\mu \in \{x, y, z\}$ and we have set the parameter $\tilde{\kappa}_5 = 1/2$ such as to make the kinetic energy density isotropic.

Introducing the notation $\bar{h} = -h$, $q \in \{x, y\}$ and the symbol $\zeta_{\alpha\beta} = 1 - 2\delta_{\alpha\beta}$, the anisotropic part of \mathcal{F} in Eq. (1b) is discretized to

$$\mathcal{F}_{\text{An}}^t = (1 + \nu) \sum_{qh} \zeta_{qy} \rho_{\mathbf{r}}^{\bar{h}} \rho_{\mathbf{r}+\hat{q}}^h \cos(\theta_{\mathbf{r}+\hat{q}}^h - \theta_{\mathbf{r}}^{\bar{h}} - A_{\mathbf{r},q}). \quad (12)$$

These terms mix the two components and give different signs of the contributions depending on the direction \hat{q} , i.e., anisotropic contributions to the kinetic energy.

The contribution $\mathcal{F}_{\text{MG}}^t$ in Eq. (9) is named the mixed gradient terms since these terms mix the gradient directions as well as the different components as seen in Eq. (1c). In the discretized form, it is given by

$$\begin{aligned} \mathcal{F}_{\text{MG}}^t = & -(1 - \nu) \sum_q \left[\rho_{\mathbf{r}}^+ \rho_{\mathbf{r}}^- \sin(\theta_{\mathbf{r}}^- - \theta_{\mathbf{r}}^+) \right. \\ & + \sum_h \zeta_{+h} \rho_{\mathbf{r}+\hat{q}}^h \rho_{\mathbf{r}}^{\bar{h}} \sin(\theta_{\mathbf{r}+\hat{q}}^h - \theta_{\mathbf{r}}^{\bar{h}} - A_{\mathbf{r},q}) \\ & \left. + \rho_{\mathbf{r}+\hat{q}}^+ \rho_{\mathbf{r}+\hat{q}}^- \sin(\theta_{\mathbf{r}+\hat{q}}^- - \theta_{\mathbf{r}+\hat{q}}^+ - (A_{\mathbf{r},q} - A_{\mathbf{r},\bar{q}})) \right], \end{aligned} \quad (13)$$

where $\bar{q} \in \{x, y\} \setminus \{q\}$.

The discretized potential part of \mathcal{F}^t is written as

$$\begin{aligned} \mathcal{F}_{\text{V}}^t = & (\rho_{\mathbf{r}}^+ \rho_{\mathbf{r}}^-)^2 (2 + \nu \cos 2(\theta_{\mathbf{r}}^+ - \theta_{\mathbf{r}}^-)) \\ & + \sum_h \left[-(\rho_{\mathbf{r}}^h)^2 + \frac{1}{2} (\rho_{\mathbf{r}}^h)^4 \right]. \end{aligned} \quad (14)$$

The first term in Eq. (14) originates with the term $2|\eta_+ \eta_-|^2 + \nu \text{Re}(\eta_+^2 \eta_-^2)$ in Eq. (1d). Of particular interest in the present context is the factor $\cos 2(\theta_{\mathbf{r}}^+ - \theta_{\mathbf{r}}^-)$. This term is minimized for $2(\theta_{\mathbf{r}}^+ - \theta_{\mathbf{r}}^-) = \pi$ for $\nu > 0$, thus potentially locking the phase difference, and breaking the global U(1) invariance of the system associated with the phase difference $\theta_{\mathbf{r}}^+ - \theta_{\mathbf{r}}^-$ down to \mathbb{Z}_2 . The last line in Eq. (14) comes from the last term in Eq. (1d) and represents a soft constraint on the fluctuations of the amplitude $\rho_{\mathbf{r}}^h$. Finally, the gauge field energy is given a noncompact discretization [53] such that $A_{\mathbf{r},\mu} \in (-\infty, \infty)$ and

$$\mathcal{F}_{\text{A}}^t = g^{-2} (\Delta \times \mathbf{A}_{\mathbf{r}})^2 = g^{-2} \sum_{\mu > \lambda} (\Delta_\mu A_{\mathbf{r},\lambda} - \Delta_\nu A_{\mathbf{r},\lambda})^2, \quad (15)$$

where $\mu, \lambda \in \{x, y, z\}$ and $\Delta_\mu A_{\mathbf{r},\lambda} = A_{\mathbf{r}+\hat{\mu},\lambda} - A_{\mathbf{r},\lambda}$.

The model in Eq. (1) has thus been formulated on a lattice in terms of two parameters, namely the coupling constant of the gauge field to the matter field g and the parameter ν describing the anisotropy of the Fermi surface. We will consider the model in this restricted parameters space to make the problem tractable in Monte-Carlo simulations. The parameter values $\nu = 0.1$ and $g = 0.3$ have been used for most of the simulation results presented in this paper.

C. XY basis and pseudo- \mathbb{CP}^1 constraint

The full Ginzburg-Landau model is still too complex to simulate on a lattice of sufficient size. Therefore, a London approximation is typically used for this kind of problem (see, e.g., Refs. [41–46]). Taking the London limit in the chiral p -wave case, however, requires special care. As discussed in detail in Ref. [47], all phase and density degrees of freedom are in general coupled. However, as discussed in the same reference, the mixing between different modes for certain parameters is small, making the London limit an adequate approximation. The required conditions that must hold in this study are: (i) the dominant length scale in magnetic field should be much larger than the core size, and (ii) the external field should be sufficiently low so that vortex cores do not overlap. Since we are interested primarily in vortex dissociation transition, the binding energy comes from mixed gradient terms, which are retained in our approximation. The low temperature configuration we obtain is consistent with the solutions found at low temperatures in the full Ginzburg-Landau model [39].

To simplify the model, we introduce a pseudo- \mathbb{CP}^1 constraint on the complex fields $\eta_{\mathbf{r}}^\pm$. Since these fields are related to corresponding xy -basis fields $\eta_{\mathbf{r}}^a$ for $a \in \{x, y\}$ through the orthonormal transformation in Eq. (3), we may rotate the expressions for the discretized free energy densities in Eqs. (14), (11), (12), and (13) back to this basis. It is this xy basis that is used in all simulations when evaluating the free energy for accepting new states through the Metropolis-Hastings algorithm, since, as we shall see, this ensures that mixed component terms are retained in the London limit.

The conventional kinetic energy contribution in Eq. (11) is invariant under the change of basis, such that

$$\mathcal{F}_{\text{K}}^t = 2 \sum_{aq} [\rho_{\mathbf{r}}^{a2} - \rho_{\mathbf{r}+\hat{\mu}}^a \rho_{\mathbf{r}}^a \cos(\theta_{\mathbf{r}+\hat{\mu}}^a - \theta_{\mathbf{r}}^a - A_{\mathbf{r},\mu})]. \quad (16)$$

The expression for the onsite potential terms, however, becomes slightly more involved, perhaps most succinctly expressed as

$$\begin{aligned} \mathcal{F}_{\text{V}}^t = & (1 + \nu) \frac{\rho_{\mathbf{r}}^{x4} + \rho_{\mathbf{r}}^{y4}}{4} + \sum_a \left[-\rho_{\mathbf{r}}^{a2} + \frac{1}{2} \rho_{\mathbf{r}}^{a4} \right] \\ & + (1 - \nu) (\rho_{\mathbf{r}}^x \rho_{\mathbf{r}}^y)^2 \left[1 + \frac{1}{2} \cos 2(\theta_{\mathbf{r}}^x - \theta_{\mathbf{r}}^y) \right]. \end{aligned} \quad (17)$$

The anisotropy term remains similar in both basis, with the xy -basis version having the form

$$\mathcal{F}_{\text{An}}^t = (1 + \nu) \sum_{aq} \zeta_{aq} \rho_{\mathbf{r}+\hat{q}}^a \rho_{\mathbf{r}}^a \cos(\theta_{\mathbf{r}+\hat{q}}^a - \theta_{\mathbf{r}}^a - A_{\mathbf{r},q}), \quad (18)$$

the minor difference being that ζ_{aq} now depends on both summation indices. Finally, the mixed-gradient terms take the form

$$\begin{aligned} \mathcal{F}_{\text{MG}}^r = & (1 - \nu) \sum_a \left[\rho_r^a \rho_r^{\bar{a}} \cos(\theta_r^a - \theta_r^{\bar{a}}) \right. \\ & - \sum_q \rho_{r+\hat{q}}^a \rho_r^{\bar{a}} \cos(\theta_{r+\hat{q}}^a - \theta_r^{\bar{a}} - A_{r,q}) \\ & \left. + \rho_{r+\hat{x}}^a \rho_{r+\hat{y}}^{\bar{a}} \cos(\theta_{r+\hat{x}}^a - \theta_{r+\hat{y}}^{\bar{a}} - (A_{r,x} - A_{r,y})) \right]. \quad (19) \end{aligned}$$

The process of discretization commutes with the basis rotation, i.e., first rotating the basis in Eq. (1) and then discretizing the result yields the same expressions for \mathcal{F}^r .

The model is now simplified by taking the London limit in the xy basis, i.e., neglecting xy -basis amplitude fluctuations such that $\rho_r^a = \rho^a \forall \mathbf{r}$. The mean field A-phase solution of Eq. (1) in the xy basis gives amplitudes $\rho^x = \rho^y = 1/\sqrt{2}$ which will be used in the following. Using the xy basis has the comparative advantage over the chiral basis in that setting the London-limit amplitudes equal to the mean field solution amplitude values does not eliminate the mixed component terms. Taking the limit in the xy basis allows the chiral basis amplitudes to fluctuate since from Eq. (3) they are related to their xy counterparts through

$$\rho_r^{\pm 2} = \frac{\rho^{x^2} + \rho^{y^2}}{2} \pm \rho^x \rho^y \sin(\theta_r^x - \theta_r^y). \quad (20)$$

From this equation, we see that the xy basis London limit implies the restriction

$$\rho_r^{+2} + \rho_r^{-2} = \rho^{x^2} + \rho^{y^2} = 1, \quad (21)$$

and in this sense the London limit in the xy basis may equivalently be viewed as a \mathbb{CP}^1 constraint on the chiral amplitudes ρ_r^h . Note that a phase locking of $\theta_r^x - \theta_r^y = \pm\pi/2$ corresponds to spontaneous time-reversal symmetry breaking in zero magnetic field, i.e., $|\eta_r^+|^2 \neq |\eta_r^-|^2$.

Since the xy -basis London limit removes two real degrees of freedom from the problem, we expect two constraints in the chiral basis as well. The second constraint takes the form of the relationship

$$\tan \theta_r^+ = \tan \left(\theta_r^- + \frac{\pi}{2} \right) \quad (22)$$

between the chiral phases. A derivation of this relationship can be found in Appendix A. This implies that $\theta^+ = \theta^- + \pi/2 + \pi n$ for $n \in \{-2, -1, 0, 1\}$ since phases are defined compactly by $\theta \in [-\pi, \pi]$. That the phases are not completely locked to each other allows there to be a vortex singularity in one component independent of the other.

D. Symmetrization and lattice potential

The discretization procedure in Eq. (10) does not in general guarantee that the resulting discrete lattice free energy is symmetric under the same transformations as the original continuum theory. It only guarantees that the continuum limit of the discrete theory satisfies these symmetries. To ensure that the lattice energy density is invariant under a fourfold rotation of the numerical lattice, we introduce a symmetrization of the

discretized xy -basis free energy density as follows

$$\mathcal{F}^s = \frac{1}{4} [\mathcal{F}^r + C_4 \mathcal{F}^r + C_4^2 \mathcal{F}^r + C_4^3 \mathcal{F}^r], \quad (23)$$

where C_4 is a counterclockwise rotation by $\pi/2$ radians about the \hat{z} axis, and we allow lattice translations because of periodic boundary conditions (see next section).

Under this rotation, we let the gauge-field link variables $A_{r,\mu}$ transform as the components of a vector field such that

$$C_4 : A_{r,\mu} = A_{C_4 r, C_4 \mu}. \quad (24)$$

Since link variables are only defined for positive directions from any numerical lattice point \mathbf{r} , we use the relationship $A_{r,-\mu} = -A_{r-\hat{\mu},\mu}$ whenever the transformation in Eq. (24) results in a negative link direction. As a nontrivial example $C_4 : A_{r+\hat{x},y} = -A_{C_4 r+\hat{y}-\hat{x},x}$.

To figure out how the complex fields η_a transform, we remember that they are the coefficients of the vector $\mathbf{d} = \sum_a \eta_a \mathbf{b}_a$ whose basis vectors $\{\mathbf{b}_a\}$ transform according to the irreducible representation Γ_{5u} [48]. Inserting the C_4 representation matrix then yields the transformation

$$C_4 : \begin{pmatrix} \eta_r^x \\ \eta_r^y \end{pmatrix} = \begin{pmatrix} 0 & -1 \\ 1 & 0 \end{pmatrix} \begin{pmatrix} \eta_{C_4 r}^x \\ \eta_{C_4 r}^y \end{pmatrix} = \begin{pmatrix} -\eta_{C_4 r}^y \\ \eta_{C_4 r}^x \end{pmatrix}. \quad (25)$$

Inserting this transformation into the continuous free energy density \mathcal{F} in Eq. (2), and remembering to also transform the covariant gradients, it is readily verified that all terms are invariant under C_4 as indeed they need to be since $C_4 \in D_{4h}$. For the discretized xy -basis version of the same free energy in Eqs. (11)–(15), it is then similarly possible to check that all terms are invariant under C_4 except for the mixed gradient terms in Eq. (19). The reason why this term is not symmetric but the continuum version is, is again that the forward difference discretization procedure in Eq. (10) introduces artificial anisotropies in the system; usually referred to as lattice potentials and does not in general guarantee that the discretized version satisfies all continuum symmetries. In this particular case, it manifests as an explicit asymmetry because the gradients are in different directions in the same term.

Since all other terms than the mixed gradient terms are already symmetric w.r.t. C_4 , it suffices to only present the rotated version of this particular term when calculating the symmetrized lattice free energy density \mathcal{F}^s . The details of this expression can be found in Appendix B.

E. Boundary conditions and Landau gauge

The gauge field link variables are split into a fluctuating and a constant part such that $A_{r,\mu} = A_{r,\mu}^f + A_{r,\mu}^c$. Periodic boundary conditions are used in the fluctuating part $A_{r,\mu}^f$, as well as in the discretized field components such that $\eta_r^a = \eta_{r+L_\mu}^a$. For the constant part $A_{r,\mu}^c$, twisted boundary conditions are used by employing the extended Landau gauge forcing a fixed magnetic flux through the system. The extended Landau gauge is given by

$$A_{r,q}^c = \frac{2\pi m_q}{L_q} r_q, \quad A_{r,z}^c = 0, \quad (26)$$

where $m_q \in \mathbb{Z}$ and the conditions in Refs. [54,55] have already been incorporated. This definition makes the full link

variable boundary conditions periodic modulo 2π , which prevents geometric frustration. Equation (26) together with periodic boundary conditions for $A_{\mathbf{r},\mu}^f$ forces the system to satisfy the property $\oint \mathbf{A} \cdot d\mathbf{r}_\perp = 2\pi f L_x L_y$. This gives a magnetic flux $\mathbf{B} = 2\pi f \hat{z}$ through the system for filling fraction

$$f = \frac{m_y}{L_x} - \frac{m_x}{L_y}. \quad (27)$$

The filling fraction then gives the number of magnetic field vortex quanta per plaquette in the xy plane. In the results presented in this paper the choice $m_y = 1, m_x = 0$, which reduces the gauge to the normal Landau gauge, has been used for a system with $L_x = L_y = 64$ which yields $f = 1/64$. The qualitative conclusions have however been tested for the symmetric choice $m_y = 1, m_x = -1$. This choice is symmetric in the sense that in this case we may write $\mathbf{A}^c = -\mathbf{r} \times \mathbf{B}/2$ for $\mathbf{B} = 4\pi/L\hat{z}$.

III. DETAILS OF THE NUMERICAL CALCULATIONS

A. Monte-Carlo update method

For the Monte-Carlo simulations, the Metropolis-Hastings method [56] was used to sample states with a probability distribution given by the free energy in Eq. (9). This method fulfills the detailed-balance criteria such that importance sampling gives thermodynamic averages as simple arithmetic averages over the sampled states [57–59]. This method, as well as all other numerics, was implemented in the Julia programming language [60] version 1.0.3.

As described in Sec. II B, the free energy was discretized on a cubic lattice of size $L_x \times L_y \times L_z$. Each lattice point contains one fluctuating variable for each of the xy -basis phases: θ_r^x and θ_r^y , and three fluctuating link variables for the gauge field, one for each direction of space: $A_{\mathbf{r},x}$, $A_{\mathbf{r},y}$, and $A_{\mathbf{r},z}$. A Monte-Carlo update consists in this case of proposing new values of all these variables, which proposes a new state of a single lattice point and then rejecting or accepting this state according to the Metropolis-Hastings method. A Monte-Carlo sweep then consists of doing this for each individual lattice point. New values of the phases were proposed uniformly on an open interval $\theta_r^x, \theta_r^y \in [0, 2\pi)$ using the Julia `rand()` function which uses the Mersenne-Twister algorithm [61]. The gauge-field link variables were updated by a uniformly distributed random value $A'_{\mathbf{r},q}$ in a symmetric region centered on the previous value $A_{\mathbf{r},q}$, such that $A'_{\mathbf{r},q} - A_{\mathbf{r},q} \in [-A, A]$. The parameter A which sets the size of the region was set to $A = 0.1$ based on the fact that at this value at high temperature, the percentage of proposed states that were accepted was $\sim 30\%$.

In order to facilitate efficient computation on highly parallelized computer systems, the numerical lattice was divided into sublattices that communicated with each other as their lattice points were updated. The number of sublattices was chosen according to what gave the fastest average performance of Monte-Carlo sweeps, which for cubic systems of size $L = 64$ turned out to be 16 sublattices. A single MC sweep was then performed in, on average, 0.11 ± 0.01 s.

B. Observables

To study the model in Eq. (1) in the chiral basis, the xy -basis variables were converted into their chiral counterparts through Eq. (3). Since the trigonometric formulas for obtaining the chiral phases θ_r^h diverge when $|\eta_\pm| \rightarrow 0$, these were expanded to fourth order to handle this case. The technical details of this can be found in Appendix C.

To characterize the vortices, we calculate the curl of the gauge-invariant phase difference of each chiral component, namely $(\nabla \times (\nabla \theta_r^h - \mathbf{A})) / 2\pi$. This amounts to calculating the lattice curl of the gauge-invariant phase difference $\Delta_q \theta_r^h - A_{\mathbf{r},q}$ around a fundamental plaquette of the numerical lattice. By adding the constant magnetic flux density f , we obtain a quantity which we will call the local vorticity of each component [53]

$$n_{\mathbf{r},z}^h = \frac{1}{2\pi} \epsilon_{zij} \Delta_i (\Delta_j \theta_r^h - A_{\mathbf{r},j})_\pi + f, \quad (28)$$

where implicit summation over indices is understood and ϵ_{zij} is the Levi-Civita symbol. $(\phi)_\pi$ is shorthand notation for $\text{mod}(\phi + \pi, 2\pi) - \pi$, which draws the argument back into the primary interval $[-\pi, \pi]$. The filling fraction f is defined in Eq. (27) and gives the number of fundamental vortex quanta per planar plaquette as determined by the extended Landau gauge [53,62,63]. Note that $\Delta_q \theta_r^h - A_{\mathbf{r},q}$ in general does not give the current of each component in the p -wave case, but is sufficient to distinguish the structure of vortices and to compare with the results in Ref. [39]. The z -averaged vorticity is then naturally defined as

$$n_{\mathbf{r}_\perp,z}^h = \frac{1}{L_z} \sum_{r_z=0}^{L_z-1} n_{\mathbf{r},z}^h, \quad (29)$$

which is used through its thermal average $\langle n_{\mathbf{r}_\perp,z}^h \rangle$ in order to obtain detailed information about the real space structure of the vortex lattices as well as of the vortex cores in the present model.

A related observable is the z -averaged gauge invariant chiral phase difference

$$\delta \theta_{\mathbf{r}_\perp} = \left\langle \frac{1}{L_z} \sum_{r_z=0}^{L_z-1} (\theta_r^+ - \theta_r^-)_\pi \right\rangle, \quad (30)$$

where $\langle \cdot \rangle$ denotes thermal averaging. This observable is also useful in studying the nature of the vortices.

To extract a clearer picture of the overall spatial correlations of the vortex lattice we define the structure function

$$S^h(\mathbf{k}_\perp) = \frac{1}{(f L_x L_y)^2} \left\langle \left| \sum_{\mathbf{r}_\perp} n_{\mathbf{r}_\perp,z}^h e^{i \mathbf{k}_\perp \cdot \mathbf{r}_\perp} \right|^2 \right\rangle, \quad (31)$$

which essentially amounts to taking the planar Fourier transform of the z -averaged vorticity. The fast-Fourier algorithm was used to efficiently compute the structure function for all Bragg points \mathbf{k}_\perp . The structure function is normalized such that $S^h(\mathbf{0}) = 1$.

For any vortex lattice signature, the structure function is expected to exhibit peaks at characteristic Bragg points situated equidistantly from the origin. For a hexagonal lattice we expect six peaks with $\pi/3$ mutual angular distance, while

for a square lattice we expect four peaks with $\pi/2$ mutual angular distance. To distinguish these two signals clearly, the histogram

$$h(\delta\Delta\phi^h) = \frac{1}{\delta\Delta\phi^h |\{\Delta\phi_i^h\}|} \sum_{\{\Delta\phi_i^h\}} \delta_{\Delta\phi_i^h \in \delta\Delta\phi^h} \quad (32)$$

is constructed, where $\delta\Delta\phi^h$ is some angular interval bin. The angular distances $\Delta\phi_i^h$ are obtained by calculating $S^h(\mathbf{k}_\perp)$ using a certain number of Monte-Carlo measurements, then finding the radius $|\mathbf{k}_\perp|_m$ which yields the largest value of $\int_0^{2\pi} S^h(|\mathbf{k}_\perp|, \phi) d\phi$. A ribbon is then constructed around this radius from which the largest value of $S^h(\mathbf{k}_\perp)$ is picked for each angle such that

$$S^h(\phi) = \max\{S^h(|\mathbf{k}_\perp|, \phi) : ||\mathbf{k}_\perp| - |\mathbf{k}_\perp|_m| < k_r\}. \quad (33)$$

The angular positions $\{\phi_i\}$ of the six highest peaks in $S^h(\phi)$ are then found. Finally all mutual distances between these positions are found $\{\Delta\phi_i\} = \{|\phi_k - \phi_j| : \phi_k < \phi_j\}$ which is used to calculate the histogram $h(\delta\Delta\phi^h)$. The process is repeated for independent Monte-Carlo measurements of $S^h(\mathbf{k}_\perp)$ until there are sufficient $\Delta\phi_i$ to construct the histogram.

The above quantities, taken together, provide considerable information on not only the symmetry of the vortex lattices at various temperatures but also on the structure of the vortex cores corresponding to each lattice symmetry. The critical temperature at the position of the upper critical field crossover line $H_{c2}(T)$ was found by examining the specific heat

$$C_v = \beta^2 (\langle E^2 \rangle - \langle E \rangle^2) \quad (34)$$

and a chiral order parameter that we will now describe. The Higgs field components η^+ and η^- are related through the time-reversal transformation, hence a difference in their density signify a spontaneous breaking of \mathbb{Z}_2 time-reversal symmetry. Since this density can be measured by the component amplitudes, a useful chiral order parameter is given by

$$\begin{aligned} \delta u^2 &= \left\langle \left(\frac{1}{L_x L_y L_z} \sum_{\mathbf{r}} (\rho_{\mathbf{r}}^{+2} - \rho_{\mathbf{r}}^{-2}) \right) \right\rangle \\ &= \frac{2\rho^x \rho^y}{L_x L_y L_z} \left\langle \left(\sum_{\mathbf{r}} \sin(\theta_{\mathbf{r}}^x - \theta_{\mathbf{r}}^y) \right) \right\rangle. \end{aligned} \quad (35)$$

From the last line it is clear that it is the locking of the xy phase difference that is responsible for the breaking of time-reversal symmetry.

C. Thermalization and measurement steps

Before measurements of observables were performed, the lattice was initialized with random values for all fluctuating variables at each lattice point, resulting in high energy states. Then, a two-step thermalization procedure was done which consisted of a stepwise decrease in temperature to decrease the chance of a metastable state, followed by a number of basic Monte-Carlo sweeps (thermalization). The steps during the cooldown procedure were distributed as a geometric series between a high and low temperature, so that more MC sweeps would be concentrated at lower temperatures. During cooldown, $\approx 1.3 \times 10^5$ MC sweeps were distributed

equally on 1024 temperature steps. This was then followed by $\approx 1.3 \times 10^5$ additional MC sweeps that were discarded before measurements began. To confirm that this yielded a properly thermalized state, we checked that the internal energy of the system as a function of MC time had converged and remained stable during measurements.

256 intermediate MC sweeps were performed between each measurement to diminish autocorrelation effects. The number of measurements of observables varied between simulations, from 1024 for sampling at high temperatures, to 4096 when estimating C_v close to the phase transition.

Measurements were performed sequentially by lowering the temperature, such that the last state of the lattice in the measurement series at one temperature was used as the initial state when thermalizing the simulation for the next lower temperature. To prevent the simulation from getting stuck in a metastable state, several series of simulations were performed using independent initial states to verify the validity of the results.

D. Post-processing

Multihistogram Ferrenberg-Swendsen reweighting [64,65] was used to calculate the specific heat C_v accurately at temperatures close to the peak in C_v . The nonlinear Ferrenberg-Swendsen equations for free energy were solved self-consistently and iteratively using the Julia NLsolve library in which automatic forward differentiation was used to find the Jacobian and a trust-region method was used as the iterative algorithm [66].

The jackknife method [67] and Ferrenberg-Swendsen reweighting [64,65] were used to compute averages and uncertainties of observables. The number of blocks dividing the measurement series in the jackknife method was set to 128. This gave a block length where the estimate of variance had leveled off, indicating that autocorrelations had effectively been reduced.

IV. LATTICE STRUCTURES

Before we present our numerical results based on our large-scale Monte-Carlo simulations, we provide a schematic introduction to the results to assist the reader. In Fig. 2, we show schematically vorticities and phase windings that we expect to find for two different types of vortices. In the following, the notation will be as follows. A phase winding in chiral component η_+ of $2\pi n_+$ and in chiral component η_- of $2\pi n_-$ will be denoted (n_+, n_-) . A vortex with $(n_+, n_-) = (1, -1)$ will be denoted as singly quantized. A vortex with $(n_+, n_-) = (2, 0)$ will be denoted as doubly quantized.

For a singly-quantized vortex, the vorticity is expected to have a magnetic field-profile centered at the origin, with a maximum magnetic field at the origin, see Fig. 2(a). The corresponding phase winding is shown in Fig. 2(c). Note the fourfold symmetry in the color pattern, the radial monotonicity in the phase value away from the origin, and the 2π discontinuity along the horizontal axis. For a doubly-quantized vortex, the vorticity is expected to have a magnetic field profile centered at the origin, with a minimum magnetic field at the origin and a ring of maxima away from the origin,

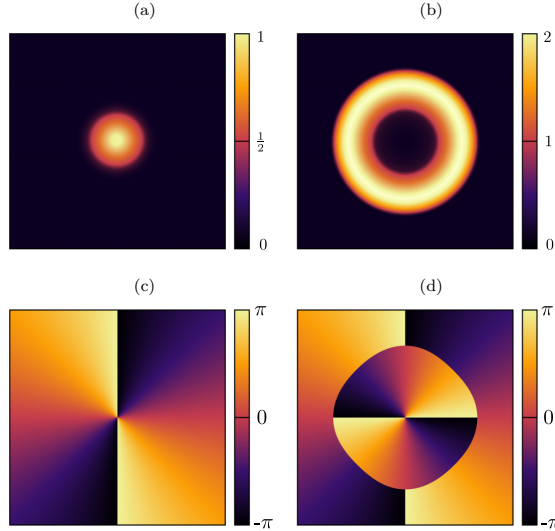


FIG. 2. Schematic of vorticities and corresponding phase difference signature $\theta^+ - \theta^-$ of vortices for $H > 0$. (a) and (c) shows vorticity and phase difference, respectively, for a singly-quantized vortex with winding number $n_+ = 1$ and $n_- = -1$. (b) and (d) shows vorticity and phase difference, respectively, for a doubly-quantized vortex with winding number $n_+ = 2$ and $n_- = 0$. The figures are directly based on the ones presented in Ref. [39].

see Fig. 2(b). The corresponding phase winding is shown in Fig. 2(d). The main difference from the phase winding in Fig. 2(c) is the inner circle close to the origin, where phase windings are rotated by $\pi/2$ compared to the phase windings in Fig. 2(c). For a detailed discussion of this point, see also Sec. III of Ref. [39].

This will be our main diagnostic tool for identifying whether vortices are singly or doubly quantized. As a check on this, we will count the total vorticity in each component and check that this corresponds to the total vorticity of the system, given by the external magnetic field.

In the following, we focus on results obtained for the parameter set $v = 0.1$, $g = 0.3$, $f = 1/64$. The parameter $v = 0.1$ corresponds to a moderately fourfold anisotropic Fermi surface. To set the temperature scale of our finite-field simulations, we have found it useful to first perform Monte-Carlo simulations in zero field to locate the maximum of the specific heat C_v . This maximum occurs at $T \approx 2.016 \pm 0.002$ for $f = 0$, which we denote as the critical temperature T_c of the superconductor. A rounded and suppressed peak in the specific heat persists at $f > 0$. For $f = 1/64$, this rounded peak (no longer a phase transition) occurs at $T = 1.86 \pm 0.04$. $T = 1.86$ is therefore a natural temperature scale for the vortex system at $f = 1/64$. For this filling fraction, we only expect to see vortex lattice structures for $T < 1.86$.

We will mainly present results starting with high temperatures and then proceeding to lower temperatures. At high temperatures, we will find a plasma phase totally dominated by thermally induced vortex loops. Proceeding to lower temperatures where a vortex-lattice forms, we find a singly-

quantized square vortex lattice. Lowering the temperatures further, we eventually find a doubly-quantized hexagonal lattice. At the end, we briefly discuss a “mixed” phase of singly-quantized and doubly-quantized vortices, located at intermediate temperature between the doubly-quantized and singly-quantized vortex lattice phases.

A. Specific heat and chiral order parameter

To investigate what the relevant temperature scale in our system is, we have performed Monte-Carlo simulations computing the specific heat and chiral order parameter at $f = 0$ and $f = 1/64$. Figure 3 shows the specific heat as a function of temperature at $f = 0$. A sharp peak is seen at a temperature $T = 2.016 \pm 0.002$ and marks the phase transition from the superconducting to the normal state. Also shown is the specific heat at $f = 1/64$, which at $T^* = 1.86 \pm 0.04$ shows a broadened and suppressed peak compared to $f = 0$. This peak marks the finite-field crossover to the normal state. In what follows we will refer to this crossover temperature as $T^*(f)$.

The inset shows the chiral order parameter as a function of T at $f = 0$ and $f = 1/64$. For $f = 0$, it vanishes at the same temperature as the sharp peak in the specific heat is located and shows that the $f = 0$ phase transition in this model is associated with spontaneous time-reversal symmetry breaking. For $f = 1/64$, the presence of a magnetic field explicitly breaks time-reversal symmetry by selecting a preferred chirality, which leads to a finite order parameter at $T^*(f)$.

These results form a useful background for choosing relevant temperatures at which to study vortex-lattice states at finite f . Below, we will study such vortex states in the temperature regime $T \in [1.5–1.8]$, and from the above results we conclude that these represent significant temperatures on the scale of the critical temperature T_c . Hence, our Monte-Carlo simulations at such temperatures will yield useful information concerning the thermal stability of the vortex states we find.

B. Vortex states upon lowering temperature

1. Plasma state

For $f = 1/64$ and at high temperatures $T \gtrsim 1.90$, the superconductor is in a normal state where thermal fluctuations have induced a proliferation of massive amounts of closed vortex loops in the system. The resulting state is therefore a vortex-plasma phase. This leads to the tableau shown in Fig. 4, which depicts results of simulations at $T = 2.0$. The uniform distribution of vorticity in space leads to a circular pattern at low k -vector magnitude with increasing value with increasing magnitude of the k vector. At higher k -vector magnitude, the value of the structure function exhibits a square anisotropy with higher values close to $\mathbf{k}_{\text{corners}} = \pi(1 - 2n, 1 - 2m)$ for $n, m \in \{0, 1\}$. This anisotropy is due to short range correlations since as \mathbf{k} approaches $\mathbf{k}_{\text{corners}}$, \mathbf{k} measures shorter and shorter correlations because of periodic boundary conditions. At these length scales, the quadratic numerical lattice upon which the continuum model has been discretized gains significance and leads to the apparent anisotropy. The limits of the color bar reveal that this anisotropy is very small, with a maximum value less than 0.010. There is no real signal of

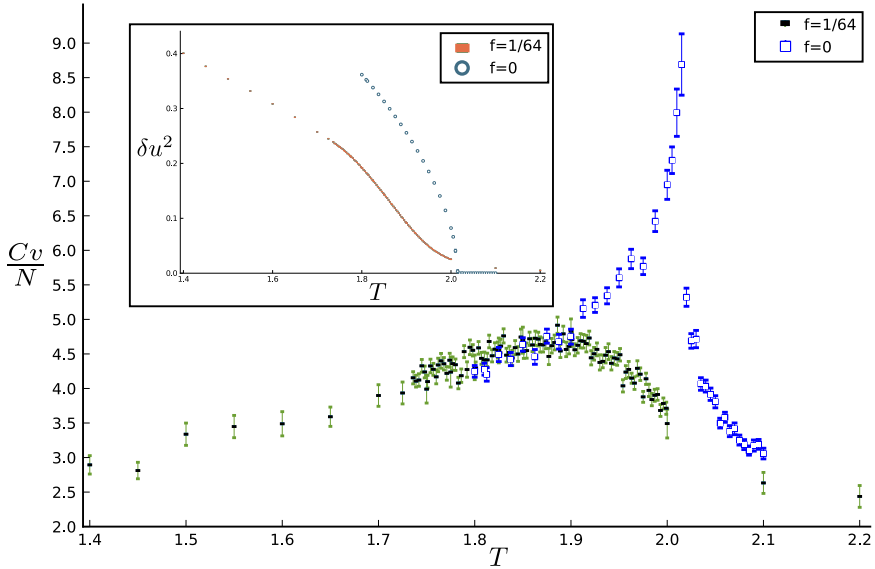


FIG. 3. Specific heat dependence on temperature for a system with $g = 0.3$, $v = 0.1$, and $L = 64$. The blue points marked by a hollow square are for $f = 0$, while the green dataset with points marked by a black dash is for a system with $f = 1/64$. The inset shows the chiral order parameter δu^2 for the two filling fractions $f = 0$ and $1/64$, with azure circles showing $f = 0$ while orange dashes show $f = 1/64$. In the inset, the error bars are for the most part too small to be seen.

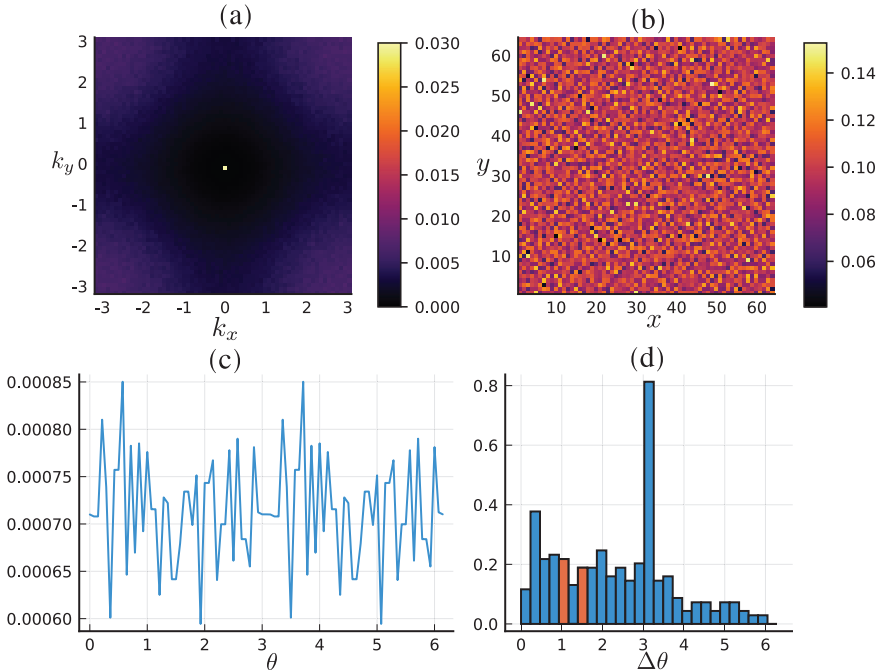


FIG. 4. Vortex state at $T = 2.0$ for a system with $v = 0.1$, $g = 0.3$, and $f = 1/64$. The system is dominated by thermally induced vortices. (a) Thermal average of the structure function. (b) Thermal average of real space vorticity. (c) Angular dependence of the structure function in a circular thin annulus around $\mathbf{k} = 0$. (d) Histogram of angular difference $\Delta\theta$ between peaks in the angular dependence of the structure function. The colored bars are the bins that include $\Delta\theta = \pi/3$ and $\Delta\theta = \pi/2$. These would correspond to hexagonal and square lattices, respectively.

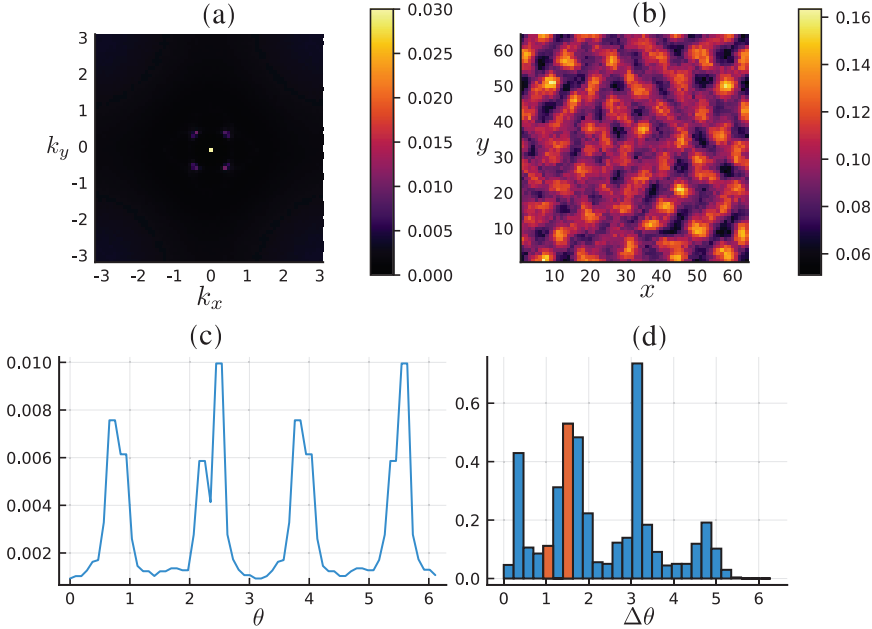


FIG. 5. Singly-quantized square vortex lattice state for a system with $v = 0.1$, $g = 0.3$, $f = 1/64$, and $T = 1.786$. (a) shows the structure function of a square vortex lattice. (b) shows the vortex lattice structure in real space. The vortices are located at the bright spots. All vortices have a field maximum at the center of the vortex, cf. Fig. 2(a), consistent with singly-quantized vortices. (c) shows the fourfold angular distribution of the structure function. (d) shows a histogram of the angular difference between peaks in the structure function. The colored histograms denote angular difference between peaks in the structure functions corresponding to $\pi/3$ and $\pi/2$. The dominant peaks are found at $\Delta\theta = \pi/2$, π , and $3\pi/2$, corresponding to a square lattice.

vortex-lattice correlations detected at this temperature. The histogram in Fig. 4(d) reveals a large spike at $\Delta\theta = \pi$. This originates with the fact that the Fourier transform has the property $\mathcal{F}(\mathbf{k}) = \mathcal{F}(-\mathbf{k})^*$, such that the structure function is equal at \mathbf{k} and $-\mathbf{k}$.

2. Singly-quantized square vortex lattice

We next discuss the vortex lattice state that first emerges as the temperature is lowered below the crossover temperature to the normal state, which is $T^* = 1.86$ at $v = 0.1$, $g = 0.3$, and $f = 1/64$. Figure 5 shows the results of Monte-Carlo simulations performed at $T = 1.786$, computing the structure function (a), vorticities (b), angular distribution of peaks in the structure function (c), and histograms of angular difference between peaks in the structure function (d). The structure function clearly has fourfold symmetry, such that the vortex lattice is square. This is also discernible in panel (b), although less obvious than in (a). The angular dependence of the structure function shown in (c) shows four clear peaks separated by $\pi/2$. The histograms of $\Delta\theta$ in (d) show that the most dominant nontrivial bin is $\pi/2$, marked by the orange bar. The broadening around the large orange bar is due to thermal fluctuations. The smaller orange bar represents the counts at angular difference of $\pi/3$, corresponding to a hexagonal lattice. The square lattice peak dominates the hexagonal peak, leading to the conclusion that the symmetry of the lattice is square, consistent with the result for the structure function in

(a). The peak in (d) at low angular value is attributed to the square lattice peaks being jagged due to the temperature being close to T_c .

Figure 5(b) shows the square lattice structure as a real space average. One notable feature of the results of Fig. 5, apart from the square vortex-lattice structure shown in (a), is that the magnetic field maximum associated with the vortices in (b) are located at the center of the vortices. Referring back to our discussion of Fig. 2, we see that this is consistent with singly-quantized vortices in each chiral component ($n_+ = 1$, $n_- = -1$).

The nature of these points of increased vorticity is investigated further by comparing the position of these points with a real-space plot of average local phase difference between the two components: $\langle \theta_r^+ - \theta_r^- \rangle$ in Fig. 6. The figures show that points of increased vorticity correspond well with intersections between two regions of positive average phase difference and two regions of negative average phase difference. This corresponds to the same phase-difference pattern that is depicted in Fig. 2(c), again characteristic of singly-quantized vortices.

The single quantum nature of the vortices is further corroborated by the fact that the boundary conditions enforce a total of 64 quanta of magnetic flux at any step of the Monte-Carlo simulations. In Fig. 5, there are 62 clearly identifiable points of increased vorticity. It could be that the system shows 62 single-quanta vortices and the remaining two vortices are too thermally distorted to form enough of a coherent thermal

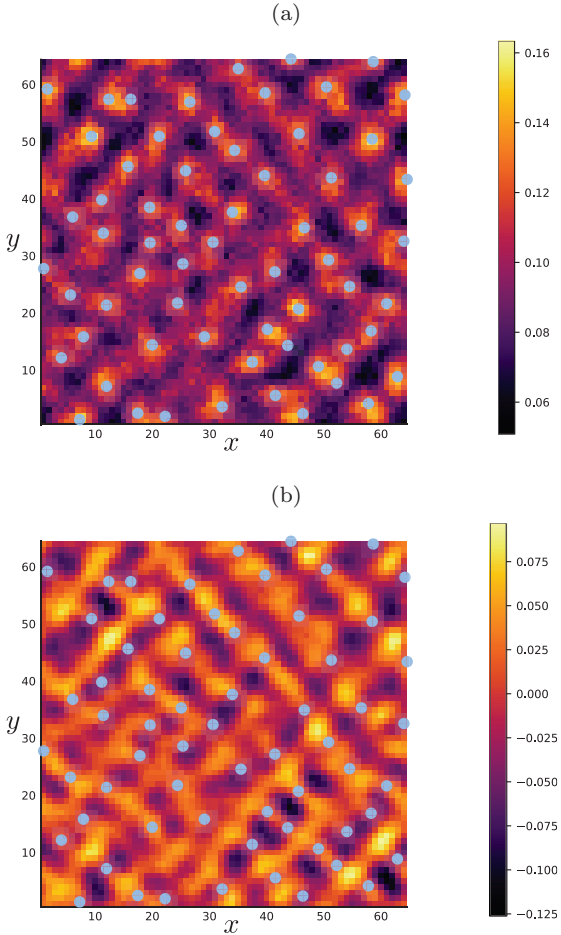


FIG. 6. Vortex positions and phase differences for the parameters used in Fig. 5. (a) shows an enhanced version of Fig. 5(b). The center of each vortex is marked by a green dot. The blue dots mark the positions of increased vorticity in the real space average. This corresponds to a maximum of the magnetic field at the center of the vortex, cf. the schematics of Fig. 2(a). (b) shows the phase difference around each vortex, whose position is indicated by a green dot. Note the fourfold symmetry of the phase-difference pattern around the vortices, cf. the schematics of Fig. 2(c). (a) and (b) corroborate, along with the results of Fig. 5, that at ($f = 1/64, T = 1.786$) the vortex lattice is a singly-quantized square lattice.

average to be identified, or it could be that the system has 60 single quanta vortices and two double-quanta vortices. In any case, it is clear that the vortex state is dominated by singly-quantized vortices.

The superconducting field amplitude of conventional superconductors is suppressed in the presence of vortices. In the case of a two-component field, the subdominant component may be induced in the vicinity of the vortex core where the dominant component is suppressed [39]. This is evident in Fig. 7 where the dominant component amplitude ρ^+ on the left exhibits dark regions that correspond to the location of

increased vorticity in Fig. 5(b) and Fig. 6(a). On the right, the subdominant component exhibits increased amplitude in these regions as is required by the pseudo- \mathbb{CP}^1 constraint in Eq. (21). We conclude from this that the stable vortex state at $v = 0.1, g = 0.3, f = 1/64, T = 1.786$ is a singly-quantized square vortex lattice.

3. Doubly-quantized hexagonal vortex lattice

We next consider the system at $f = 1/64$ and a lower temperature $T = 1.5$. The plot of the average structure function in Fig. 8(a) shows six clear, equidistantly placed peaks. Figure 8(b) shows the average vorticities in real space. The vorticity distribution around each vortex is clearly of the same type as depicted in Fig. 2(b), characteristic of doubly-quantized vortices. The angular dependence of the structure function in a thin annulus around $\mathbf{k} = 0$ is shown in Fig. 8(c), where six clear equidistantly placed peaks are seen. This is again reflected in the histogram for $\Delta\theta$ in Fig. 8(d) where a large peak is observed at $\Delta\theta = \pi/3$ followed by peaks at integer multiples of this. The real space vorticity average shows 32 independent ring structures (note that periodic boundary conditions have been used), which indicates that each structure has two quanta of magnetic flux.

Figure 9(a) shows an enhanced version of Fig. 8(b). The ringlike structure of enhanced vorticity surrounding the center of each vortex is clearly seen, consistent with what is depicted in Fig. 2(b). This is indicative of doubly-quantized vortices ($n_+ = 2, n_- = 0$). The double quantum nature of the vortices is also observed in the plot of real space phase difference average in Fig. 9(b). It shows a clear inner 4π phase change at low radius from the vortex center, where positive phase difference is observed at an angle $\pi/4$ and $5\pi/4$ from the vortex center and negative phase difference at $3\pi/4$ and $7\pi/4$. This pattern is repeated at larger radii away from the vortex core but then rotated by $\pi/2$ degrees giving the vortices a distinct core structure not observed in the single-quantum case. It is finally noted that the real space average vorticity in Fig. 8 shows decreased vorticity in the vortex core for the positive component.

The component amplitudes in Fig. 10 again reflect the hexagonal lattice pattern in Figs. 8 and 9. The dominant component on the left is clearly seen to be suppressed in the vicinity of the vortex cores, while the amplitude plot of the subdominant component on the right shows that this component is coincidentally induced.

The conclusion is thus that the simulations at $f = 1/64, T = 1.5$ clearly show a hexagonal lattice of doubly-quantized vortices. Our simulations show that these doubly-quantized vortex states remain stable down to the lowest temperatures we have considered and persist up to temperatures of $T = 1.7$. The temperature regime $T \in [1.7-1.75]$ will be discussed further below.

4. Mixed doubly and singly quantized vortex lattices

We next discuss the temperature regime where the transition from a higher-temperature singly-quantized square vortex lattice to a lower-temperature doubly-quantized hexagonal vortex lattice takes place. For $f = 1/64$, the transition takes place in the narrow range $T \in [1.73-1.775]$. Recall

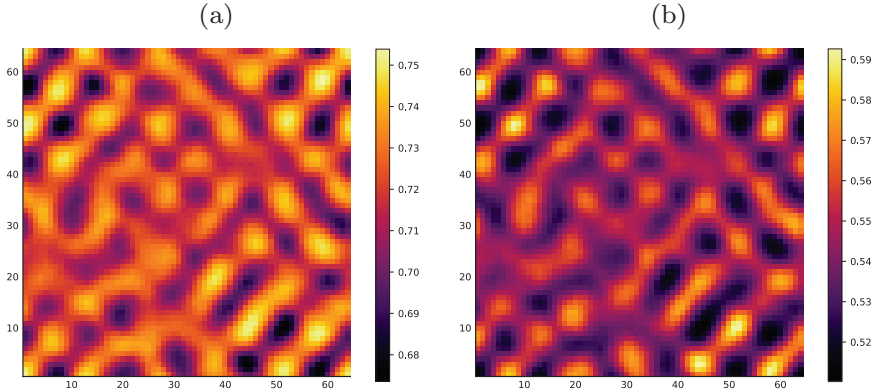


FIG. 7. Component amplitudes averaged in the z direction for a system with $v = 0.1$, $g = 0.3$, $f = 1/64$, and $T = 1.786$. (a) shows $\langle \rho_{r\perp}^+ \rangle$ while (b) shows $\langle \rho_{r\perp}^- \rangle$. The color limits are set to amplify the spatial dependence, but we note that the average of ρ^+ is significantly higher than ρ^- .

that the zero-field transition takes place at $T_c = 2.016$ and the crossover temperature to the normal state at $f = 1/64$ is $T \approx 1.86$. The four tableaus in Fig. 11 show examples of states of the system at intermediate temperatures $T = 1.7$, 1.725 , 1.742 , $T = 1.751$.

At $T = 1.7$ and $T = 1.725$, the dominant structure is a doubly-quantized hexagonal vortex lattice. The structure function of the vortex lattice is predominantly hexagonal, see

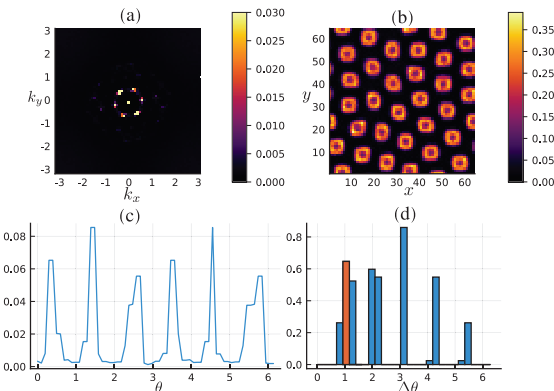


FIG. 8. Doubly-quantized hexagonal vortex lattice state for a system with $v = 0.1$, $g = 0.3$, $f = 1/64$, and $T = 1.5$. (a) shows the structure function, showing a hexagonal lattice. (b) shows the lattice structure in real space. Vortices are located at the dark spots surrounded by a bright ring. All vortices have a vorticity maximum distributed in a ring around the center of the vortex, and a careful count shows that there are 32 such doubly-quantized vortices, consistent with the system size $L_x \times L_y = 64 \times 64$ and $f = 1/64$. This vortex distribution is to be compared with the schematics of the upper right panel of Fig. 2. (c) shows the sixfold angular distribution of the structure function. (d) shows a histogram of the angular difference between peaks in the structure function. The colored histogram corresponds to an angular difference between peaks in the structure function of $\pi/3$. We see that the dominant peaks are found at $\Delta\theta = \pi/3$ and $2\pi/3$, which corresponds to a hexagonal lattice.

Figs. 11(a) and 11(e), but note the weakening of four of the peaks in the structure function in Fig. 11(e) compared to 11(a). $\langle n_{r\perp,z}^h \rangle$ in Figs. 11(b) and 11(f) shows vortices characterized by a center with low vorticity surrounded by a ring of higher vorticity. In this background, vortex structures start to appear that have a center of high vorticity, characteristic of singly-quantized vortices. Increasing the temperature further, the hexagonal pattern in the structure function is gradually replaced by a square pattern.

At $T = 1.742$, the structure function features two strong peaks at opposite wave vectors, with two weaker peaks in the orthogonal directions. The overall symmetry of the structure function is now closer to one characteristic of a square lattice, see Fig. 11(i). Namely, the four weaker spots in the sixfold symmetric structure functions in Figs. 11(a) and 11(e) have moved closer to each other. Although there is still a considerable number of doubly-quantized vortices present, i.e., vortices with low vorticity at the center surrounded by a ring of higher vorticity, it is evident that a substantial number of singly-quantized vortices have appeared, see Fig. 11(j).

Increasing the temperature slightly to $T = 1.751$, this becomes more pronounced. In Fig. 11(m), the fourfold symmetry of the structure function is evident, while Fig. 11(n) shows that there are still doubly-quantized vortices present. The transition from hexagonal to square vortex lattices upon increasing the temperature from $T = 1.7$ to $T = 1.75$ is mirrored in the peak-distance histogram with the bin at $\Delta\theta = \pi/3$ losing value and eventually being superseded by the bin at $\Delta\theta = \pi/2$, see Figs. 11(c), 11(g), 11(k), and 11(o), as well as Figs. 11(d), 11(h), 11(l), and 11(p).

For a clearer picture of the temperature range over which this transition happens, we have computed the temperature dependence of these two histogram bins, shown in Fig. 12. The bin at $\Delta\theta = \pi/3$ (hexagonal vortex lattice) clearly dominates at lower temperatures and becomes equal in height to the bin at $\Delta\theta = \pi/2$ (square vortex lattice) at $T \approx 1.75$. The temperature dependence of the two bins mirrors the dissociation of double quanta vortices into single quanta vortices which we have noted is already starting at $T \approx 1.7$. The histogram bins approach the value $h^+(\delta\Delta\theta) = 1/2\pi$ after the $U(1)$ crossover

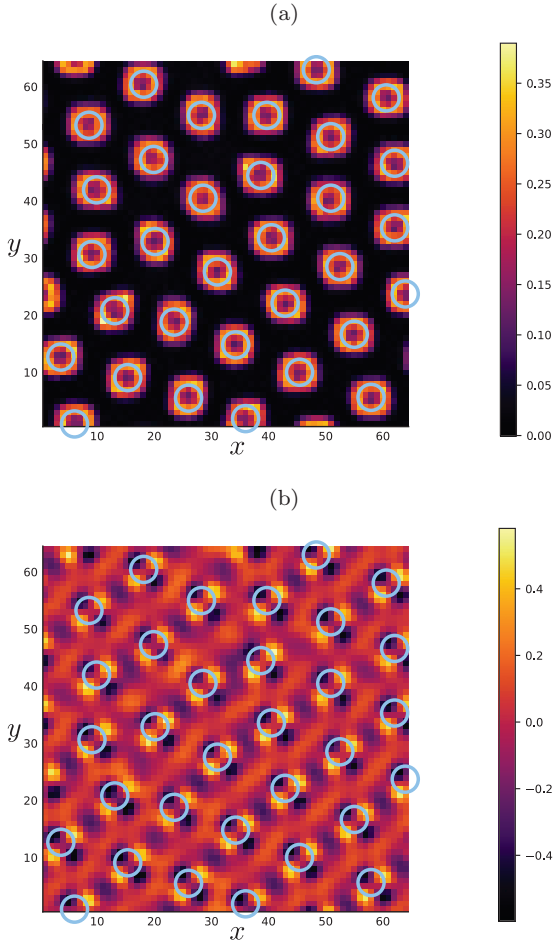


FIG. 9. Phase difference and + vorticity of the system in Fig. 8. The blue circles represent rings with increased vorticity in (a). These rings are then overlaid on the real space average of phase difference in (b).

transition, which is an equal weight of the histogram on all bins. The lack of angular variations in the structure function means that the system is in the vortex plasma phase.

The temperature regime in which the lattice reconstruction takes place is thus rather narrow and close to the $H_{c2}(T)$ crossover line. This is consistent with previous computations that ignored thermal fluctuations [39], where the transition was induced by increasing the strength of the magnetic field up to values close to H_{c2} .

V. COMPARISON WITH MEAN-FIELD THEORY

Figure 12 gives a precise indication of where the vortex-lattice melting temperature in this system is, which is the temperature at which the two bins approach equal values and above which their values remain constant. This occurs at $T^* \approx 1.88$, only slightly above the estimated T where the broad

peak in the specific heat is located at $T = 1.86$. The temperature window for which a square singly-quantized vortex lattice dominates is therefore conservatively estimated to be in the range $T \in [1.75–1.86]$. Below $T = 1.7$, a doubly-quantized hexagonal vortex lattice is stabilized. Using the melting temperature as a measure of the transition to the normal state, i.e., as a measure of the upper critical field line, we see that the hexagonal lattice of double-quanta vortices is stable up to a temperature of about $0.9T^*$.

We now compare these results quantitatively with previously found mean-field results, where entropic effects were not fully accounted for [39]. Figure 13 displays three qualitatively different vortex phases obtained from simulations of mean-field theory in an external field at various temperatures. The procedure is to discretize the physical degrees of freedom η_\pm , and \mathbf{A} using a finite-element framework, and to numerically minimize the free energy (1d) in an external magnetic field (for details, see Ref. [39]).

The mean-field temperature is accounted for by modifying the quadratic term of the potential (1d) to be $(T_{MF} - 1)|\eta_h|^2$. There, the zero-field critical temperature is $T_{c,MF} = 1$, and the crossover line to the normal state at $f_{MF} \approx 1/30$ is estimated from our numerical results to be $T_{MF}^* = 0.9$. For a better comparison of the role of the temperatures for the fluctuating theory with that of the mean field, the results of the temperatures for mean-field simulations are expressed in units of the crossover temperature T_{MF}^* .

At low temperatures, the minimal energy state is clearly a hexagonal lattice of double-quanta vortices. When approaching the crossover temperature, the double-quanta vortices start to split into single-quanta vortices. Around $0.86T_{MF}^*$, there are few single quantum vortices, and the double quanta still dominate. Closer to the crossover, around $0.92T_{MF}^*$, most of the vortices have dissociated and the single quantum vortices dominate. Eventually, the entire hexagonal lattice of double-quanta vortices has dissociated into a structure of single-quanta vortices. A generous estimate gives that the range of the mean-field temperature where the single-quanta vortices dominate is about $0.1T_{MF}^*$. In general the entropic effects promote stability of the lattice of single-quanta vortices. However, our Monte-Carlo simulations demonstrate that in the regime of parameters we have considered, the double-quanta vortex lattice is robust in a regime of temperatures approximately equal to what was found in previous work [39].

VI. SUMMARY

In this paper, we have considered effects of thermal fluctuations on the vortex states in a model of a chiral p -wave superconductor with two complex matter fields (η^+ , η^-) with opposite chiralities, for a filling fraction of $f = 1/64$ vortices per square plaquette in the (x, y) plane of a cubic numerical lattice, with an applied magnetic field in the z direction. We have considered temperatures in the interval $T \in 1.5–2.0$, with the zero-field critical temperature ($f = 0$) estimated to be $T_c = 2.016 \pm 0.002$ and the crossover line to the normal state at $f = 1/64$, estimated to be $T^* = 1.86 \pm 0.04$.

At $T = 1.5$ we have found that the stable field-induced vortex configuration is a hexagonal vortex lattice of doubly-quantized vortices. At the higher temperature $T \approx 1.75$, this

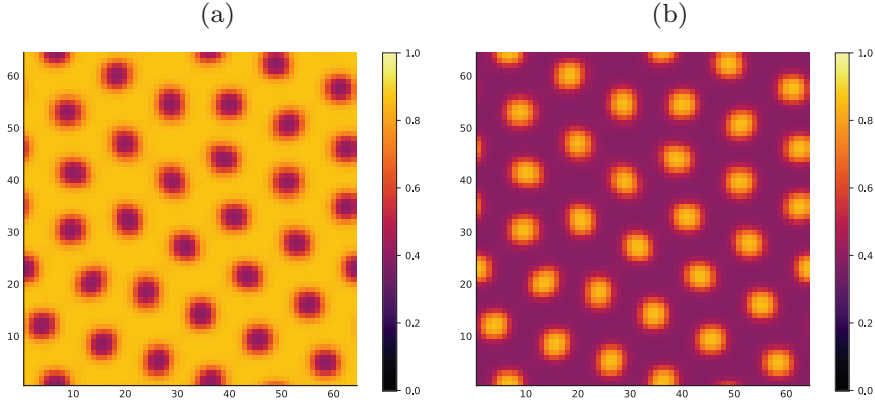


FIG. 10. Component amplitudes averaged in the z direction for a system with $v = 0.1$, $g = 0.3$, $f = 1/64$, and $T = 1.5$. (a) shows $\langle \rho_{r_\perp}^+ \rangle$ while (b) shows $\langle \rho_{r_\perp}^- \rangle$. In contrast to Fig. 7 the color limits are the same in both subplots since the lower temperature signal does not require amplification to discern spatial variance.

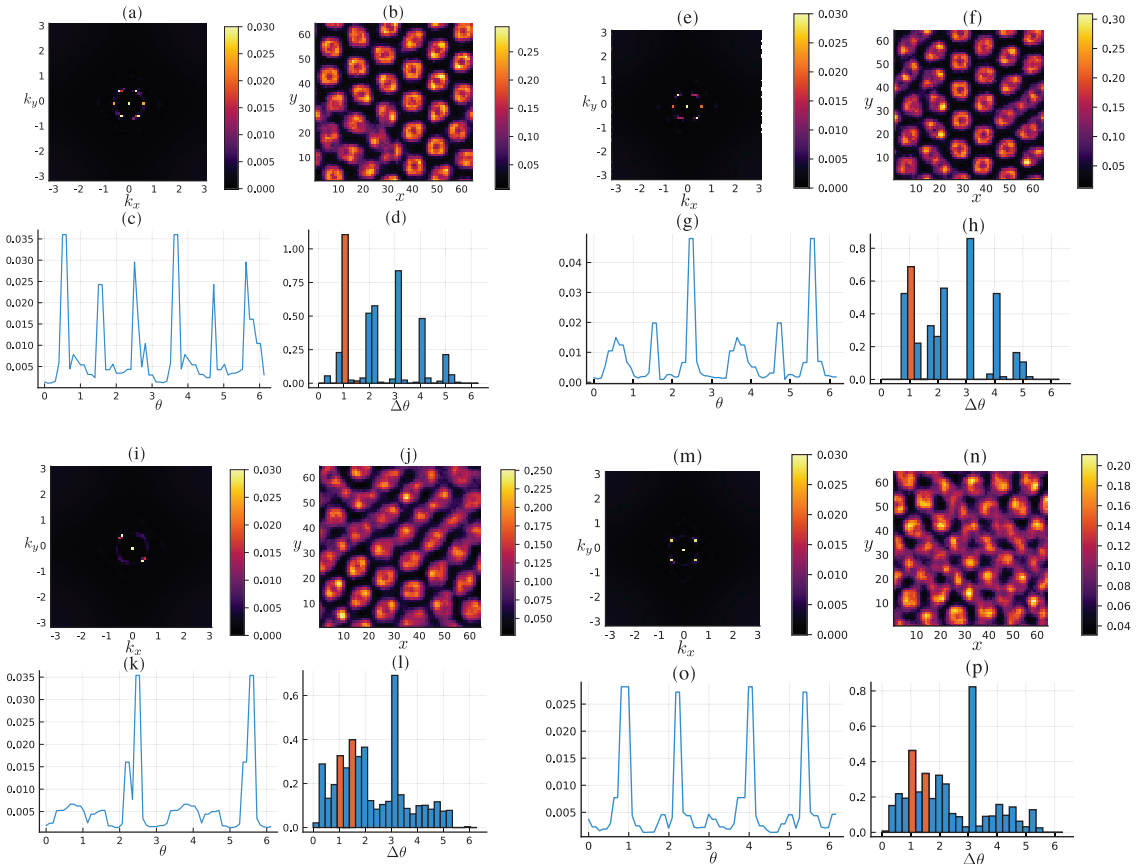


FIG. 11. A tableau of simulation results for the temperatures $T = \{1.7, 1.725, 1.742, 1.751\}$ in ascending order from left to right and top to bottom. The system has parameters $v = 0.1$, $g = 0.3$, and $f = 1/64$. The real space z -averaged vorticity in (b), (f), (j), and (n) exhibits both single and double quanta lattice structures. The remaining figures show the transition from signals of a hexagonal lattice to a square lattice as the temperature increases.

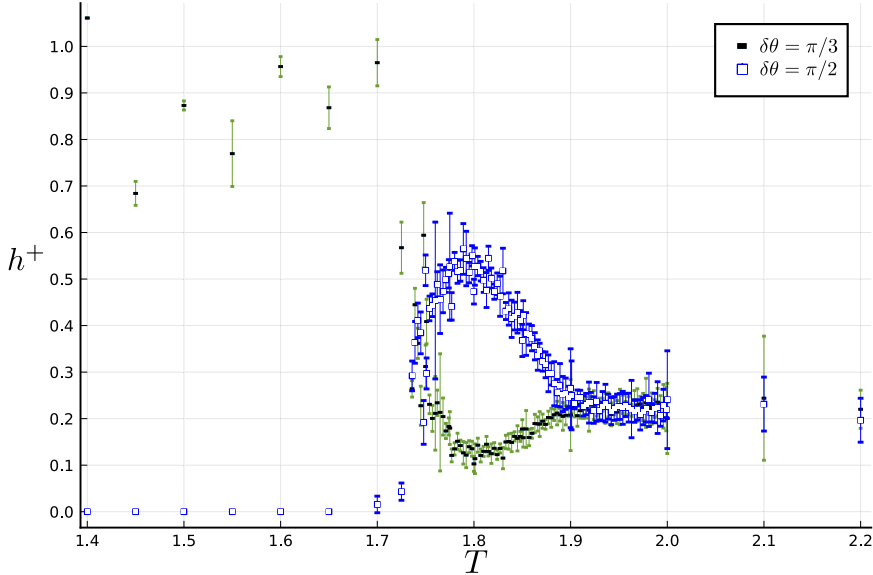


FIG. 12. Histogram temperature dependence for two different bins in a system with $f = 1/64$, $g = 0.3$, $v = 0.1$, and $L = 64$. The histogram is given by Eq. (32) and gives normalized bins of the angular distance $\Delta\theta$ between peaks in the structure function. The bin at $\Delta\theta = \pi/2$ corresponds to the signal of a square lattice structure in the structure function and is marked with blue hollow squares. The bin at $\Delta\theta = \pi/3$ is the signal for a hexagonal vortex lattice and is marked with black bar markers and green error bars. The transition from a doubly-quantized hexagonal lattice to a singly-quantized square lattice as T increases occurs at $T \approx 1.75$.

vortex lattice transitions, over a narrow temperature regime, to a square vortex lattice of singly-quantized vortices. At even higher temperatures, the vortex lattice structure function is washed out by thermally induced vortex loops when temperatures approach and cross the crossover line at $f = 1/64$, $T^* = 1.86 \pm 0.04$, rendering the system in a vortex-plasma phase. Our results indicate that double-quanta vortices can be quite robust and do not very easily dissociate into single quanta vortices when thermal fluctuations are included.

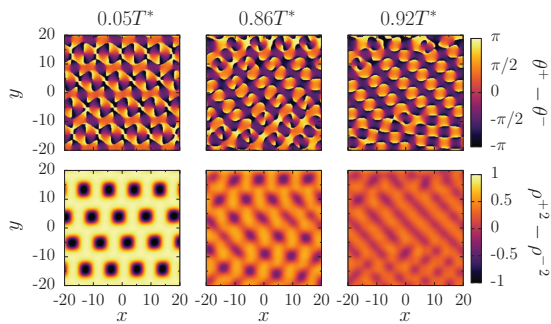


FIG. 13. Vortex phases of the mean-field theory in an external field for $g = 0.3$ and $v = 0.3$ with the corresponding filling fraction is $f_{\text{MF}} \approx 1/30$. The panels on the top line display the relative phase Eq. (30) while the bottom line shows the relative densities defined in Eq. (35). Note that both relative phase and densities in the mean field are not thermal average.

Thus, previous results, based on ground state computations and minimization of internal energy, predicting doubly-quantized hexagonal vortex lattices at low magnetic fields transitioning to singly-quantized square vortex lattices at higher magnetic fields very close to H_{c2} , are stable to fully accounting for entropic effects in the free energy. Therefore, double-quanta vortices are a quite robust property of chiral p -wave superconductors. Our results, however, do indicate a slight broadening of the temperature regime above which a square vortex lattice is entropically stabilized compared to earlier mean-field results. The main finding is that, for the regimes considered in the paper, this entropic stabilization does not significantly diminish the temperature range where a doubly-quantized hexagonal vortex state exists.

ACKNOWLEDGMENTS

F.N.K and A.S. would like to thank T.A. Bojesen for numerous invaluable discussions. This work was supported by an NTNU University Grant, the Research Council of Norway Project No. 250985 “Fundamentals of Low-dissipative Topological Matter,” and the Research Council of Norway through its Centres of Excellence funding scheme, Project No. 262633, “QuSpin.” E.B. was supported by the Swedish Research Council Grants No. 642-2013-7837, No. 2016-06122, and No. 2018-03659, and Göran Gustafsson Foundation for Research in Natural Sciences and Medicine and Olle Engkvists Stiftelse. We acknowledge support from the Norwegian High-Performance Computing Consortium NOTUR, Project NN2819K.

APPENDIX A: DERIVATION OF EQ. (22)

Writing $\tan \theta^\pm$ in terms of the complex fields yields

$$\tan \theta^\pm = -i \frac{\eta^\pm - \eta^{\pm*}}{\eta^\pm + \eta^{\pm*}}. \quad (\text{A1})$$

Inserting the transformation to the xy basis in Eq. (3) and making the London-limit approximation $|\eta^x| = |\eta^y|$, Eq. (A1) becomes

$$\tan \theta^h = \frac{\sin \theta^x + h \cos \theta^y}{\cos \theta^x - h \sin \theta^y}. \quad (\text{A2})$$

Using the trigonometric identity

$$\sin x + \cos y = 2 \sin \left(\frac{x-y}{2} + \frac{\pi}{4} \right) \sin \left(\frac{x+y}{2} + \frac{\pi}{4} \right), \quad (\text{A3})$$

after including h and $-h$ in the argument of sin in the numerator and denominator of Eq. (A2) respectively, $\tan \theta^h$ can be

written

$$\begin{aligned} \tan \theta^h &= h \frac{\sin \left(\frac{h\theta^x - \theta^y}{2} + \frac{\pi}{4} \right) \sin \left(\frac{h\theta^x + \theta^y}{2} + \frac{\pi}{4} \right)}{\sin \left(-\frac{\theta^x + h\theta^y}{2} + \frac{\pi}{4} \right) \sin \left(\frac{\theta^x - h\theta^y}{2} + \frac{\pi}{4} \right)} \\ &= -h \frac{\sin \left(\frac{\theta^x + \theta^y}{2} + h \frac{\pi}{4} \right)}{\sin \left(\frac{\theta^x + \theta^y}{2} - h \frac{\pi}{4} \right)} \\ &= -\frac{1}{-\bar{h} \frac{\sin \left(\frac{\theta^x + \theta^y}{2} + \bar{h} \frac{\pi}{4} \right)}{\sin \left(\frac{\theta^x + \theta^y}{2} - \bar{h} \frac{\pi}{4} \right)}} = -\frac{1}{\tan \theta^{\bar{h}}}. \end{aligned} \quad (\text{A4})$$

This equation shows that both $\tan \theta^+$ and $\tan \theta^-$ are determined by one variable, $\theta^x + \theta^y$, which is what makes it possible to relate θ^+ to θ^- . Finally, by shifting the argument of the last tan we get Eq. (22), i.e., the relationship $\tan \theta^h = \tan(\theta^{\bar{h}} + \pi/2)$.

APPENDIX B: SYMMETRIZED MIXED GRADIENT TERM

Using the transformation properties of η_r^a and $A_{r,\mu}$ in Eqs. (24) and (25) on the expression for the discretized mixed gradient term in the xy basis in Eq. (19) repeated here for convenience:

$$\begin{aligned} \mathcal{F}_{\text{MG}}^r &= (1-\nu) \sum_a [\rho_{r+\hat{x}}^a \rho_{r+\hat{y}}^{\bar{a}} \cos(\theta_{r+\hat{x}}^a - \theta_{r+\hat{y}}^{\bar{a}} - (A_{r,x} - A_{r,y})) - \rho_{r+\hat{x}}^a \rho_r^{\bar{a}} \cos(\theta_{r+\hat{x}}^a - \theta_r^{\bar{a}} - A_{r,x}) \\ &\quad - \rho_{r+\hat{y}}^a \rho_r^{\bar{a}} \cos(\theta_{r+\hat{y}}^a - \theta_r^{\bar{a}} - A_{r,y}) + \rho_r^a \rho_r^{\bar{a}} \cos(\theta_r^a - \theta_r^{\bar{a}})], \end{aligned} \quad (\text{B1})$$

we obtain the rotated mixed gradient terms

$$\begin{aligned} C_4 \mathcal{F}_{\text{MG}}^r &= -(1-\nu) \sum_a [\rho_{r-\hat{x}}^a \rho_{r+\hat{y}}^{\bar{a}} \cos(\theta_{r-\hat{x}}^a - \theta_{r+\hat{y}}^{\bar{a}} + (A_{r,y} + A_{r-\hat{x},x})) - \rho_{r-\hat{x}}^a \rho_r^{\bar{a}} \cos(\theta_{r-\hat{x}}^a - \theta_r^{\bar{a}} + A_{r-\hat{x},x}) \\ &\quad - \rho_r^a \rho_{r+\hat{y}}^{\bar{a}} \cos(\theta_r^a - \theta_{r+\hat{y}}^{\bar{a}} + A_{r,y}) + \rho_r^a \rho_r^{\bar{a}} \cos(\theta_r^a - \theta_r^{\bar{a}})], \end{aligned} \quad (\text{B2})$$

$$\begin{aligned} C_4^2 \mathcal{F}_{\text{MG}}^r &= (1-\nu) \sum_a [\rho_{r-\hat{x}}^a \rho_{r-\hat{y}}^{\bar{a}} \cos(\theta_{r-\hat{x}}^a - \theta_{r-\hat{y}}^{\bar{a}} - (A_{r-\hat{y},y} - A_{r-\hat{x},x})) - \rho_{r-\hat{x}}^a \rho_r^{\bar{a}} \cos(\theta_{r-\hat{x}}^a - \theta_r^{\bar{a}} + A_{r-\hat{x},x}) \\ &\quad - \rho_r^a \rho_{r-\hat{y}}^{\bar{a}} \cos(\theta_r^a - \theta_{r-\hat{y}}^{\bar{a}} - A_{r-\hat{y},y}) + \rho_r^a \rho_r^{\bar{a}} \cos(\theta_r^a - \theta_r^{\bar{a}})], \end{aligned} \quad (\text{B3})$$

$$\begin{aligned} C_4^3 \mathcal{F}_{\text{MG}}^r &= -(1-\nu) \sum_a [\rho_{r-\hat{y}}^{\bar{a}} \rho_{r+\hat{x}}^a \cos(\theta_{r-\hat{y}}^{\bar{a}} - \theta_{r+\hat{x}}^a + (A_{r-\hat{y},y} + A_{r,x})) - \rho_{r-\hat{y}}^{\bar{a}} \rho_r^a \cos(\theta_{r-\hat{y}}^{\bar{a}} - \theta_r^a + A_{r-\hat{y},y}) \\ &\quad - \rho_r^{\bar{a}} \rho_{r+\hat{x}}^a \cos(\theta_r^{\bar{a}} - \theta_{r+\hat{x}}^a - A_{r,x}) + \rho_r^{\bar{a}} \rho_r^a \cos(\theta_r^{\bar{a}} - \theta_r^a)]. \end{aligned} \quad (\text{B4})$$

In these expressions, $a, q \in \{x, y\}$. Adding Eqs. (B1)–(B4), several terms cancel. As is immediately obvious, all the onsite terms such as the last term in Eq. (B1) cancel each other. Considering the last term on the first line of Eq. (B2), we let $r \rightarrow r + \hat{x}$ which is allowed because of periodic boundary conditions, and we see that this cancels the last term on the first line of Eq. (B1). The first term on the last line of Eqs. (B2) and (B1) can be seen to cancel through a simple relabeling of the a summation index. The same cancellations happen for the analogous terms in Eqs. (B3) and (B4) such that the average of Eqs. (B1)–(B4) and thus the full symmetrized expression for the mixed gradient terms can be written on the simple form

$$\mathcal{F}_{\text{MG}}^s = \frac{(1-\nu)}{4} \sum_a \sum_{h,h'=\pm} hh' \rho_{r+h\hat{x}}^a \rho_{r+h'\hat{y}}^{\bar{a}} \cos(\theta_{r+h\hat{x}}^a - \theta_{r+h'\hat{y}}^{\bar{a}} - A_{r,hx} + A_{r,h'y}). \quad (\text{B5})$$

This expression, together with Eqs. (15), (16), (17), and (18), constitute the free energy used in the simulations.

APPENDIX C: NUMERICAL BASIS ROTATION

In this Appendix, we present the numerical details for how chiral matter field amplitudes and phases are calculated from their xy -basis counterparts. The chiral amplitudes ρ_r^h are easily found from the xy -basis variables through Eq. (20):

$$\rho_r^h = \sqrt{\frac{\rho^x{}^2 + \rho^y{}^2}{2} + h\rho^x\rho^y \sin(\theta_r^x - \theta_r^y)}. \quad (\text{C1})$$

The chiral phases are obtained by the set of equations

$$\sin \theta_r^h = \frac{\rho^x \sin \theta_r^x + h \rho^y \cos \theta_r^y}{\sqrt{2}\rho_r^h}, \quad (\text{C2})$$

$$\cos \theta_r^h = \frac{\rho^x \cos \theta_r^x - h \rho^y \sin \theta_r^y}{\sqrt{2}\rho_r^h}. \quad (\text{C3})$$

As long as $\rho_r^h > 0$, $\theta_r^h \in [-\pi, \pi]$ can be found through simple trigonometric relations which we include for completeness. Given that $\cos \theta_r^h > 0$ then $\theta_r^h = \tan^{-1} \tan \theta_r^h$. If $\cos \theta_r^h < 0$ then $\theta_r^h = \tan^{-1} \tan \theta_r^h - \pi \operatorname{sgn} \tan \theta_r^h$. The final case is that $\cos \theta_r^h = 0$ in which case $\theta_r^h = \pi/2 \operatorname{sgn} \sin \theta_r^h$.

In the chiral ground state of the system $\theta_r^x - \theta_r^y \rightarrow -h\pi/2$ which makes $\rho_r^h \rightarrow 0$ when $\rho^x = \rho^y$. This makes Eqs. (C2) and (C3) numerically unstable as both numerator and de-

nominator approach zero. To accurately calculate θ_r^h , these equations are expanded around the ground state value. Setting $\theta_r^x - \theta_r^y = -h\pi/2 + 2\pi n + \delta$ and expanding to fourth order in δ yields

$$\begin{aligned} \sin \theta_r^h &\rightarrow \frac{\delta}{|\delta|} \cos \theta_r^x \left[1 - \frac{\delta^2}{8} + \frac{\delta^4}{384} \right] \\ &\quad - \frac{|\delta|}{2} \sin \theta_r^x \left[1 - \frac{\delta^2}{24} + \frac{\delta^4}{1920} \right], \end{aligned} \quad (\text{C4a})$$

$$\begin{aligned} \cos \theta_r^h &\rightarrow \frac{|\delta|}{2} \cos \theta_r^x \left[1 - \frac{\delta^2}{24} + \frac{\delta^4}{1920} \right] \\ &\quad - \frac{\delta}{|\delta|} \sin \theta_r^x \left[1 - \frac{\delta^2}{8} + \frac{\delta^4}{384} \right]. \end{aligned} \quad (\text{C4b})$$

The expressions on the right are independent of h . Then if $\sin \theta_r^h \leq 0$, $\theta_r^h = -\cos^{-1} \cos \theta_r^h$. If not, then $\theta_r^h = \cos^{-1} \cos \theta_r^h$. To find δ we simply calculate $\delta = \operatorname{mod}(\theta_r^x - \theta_r^y, 2\pi) - 3\pi/2$ for $h = +$ and $\delta = \operatorname{mod}(\theta_r^x - \theta_r^y, 2\pi) - \pi/2$ for $h = -$. With this expansion in δ , the errors from calculating θ_r^h were found to be smaller than the floating point error.

-
- [1] D. D. Osheroff, W. J. Gully, R. C. Richardson, and D. M. Lee, New Magnetic Phenomena in Liquid He³ Below 3 mK, *Phys. Rev. Lett.* **29**, 920 (1972).
- [2] D. D. Osheroff, R. C. Richardson, and D. M. Lee, Evidence for a New Phase of Solid He³, *Phys. Rev. Lett.* **28**, 885 (1972).
- [3] A. Leggett, The spin dynamics of an anisotropic fermi superfluid (³He?), *Ann. Phys.* **85**, 11 (1974).
- [4] A. J. Leggett, A theoretical description of the new phases of liquid ³He, *Rev. Mod. Phys.* **47**, 331 (1975).
- [5] Note that we deliberately avoid the use of the term order parameter when discussing the matter field. The reason is, while the identification of the matter field as a local order parameter would be perfectly fine in a 3D superfluid, this is not so for a superconductor. In a superconductor, with a charged condensate coupling minimally to a gauge field, there exists no local order parameter in any dimension, at any temperature [68]. Throughout our paper, we simply refer to what is normally called the superconducting order parameter as a *field*. Under certain circumstances the Higgs mass of the gauge field acquired upon entering the superconducting state may be interpreted as an order parameter.
- [6] N. D. Mermin and T.-L. Ho, Circulation and Angular Momentum in the A Phase of Superfluid Helium-3, *Phys. Rev. Lett.* **36**, 594 (1976).
- [7] P. W. Anderson and G. Toulouse, Phase Slippage without Vortex Cores: Vortex Textures in Superfluid ³He, *Phys. Rev. Lett.* **38**, 508 (1977).
- [8] N. D. Mermin, The topological theory of defects in ordered media, *Rev. Mod. Phys.* **51**, 591 (1979).
- [9] Y. Maeno, H. Hashimoto, K. Yoshida, S. Nishizaki, T. Fujita, J. G. Bednorz, and F. Lichtenberg, Superconductivity in a layered perovskite without copper, *Nature (London)* **372**, 532 (1994).
- [10] A. P. Mackenzie, S. R. Julian, A. J. Diver, G. J. McMullan, M. P. Ray, G. G. Lonzarich, Y. Maeno, S. Nishizaki, and T. Fujita, Quantum Oscillations in the Layered Perovskite Superconductor Sr₂RuO₄, *Phys. Rev. Lett.* **76**, 3786 (1996).
- [11] Y. Maeno, M. Rice, and M. Sigrist, The intriguing superconductivity of Sr₂RuO₄, *Phys. Today* **54**(1), 42 (2001).
- [12] A. P. Mackenzie, T. Scaffidi, C. W. Hicks, and Y. Maeno, Even odder after twenty-three years: the superconducting order parameter puzzle of Sr₂RuO₄, *npj Quantum Mater.* **2**, 40 (2017).
- [13] A. P. Mackenzie, R. K. W. Haselwimmer, A. W. Tyler, G. G. Lonzarich, Y. Mori, S. Nishizaki, and Y. Maeno, Extremely Strong Dependence of Superconductivity on Disorder in Sr₂RuO₄, *Phys. Rev. Lett.* **80**, 161 (1998).
- [14] A. P. Mackenzie and Y. Maeno, The superconductivity of Sr₂RuO₄ and the physics of spin-triplet pairing, *Rev. Mod. Phys.* **75**, 657 (2003).
- [15] K. Ishida, H. Mukuda, Y. Kitaoka, K. Asayama, Z. Q. Mao, Y. Mori, and Y. Maeno, Spin-triplet superconductivity in Sr₂RuO₄ identified by ¹⁷O Knight shift, *Nature (London)* **396**, 658 (1998).
- [16] K. Ishida, M. Manago, T. Yamanaka, H. Fukazawa, Z. Q. Mao, Y. Maeno, and K. Miyake, Spin polarization enhanced by spin-triplet pairing in Sr₂RuO₄ probed by NMR, *Phys. Rev. B* **92**, 100502(R) (2015).
- [17] K. Izawa, H. Takahashi, H. Yamaguchi, Y. Matsuda, M. Suzuki, T. Sasaki, T. Fukase, Y. Yoshida, R. Settai, and Y. Onuki, Superconducting Gap Structure of Spin-Triplet Superconductor Sr₂RuO₄ Studied by Thermal Conductivity, *Phys. Rev. Lett.* **86**, 2653 (2001).
- [18] S. Nishizaki, Y. Maeno, S. Farner, S.-i. Ikeda, and T. Fujita, Evidence for unconventional superconductivity of Sr₂RuO₄ from specific-heat measurements, *J. Phys. Soc. Jpn.* **67**, 560 (1998).

- [19] I. A. Firmino, S. Lederer, C. Lupien, A. P. Mackenzie, J. C. Davis, and S. A. Kivelson, Evidence from tunneling spectroscopy for a quasi-one-dimensional origin of superconductivity in Sr_2RuO_4 , *Phys. Rev. B* **88**, 134521 (2013).
- [20] G. M. Luke, Y. Fudamoto, K. M. Kojima, M. I. Larkin, J. Merrin, B. Nachumi, Y. J. Uemura, Y. Maeno, Z. Q. Mao, Y. Mori, H. Nakamura, and M. Sigrist, Time-reversal symmetry-breaking superconductivity in Sr_2RuO_4 , *Nature (London)* **394**, 558 (1998).
- [21] J. Xia, Y. Maeno, P. T. Beyersdorf, M. M. Fejer, and A. Kapitulnik, High Resolution Polar Kerr Effect Measurements of Sr_2RuO_4 : Evidence for Broken Time-Reversal Symmetry in the Superconducting State, *Phys. Rev. Lett.* **97**, 167002 (2006).
- [22] V. Grinenko, S. Ghosh, R. Sarkar, J.-C. Orain, A. Nikitin, M. Elender, D. Das, Z. Guguchia, F. Bruckner, M. E. Barber, J. Park, N. Kikugawa, D. A. Sokolov, J. S. Bobowski, T. Miyoshi, Y. Maeno, A. P. Mackenzie, H. Luetkens, C. W. Hicks, and H.-H. Klauss, Split superconducting and time-reversal symmetry-breaking transitions, and magnetic order in Sr_2RuO_4 under uniaxial stress, *Nat. Phys.* **17**, 748 (2021).
- [23] P. J. Curran, S. J. Bending, W. M. Desoky, A. S. Gibbs, S. L. Lee, and A. P. Mackenzie, Search for spontaneous edge currents and vortex imaging in Sr_2RuO_4 mesostructures, *Phys. Rev. B* **89**, 144504 (2014).
- [24] A. Pustogow, Y. Luo, A. Chronister, Y.-S. Su, D. A. Sokolov, F. Jerzembeck, A. P. Mackenzie, C. W. Hicks, N. Kikugawa, S. Raghu, E. D. Bauer, and S. E. Brown, Constraints on the superconducting order parameter in Sr_2RuO_4 from oxygen-17 nuclear magnetic resonance, *Nature (London)* **574**, 72 (2019).
- [25] S. Benhabib, C. Lupien, I. Paul, L. Berges, M. Dion, M. Nardone, A. Zitouni, Z. Mao, Y. Maeno, A. Georges *et al.*, Ultrasound evidence for a two-component superconducting order parameter in Sr_2RuO_4 , *Nat. Phys.* **17**, 194 (2021).
- [26] S. Ghosh, A. Shekhter, F. Jerzembeck, N. Kikugawa, D. A. Sokolov, M. Brando, A. Mackenzie, C. W. Hicks, and B. Ramshaw, Thermodynamic evidence for a two-component superconducting order parameter in Sr_2RuO_4 , *Nat. Phys.* **17**, 199 (2021).
- [27] S. J. Ray, A. S. Gibbs, S. J. Bending, P. J. Curran, E. Babaev, C. Baines, A. P. Mackenzie, and S. L. Lee, Muon-spin rotation measurements of the vortex state in Sr_2RuO_4 : Type-1.5 superconductivity, vortex clustering, and a crossover from a triangular to a square vortex lattice, *Phys. Rev. B* **89**, 094504 (2014).
- [28] S. A. Kivelson, A. C. Yuan, B. J. Ramshaw, and R. Thomale, A proposal for reconciling diverse experiments on the superconducting state in Sr_2RuO_4 , *npj Quantum Mater.* **5**, 43 (2020).
- [29] A. T. Rømer, D. D. Scherer, I. M. Eremin, P. J. Hirschfeld, and B. M. Andersen, Knight Shift and Leading Superconducting Instability from Spin Fluctuations in Sr_2RuO_4 , *Phys. Rev. Lett.* **123**, 247001 (2019).
- [30] T. A. Tokuyasu, D. W. Hess, and J. A. Sauls, Vortex states in an unconventional superconductor and the mixed phases of UPt_3 , *Phys. Rev. B* **41**, 8891 (1990).
- [31] K. E. Avers, W. J. Gannon, S. J. Kuhn, W. P. Halperin, J. A. Sauls, L. DeBeer-Schmitt, C. D. Dewhurst, J. Gavilano, G. Nagy, U. Gasser, and M. R. Eskildsen, Broken time-reversal symmetry in the topological superconductor UPt_3 , *Nat. Phys.* **16**, 531 (2020).
- [32] T. Tokuyasu and J. Sauls, Stability of doubly quantized vortices in unconventional superconductors, *Physica B+C* **165-166**, 347 (1990).
- [33] M. Sigrist and K. Ueda, Phenomenological theory of unconventional superconductivity, *Rev. Mod. Phys.* **63**, 239 (1991).
- [34] D. F. Agterberg, Vortex Lattice Structures of Sr_2RuO_4 , *Phys. Rev. Lett.* **80**, 5184 (1998).
- [35] R. Heeb and D. F. Agterberg, Ginzburg-Landau theory for a p -wave Sr_2RuO_4 superconductor: Vortex core structure and extended London theory, *Phys. Rev. B* **59**, 7076 (1999).
- [36] J. Garaud and E. Babaev, Properties of skyrmions and multi-quanta vortices in chiral p -wave superconductors, *Sci. Rep.* **5**, 17540 (2015).
- [37] J. Garaud and E. Babaev, Skyrmionic state and stable half-quantum vortices in chiral p -wave superconductors, *Phys. Rev. B* **86**, 060514(R) (2012).
- [38] J. A. Sauls and M. Eschrig, Vortices in chiral, spin-triplet superconductors and superfluids, *New J. Phys.* **11**, 075008 (2009).
- [39] J. Garaud, E. Babaev, T. A. Bojesen, and A. Sudbø, Lattices of double-quanta vortices and chirality inversion in $p_x + ip_y$ superconductors, *Phys. Rev. B* **94**, 104509 (2016).
- [40] S. B. Chung and S. A. Kivelson, Entropy-driven formation of a half-quantum vortex lattice, *Phys. Rev. B* **82**, 214512 (2010).
- [41] C. Dasgupta and B. I. Halperin, Phase Transition in a Lattice Model of Superconductivity, *Phys. Rev. Lett.* **47**, 1556 (1981).
- [42] M. E. Peskin, Mandelstam-'t Hooft duality in abelian lattice models, *Ann. Phys. (NY)* **113**, 122 (1978).
- [43] H. Kleinert, *Gauge Fields in Condensed Matter: Vol. 1: Superflow and Vortex Lines (Disorder Fields, Phase Transitions) Vol. 2: Stresses and Defects (Differential Geometry, Crystal Melting)* (World Scientific, Singapore, 1989).
- [44] S. Mo, J. Hove, and A. Sudbø, Order of the metal-to-superconductor transition, *Phys. Rev. B* **65**, 104501 (2002).
- [45] J. Smiseth, E. Smørgrav, E. Babaev, and A. Sudbø, Field- and temperature-induced topological phase transitions in the three-dimensional N -component london superconductor, *Phys. Rev. B* **71**, 214509 (2005).
- [46] K. Fossheim and A. Sudbø, *Superconductivity: Physics and Applications* (John Wiley & Sons, Chichester, 2005).
- [47] M. Speight, T. Winyard, and E. Babaev, Chiral p -wave superconductors have complex coherence and magnetic field penetration lengths, *Phys. Rev. B* **100**, 174514 (2019).
- [48] F. N. Krogh and A. Sudbø, Derivation of a Ginzburg-Landau free energy density of a $p + ip$ superconductor from spin-orbit coupling with mixed gradient terms, *Phys. Rev. B* **98**, 014510 (2018).
- [49] D. F. Agterberg, Square vortex lattices for two-component superconducting order parameters, *Phys. Rev. B* **58**, 14484 (1998).
- [50] J.-X. Zhu, C. S. Ting, J. L. Shen, and Z. D. Wang, Ginzburg-Landau equations for layered p -wave superconductors, *Phys. Rev. B* **56**, 14093 (1997).
- [51] G. Münster and M. Walzl, Lattice gauge theory - a short primer, *arXiv:hep-lat/0012005*.
- [52] P. N. Galteland, E. Babaev, and A. Sudbø, Fluctuation effects in rotating Bose-Einstein condensates with broken $SU(2)$ and $U(1) \times U(1)$ symmetries in the presence of intercomponent density-density interactions, *Phys. Rev. A* **91**, 013605 (2015).

- [53] A. Shimizu, H. Ozawa, I. Ichinose, and T. Matsui, Lattice Ginzburg-Landau model of a ferromagnetic p -wave pairing phase in superconducting materials and an inhomogeneous co-existing state, *Phys. Rev. B* **85**, 144524 (2012).
- [54] A. K. Nguyen and A. Sudbø, Topological phase fluctuations, amplitude fluctuations, and criticality in extreme type-II superconductors, *Phys. Rev. B* **60**, 15307 (1999).
- [55] A. K. Nguyen and A. Sudbø, A new broken $U(1)$ -symmetry in extreme type-II superconductors, *Europhys. Lett.* **46**, 780 (1999).
- [56] W. K. Hastings, Monte carlo sampling methods using markov chains and their applications, *Biometrika* **57**, 97 (1970).
- [57] H. G. Katzgraber, Introduction to Monte Carlo methods, [arXiv:0905.1629](https://arxiv.org/abs/0905.1629).
- [58] W. H. Press, S. A. Teukolsky, W. T. Vetterling, and B. P. Flannery, *Numerical Recipes*, 3rd ed. (Cambridge University Press, New York, 2007).
- [59] M. Newman and G. Barkema, *Monte Carlo Methods in Statistical Physics* (Clarendon Press, Oxford, 1999).
- [60] J. Bezanson, A. Edelman, S. Karpinski, and V. B. Shah, Julia: A fresh approach to numerical computing, *SIAM Rev.* **59**, 65 (2017).
- [61] M. Matsumoto and T. Nishimura, Mersenne twister: A 623-dimensionally equidistributed uniform pseudo-random number generator, *ACM Trans. Model. Comput. Simul.* **8**, 3 (1998).
- [62] Y.-H. Li and S. Teitel, Vortex-line fluctuations in model high-temperature superconductors, *Phys. Rev. B* **47**, 359 (1993).
- [63] S. Kragsæt, E. Babaev, and A. Sudbø, Effects of boundaries and density inhomogeneity on states of vortex matter in Bose-Einstein condensates at finite temperature, *Phys. Rev. A* **77**, 043605 (2008).
- [64] A. M. Ferrenberg and R. H. Swendsen, New Monte Carlo Technique for Studying Phase Transitions, *Phys. Rev. Lett.* **61**, 2635 (1988).
- [65] A. M. Ferrenberg and R. H. Swendsen, Optimized Monte Carlo Data Analysis, *Phys. Rev. Lett.* **63**, 1195 (1989).
- [66] J. Nocedal and S. J. Wright, Trust-region methods, in *Numerical Optimization* (Springer, New York, 2006), Chap. 4, pp. 66–100.
- [67] B. Efron, Bootstrap methods: Another look at the jackknife, *The Annals of Statistics* **7**, 1 (1979).
- [68] S. Elitzur, Impossibility of spontaneously breaking local symmetries, *Phys. Rev. D* **12**, 3978 (1975).

Paper III

**Håvard Homleid Haugen, Egor Babaev, Fredrik Nicolai Krohg, and
Asle Sudbø**

First order superconducting phase transition in chiral p + ip system

ARXIV: 2106.01007

First order superconducting phase transition in chiral $p + ip$ system

Håvard Homleid Haugen,^{1,2} Egor Babaev,³ Fredrik Nicolai Krohg,^{1,2} and Asle Sudbø^{1,2}

¹*Department of Physics, Norwegian University of Science and Technology, NO-7491, Trondheim, Norway*

²*Center for Quantum Spintronics, Department of Physics,*

Norwegian University of Science and Technology, NO-7491, Trondheim, Norway

³*Department of Physics, KTH-Royal Institute of Technology, Stockholm SE-10691, Sweden*

(Dated: June 25, 2021)

We use large-scale Monte Carlo computations to study the phase transitions of a two-component chiral p -wave superconductor in zero external magnetic field. We find a first order phase transition from the normal state to a chiral superconducting state, due to interplay between vortices and domain walls.

I. INTRODUCTION

Chiral superconductors constitute a class of unconventional superconductors whose order parameter features finite angular momentum and a phase that winds around the Fermi surface [1]. The chiral nature of the gap function arises from spontaneously broken time reversal symmetry (TRS), which yields a two-fold degenerate superconducting state with broken $U(1) \times Z_2$ -symmetry. Chiral superconductors are of fundamental interest because they are predicted to display topological properties such as Majorana modes in vortex cores and edge currents leading to a quantized thermal Hall conductance [2–5].

The prototypical chiral p -wave superfluid state is realized in A -phase of superfluid ^3He [6–8]. The search for chiral p -wave pairing in a bulk superconductor has been going on since the discovery of superfluid ^3He . For many years, the leading candidate has been the extensively investigated superconductor Sr_2RuO_4 : a highly anisotropic layered material with tetragonal crystal structure and strong spin-orbit coupling [9–13]. ARPES-measurements have revealed three bands crossing the Fermi-surface, supporting a multi-component theory [14]. Several groups have also found that in zero field there is a single phase transition, where TRS is broken along with the onset of superconductivity [10, 11, 15, 16], while split transitions were reported to arise under strain [17]. However the evidence against the chiral p -wave superconductivity has been growing in recent years. The first notable example was the absence of chiral edge currents that should produce magnetic signatures at the boundary between domains of opposite chirality [18–20]. Recently, the mounting evidence against the chiral p -wave pairing lead to the discussion of other order parameters in an attempt to reconcile all the experimental data, such as near-degenerate between d - and g -wave pairing for Sr_2RuO_4 [21, 22]. Recent studies of ultrasound [23, 24], and vortex state [25] point to multicomponent order parameter.

Another candidate for chiral triplet superconductivity is the type-II heavy fermion superconductor UPt_3 [26–28]. Unlike Sr_2RuO_4 , it is claimed to feature two separate phase transitions in zero applied magnetic field, where TRS is spontaneously broken within the superconduct-

ing phase [29–31]. The superconducting state in UPt_3 is believed to be chiral f -wave with an order parameter that has the two-dimensional irreducible representation E_{2u} [32]. Although this is a higher order pairing than chiral p -wave, our theoretical description will be relevant for UPt_3 since the order parameter symmetry group has the same irreducible representation. In more recent works, chiral superconductivity has also been claimed in other systems, such as Van der Waals materials and nano tubes [33–35].

Even after decades of research, the nature of multicomponent superconductivity in Sr_2RuO_4 remains a puzzle. This fact and the emergence of new candidates for chiral superconductors raise the need to understand the nature of superconducting phase transition in a chiral p -wave superconductor beyond mean-field approximations and possible clues it may yield in real materials.

The question of fluctuations in a chiral p -wave superconductor is nontrivial because it breaks two symmetries: $U(1)$ and Z_2 . Therefore, in general, fluctuations can cause a single transition or a sequence of transitions. A similar question arises for $s+is$ superconductors, that shares the $U(1) \times Z_2$ symmetry and has been studied by numerical methods [36, 37]. Recent experiments reported fluctuations-induced splitting of the phase transition [38]. Analogous questions for chiral p -wave superconductors were studied in [39], but no Monte-Carlo calculations were performed for this problem. In this paper, we use large-scale Monte-Carlo calculations to study the phase transition a chiral two-component superconductor transition in Ginzburg Landau (GL)-theory for an E_{2u} order parameter. Before we proceed to calculations, we note that the problem is related to the more general question of the phase transitions in multicomponent gauge theories, where large-scale Monte-Carlo studies were performed. For a $U(1) \times U(1)$ two-component London superconductor, it has been shown that for moderate values of the gauge charge and equal amplitudes in the two ordering fields there is a single first order phase transition where both symmetries are broken at the same temperature. For high values of the gauge charge the single transition line splits into two separate transitions predicting an intermediate metallic superfluid with broken global $U(1)$ symmetry but restored local $U(1)$ symmetry [40–44]. In Refs. [40, 45] the merg-

ing of the two phase transitions was coined a preemptive phase-transition, where ordering in one symmetry sector of the model leads to ordering in the other. For the case of interacting $U(1) \times U(1)$ neutral superfluid a detailed study of the first order character of the phase transition was presented in [42], where also the existence of a tricritical point was reported. Similarly, for a $SU(2)$ -symmetric model, where the amplitudes of the two matter fields (Ψ_1, Ψ_2) are related by a CP^1 constraint $|\Psi_1|^2 + |\Psi_2|^2 = 1$, a single transition was found for moderate values of the gauge charge, which split into two transitions for higher values [46, 47]. The model we consider in this paper is different from a $U(1) \times U(1)$ London superconductor, due to the presence of a term that explicitly breaks the global $U(1)$ symmetry down to a Z_2 -symmetry. It is also different from $s + is$ superconductor due to the structure of a so-called mixed gradient terms (MGT). These terms are products of two gradient terms, as in the standard kinetic energy, but where the two factors are gradients in different directions involving different order-parameter components (see below). Such terms are common for chiral p-wave superconductors [48] and can also originate for instance with spin-orbit coupling [49]. Such terms will provide an additional direct coupling between the $U(1)$ - and Z_2 -symmetry sectors of the model.

II. MODEL

A. Ginzburg Landau model

We consider a superconductor with tetragonal crystal structure and spin orbit coupling, belonging to the point group D_{4h} . Gauge invariance and TRS yields the full symmetry group of the system $\mathcal{G} = D_{4h} \times U(1) \times Z_2$. In the two-dimensional odd-parity representation E_{2u} , the superconducting gap function may be written as $\mathbf{d}(\mathbf{k}) = (\eta_x k_x + \eta_y k_y) \hat{z}$. The complex matter fields (components) describe two types of Cooper pairs in the theory, and can be written in terms of an amplitude and a phase on the form $\eta_i = \rho_i e^{i\theta_i}$. This leads to a GL energy functional $E = \int f d^3r$ where the dimensionless energy density is given by [48, 50, 51]

$$f = -\alpha(|\eta_x|^2 + |\eta_y|^2) + \frac{u_0}{2}(|\eta_x|^4 + |\eta_y|^4) \quad (1a)$$

$$+ \gamma |\eta_x \eta_y|^2 \cos 2(\theta_x - \theta_y) \quad (1b)$$

$$+ |\mathbf{D}\eta_x|^2 + |\mathbf{D}\eta_y|^2 + |\nabla \times \mathbf{A}|^2 \quad (1c)$$

$$+ \gamma_m [(D_x \eta_x)(D_y \eta_y)^* + (D_y \eta_x)(D_x \eta_y)^* + \text{h.c.}]$$

$$(1c)$$

The matter fields are minimally coupled to the gauge field \mathbf{A} through covariant derivatives $\mathbf{D} = \nabla - ig\mathbf{A}$ and the energy is normalized to the condensation energy $B_c^2/4\pi$. The decay of magnetic fields in this model usually involves multiple modes and multiple length scales [52], that yields further differences compared to $s + is$

models previously studied in Monte-Carlo simulations [36, 37]. These are parametrized by the gauge-charge through g . In what follows we will not distinguish between the subdominant electromagnetic scales.

The mean field ground state of Eq. (1) is found by setting $\mathbf{A} = 0$ and ignoring spatial variations in the matter fields. Minimization of the potential energy in Eq. (1a) then yields the ground state

$$|\eta_x| = |\eta_y| = \sqrt{\frac{\alpha}{u_0 - \gamma}} \equiv \rho_0, \quad (2)$$

$$\theta_x - \theta_y = \pm\pi/2 \equiv \theta_0. \quad (3)$$

We find two degenerate solutions due to the phase-locking term. These are related by a Z_2 symmetry operation which will be discussed in more detail in Sec. II C. Finally, we note that this ground state gives an order parameter on the form $k_x \pm ik_y$, corresponding to a superconducting state with chiral p -wave pairing which spontaneously breaks the $U(1) \times Z_2$ symmetry of the theory.

B. The London limit

In order to perform Monte Carlo simulations on the free energy introduced in Eq. (1), we will work within the London approximation where the amplitudes of the matter fields are frozen. The London limit is commonly used for similar models [40, 41]. However, in the case of a multi-component order parameter, and with the addition of Ising anisotropy and MGT, such an approach requires considerable care and is generally not applicable [52].

We will first explicitly assess the validity of this approach, following a similar but not identical method to the one presented in [52]. To this end, we expand all fluctuating fields to second order in deviations from their mean-field values, introducing

$$\epsilon_i = \rho_i - \rho_0, \quad (4)$$

$$\theta_\Delta = \frac{1}{2}(\theta_x - \theta_y - \theta_0), \quad (5)$$

$$p_i = A_i - \frac{1}{g} \partial_i \theta_\Sigma, \quad (6)$$

$$\theta_\Sigma = (\theta_x + \theta_y)/2, \quad (7)$$

where p_i essentially is a gauge-invariant current. Expanding the energy to second order in these fluctuations and Fourier transforming, we obtain an expression on the form

$$f = f_0 + \mathbf{v} \mathbf{G} \mathbf{v}^\dagger, \quad (8)$$

where f_0 is the ground state energy, $\mathbf{G}(\mathbf{k})$ is a matrix describing the coupling between fluctuations in different fields and \mathbf{v} is the fluctuation vector given by

$$\mathbf{v}(\mathbf{k}) = (\epsilon_+ \ \epsilon_- \ \theta_\Delta \ p_x \ p_y). \quad (9)$$

We have introduced a rotated amplitude basis $\epsilon_\pm = (\epsilon_x \pm \epsilon_y)/\sqrt{2}$ in order to simplify the structure of the coupling matrix. The exact form of the coupling matrix, along with details of the derivation are given in Appendix A.

To determine what fluctuations are most important, the coupling matrix is diagonalized to obtain the lowest eigenvalue λ_* along with the corresponding eigenvector ψ_* . In the absence of MGT, the coupling matrix is already diagonal and the eigenvectors are pure modes with fluctuations in only one field. In the long wavelength limit, we then find that the phase-difference mode θ_Δ corresponds to the lowest eigenvalue for low values of the Ising anisotropy

$$\gamma \leq 0.17 \quad (10)$$

when $\alpha = u_0 = g = 1.0$. Above this value amplitude fluctuations become important as the ϵ_- mode corresponds to the lowest eigenvalue. The effect of MGT is that the eigenvectors become mixed modes with multiple non-zero entries for non-zero momentum [52]. To investigate the degree of mixing, we plot the k -dependence of the non-zero entries in ψ_* in Fig. 1b with the corresponding parameters without MGT in Fig. 1a. For low momentum magnitude k the phase difference mode is now weakly mixed with ϵ_+ amplitude fluctuations, but phase difference fluctuations are still dominant.

Note that although taking a London limit eliminates some of the mixing at the level of bare model, we find below that the phase transition is first order, so in a fluctuating model the mixing should reappear at the level of a large-scale effective field theory. Otherwise, at the level of bare model, the London limit is a good approximation for the regime of small mixing.

C. Charged and chiral symmetry sectors

In this section we introduce the chiral basis, which is obtained by a unitary transformation $\eta_\pm = (\eta_x \pm i\eta_y)/\sqrt{2}$. Under TRS, the chiral components transform as $\tilde{\mathcal{K}}\eta_\pm = \eta_\mp^*$. It is common to recast the model in terms of these chiral components [51, 53, 54], but in the present setting we introduce them because they provide an order parameter in the Z_2 symmetry sector. If we calculate the chiral component amplitudes in terms of the xy -components, we find

$$|\eta_\pm| = \sqrt{\frac{1}{2} [|\eta_x|^2 + |\eta_y|^2 \pm 2|\eta_x\eta_y|\sin(\theta_x - \theta_y)]}. \quad (11)$$

By inserting the ground state values from Eqs. (2) and (3), we see that one of the chiral amplitudes is spontaneously chosen. Coming from the low-temperature

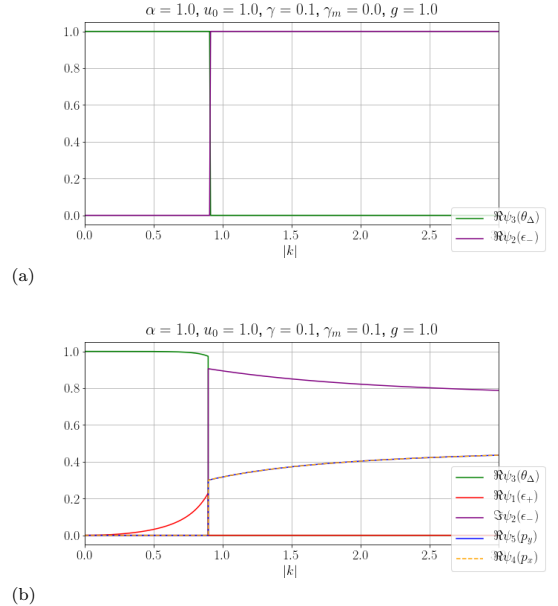


FIG. 1. Non-zero entries of the eigenvector ψ_* corresponding to the lowest eigenvalue of the coupling matrix, plotted along the line $k_x = k_y$. In (a) there are no MGT and the coupling matrix is diagonal with pure modes. In (b) we have included MGT, which cause mixed modes with fluctuations in multiple fields. In both cases fluctuations in the phase difference are dominant in the long wavelength limit.

regime, chiral symmetry is then restored by a proliferation of topological defects in the form of Ising domain walls separating areas of opposite chirality. From Eq. (11) we see that these domain walls can be described by a gradient in the phase-difference of the xy -components.

The superconducting phase transition is associated with spontaneous symmetry breaking of the local $U(1)$ -symmetry. The low temperature phase is well understood at mean-field level, where the gauge field \mathbf{A} acquires a mass, yielding a Meissner-effect. In the context of single-component superconductors it has been shown that going beyond mean-field, the (non-local) order parameter of the $U(1)$ -sector is still the gauge field mass, which now corresponds to the inverse magnetic penetration length of the problem. Upon heating the system, the mass of the gauge field is eventually destroyed at some critical temperature. The phase transition is driven by a proliferation of thermally excited topological defects in the form of charged vortex-loops [55, 56].

In the London limit, we can perform a separation of variables to rewrite the model in terms of charged and chiral terms

$$f = \frac{\rho_0^2}{2} [\nabla(\theta_x + \theta_y) - 2g\mathbf{A}]^2 + \frac{\rho_0^2}{2} [\nabla(\theta_x - \theta_y)]^2 + \gamma\rho_0^4 \cos 2(\theta_x - \theta_y) + |\nabla \times \mathbf{A}|^2 + \gamma_m \rho_0^2 \cos(\theta_x - \theta_y) \{[\partial_x(\theta_x + \theta_y) - 2gA_x][\partial_y(\theta_x + \theta_y) - 2gA_y] - [\partial_x(\theta_x - \theta_y)][\partial_y(\theta_x - \theta_y)]\}. \quad (12)$$

This form highlights the interplay between the symmetry sectors of the model in an intuitive way. We have the charged sector given by the phase-sum coupling to a gauge field with strength $2g$. The chiral sector is governed by the phase-difference, where we have a 3D XY-model with an easy axis anisotropy that demotes the symmetry from global $U(1)$ down to Z_2 . Then finally there are the MGT that provide an explicit coupling between the two sectors. Note that even in the absence of MGT, the two symmetry sectors are still connected as the phase-sum and phase-difference are not independent variables.

III. MONTE CARLO SIMULATIONS

The critical properties of the model in Eq. (1) in the London limit are investigated using Monte Carlo simulations. This is achieved by discretizing the model on a numerical cubic lattice, where the matter-fields live on lattice points and the gauge field is discretized through renormalized non-compact link-variables [57]. Periodic boundary conditions are used because we are interested in bulk properties of the model. In simulations, we use the Metropolis Hastings algorithm with a local update scheme and parallel tempering between different temperatures to numerically evaluate various observables [58–60]. The gauge-field is discretized through renormalized non-compact link-variables defined as

$$A_{\mathbf{r},\mu} \equiv -\frac{1}{g} \int_{\mathbf{r}}^{\mathbf{r}+\hat{\mu}} A_\mu(\mathbf{r}') d\mathbf{r}' \in (-\infty, \infty), \quad (13)$$

for $\mu \in \{x, y, z\}$. These are non-compact in the sense that they don't have a 2π periodicity [57] and this means that the discretization of the pure gauge term in Eq. (1b) will have the form

$$\int d^3r |\nabla \times \mathbf{A}|^2 \mapsto f_A^r = \frac{1}{g^2} \sum_{\mathbf{r},\mu} (\Delta \times \mathbf{A})_\mu^2, \quad (14)$$

where $(\Delta \times \mathbf{A})_\mu = \epsilon_{\mu\nu\lambda} \Delta_\nu A_{\mathbf{r},\lambda}$ using the Levi-Civita symbol and summation over repeated indices. Δ_μ is a discrete forward difference operator such that $\Delta_\mu A_{\mathbf{r},\nu} = A_{\mathbf{r}+\hat{\mu},\nu} - A_{\mathbf{r},\nu}$. We note that writing out the sums over μ , ν and λ , Eq. (14) can be written in term of plaquette sums. The link variables are renormalized in the sense that we multiply the field by a factor $-1/g$ to simplify the covariant derivatives.

The covariant derivatives are discretized using forward difference where the order-parameter component value at

$\mathbf{r} + \hat{\mu}$ is parallel-transported back to \mathbf{r} by the gauge-field link variables by

$$D_\mu \eta_a(\mathbf{r}) \mapsto \eta_{\mathbf{r}+\hat{\mu}}^a e^{-iA_{\mathbf{r},\mu}} - \eta_{\mathbf{r}}^a. \quad (15)$$

This ensures that the resulting lattice-discretized GL-theory remains invariant under the gauge-transformation

$$\begin{aligned} \eta_{\mathbf{r}}^a &\mapsto e^{i\lambda_{\mathbf{r}}} \eta_{\mathbf{r}}^a \\ A_{\mathbf{r},\mu} &\mapsto A_{\mathbf{r},\mu} + \Delta_\mu \lambda_{\mathbf{r}}, \end{aligned} \quad (16)$$

where $\lambda_{\mathbf{r}}$ is an arbitrary real field.

The resulting lattice theory is, from a renormalization point of view, a member of the same universality class as the continuum GL-model and is therefore expected to yield the same quantitative behaviour, at least in strongly type-II regime [61]. The remaining expressions for the discretized effective free energy density f^r are presented in Appendix B.

To measure ordering in each of the symmetry sectors at the phase transition, we introduce two order parameters. As discussed in section II C, the Z_2 transition is characterized by an imbalance between the chiral components introduced in Eq. (11). Hence, we can measure spontaneous symmetry-breaking of TRS using the chiral amplitude difference

$$\delta\eta_\pm = \left\langle \left| \frac{1}{L^3} \sum_{\mathbf{r}} |\eta_+(\mathbf{r})|^2 - |\eta_-(\mathbf{r})|^2 \right| \right\rangle. \quad (17)$$

This is zero in the high-temperature phase and tends to $2\rho_0^2$ in the low-temperature phase. The superconducting phase is characterized by a non-zero gauge field mass $m = \lambda_L^{-1}$. This can be computed via the dual stiffness [41]

$$\rho_{\mathbf{q}}^{\mu\mu} = \frac{1}{(2\pi)^2 L^3} \left\langle \left| \sum_{\mathbf{r}} (\Delta \times \mathbf{A})_\mu e^{i\mathbf{qr}} \right| \right\rangle \sim \frac{q^2}{q^2 + \lambda_L^{-2}}. \quad (18)$$

The low \mathbf{q} -limit of this expression tends to zero in the superconducting phase, where λ_L is finite, and some constant in the normal state, where λ_L is infinite. Hence, we measure the dual stiffness at the lowest non-zero momentum allowed by our discretization as an order parameter in the $U(1)$ -symmetry sector. Finally, both phase-transitions are accompanied by singularities in the specific heat

$$C_v = \beta^2 \langle (E - \langle E \rangle)^2 \rangle, \quad (19)$$

where β is the inverse temperature.

In numerical simulations, we thermalise systems of sizes up to 32^3 from both an ordered state given by Eqs. (2) and (3), or fully disordered states in some cases, over 3×10^5 Monte Carlo sweeps. We then make measurements of the energy, dual stiffness and chiral order parameter over 1×10^6 Monte Carlo sweeps. The measurements are done every 40'th sweep to account for the auto-correlation time. Ferrenberg-Swendsen multi histogram reweighting has been used to post-process the raw data [62, 63].

IV. RESULTS

In this section we present results from large scale Monte Carlo simulations using the parameter regime discussed in Sec. II B. For all simulations we have fixed $\alpha = 1.0$, $u_0 = 1.0$ and $g = 1.0$.

A. Model without mixed gradient terms

Results without MGT, $\gamma_m = 0$, are shown in Fig. 2. We find that ordering in both symmetry sectors occurs simultaneously. In Fig. 2a the chiral order parameter has a kink as it drops to zero at the critical temperature. The dual stiffness in Fig. 2b displays similar behaviour; in the Meissner phase, where λ_L is finite, it tends to zero and in the normal state it grows, as the thermal gauge fluctuations become larger. The normal phase and Meissner phase are separated by a jump in both order parameters accompanied by a singularity in the specific heat in Fig. 2c. In summary, we find that with decreasing temperature the system goes from a normal state to a chiral superconducting state with spontaneously broken $U(1) \times Z_2$ symmetry.

The fact that they coincide is explained by a preemptive phase transition scenario, discussed previously for multi-component superfluids and superconductors [40, 45], see the earlier discussion in terms of j -currents in [42]. The process of proliferating topological defects in the two symmetry sectors is cooperative. Namely, as the charged vortices in the $U(1)$ -sector proliferate, the stiffness of the Ising domain walls drops to zero triggering a proliferation in the Z_2 sector. The smoking gun signature of a preemptive phase transition is that it is first order, with a latent heat related to the sudden drop in the chiral/charged order parameters at the phase transition. An intuitive way of understanding this is to consider the case where the two symmetry sectors are completely decoupled. The chiral sector is then, with increasing temperature, headed towards a continuous second order phase transition in the Ising universality class. At some lower temperature, charged vortices in the $U(1)$ -sector will proliferate which also triggers the Z_2 phase transition due to the interplay between domain walls and vortices. This scenario is sketched in Fig. IV A, where the order parameters in both symmetry sectors are cut off at the

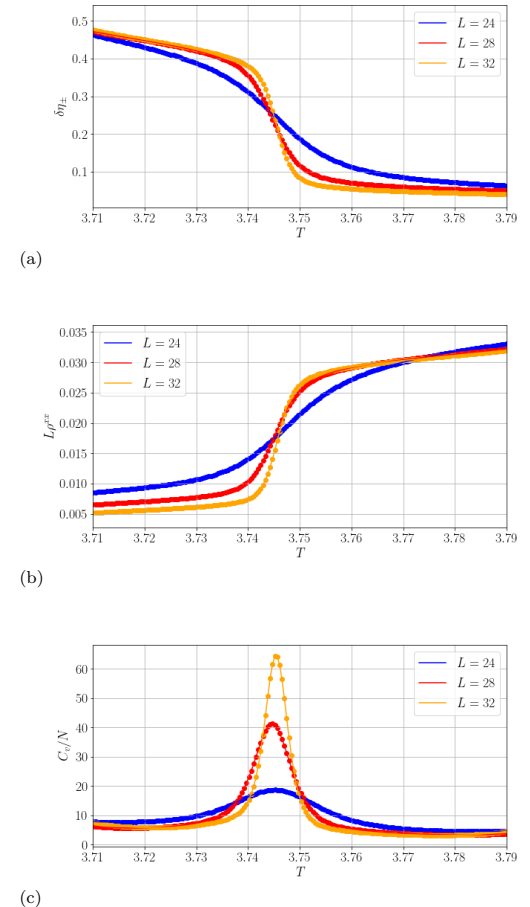


FIG. 2. Results from Monte Carlo simulations of model in Eq. (1) with $\gamma = 0.1$ and $\gamma_m = 0.0$ for $L = 24, 28, 32$. (a) Chiral amplitude difference given by Eq. (17). (b) Dual stiffness given by Eq. (18). (c) Specific heat given by Eq. (19). We find a single phase transition at $T_c \simeq 3.745$ characterized by ordering in both symmetry sectors and a singularity in the specific heat.

preemptive transition temperature resulting in a single first order transition. To investigate this numerically, we plot the energy probability distribution in Fig. 4a. We find a pronounced double peak, indicative of a first order phase transition where two phases co-exist at the critical temperature. Furthermore, we have performed a finite-size scaling analysis of the difference in free energy between the double peak value and the valley minimum $\Delta F = \ln(P_{max}/P_{min})/\beta$, where P_{max} and P_{min} are the energy probabilities at the double peak and the valley minimum, respectively. For a first order phase transi-

tion, this quantity should scale asymptotically as L^{d-1} [64] for large system sizes. Such scaling is confirmed in Fig. 4b.

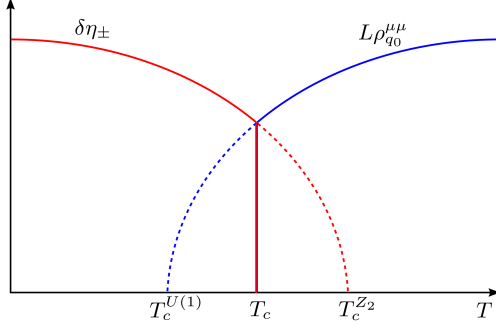
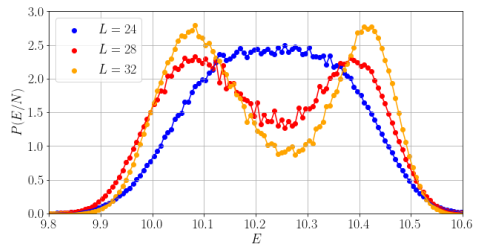


FIG. 3. Schematic drawing of the preemptive phase transition scenario. The chiral and charged order parameters would exhibit two separate continuous phase transitions, were it not for the mutual interplay between the two sectors. At some intermediate temperature, interplay between topological defects in the two symmetry sectors lead to ordering in both, resulting in a single first order phase transition at T_c .

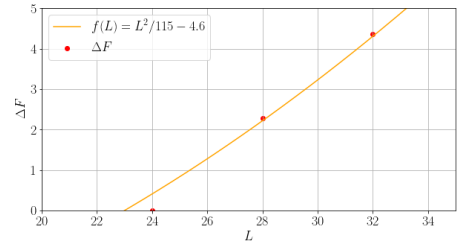
B. Full model

We now consider the full model in Eq. (1) and examine how the MGT modify results from the previous section. In Ref. [48] the MGT share coefficient with the Ising anisotropy term, so due to the restrictions on γ we stick to low values of γ_m . Fig. 5 shows results for the phase transition at $\gamma_m = 0.1$. The results are very similar to the case without MGT, which can be seen by comparing with Fig. 2. The critical temperature decreases slightly, and we can also see that finite size effects become more prominent as the peak in specific heat changes more with system size. To investigate whether this is still a preemptive phase transition, the energy probability distribution along with finite size scaling of ΔF are plotted in Fig. 6. We find a clear double peak and quadratic scaling, which both indicate a first order preemptive phase transition. By comparing with Fig. 4, we observe that the first order behavior is even stronger in case of non-zero MGT, as the double peak structure is now resolved for the smallest system with $L = 24$.

To characterize the strength of the transition, we calculate the difference in entropy between the two coexisting states at the phase transition. The entropy is calculated from the free energy $F = E - TS$. Because the two states have the same free energy the entropy difference is given by $\Delta S = \Delta E/T_c \equiv ck_b$. In Table I we show the coefficient c for the change in entropy per lattice site for



(a)



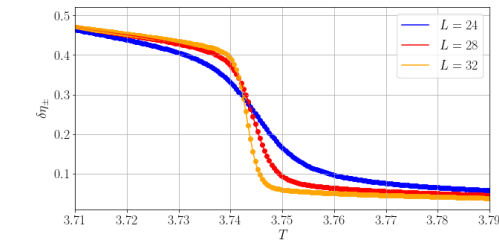
(b)

FIG. 4. (a) Energy per lattice site probability distribution at the critical temperature for system parameters $\gamma = 0.1$ and $\gamma_m = 0.0$ and system sizes $L = 24, 28, 32$. For larger system sizes we see an increasingly pronounced double peak, indicating a first order phase transition. (b) Finite size scaling of the difference in free energy between the double peak value P_{max} and the valley minimum P_{min} , $\Delta F = \ln(P_{max}/P_{min})/\beta$, measured at the critical point. Ferrenberg Swendsen multi histogram reweighting has been used to obtain histograms with peaks of similar height.

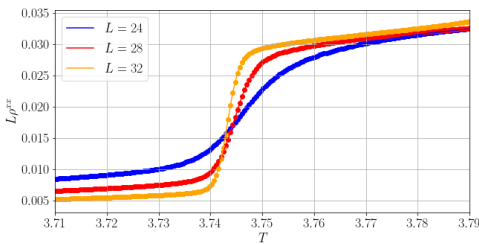
γ_m	T_c	c
0.0	3.745	0.091
0.1	3.743	0.120
0.2	3.736	0.121

TABLE I. Critical temperature T_c and coefficient for the change in entropy $\Delta S = ck_B$ for different strengths of the MGT with $\gamma = 0$. As γ_m increases the critical temperature decreases and the change in entropy increases, making the phase transition stronger first order. Data is taken from simulations with $L = 32$, and T_c is determined using multi histogram re-weighting to find the temperature where the two peaks in the energy probability distribution have the same height.

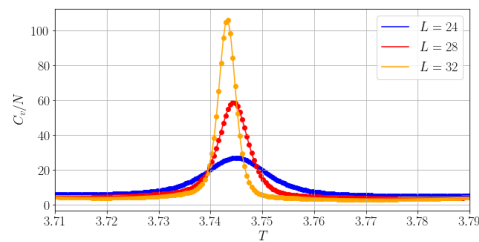
increasing values of γ_m . We see a significant increase from the case without to the case with MGT, meaning the phase transition becomes more strongly first order. As γ_m is increased further, this trend continues. This can be explained by the fact that the MGT introduce stronger interaction between vortices and domain walls that results in a larger latent heat and stronger first order behaviour.



(a)



(b)



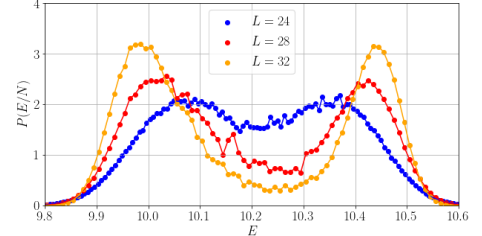
(c)

FIG. 5. Results from Monte Carlo simulations of model in Eq. (1) with $g = 1.0$, $\gamma = 0.1$ and $\gamma_m = 0.1$ for $L = 24, 28, 32$. (a) Chiral amplitude difference given by Eq. (17). (b) Dual stiffness given by Eq. (18). (c) Specific heat given by Eq. (19). We find a single phase transition at $T_c \approx 3.743$ characterized by ordering in both symmetry sectors and a singularity in the specific heat.

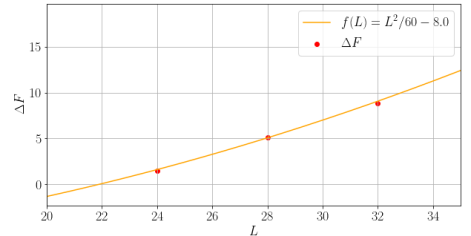
V. SUMMARY

In this paper we have investigated fluctuation effects on the phase transition in a GL model for chiral superconductivity. Within the parameter regime used, a single phase transition from the normal state to a chiral superconducting state with spontaneously broken $U(1) \times Z_2$

symmetry is found. We show that this is a preemptive first-order phase-transition, where interplay between the topological defects in both symmetry sectors cause them both to disorder at the same temperature. We have also



(a)



(b)

FIG. 6. (a) Energy per lattice site probability distribution at the critical temperature for system parameters $\gamma = 0.1$ and $\gamma_m = 0.1$ and system sizes $L = 24, 28, 32$. For larger system sizes we see an increasingly pronounced double peak, indicating a first order phase transition. (b) Finite size scaling of ΔF . Ferrenberg Swendsen multi histogram re-weighting has been used to obtain histograms with peaks of similar height.

investigated the effect of MGT, which enhance the first order character of the phase-transition.

VI. ACKNOWLEDGEMENTS

We acknowledge financial support from the Research Council of Norway Grant No. 262633 “Center of Excellence on Quantum Spintronics,” and Grant No. 250985, “Fundamentals of Low Dissipative Topological Matter.” EB was supported by the Swedish Research Council Grants 2016-06122, 2018-03659, the Göran Gustafsson Foundation for Research in Natural Sciences and Medicine.

[1] C. Kallin and J. Berlinsky, *Reports on Progress in Physics* **79**, 054502 (2016).

[2] N. Read and D. Green, *Physical Review B* **61**, 10267 (2000).

- [3] M. Stone and R. Roy, *Phys. Rev. B* **69**, 184511 (2004).
- [4] T. Senthil, J. B. Marston, and M. P. A. Fisher, *Phys. Rev. B* **60**, 4245 (1999).
- [5] Y. Imai, K. Wakabayashi, and M. Sigrist, *Phys. Rev. B* **93**, 024510 (2016).
- [6] P. W. Anderson and P. Morel, *Phys. Rev. Lett.* **5**, 136 (1960).
- [7] P. W. Anderson and W. F. Brinkman, *Phys. Rev. Lett.* **30**, 1108 (1973).
- [8] R. Balian and N. R. Werthamer, *Phys. Rev.* **131**, 1553 (1963).
- [9] Y. Maeno, H. Hashimoto, K. Yoshida, S. Nishizaki, T. Fujita, J. G. Bednorz, and F. Lichtenberg, *Nature* **372**, 532 (1994).
- [10] G. M. Luke, Y. Fudamoto, K. M. Kojima, M. I. Larkin, J. Merrin, B. Nachumi, Y. J. Uemura, Y. Maeno, Z. Q. Mao, Y. Mori, H. Nakamura, and M. Sigrist, *Nature* **394**, 558 (1998).
- [11] J. Xia, Y. Maeno, P. T. Beyersdorf, M. M. Fejer, and A. Kapitulnik, *Phys. Rev. Lett.* **97**, 167002 (2006).
- [12] J. Jang, D. G. Ferguson, V. Vakaryuk, R. Budakian, S. B. Chung, P. M. Goldbart, and Y. Maeno, *Science* **331**, 186 (2011).
- [13] A. P. Mackenzie, T. Scaffidi, C. W. Hicks, and Y. Maeno, *npj Quantum Materials* **2**, 40 (2017).
- [14] A. Damascelli, D. H. Lu, K. M. Shen, N. P. Armitage, F. Ronning, D. L. Feng, C. Kim, Z.-X. Shen, T. Kimura, Y. Tokura, Z. Q. Mao, and Y. Maeno, *Phys. Rev. Lett.* **85**, 5194 (2000).
- [15] S. Nishizaki, Y. Maeno, S. Farner, S. Ikeda, and T. Fujita, *Physica C: Superconductivity* **282-287**, 1413 (1997).
- [16] V. Grinenko, D. Das, R. Gupta, B. Zinkl, N. Kikugawa, Y. Maeno, C. W. Hicks, H.-H. Klauss, M. Sigrist, and R. Khasanov, *arXiv preprint arXiv:2103.03600* (2021).
- [17] V. Grinenko, S. Ghosh, R. Sarkar, J.-C. Orain, A. Nikitin, M. Elender, D. Das, Z. Guguchia, F. Brückner, M. E. Barber, *et al.*, *arXiv preprint arXiv:2001.08152* (2020).
- [18] P. J. Curran, S. J. Bending, W. M. Desoky, A. S. Gibbs, S. L. Lee, and A. P. Mackenzie, *Phys. Rev. B* **89**, 144504 (2014).
- [19] J. Kirtley, C. Kallin, C. Hicks, E.-A. Kim, Y. Liu, K. Moler, Y. Maeno, and K. Nelson, *Physical Review B* **76**, 014526 (2007).
- [20] C. W. Hicks, J. R. Kirtley, T. M. Lippman, N. C. Koshnick, M. E. Huber, Y. Maeno, W. M. Yuhasz, M. B. Maple, and K. A. Moler, *Physical Review B* **81**, 214501 (2010).
- [21] A. Romer, D. Scherer, I. Eremin, P. Hirschfeld, and B. Andersen, *Physical review letters* **123**, 247001 (2019).
- [22] S. A. Kivelson, A. C. Yuan, B. Ramshaw, and R. Thomale, *npj Quantum Materials* **5**, 1 (2020).
- [23] S. Ghosh, A. Shekhter, F. Jerzembeck, N. Kikugawa, D. A. Sokolov, M. Brando, A. Mackenzie, C. W. Hicks, and B. Ramshaw, *Nature Physics* **17**, 199 (2021).
- [24] S. Benhabib, C. Lupien, I. Paul, L. Berges, M. Dion, M. Nardone, A. Zitouni, Z. Mao, Y. Maeno, A. Georges, *et al.*, *Nature physics* **17**, 194 (2021).
- [25] S. Ray, A. Gibbs, S. Bending, P. Curran, E. Babaev, C. Baines, A. Mackenzie, and S. Lee, *Physical Review B* **89**, 094504 (2014).
- [26] R. Joynt and L. Taillefer, *Rev. Mod. Phys.* **74**, 235 (2002).
- [27] J. D. Strand, D. J. Van Harlingen, J. B. Kycia, and W. P. Halperin, *Phys. Rev. Lett.* **103**, 197002 (2009).
- [28] E. R. Schemm, W. J. Gannon, C. M. Wishne, W. P. Halperin, and A. Kapitulnik, *Science* **345**, 190 (2014).
- [29] R. A. Fisher, S. Kim, B. F. Woodfield, N. E. Phillips, L. Taillefer, K. Hasselbach, J. Flouquet, A. L. Giorgi, and J. L. Smith, *Phys. Rev. Lett.* **62**, 1411 (1989).
- [30] S. Adenwalla, S. W. Lin, Q. Z. Ran, Z. Zhao, J. B. Kettersson, J. A. Sauls, L. Taillefer, D. G. Hinks, M. Levy, and B. K. Sarma, *Phys. Rev. Lett.* **65**, 2298 (1990).
- [31] K. E. Avers, W. J. Gannon, S. J. Kuhn, W. P. Halperin, J. A. Sauls, L. DeBeer-Schmitt, C. D. Dewhurst, J. Gavilano, G. Nagy, U. Gasser, and M. R. Eskildsen, *Nature Physics* **16**, 531 (2020).
- [32] J. Sauls, *Advances in Physics* **43**, 113 (1994).
- [33] A. Ribak, R. M. Skiff, M. Mograbi, P. Rout, M. Fischer, J. Ruhman, K. Chashka, Y. Dagan, and A. Kanigel, *Science advances* **6**, eaax9480 (2020).
- [34] F. Qin, W. Shi, T. Ideue, M. Yoshida, A. Zak, R. Tenne, T. Kikitsu, D. Inoue, D. Hashizume, and Y. Iwasa, *Nature communications* **8**, 1 (2017).
- [35] L. Jiao, S. Howard, S. Ran, Z. Wang, J. O. Rodriguez, M. Sigrist, Z. Wang, N. P. Butch, and V. Madhavan, *Nature* **579**, 523 (2020).
- [36] T. A. Bojesen, E. Babaev, and A. Sudbø, *Phys. Rev. B* **88**, 220511 (2013).
- [37] T. A. Bojesen, E. Babaev, and A. Sudbø, *Phys. Rev. B* **89**, 104509 (2014).
- [38] V. Grinenko, D. Weston, F. Caglieris, C. Wuttke, C. Hess, T. Gottschall, J. Wosnitza, A. Rydh, K. Kihou, C.-H. Lee, R. Sarkar, S. Dengre, I. Maccari, J. Garaud, A. Charnukha, R. Hühne, K. Nielsch, B. Büchner, H.-H. Klauss, and E. Babaev, *arXiv preprint arXiv:2103.17190* (2021).
- [39] M. H. Fischer and E. Berg, *Physical Review B* **93**, 054501 (2016).
- [40] E. V. Herland, E. Babaev, and A. Sudbø, *Phys. Rev. B* **82**, 134511 (2010).
- [41] J. Smiseth, E. Smørgrav, E. Babaev, and A. Sudbø, *Phys. Rev. B* **71**, 214509 (2005).
- [42] A. Kuklov, N. Prokof'Ev, B. Svistunov, and M. Troyer, *Annals of Physics* **321**, 1602 (2006).
- [43] E. Babaev, *Nuclear Physics B* **686**, 397 (2004).
- [44] E. Babaev, A. Sudbø, and N. Ashcroft, *Nature* **431**, 666 (2004).
- [45] E. Dahl, E. Babaev, S. Kragset, and A. Sudbø, *Physical Review B* **77**, 144519 (2008).
- [46] A. Kuklov, M. Matsumoto, N. Prokof'Ev, B. Svistunov, and M. Troyer, *Physical review letters* **101**, 050405 (2008).
- [47] E. V. Herland, T. A. Bojesen, E. Babaev, and A. Sudbø, *Phys. Rev. B* **87**, 134503 (2013).
- [48] D. F. Agterberg, *Phys. Rev. Lett.* **80**, 5184 (1998).
- [49] F. N. Krogh and A. Sudbø, *Phys. Rev. B* **98**, 014510 (2018).
- [50] M. Sigrist and K. Ueda, *Rev. Mod. Phys.* **63**, 239 (1991).
- [51] J. Garaud, E. Babaev, T. A. Bojesen, and A. Sudbø, *Phys. Rev. B* **94**, 104509 (2016).
- [52] M. Speight, T. Winyard, and E. Babaev, *Physical Review B* **100**, 174514 (2019).
- [53] D. F. Agterberg, *Phys. Rev. B* **58**, 14484 (1998).
- [54] R. Heeb and D. F. Agterberg, *Phys. Rev. B* **59**, 7076 (1999).

- [55] C. Dasgupta and B. I. Halperin, *Phys. Rev. Lett.* **47**, 1556 (1981).
- [56] A. K. Nguyen and A. Sudbø, *Phys. Rev. B* **60**, 15307 (1999).
- [57] A. Shimizu, H. Ozawa, I. Ichinose, and T. Matsui, *Phys. Rev. B* **85**, 144524 (2012).
- [58] H. G. Katzgraber, “Introduction to Monte Carlo Methods,” (2009), arXiv:0905.1629.
- [59] W. H. Press, S. A. Teukolsky, W. T. Vetterling, and B. P. Flannery, *Numerical Recipes*, 3rd ed. (Cambridge Univ. Press, 2007).
- [60] M. Newman and G. Barkema, *Monte Carlo Methods in Statistical Physics* (Clarendon Press, 1999).
- [61] A. K. Nguyen and A. Sudbø, *Phys. Rev. B* **60**, 15307 (1999).
- [62] A. M. Ferrenberg and R. H. Swendsen, *Phys. Rev. Lett.* **61**, 2635 (1988).
- [63] A. M. Ferrenberg and R. H. Swendsen, *Computers in Physics* **3**, 101 (1989).
- [64] J. Lee and J. M. Kosterlitz, *Phys. Rev. Lett.* **65**, 137 (1990).

Appendix A: Coupling matrix

The energy in Eq. (1) is expanded to second order in the fluctuation fields introduced in Eqs. (4)-(6). For the

potential in Eq. (1a), we find

$$\begin{aligned} f_V = & -\alpha(u_x^2 + u_y^2) + \frac{u_0}{2}(u_x^4 + u_y^4) - \gamma u_x^2 u_y^2 \\ & + (-\alpha + 3u_0 u_x^2 - \gamma u_y^2)\epsilon_x^2 + (-\alpha + 3u_0 u_y^2 - \gamma u_x^2)\epsilon_y^2 \\ & - 4\gamma u_x u_y \epsilon_x \epsilon_y + 8\gamma u_x^2 u_y^2 \theta_\Delta^2, \end{aligned} \quad (\text{A1})$$

where f_0 is the ground state energy. The Maxwell term keeps the exact same form to second order in \mathbf{p} , since it only differs by a gradient from \mathbf{A}

$$f_A = |\nabla \times \mathbf{p}|^2. \quad (\text{A2})$$

Finally for the various gradient terms, we expand the gradients to first order since all relevant combinations are squared

$$D_i \eta_x = [\partial_i \epsilon_x - i(gp_i - \partial_i \theta_\Delta)u_x] e^{i(\theta_\Sigma + \theta_0/2)}, \quad (\text{A3})$$

$$D_i \eta_y = [\partial_i \epsilon_y - i(gp_i + \partial_i \theta_\Delta)u_y] e^{i(\theta_\Sigma - \theta_0/2)}. \quad (\text{A4})$$

These expressions can now be combined to form all the terms in the energy functional. After Fourier transforming and rotating the amplitude basis, we can write the energy on the form in Eq. (8)

$$f = f_0 + \mathbf{v} \mathbf{G} \mathbf{v}^\dagger. \quad (\text{A5})$$

where \mathbf{v} is given in Eq. (9). We can write the coupling matrix as a sum of three contributions, a diagonal part with massive terms, a diagonal part with k -dependant terms and an off-diagonal part from the MGT.

$$\mathbf{G} = \mathbf{G}_D + \mathbf{G}_{MGT} \quad (\text{A6})$$

$$\mathbf{G}_D = \begin{pmatrix} \frac{2\alpha(u_0+\gamma)}{u_0-\gamma} + k^2 & 0 & 0 & 0 & 0 \\ 0 & 2\alpha + k^2 & 0 & 0 & 0 \\ 0 & 0 & \frac{8\gamma\alpha^2}{(u_0-\gamma)^2} + \frac{2\alpha}{u_0-\gamma}k^2 & 0 & 0 \\ 0 & 0 & 0 & \frac{2\alpha}{u_0-\gamma}g^2 + k^2 & 0 \\ 0 & 0 & 0 & 0 & \frac{2\alpha}{u_0-\gamma}g^2 + k^2 \end{pmatrix} \quad (\text{A7})$$

$$\mathbf{G}_{MGT} = \pm \gamma_m \sqrt{\frac{2\alpha}{u_0 - \gamma}} \begin{pmatrix} 0 & 0 & -2k_x k_y & 0 & 0 \\ 0 & 0 & 0 & -igk_y & -igk_x \\ -2k_x k_y & 0 & 0 & 0 & 0 \\ 0 & igk_y & 0 & 0 & 0 \\ 0 & igk_x & 0 & 0 & 0 \end{pmatrix} \quad (\text{A8})$$

In Eq. (A7), we note that the Meissner effect gives rise to massive gauge-field fluctuations, which yield a massless Goldstone mode associated with the phase-sum when $g = 0$. The phase-difference mode is also seen to evolve to a massless Goldstone mode when the Ising-anisotropy

parameter $\gamma = 0$. Furthermore, Eq. (A8) shows that the MGT have an effect for $g = 0$, coupling fluctuations in the ϵ_+ amplitude mode to fluctuations in the phase difference θ_Δ . Finite g will moreover couple the ϵ_- amplitude mode to gauge-invariant currents. Contrary to the

one-component case, the eigenmodes are in general complicated linear combinations of amplitude modes, phase-difference modes, and gauge-invariant currents [52]. Only in a limited parameter regime do the eigenmodes simplify significantly.

Appendix B: Lattice regularized free energy

In this section we apply the regularization procedure introduced in Section III to the dimensionless effective free energy density in Eq. (1). The resulting expression was used in the Metropolis-Hastings algorithm to find the energy-difference between different field-configurations as well as when calculating the energy as an observable which again was used in calculating of the specific heat.

Inserting the discretization of the covariant derivative in Eq. (15) yields

$$\begin{aligned} |D_\mu \eta_a|^2 &\mapsto |\eta_{\mathbf{r}+\hat{\mu}}^a|^2 + |\eta_{\mathbf{r}}^a|^2 - 2 \operatorname{Re} (\eta_{\mathbf{r}+\hat{\mu}}^a \eta_{\mathbf{r}}^{a*} e^{-iA_{\mathbf{r},\mu}}) \\ &\quad - 2 \left[(\rho_{\mathbf{r}}^a)^2 - \rho_{\mathbf{r}+\hat{\mu}}^a \rho_{\mathbf{r}}^a \cos(\theta_{\mathbf{r}+\hat{\mu}}^a - \theta_{\mathbf{r}}^a - A_{\mathbf{r},\mu}) \right]. \end{aligned} \quad (B1)$$

In the second line we have introduced the notation $\eta_{\mathbf{r}}^a = \rho_{\mathbf{r}}^a e^{i\theta_{\mathbf{r}}^a}$ for the amplitude and phase of the components of the order parameter. We have also used periodic boundary conditions to map the term $|\eta_{\mathbf{r}+\hat{\mu}}^a|^2$ back to $|\eta_{\mathbf{r}}^a|^2$ by a simple shift of the index in the sum $\sum_{\mathbf{r}} f_{\mathbf{r}}$.

Using the formula above we immediately get the lattice-regularized conventional kinetic energy density

$$\begin{aligned} f_K^r &= \operatorname{reg} \left\{ \sum_a |D_\mu \eta_a|^2 \right\} = \sum_{\mu a} \operatorname{reg} \{ |D_\mu \eta_a|^2 \} \\ &= 2 \sum_{\mu a} \left[(\rho_{\mathbf{r}}^a)^2 - \rho_{\mathbf{r}+\hat{\mu}}^a \rho_{\mathbf{r}}^a \cos(\theta_{\mathbf{r}+\hat{\mu}}^a - \theta_{\mathbf{r}}^a - A_{\mathbf{r},\mu}) \right], \end{aligned} \quad (B2)$$

where μ runs over x, y and z , while $a \in \{x, y\}$. Using the notation

$$\bar{a} = \begin{cases} y & : a = x \\ x & : a = y \end{cases}. \quad (B3)$$

the MGT in Eq. (1c) can be written on the more compact form

$$f_{\text{MGT}} = 2\gamma_m \sum_a \operatorname{Re} \left[D_x \eta_a (D_y \eta_{\bar{a}})^* \right]. \quad (B4)$$

Inserting the discretization of covariant derivatives we find in Eq. (15) gives

$$\begin{aligned} D_x \eta_a (D_y \eta_{\bar{a}})^* &= \left(\rho_{\mathbf{r}+\hat{x}}^a e^{i(\theta_{\mathbf{r}+\hat{x}}^a - A_{\mathbf{r},x})} - \rho_{\mathbf{r}}^a e^{i\theta_{\mathbf{r}}^a} \right) \\ &\quad \times \left(\rho_{\mathbf{r}+\hat{y}}^{\bar{a}} e^{-i(\theta_{\mathbf{r}+\hat{y}}^{\bar{a}} - A_{\mathbf{r},y})} - \rho_{\mathbf{r}}^{\bar{a}} e^{-i\theta_{\mathbf{r}}^{\bar{a}}} \right) \\ &= \rho_{\mathbf{r}+\hat{x}}^a \rho_{\mathbf{r}+\hat{y}}^{\bar{a}} e^{i(\theta_{\mathbf{r}+\hat{x}}^a - \theta_{\mathbf{r}+\hat{y}}^{\bar{a}} - (A_{\mathbf{r},x} - A_{\mathbf{r},y}))} \\ &\quad - \rho_{\mathbf{r}+\hat{x}}^a \rho_{\mathbf{r}}^{\bar{a}} e^{i(\theta_{\mathbf{r}+\hat{x}}^a - \theta_{\mathbf{r}}^{\bar{a}} - A_{\mathbf{r},x})} \\ &\quad - \rho_{\mathbf{r}}^a \rho_{\mathbf{r}+\hat{y}}^{\bar{a}} e^{-i(\theta_{\mathbf{r}+\hat{y}}^{\bar{a}} - \theta_{\mathbf{r}}^a - A_{\mathbf{r},y})} \\ &\quad + \rho_{\mathbf{r}}^a \rho_{\mathbf{r}}^{\bar{a}} e^{i(\theta_{\mathbf{r}}^a - \theta_{\mathbf{r}}^{\bar{a}})} \end{aligned} \quad (B5)$$

Taking the real part of this gives

$$\begin{aligned} \operatorname{Re} \left[D_x \eta_a (D_y \eta_{\bar{a}})^* \right] &= \rho_{\mathbf{r}+\hat{x}}^a \rho_{\mathbf{r}+\hat{y}}^{\bar{a}} \cos(\theta_{\mathbf{r}+\hat{x}}^a - \theta_{\mathbf{r}+\hat{y}}^{\bar{a}} - (A_{\mathbf{r},x} - A_{\mathbf{r},y})) \\ &\quad - \rho_{\mathbf{r}+\hat{x}}^a \rho_{\mathbf{r}}^{\bar{a}} \cos(\theta_{\mathbf{r}+\hat{x}}^a - \theta_{\mathbf{r}}^{\bar{a}} - A_{\mathbf{r},x}) \\ &\quad - \rho_{\mathbf{r}+\hat{y}}^{\bar{a}} \rho_{\mathbf{r}}^a \cos(\theta_{\mathbf{r}+\hat{y}}^{\bar{a}} - \theta_{\mathbf{r}}^a - A_{\mathbf{r},y}) \\ &\quad + \rho_{\mathbf{r}}^a \rho_{\mathbf{r}}^{\bar{a}} \cos(\theta_{\mathbf{r}}^a - \theta_{\mathbf{r}}^{\bar{a}}), \end{aligned} \quad (B6)$$

This gives the final expression for the discretized MGT

$$\begin{aligned} f_{\text{MGT}}^r &= 2\gamma_m \sum_a \left[\rho_{\mathbf{r}}^a \rho_{\mathbf{r}}^{\bar{a}} \cos(\theta_{\mathbf{r}}^a - \theta_{\mathbf{r}}^{\bar{a}}) \right. \\ &\quad - \rho_{\mathbf{r}+\hat{x}}^a \rho_{\mathbf{r}}^{\bar{a}} \cos(\theta_{\mathbf{r}+\hat{x}}^a - \theta_{\mathbf{r}}^{\bar{a}} - A_{\mathbf{r},x}) \\ &\quad - \rho_{\mathbf{r}+\hat{y}}^{\bar{a}} \rho_{\mathbf{r}}^a \cos(\theta_{\mathbf{r}+\hat{y}}^{\bar{a}} - \theta_{\mathbf{r}}^a - A_{\mathbf{r},y}) \\ &\quad \left. + \rho_{\mathbf{r}+\hat{x}}^a \rho_{\mathbf{r}+\hat{y}}^{\bar{a}} \cos(\theta_{\mathbf{r}+\hat{x}}^a - \theta_{\mathbf{r}+\hat{y}}^{\bar{a}} - (A_{\mathbf{r},x} - A_{\mathbf{r},y})) \right], \end{aligned} \quad (B7)$$

where we have switched the superscripts $a \leftrightarrow \bar{a}$ on the third line. To ensure that this discretized term is rendered invariant under the four-fold rotations of the square numerical lattice, we may average as follows

$$f_{\text{MGT}}^r \rightarrow \tilde{f}_{\text{MGT}}^r \quad (B8)$$

$$= \frac{1}{4} [f_{\text{MGT}}^r + C_4 f_{\text{MGT}}^r + C_4^2 f_{\text{MGT}}^r + C_4^3 f_{\text{MGT}}^r] \quad (B9)$$

where C_4 denotes a 90 degree counterclockwise rotation of the xy-coordinate system. We then find

$$\begin{aligned} \tilde{f}_{\text{MGT}}^r &= \frac{\gamma_m}{2} \sum_a \left[\rho_{\mathbf{r}+\hat{x}}^a \rho_{\mathbf{r}+\hat{y}}^{\bar{a}} \cos(\theta_{\mathbf{r}+\hat{x}}^a - \theta_{\mathbf{r}+\hat{y}}^{\bar{a}} - (A_{\mathbf{r},x} - A_{\mathbf{r},y})) \right. \\ &\quad - \rho_{\mathbf{r}-\hat{x}}^a \rho_{\mathbf{r}+\hat{y}}^{\bar{a}} \cos(\theta_{\mathbf{r}-\hat{x}}^a - \theta_{\mathbf{r}+\hat{y}}^{\bar{a}} + (A_{\mathbf{r}-\hat{x},x} + A_{\mathbf{r},y})) \\ &\quad + \rho_{\mathbf{r}-\hat{x}}^a \rho_{\mathbf{r}-\hat{y}}^{\bar{a}} \cos(\theta_{\mathbf{r}-\hat{x}}^a - \theta_{\mathbf{r}-\hat{y}}^{\bar{a}} - (A_{\mathbf{r}-\hat{y},y} - A_{\mathbf{r}-\hat{x},x})) \\ &\quad \left. - \rho_{\mathbf{r}+\hat{x}}^a \rho_{\mathbf{r}-\hat{y}}^{\bar{a}} \cos(\theta_{\mathbf{r}+\hat{x}}^a - \theta_{\mathbf{r}-\hat{y}}^{\bar{a}} - (A_{\mathbf{r},x} + A_{\mathbf{r}-\hat{y},y})) \right], \end{aligned} \quad (B10)$$

The potential terms in Eq. (1) are simply discretized by mapping to the amplitude phase-notation and become

$$f_V^r = \sum_a \left[-\alpha(\rho_{\mathbf{r}}^a)^2 + \frac{u_0}{2}(\rho_{\mathbf{r}}^a)^4 \right] + \gamma(\rho_{\mathbf{r}}^x \rho_{\mathbf{r}}^y)^2 \cos 2(\theta_{\mathbf{r}}^x - \theta_{\mathbf{r}}^y). \quad (B11)$$

These expressions together with the regularization of the pure gauge-potential term in Eq. (14) then give the complete discretized free energy density

$$f^r = f_V^r + f_K^r + \tilde{f}_{\text{MGT}}^r + f_A^r. \quad (B12)$$